RECOMBINATION DYNAMICS IN III-NITRIDE QUANTUM WELLS OF VARIOUS CRYSTAL ORIENTATIONS

Von der Fakultät für Elektrotechnik, Informationstechnik, Physik
der Technischen Universität Carolo-Wilhelmina zu Braunschweig

zur Erlangung des Grades eines Doktors
der Naturwissenschaften (Dr. rer. nat.)

genehmigte Dissertation

von Philipp Henning

aus Kassel

eingereicht am: 17.12.2020

Disputation am: 24.03.2021

1. Referent: Prof. Dr. Andreas Hangleiter

2. Referent: Prof. Dr. Jürgen Gutowski

Druckjahr: 2021

Dedicated to my family.

ZUSAMMENFASSUNG

Die vorliegende Arbeit beschäftigt sich mit der Rekombinationsdynamik in Gruppe-III-Nitrid-Quantenfilmen, die das Herzstück jeder modernen Leuchtdiode darstellen. Insbesondere die Rekombinationsprozesse von GaInN/GaN-Quantenfilmen verschiedener Kristallorientierungen werden mithilfe von zeitaufgelöster Photolumineszenzspektroskopie untersucht, was Einblicke in grundlegende Materialeigenschaften, sowie in Verlustprozesse erlaubt.

Auf der einen Seite verdeutlichen die Ergebnisse den Einfluss von Verzerrung und Quantenfilmdicke auf die strahlende Rekombination in Quantenfilmen in nicht-polarer Kristallorientierung. Verglichen mit polaren c-planaren Strukturen, bei denen die strahlende Rekombination den internen Polarisationsfeldern, und damit dem „Quantum-confined Stark-Effekt“ unterworfen ist, zeigen nicht-polare Quantenfilme eine deutlich erhöhte strahlende Emission. Die Kombination von verschwindendem piezoelektrischem Feld, erhöhter Exzitonen-Bindungsenergie, sowie anisotroper Verzerrung, die die Valenzbandstruktur beeinflusst und zu höheren effektiven Lochmassen führt, erklären diesen Umstand. Durch eine teilweise relaxierte AlInN-Pufferschicht wird der Einfluss der Verzerrung zwar verringert, die strahlende Rekombination ist im Vergleich zu c-planaren Strukturen jedoch nach wie vor gesteigert. Des Weiteren nimmt die strahlende Emission von nicht-polaren Quantenfilmen mit zunehmender Quantenfilmdicke signifikant ab, was mit verbotenen Dipolübergängen im feldfreien Quantenfilm zusammenhängt. Darüber hinaus wird für Quantenfilme jeglicher Orientierungen eine drastische Abnahme der strahlenden Rate bei erhöhten Temperaturen beobachtet, die in der Flucht von Ladungsträgern in die Barrieren, oder in Exzitonendissoziation begründet ist.

Auf der anderen Seite hängt die Verzerrung mit der strahlungslosen Rekombination über Defektzustände zusammen, wie in semi-polaren Quantenfilmen beobachtet. Frühere Ergebnisse zeigten einen ähnlichen Effekt für c-planare Quantenfilme. Durch eine verspannungsreduzierende AlInN-Pufferschicht kann die nicht-strahlende Rekombination signifikant reduziert werden, was perspektivisch die Überwindung des „green gap“ ermöglicht.

Schließlich wird eine verlässliche Methode zur Bestimmung der internen Quanteneffizienz, die durch das Wechselspiel von strahlender und strahlungsloser Rekombination festgelegt ist, eingeführt. Indem die charakteristische Temperaturabhängigkeit von strahlender und strahlungsloser Rekombinationsrate über den gesamten Temperaturbereich modelliert wird, kann ein zuverlässiger Indikator für das Fehlen

strahlungsloser Prozesse bei kryogenen Temperaturen gefunden werden: Ein synchroner Anstieg von effektiver und strahlender Lebensdauer der Ladungsträger mit der Temperatur belegt eine interne Quanteneffizienz von 100%. Dies ermöglicht die Messung von absoluten internen Quanteneffizienzen.

ABSTRACT

The present research focuses on the recombination dynamics in III-nitride quantum wells, which represent the key structures for modern solid state lighting. In particular, the recombination processes in GaInN/GaN quantum wells of various crystal orientations are measured by time-resolved photoluminescence spectroscopy, which allows insight into basic material properties and loss mechanisms.

On the one hand, the results emphasize the effects of strain and well width on the radiative recombination in quantum wells in nonpolar orientations. Compared to polar c-plane structures, where the radiative recombination is dominated by the internal polarization fields, and the quantum-confined Stark effect, nonpolar quantum wells show significantly increased radiative emission. This can be explained by a combination of the vanishing piezoelectric polarization, an enhanced exciton binding energy, and, beyond that, the anisotropic in-plane strain that affects the valence band structure, leading to higher effective hole masses. Introducing a partially relaxed AlInN buffer layer reduces the impact of strain, but still yields enhanced radiative recombination compared to c-plane structures. Additionally, the radiative emission of nonpolar quantum wells is decreasing significantly for larger well widths, which is related to forbidden dipole transitions in the field-free quantum well. Furthermore, a drastic reduction of the radiative rate is found towards higher temperatures for quantum wells of all orientations, related to the loss of charge carriers into the barriers, or even exciton dissociation.

On the other hand, strain is found to be related to defect-related nonradiative recombination in semipolar quantum wells. Previously, a similar effect was observed for c-plane quantum wells. By introducing a strain-reducing, partially relaxed AlInN buffer layer, the nonradiative recombination can be reduced significantly, which opens a perspective to overcome the *green gap*.

Finally, a reliable determination of the internal quantum efficiency, given by the interplay of radiative and nonradiative recombination, is introduced. Modeling the characteristic temperature dependence of radiative and nonradiative recombination rates over the whole temperature range, a safe indicator for the absence of nonradiative recombination at cryogenic temperatures is developed. Namely, a synchronous rise of the effective and radiative carrier lifetimes with temperature indicates an internal quantum efficiency of 100%. Thereby, the measurement of absolute internal quantum efficiencies becomes possible.

CONTENTS

II RESULTS

III SUMMARY

APPENDIX

INTRODUCTION

More light!
— J. W. von Goethe, 1832

In over thirty years, the research on III-nitride semiconductors has made huge progress. This was highlighted by the Nobel Prize in 2014, which was awarded for the invention of efficient blue light-emitting diodes [1]. Structures and devices based on gallium nitride (GaN), indium nitride (InN), and aluminum nitride (AlN) have a high potential for applications, ranging from high-frequency and power electronics to light emitters that cover the whole visible spectral range, extending into the ultraviolet and infrared spectrum [2–5]. The past years have shown that these technologies become more and more mature, and yield increasing importance in everyday life. Also, the light-emitting devices show high efficiencies, close to unity, nowadays.

This marks a huge technological progress, especially when visualizing the major drawbacks that the III-nitride material system brings along. First and foremost, the fabrication of material with high crystalline quality is extremely challenging, and usually relies on the epitaxial growth on foreign substrates [6, 7]. Also high-quality material exhibits relatively large defect densities, as compared to other semiconductors like gallium arsenide or even silicon. Additionally, large internal polarization fields that occur especially in heterostructures, or quantum wells, complicate their utilization for light emission, particularly on the basal c-plane, where the manufacturing methods are most mature [8].

At the same time, issues regarding the basic physical properties of the III-nitride material system itself are not yet fully explored. This includes the effect of strain on the crystalline material, which affects not only basic semiconductor properties like band gap or effective carrier mass, but is also involved in material degradation by formation of crystal defects [9]. Therefore, strain and related effects are considered to be of tremendous importance in the III-nitride material system. Also, the understanding of processes on other crystal orientations than the basal c-plane is often meeting its limits. These fundamental issues come along with application-related problems, which remain unsolved up to now. This includes the so-called *green gap*, i.e. the drastically reduced efficiency of light emitters in the green spectral range and beyond, or the efficiency droop for large driving currents of such devices [2, 10]. Also the details of charge carrier recombination dynamics are not fully understood in

III-nitride structures, since the well-known ABC model, usually used to describe recombination in semiconductors, is found to be invalid in the III-nitrides [11–13]. Furthermore, a reliable determination of quantum efficiencies in III-nitride structures is challenging [14].

The present thesis focuses on recombination dynamics in III-nitride quantum wells, measured by time-resolved photoluminescence spectroscopy, which provides a powerful tool to determine the recombination behavior of charge carriers. Thereby, insight into the basic material properties is gained, which in turn determine the radiative emission, as well as the nonradiative loss processes in quantum well structures. The investigated structures consist of GaInN/GaN quantum wells on various crystal orientations. Further, the influence of the structural parameters like composition and quantum well width are examined, as well as the impact of underlayers on the recombination dynamics.

This work is divided into three parts, covering the theoretical and experimental background (part I), the experimental results (part II), and finally, the summary and outlook (part III). In Ch. 1, the theoretical background of the III-nitride material system in general, and GaInN/GaN quantum wells in particular, is introduced. Ch. 2 covers the background of radiative and nonradiative recombination processes, while Ch. 3 describes the experimental details, including the measurement setups and evaluation methods. In Ch. 4, results on the radiative recombination, especially in nonpolar quantum wells, are presented. This includes the dependence of the radiative emission on strain and quantum well width, complemented by band structure calculations, as well as the identification of loss mechanisms at elevated temperatures. Ch. 5 covers the reduction of nonradiative recombination in semipolar quantum wells, making use of strain-reducing buffer layers. There, possible origins and approaches to overcome the *green gap* are discussed. At last, using the distinct temperature behavior of radiative and nonradiative lifetime, a method to determine absolute values of the internal quantum efficiency is developed in Ch. 6. Finally, the results are summarized in Ch. 7. Note that the appendix contains information about the investigated samples, and the used notation.

Part I

THEORETICAL AND EXPERIMENTAL BACKGROUND

1

III-NITRIDE SEMICONDUCTORS

The class of III-nitride semiconductors can be reduced to the prominent compounds gallium nitride (GaN), indium nitride (InN) and aluminum nitride (AlN). Among those, GaN is probably the most important one and, regarding the basic material properties, exemplary for the group as a whole. Together with the binaries InN and AlN, ternary or even quaternary alloys can be formed. In the first part of this chapter, the most important bulk properties of the III-nitrides are introduced. The advantages and peculiarities of quantum wells, i.e. two-dimensional heterostructures, are discussed in the second part, where the focus is on GaInN-based structures.

1.1 III-NITRIDE MATERIAL PROPERTIES

Generally, the three most important bulk properties of a semiconductor are the band gap, the lattice parameter, and the effective carrier mass. First of all, the band gap, probably most fundamental for the optical properties, is introduced in Sec. 1.1.1. The lattice parameters, together with the underlying crystal structure and its characteristic properties, are treated in Sec. 1.1.2. Additional considerations on the elastic properties and internal polarization fields follow in Sec. 1.1.3 and Sec. 1.1.4. Finally, the band structure of III-nitrides, which determines the effective carrier masses, is discussed in Sec. 1.1.5.

TABLE 1.1: Band gap values at room temperature (300 K) and low temperature (0 K) for wurtzitic GaN, InN and AlN, taken from Ref. [15].

Band gap	GaN	InN	AlN
$E_{\mathrm{g,300K}}$ (eV)	3.437	0.608	6.00
$E_{\mathrm{g,0K}}$ (eV)	3.510	0.69	6.10

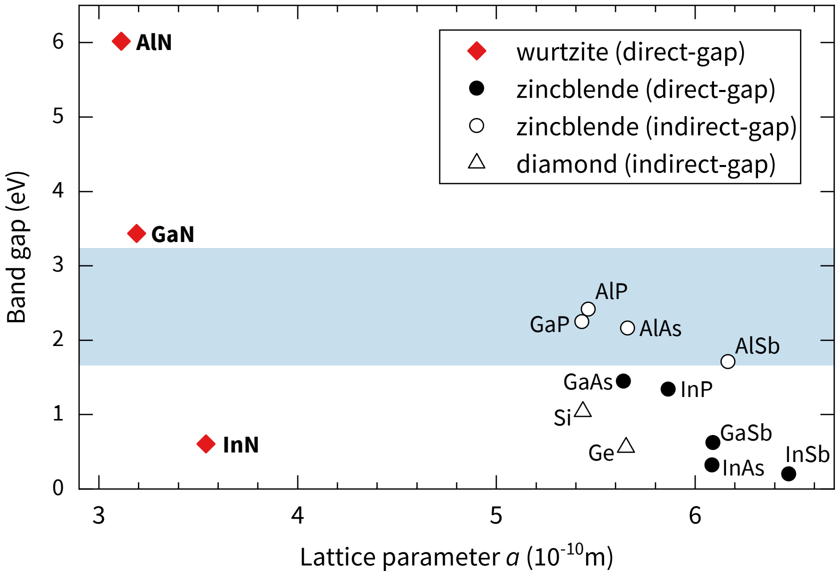

FIGURE 1.1: Band gaps and lattice parameters of III-nitrides in wurtzite structure, in comparison to classical semiconductors like III-V compounds in zincblende structure with with direct and indirect band gap, as well as group IV single-element seminconductors. Adapted from Ref. [5, Ch. 1].

1.1.1 *Band gap*

The III-nitrides exhibit a direct band gap, i.e. the conduction band minimum and the valence band maximum are located both at the center of the Brillouin zone (Γ-point). The band gaps are listed in Tab. 1.1, and range from ~0.6 eV for InN, over ~3.4 eV for GaN, up to ~6 eV for AlN. The band gap in the corresponding ternary alloys can be tuned to match light emission from the infrared to the deep ultraviolet spectral region. Especially GaInN, which can in principle cover the whole visible spectrum, is of interest for optoelectronics in general, and in particular also in this thesis. The band gap of a $\mathrm{Ga}_{1-x}\mathrm{In}_x\mathrm{N}$ alloy, where x denotes the InN mole fraction, can be estimated by [5, Ch. 1]

$$E_{\mathrm{g,GaInN}}(x) = E_{\mathrm{g,GaN}}\,(1-x) + E_{\mathrm{g,InN}}\,x - b\,x(1-x)\,. \tag{1.1}$$

Here, $E_{\mathrm{g,GaN/InN}}$ denotes the band gap of the binary constituents, and the bowing parameter b is necessary to account for a nonlinear behavior of the band gap with composition. The values of b differ considerably, depending on the applied measurement

TABLE 1.2: Lattice parameters a and c for free-standing wurtzitic GaN, InN and AlN at room temperature. All III-nitride compounds show deviations from the ideal c/a ratio of $\sqrt{8/3} \approx 1.633$ of the undistorted wurtzitic crystal.

Lattice parameter	GaN	InN	AlN
a (Å)	3.189 [a]	3.538 [b]	3.112 [c]
c (Å)	5.185 [a]	5.704 [b]	4.981 [c]
c/a	1.626	1.612	1.601

[a] Ref. [19] [b] Ref. [20] [c] Ref. [21]

method. Wu et al. find a value of $b = 1.43\,\text{eV}$ from absorption measurements [16], while Davydov et al. report on $b = 2.5\,\text{eV}$, which is obtained by photoluminescence measurements [17]. The difference between those values is usually attributed to inhomogeneously distributed indium atoms in the material. While in photoluminescence, the transitions with lowest energy are dominant, the transition energy in absorption measurements represents a mean value of the material. Although it may underestimate the band gap of GaInN slightly, a bowing parameter of $b = 2.5\,\text{eV}$ is used here, which seems more appropriate to describe PL measurements that are analyzed. In a first approximation, the band gap defines the energy of photons that are emitted via radiative recombination in a semiconductor. In the following sections, however, it will be shown that the photon energy depends not only on the band gap, but also on quantization effects in low-dimensional structures, on the presence of internal polarization fields, and on the binding energy of excitons (electron-hole quasiparticles). More details on the properties of two-dimensional heterostructures (quantum wells) based on GaInN are discussed in Sec. 1.2.4.

1.1.2 *Crystal structure and orientation*

The native crystal structure of all III-nitride compounds is the wurtzite structure, which consists of hexagonally close packed nitrogen atoms, where half of the tetrahedral sites are filled with group III metal atoms [18, Ch. 1],[5, Ch. 1]. In the resulting crystal the atoms of one type are tetrahedrally surrounded by atoms of the other type with a III/N ratio of 1:1. The wurtzite structure can be characterized by a hexagonal unit cell, where atoms of one type have distance a in the basal plane, while the unit cell has height c. Fig. 1.2(a) shows a ball-and-stick model of a wurtzite GaN crystal. The a and c lattice parameters for wurtzitic GaN, InN and AlN can be found in Tab. 1.2. To estimate the lattice parameters of a ternary compound, the values are linearly

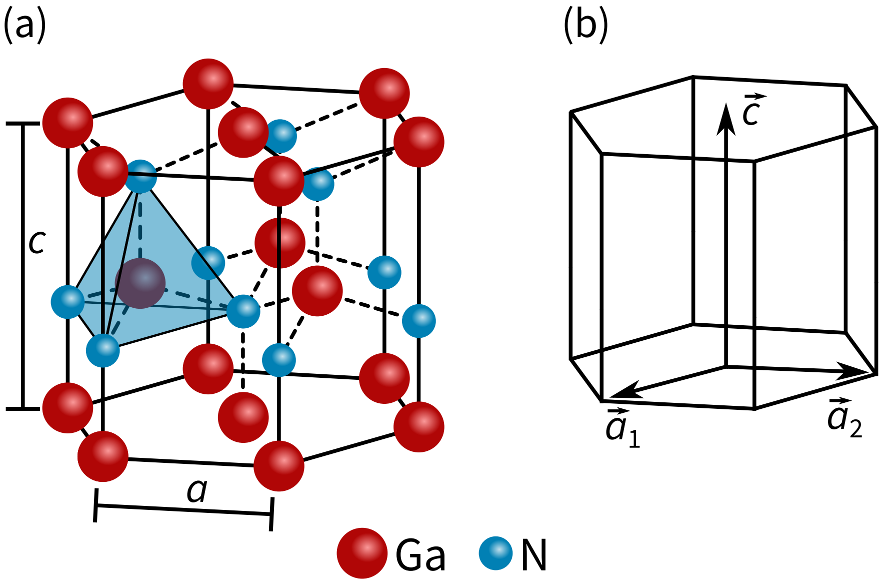

FIGURE 1.2: Ball-stick-model of the wurtzite structure (a) with gallium and nitrogen atoms as red and blue balls. The lattice parameters c and a are indicated, as well as the tetrahedral coordination in the structure. Solid lines mark the hexagonal unit cell, while dahsed lines indicate the interatomic bonds. Hexagonal unit cell (b) with real-space lattice vectors $\mathbf{a}_1$, $\mathbf{a}_2$ and $\mathbf{c}$. Adapted from Ref. [18, Ch. 1].

interpolated between the binary constituents. This relation is known as Vegard's law [22], and is given here exemplary for $Ga_{1-x}In_xN$:

$$a_{\mathrm{GaInN}}(x) = (1-x)\,a_{\mathrm{GaN}} + x\,a_{\mathrm{InN}}\,, \tag{1.2}$$

where x, the InN mole fraction, determines the composition. Along the c-direction, i.e. perpendicular to the basal c-plane, the wurtzite crystal has a stacking sequence of $ABAB\ldots$ with alternating layers of nitrogen and metal atoms. Contrary, the similar zinc blende structure has a cubic unit cell and a stacking sequence of $ABCABC\ldots$ along the $\langle 111\rangle$ direction. While this is the native structure for other III-V compounds like GaAs, III-nitrides in zinc blende structure can be stabilized only by epitaxial growth on cubic substrates. Furthermore, the rock salt modification (simple cubic) is only found under extremely high pressures, e.g. ~52 GPa for GaN [23], [5, Ch. 1].

Due to the strong difference in electronegativity between group III atoms and nitrogen, the inter-atomic bond has a strong covalent, or even partially ionic character [24]. The large difference in electronegativity also leads to deviations from

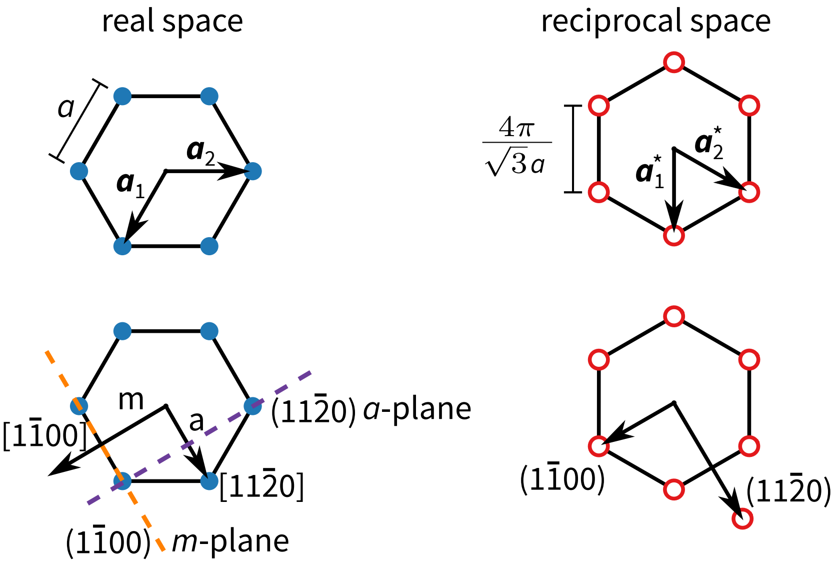

FIGURE 1.3: Real space (a) and reciprocal space (b) crystal lattice projected onto the basal c-plane. Using Eq. 1.4, the basis vectors $\mathbf{a}_{1/2}$ and $\mathbf{a}^*_{1/2}$ in real and reciprocal space can be used to denote crystal planes and directions. In this projection, the out-of-plane vector $\mathbf{c}$ points upwards in real and reciprocal space. Here, the $(1\bar{1}00)$ m-plane, as well as the $(11\bar{2}0)$ a-plane are indicated in real space, which are perpendicular to the corresponding reciprocal lattice vector by definition. Adapted from Refs. [25, Ch. 5] and [5, Ch. 1].

the ideal bonding lengths in the wurtzite crystal. In an ideal wurtzite structure, the tetrahedral arrangement of atoms leads to a lattice parameter ratio of $c/a = \sqrt{8/3}$. Since the electron density is higher around the nitrogen atoms in the crystal, the tetrahedrons are slightly distorted, which causes deviations from the ideal c/a ratio (Tab. 1.2) [5, Ch. 1]. Together with the lack of inversion symmetry in the wurtzite crystal, this gives rise to a permanent non-zero polarization, pointing along the c-axis, see Sec. 1.1.4.

Polar, semipolar and nonpolar crystal orientations

As shown in Fig. 1.2(b), the primitive wurtzite unit cell in real space is spanned by the basis vectors $\mathbf{a}_1$, $\mathbf{a}_2$ and $\mathbf{c}$. The projection onto the basal c-plane is shown in Fig. 1.3, where also the in-plane basis vectors $\mathbf{a}^*_1$ and $\mathbf{a}^*_2$ of reciprocal spcae are given. In this projection, the out-of-plane reciprocal vector $\mathbf{c}^*$ points upwards. The basis vectors are linearly independent, and obey the relation $a_\mathrm{i} a_\mathrm{j}^* = 2\pi\delta_\mathrm{ij}$. Using Bravais-Miller indices h, k, i, l, the crystal planes and directions can be described by vectors

$$R_\mathrm{hkl} = h\,\mathbf{a}_1 + k\,\mathbf{a}_2 + l\,\mathbf{c} \qquad \text{for direction } [hkil] \tag{1.3}$$

$$G_\mathrm{hkl} = h\,\mathbf{a}_1^* + k\,\mathbf{a}_2^* + l\,\mathbf{c}^* \qquad \text{for plane } (hkil)\,. \tag{1.4}$$

The index $i \equiv -(h+k)$ is redundant, but useful to find all symmetrically equivalent planes $\{hkil\}$ and directions $\langle hkil\rangle$ by permutation of h, k, i. In this notation, the plane $(hkil)$ is characterized by a reciprocal lattice vector, which is perpendicular to the plane in real space. This is obvious for the basal c-plane, or (0001) in Bravais-Miller notation. Since the internal polarization in the III-nitride crystal structure points along the $[0001]$ c-direction, this plane is under strong influence of those fields, and thus referred to as polar plane. Furthermore, Fig. 1.3 shows the construction of the crystallographic $[11\bar{2}0]$ a-direction, and the a-plane, which is perpendicular to the $(11\bar{2}0)$ vector in reciprocal space. The same is shown for the $(1\bar{1}00)$ m-plane, whose equivalent planes form the side facets of the hexagonal unit cell. The internal polarization has no component in a- or m-direction, and thus, those planes are referred to as nonpolar [26]. In Sec. 1.1.4, the magnitude of internal polarization fields is treated. The influence of internal polarization fields becomes lower for crystal planes that are inclined with respect to the polar c-plane, and between the polar and nonpolar orientations there exists a variety of semipolar planes. Most important for this thesis is the semipolar $(11\bar{2}2)$ plane at an inclination angle of approximately 58°. Fig. 1.4 shows the polar c-plane, the nonpolar m-plane, and the semipolar $(11\bar{2}2)$ plane schematically in the hexagonal unit cell. The crystal directions defined above form a Cartesian coordinate system:

$$\begin{pmatrix} a \\ m \\ c \end{pmatrix} \longmapsto \begin{pmatrix} x \\ y \\ z \end{pmatrix} \tag{1.5}$$

which is referred to as the crystal coordinate system. In the case that crystal growth proceeds not along z, i.e. in c-direction, the use of a rotated (primed) growth coordinate system is useful, where the growth direction points along z'. This is achieved by applying a unitary matrix $U(\phi,\theta)$, which rotates the crystal coordinate system about an angle ϕ around the x-axis, and about an angle θ around the y-axis [28]:

$$\begin{pmatrix} x' \\ y' \\ z' \end{pmatrix} = U(\phi,\theta) \begin{pmatrix} x \\ y \\ z \end{pmatrix} = \begin{pmatrix} \cos\phi\cos\theta & \sin\phi\cos\theta & -\sin\theta \\ -\sin\phi & \cos\phi & 0 \\ \cos\phi\sin\theta & \sin\phi\sin\theta & \cos\theta \end{pmatrix} \begin{pmatrix} x \\ y \\ z \end{pmatrix} \tag{1.6}$$

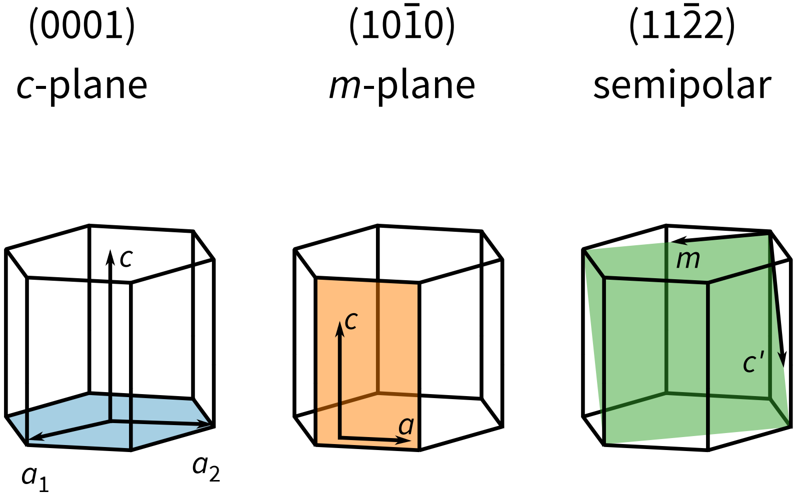

Figure 1.4: Schematic of the polar c-plane, the nonpolar m-plane, and the semipolar $(11\bar{2}2)$-plane in the hexagonal unit cell, together with the respective in-plane directions. Adapted from Ref. [27].

With $\phi = 0$, and $\theta \approx 58°$, the growth direction points along $z' = [11\bar{2}2]$, with in-plane directions $[1\bar{1}00]$ (m) and $[11\bar{2}\bar{3}]$, referred to as c'. The exact value of θ depends also on the c/a ratio, and thus on composition. For growth along the m-direction, $\theta = 0$, $\phi = 90°$ is used, and the resulting in-plane directions are a and c.

1.1.3 *Stress and strain*

In this section, the elasticity theory needed to describe the deformation of wurtzite crystals is introduced briefly. The strain relations are given for the specific cases of polar c-plane and nonpolar m-plane orientation. The strain that is present in heterostructures is an important source of internal polarization fields (Sec. 1.1.4), while the strain anisotropy in III-nitrides has strong influence on the band structure (Sec. 1.1.5).

TABLE 1.3: Elastic constants for wurtzite GaN, InN and AlN used in this thesis.

Elastic constant	GaN	InN	AlN
C_{11} (GPa)	374 [a]	237 [a]	395 [b]
C_{12} (GPa)	138 [a]	106 [a]	137 [b]
C_{13} (GPa)	101 [a]	85 [a]	107 [b]
C_{33} (GPa)	395 [a]	236 [a]	404 [b]
C_{44} (GPa)	98 [a]	53 [a]	117 [b]

[a] Ref. [30] [b] Ref. [31]

Theory of elasticity

The effect of a force, or stress (σ), that is applied to a crystal is deformation, or strain (ε). Both are linearly related according to Hooke's law [29, Ch. 8]:

$$\sigma_{\mathrm{ij}} = \sum_{\mathrm{k,l}} C_{\mathrm{ijkl}}\varepsilon_{\mathrm{kl}} \qquad \text{with } i, j, k, l \in \{x, y, z\}\,, \tag{1.7}$$

where σ_{ij} are elements of the second-order stress tensor, $\varepsilon_{\mathrm{kl}}$ are elements of the second-order strain tensor, and C_{ijkl} are elements of the fourth-order elastic tensor. Instead of x, y, z, the equivalent indices 1, 2, 3 can be used. Considering a wurtzitic III-nitride crystal with hexagonal symmetry, the elastic tensor can be reduced to a 6×6 matrix C_{ij}, which simplifies Eq. 1.7 to :

$$\begin{pmatrix} \sigma_{\mathrm{xx}} \\ \sigma_{\mathrm{yy}} \\ \sigma_{\mathrm{zz}} \\ \sigma_{\mathrm{zy}} \\ \sigma_{\mathrm{zx}} \\ \sigma_{\mathrm{xy}} \end{pmatrix} = \begin{pmatrix} C_{11} & C_{12} & C_{13} & 0 & 0 & 0 \\ C_{12} & C_{22} & C_{13} & 0 & 0 & 0 \\ C_{13} & C_{13} & C_{33} & 0 & 0 & 0 \\ 0 & 0 & 0 & C_{44} & 0 & 0 \\ 0 & 0 & 0 & 0 & C_{55} & 0 \\ 0 & 0 & 0 & 0 & 0 & C_{66} \end{pmatrix} \begin{pmatrix} \varepsilon_{\mathrm{xx}} \\ \varepsilon_{\mathrm{yy}} \\ \varepsilon_{\mathrm{zz}} \\ \varepsilon_{\mathrm{yz}} \\ \varepsilon_{\mathrm{zx}} \\ \varepsilon_{\mathrm{xy}} \end{pmatrix} \tag{1.8}$$

Here, the Voigt notation is used to simplify the indices: $xx \rightarrow 1$, $yy \rightarrow 2$, $zz \rightarrow 3$, $yz, zy \rightarrow 4$, $xz, zx \rightarrow 5$, $xy, yx \rightarrow 6$ [5, Ch. 2], [29, Ch. 8]. Elastic constants for GaN, InN and AlN can be found in Tab. 1.3.

Lattice mismatch

Typically, crystalline III-N layers are prepared by epitaxial methods on a foreign substrate. At the interface, the lattice parameter of the substrate (a) is adopted by the epitaxial layer, whose relaxed lattice parameter is described by a_0. The lattice mismatch between substrate and layer ($a \neq a_0$) results in a strain $\varepsilon = \frac{a-a_0}{a_0}$ in the growth plane.

Considering the polar c-plane as growth surface, the epitaxial layer is isotropically strained in-plane ($\varepsilon_{\mathrm{xx}} = \varepsilon_{\mathrm{yy}}$), which can be compensated only by distortion in the c-direction. Therefore, the stress in c-direction (σ_{zz}), as well as all components $\varepsilon_{\mathrm{ij}}$ with $i \neq j$, i.e. shear components, vanish. Using Eq. 1.8, and noting that $C_{11} = C_{22}$, this leads to

$$\varepsilon_{\mathrm{xx}} = \varepsilon_{\mathrm{yy}} = \frac{a - a_0}{a_0}\,, \qquad \varepsilon_{\mathrm{zz}} = -2\frac{C_{13}}{C_{33}}\varepsilon_{\mathrm{xx}}\,. \tag{1.9}$$

For compressive strain in the growth plane ($\varepsilon_{\mathrm{xx}} < 0$), the crystal will expand in c-direction ($c > c_0$), as indicated by the negative sign.

For growth along other crystal directions, the strain, stress and elastic tensors have to be transformed to the growth coordinate system, which is covered in Refs. [32] and [29, Ch. 9] in detail. Here, only the case of the $(1\bar{1}00)$ m-plane as growth surface is considered explicitly, for which the in-plane strain becomes anisotropic ($\varepsilon_{\mathrm{xx}} \neq \varepsilon_{\mathrm{zz}}$). Similar to the c-plane case, all shear components vanish, but the growth proceeds in y-direction in the crystal coordinate system, or along z' in the growth coordinate system. Thus, $\sigma'_{\mathrm{zz}} = \sigma_{\mathrm{yy}} = 0$ and the out-of-plane strain becomes

$$\varepsilon_{\mathrm{yy}} = -\frac{C_{12}\varepsilon_{\mathrm{xx}} + C_{13}\varepsilon_{\mathrm{zz}}}{C_{11}}\,. \tag{1.10}$$

Using the above relations, the out-of-plane strain in a heterostructure can be estimated for a thin layer, where the in-plane lattice parameters are determined by the underlying substrate. For semipolar growth orientations, the shear components are not vanishing, which allows more possibilities for the crystal to accomodate for epitaxial stress. Ref. [32] covers the strain relations for semipolar growth orientations.

Relaxation in heterostructures

With increasing thickness, the lattice parameters of a strained layer will show the tendency to relax towards the bulk value. This is the necessary consequence of the built-up strain energy that needs to be reduced to approach the thermodynamic equilibrium. The strain energy density per unit volume is given by [29, Ch. 8]

$$u = \frac{1}{2}\boldsymbol{\sigma} \cdot \boldsymbol{\varepsilon} = \frac{1}{2}\sum_{\mathrm{i,j}} C_{\mathrm{ij}}\varepsilon_{\mathrm{i}}\varepsilon_{\mathrm{j}}\,. \tag{1.11}$$

With increasing strain it becomes thermodynamically preferable for the crystal to incorporate misfit dislocations, i.e. extended crystallographic defects, in order to reduce the strain energy in the layer. The Matthews-Blakeslee limit provides an estimate of the critical layer thickness at which the formation of dislocations starts to take place [33]. Layers that do not exceed this thickness limit are likely to withstand the accumulated strain energy without additional formation of misfit dislocations. For III-nitrides, the critical thickness for a GaInN layer deposited on a GaN substrate is only 3.6 nm for an InN mole fraction of 20 % [34]. Although this provides only a rough estimate, such a thin layer can be expected to adopt the substrate's in-plane lattice parameter, and will not show relaxation until the critical thickness is reached.

For thicker layers, formation of crystallographic defects will reduce the strain energy. Misfit dislocations can be present at the interface between substrate and epitaxial layer, and accomodate for the lattice mismatch between both. Classical examples of extended defects are dislocations of either screw- or edge-type. An ideal misfit dislocation is neither propagating in growth direction, nor penetrating subsequent layers, which makes them desirable for strain reduction in heteroepitaxy. Nevertheless, threading dislocations, which run through the layer in growth direction, play an important role in III-nitride structures. They can have screw-, edge- or mixed character, and are often formed at the interface during heteroepitaxial growth. Since they propagate in growth direction and can penetrate the subsequent layers, they affect the optical and electronic properties of the material. In typical III-nitride structures prepared by heteroepitaxy, threading dislocation densities of $1 \times 10^8 - 1 \times 10^{10}/\mathrm{cm}^2$ are found. Furthermore, they can be transformed or linked to misfit dislocations at interfaces [35, 36].

Other examples of defects are inversion domain boundaries, where a change in crystal structure, e.g. from Ga-polar to N-polar, forms an interface that is considered a planar defect. Related to those are stacking faults, where the stacking order of atomic layers changes from AB…to ABC…, which is characteristic for the cubic zincblende structure. This defect type results in (monolayer-thick) cubic insertions in the hexagonal host crystal [5, Ch. 4].

Apart from extended crystallographic defects, there are point defects in III-nitride crystals. Those can be impurity atoms, interstitials, or vacancies and related complexes [5, Ch. 4]. Point defects, as well as extended crystallographic defects, can act as nonradiative recombination centers.

1.1.4 *Internal polarization fields*

All III-nitrides in wurtzite structure show internal polarization fields. The polarization vectors are pointing from nitrogen to metal atoms, as depicted in Fig. 1.5(a). For the tetrahedrally coordinated atoms in an ideal and infinite crystal, the polarization vectors cancel each other out, and the net polarization vanishes. Contrary, the pres-

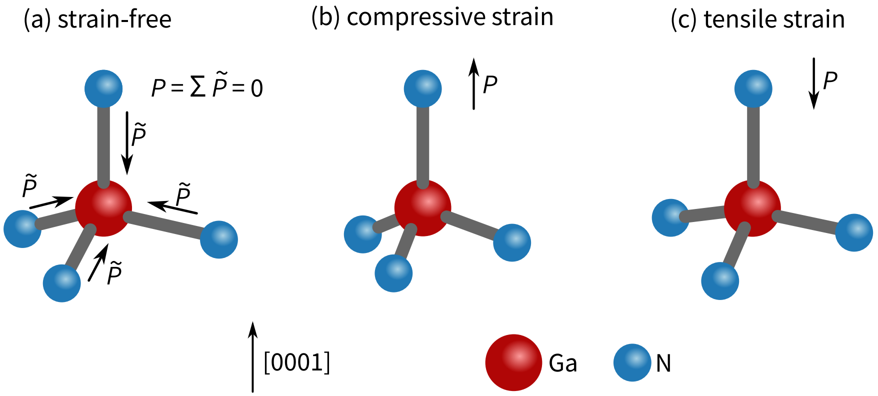

FIGURE 1.5: Ball-and-stick model of tetrahedrally coordinated atoms in a wurtzite III-nitride crystal. The polarization vectors $\tilde{\mathbf{P}}$ point from the nitrogen to the metal atom, and cancel out within the tetrahedron for the strain-free case (a). Distortion of the tetrahedron induces a piezoelectric polarization that points in [0001]-direction for compressive strain (b), and in $[000\bar{1}]$-direction for tensile strain (c) in the basal plane. Adapted from Ref. [5, Ch. 1].

ence of interfaces gives rise to a permanent spontaneous polarization in the crystal, denoted by P_0. Deviations from the ideal c/a ratio in a wurtzite crystal can have the same effect. In general, the spontaneous component points in $[000\bar{1}]$-direction. Any additional strain, i.e. distortion of tetrahedrons, induces a piezoelectric polarization (P_{pz}), as illustrated in Fig. 1.5(b) and (c). For biaxial strain in the basal plane, the induced piezoelectric polarization points in [0001]-direction for compressive, and in $[000\bar{1}]$-direction for tensile strain [37]. Thus, both components can have parallel or antiparallel orientation, and the resulting net polarization becomes

$$\mathbf{P} = \mathbf{P}_0 + \mathbf{P}_{\mathrm{pz}}(\boldsymbol{\varepsilon})\,. \tag{1.12}$$

The piezoelectric polarization depends on strain according to

$$\mathbf{P}^{\mathrm{pz}}(\boldsymbol{\varepsilon}) = \mathbf{e}\,\boldsymbol{\varepsilon} = \begin{pmatrix} 0 & 0 & 0 & 0 & e_{15} & 0 \\ 0 & 0 & 0 & e_{15} & 0 & 0 \\ e_{31} & e_{31} & e_{33} & 0 & 0 & 0 \end{pmatrix} \begin{pmatrix} \varepsilon_{\mathrm{xx}} \\ \varepsilon_{\mathrm{yy}} \\ \varepsilon_{\mathrm{zz}} \\ \varepsilon_{\mathrm{yz}} \\ \varepsilon_{\mathrm{zx}} \\ \varepsilon_{\mathrm{xy}} \end{pmatrix}, \tag{1.13}$$

TABLE 1.4: Piezoelectric moduli and spontaneous polarization for GaN, InN and AlN, taken from Ref. [15].

	GaN	InN	AlN
d_{15} (pm/V)	3.1	5.5	3.6
d_{31} (pm/V)	−1.0	−3.5	−2.1
d_{33} (pm/V)	1.9	7.6	5.4
P^0 (C/m^2)	−0.034	−0.042	−0.090

where $\boldsymbol{\varepsilon}$ denotes the strain tensor, see Sec. 1.1.3. The piezoelectric tensor **e** is already simplified due to the symmetry of the hexagonal wurtzite structure, and thus contains only three independent components [29, Ch. 5], [5, Ch. 2]. Thereby, the single components of the piezoelectric polarization become

$$\begin{pmatrix} P_{\mathrm{pz,x}} \\ P_{\mathrm{pz,y}} \\ P_{\mathrm{pz,z}} \end{pmatrix} = \begin{pmatrix} e_{15}\,\varepsilon_{\mathrm{zx}} \\ e_{15}\,\varepsilon_{\mathrm{yz}} \\ e_{31}(\varepsilon_{\mathrm{xx}} + \varepsilon_{\mathrm{yy}}) + e_{33}\varepsilon_{\mathrm{zz}} \end{pmatrix} . \tag{1.14}$$

Alternatively, piezoelectric moduli d_{ij} instead of piezoelectric constants e_{ij} can be used to describe the relation between strain and piezoelectric polarization:

$$P_{\mathrm{pz,i}} = \sum_{\mathrm{j}} d_{\mathrm{ij}}\sigma_{\mathrm{j}} = \sum_{\mathrm{j}} e_{\mathrm{ij}}\varepsilon_{\mathrm{j}} \quad \text{with } i \in \{1, 2, 3\} , \tag{1.15}$$

where x, y, z are replaced by $1, 2, 3$ for convenience, and σ_{j} and ε_{j} denote the stress and strain components according to Eq. 1.8. The piezoelectric moduli and constants are related by

$$e_{31} = (C_{11} + C_{12})d_{31} + C_{13}d_{33} , \tag{1.16}$$

$$e_{33} = 2C_{13}d_{31} + C_{33}d_{33} , \tag{1.17}$$

$$e_{15} = -C_{44}d_{15} . \tag{1.18}$$

In the absence of shear strain, which can be assumed for III-N layers grown in c- or m-plane orientation, the x- and y-components vanish ($P_{\mathrm{pz,x}} = P_{\mathrm{pz,y}} = 0$), and the piezoelectric polarization points in z-direction, namely along $[0001]$. The piezoelectric moduli and the spontaneous polarizations are given in Tab. 1.4. In heterostructures, the net polarization at the interface (ΔP) is determined only by

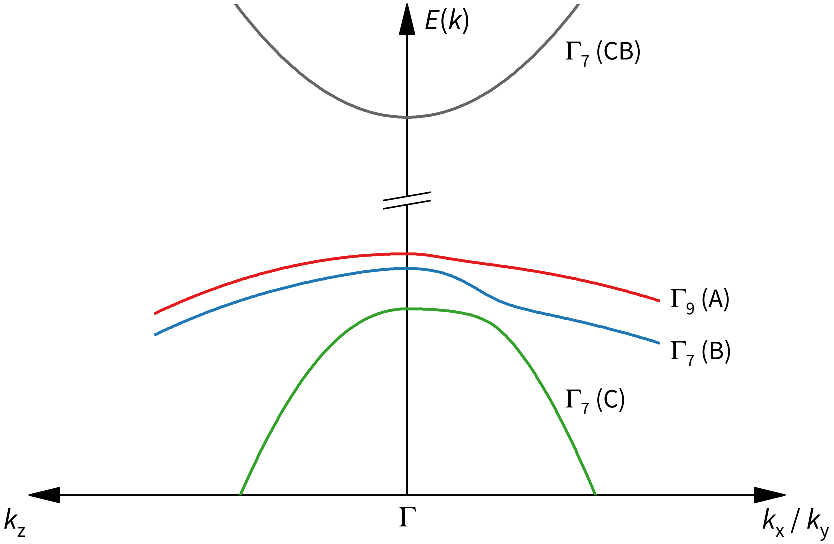

FIGURE 1.6: Schematic of the band structure of wurtzitic bulk GaN near the Γ-point, showing one conduction band (CB, Γ_7) and three valence bands, labeled as A (Γ_9), B (upper Γ_7), and C (lower Γ_7). Due to spin-orbit and crystal-field splitting, the valence bands are non-degenerate, and the strong anisotropy along k_z and $k_\mathrm{x/y}$ becomes obvious. Adapted from Ref. [5, Ch. 2].

differences between the net polarizations of the two adjacent materials. For a c-plane-oriented GaInN layer grown epitaxially on a GaN substrate, the field induced by the piezoelectric component amounts to ~2.7 MV/cm for an InN mole fraction of 20 %. For crystal growth in semipolar orientations, the shear component $\varepsilon_\mathrm{zx} \neq 0$ needs to be regarded. Generally, the respective growth coordinate system in this case is rotated around the y-axis by an angle θ. The net polarization along z', including the piezoelectric and spontaneous contribution, becomes [28]

$$P_{\mathrm{z}'} = P_\mathrm{x} \sin\theta + P_\mathrm{z} \cos\theta\,, \qquad \text{where } P_\mathrm{z} = P_0 + P_\mathrm{pz,z}\,. \tag{1.19}$$

1.1.5 *Band structure*

The III-nitrides are direct gap semiconductors, i.e. the band extrema are located at the Γ point in the Brillouin zone. Thus, the wave functions at the band edges can be described by atomic s-orbitals for the conduction band, and by atomic p-orbitals for the valence band, similar to other III-V semiconductors like GaAs [38, Ch. 2], [5, Ch. 2]. Accordingly, a single conduction band and three valence bands (p_x, p_y, p_z) occur. In Fig. 1.6, the band structure of bulk GaN is shown schematically. The upper two valence bands are non-degenerate due to the spin-orbit interaction, which is relatively low in III-nitrides [39]. Furthermore, the third valence band is shifted to lower energies due to the large crystal field present in wurtzite III-nitrides. From top to bottom, the valence bands are usually labeled A (Γ_9), B (upper Γ_7) and C (lower Γ_7). The notation using heavy- and light-hole bands should be avoided, since the valence band character is strongly anisotropic and may change when moving from the center of the Brillouin zone to higher k-values.

In order to calculate the band structure, i.e. the dispersion relation $E(\mathbf{k})$, within the whole Brillouin zone, tight-binding calculations or other theoretical approaches using pseudopotentials are available [40–43]. Here, optical transitions are investigated, which in principle involve only states within a few $k_B T$ from the band edges. For this purpose, the use of $\mathbf{k} \cdot \mathbf{p}$ theory is suitable, which provides a straightforward method to calculate the dispersion relation near the Γ-point using second-order perturbation theory. The effect of strain can easily be included, and the application to quantum well structures is described in Sec. 1.2.5.

$k \cdot p$ perturbation theory

The dispersion relation $E(\mathbf{k})$, plotted in Fig. 1.6 for bulk material, can be derived using single-electron theory in a first approximation. The energies $E(\mathbf{k})$ are eigenvalues, and the corresponding bulk wave functions $\psi(\mathbf{r})$ are eigenfunctions of the single-electron Hamiltonian H_0, which includes the periodic crystal potential $V(\mathbf{r})$. Neglecting spin, the Schrödinger equation can be written as

$$H_0 \varphi(\mathbf{r}) = \left(\frac{\mathbf{p}^2}{2m_0} + V(\mathbf{r}) \right) \varphi(\mathbf{r}) = E\, \varphi(\mathbf{r}) \,, \tag{1.20}$$

with the momentum operator $\mathbf{p} = -i\hbar\nabla$, and the free electron mass m_0. The solutions to this equation are Bloch functions, consisting of a crystal-periodic function U_n and a plane wave

$$\varphi_n(\mathbf{r}, \mathbf{k}) = \frac{1}{\sqrt{\tilde{V}}}\, U_n(\mathbf{r}, \mathbf{k})\, e^{i\mathbf{k}\cdot\mathbf{r}} \,, \tag{1.21}$$

where n is the band index of the corresponding conduction or valence band, and $\tilde{V}$ denotes the crystal volume. The Bloch functions are periodic under translation and obey the relation

$$\varphi_n(\mathbf{r} + \mathbf{R}, \mathbf{k}) = \varphi_n(\mathbf{r}, \mathbf{k})\, e^{i\mathbf{k}\cdot\mathbf{R}} \,, \tag{1.22}$$

with **R** being a vector of the Bravais lattice. Using Eq. 1.21 in Eq. 1.20, the Schrödinger equation for the cell-periodic functions U_n is obtained [44, Ch. 4]:

$$\left(\frac{\mathbf{p}^2}{2m_0} + \frac{\hbar^2 k^2}{2m_0} + \frac{\hbar}{m_0} \mathbf{k} \cdot \mathbf{p} + V(\mathbf{r}) \right) U_\mathrm{n}(\mathbf{r}, \mathbf{k}) = E_\mathrm{n}\, U_\mathrm{n}(\mathbf{r}, \mathbf{k}) \,. \tag{1.23}$$

Around the Γ point, the periodic wave functions $U_\mathrm{n}(\mathbf{r}, \mathbf{k})$ can be described by the atomic *s*- and *p*-wave functions $|S\rangle$, $|P_\mathrm{x}\rangle$, $|P_\mathrm{y}\rangle$, $|P_\mathrm{z}\rangle$, or their linear combinations. These cell-periodic wave functions form a complete orthonormal basis for every band (index n) and every wave vector **k**. Thus, the wave function ψ of an electron with wave vector **k** in the n-th band can be written as

$$\psi_\mathrm{n}(\mathbf{r}, \mathbf{k}) = \sum_\mathrm{m} c_\mathrm{m} U_\mathrm{m}(\mathbf{r}, \mathbf{k} = 0) \,, \tag{1.24}$$

with prefactors c_m. From here on, perturbation theory can be applied to calculate the $\mathbf{k} \cdot \mathbf{p}$ terms in Eq. 1.23. While the $\mathbf{k} \cdot \mathbf{p}$ theory was introduced by Bardeen [45] and Seitz [46], it has been refined over the years to account for specifics of III-V semiconductors and other material classes. In particular, degenerate bands were included in the model of Luttinger and Kohn [47], and the spin-orbit interaction was introduced by Kane [48]. To include the spin-orbit interaction of crystal electrons, an additional term H_so is added to the Hamiltonian. To account for closely spaced valence bands, perturbation theory for degenerate bands has to be applied, and thus the inner product $\mathbf{k} \cdot \mathbf{p}$ in Eq. 1.23 is converted to $\mathbf{k} \cdot \mathbf{\Pi}$, where

$$\mathbf{\Pi} = \mathbf{p} + \frac{\hbar}{4 m_0 c^2} \boldsymbol{\sigma} \times \nabla V(\mathbf{r}) \,, \tag{1.25}$$

and $\boldsymbol{\sigma}$ denotes the electron spin in terms of the Pauli matrices. Thus, the total Hamiltonian becomes

$$\left(H_0 + \frac{\hbar^2 k^2}{2m_0} + \frac{\hbar}{m_0} \mathbf{k} \cdot \mathbf{\Pi} + H_\mathrm{so} \right) U_\mathrm{n}(\mathbf{r}, \mathbf{k}) = E_\mathrm{n}\, U_\mathrm{n}(\mathbf{r}, \mathbf{k}) \,, \tag{1.26}$$

where

$$H_\mathrm{so} = \frac{\hbar}{4 m_0^2 c^2} \left(\nabla V \times \mathbf{p} \right) \cdot \boldsymbol{\sigma} \,. \tag{1.27}$$

Furthermore, Rashba and Sheka [49, 50] introduced the Hamiltonian for the wurtzite structure, and Pikus and Bir [51, 52] adapted the theory for strained layers. Based on this, there exist several similar approaches to treat III-nitride semiconductors using $\mathbf{k} \cdot \mathbf{p}$ calculations [53–56]. Generally, the $\mathbf{k} \cdot \mathbf{p}$ terms are calculated up to the second order by Löwdin's perturbation method [57]. In the following, the approach of Chuang and Chang [53], and in particular the implementation given in Ref. [58] are described.

Since every band has two spin components, in principle eight bands, i.e. two conduction and six valence bands, have to be taken into account. Note that the valence bands are nearly spin-degenerate, and thus, the two spin components are omitted in the band structure plots. Due to the large III-nitride band gaps, the coupling of conduction and valence bands can be neglected, which separates the problem into finding two conduction band and six valence band states [39]. For the valence band, the respective Schrödinger equation can be written as

$$H_\mathrm{h}(\mathbf{r},\mathbf{k})\,\psi_\mathrm{h}(\mathbf{r},\mathbf{k}) = E_\mathrm{h}\,\psi_\mathrm{h}(\mathbf{r},\mathbf{k})\,, \tag{1.28}$$

$$\text{with} \qquad \psi_\mathrm{h}(\mathbf{r},\mathbf{k}) = \sum_{\mathrm{m}=1}^{6} c_\mathrm{m} U_\mathrm{m}(\mathbf{r})\,, \tag{1.29}$$

where H_h is a 6×6 matrix. Accordingly, the wave function ψ_h is composed of six basis wave functions U_m, and can be expressed in terms of a vector. As mentioned above, the atomic *s*- and *p*-like wave functions at the Γ-point can be employed to define a set of basis functions U_m. For the valence band, the following basis functions are chosen:

$$\begin{aligned}
&|U_1\rangle = -\frac{1}{\sqrt{2}}\left(|P_\mathrm{x}\uparrow\rangle + i\,|P_\mathrm{y}\uparrow\rangle\right), && |U_2\rangle = \frac{1}{\sqrt{2}}\left(|P_\mathrm{x}\uparrow\rangle - i\,|P_\mathrm{y}\uparrow\rangle\right),\\
&|U_3\rangle = |P_\mathrm{z}\uparrow\rangle\,, &&\\
&|U_4\rangle = \frac{1}{\sqrt{2}}\left(|P_\mathrm{x}\downarrow\rangle - i\,|P_\mathrm{y}\downarrow\rangle\right), && |U_5\rangle = -\frac{1}{\sqrt{2}}\left(|P_\mathrm{x}\downarrow\rangle + i\,|P_\mathrm{y}\downarrow\rangle\right),\\
&|U_6\rangle = |P_\mathrm{z}\downarrow\rangle\,. &&
\end{aligned} \tag{1.30}$$

The spin components (up/down) are indicated by arrows (↑ / ↓). In this set of basis functions, the valence band Hamiltonian becomes

$$H_\mathrm{h}(\mathbf{k}) = \begin{pmatrix}
F & -K^* & -H^* & 0 & 0 & 0\\
-K & G & H & 0 & 0 & \Delta\\
-H & H^* & \Lambda & 0 & \Delta & 0\\
0 & 0 & 0 & F & -K & H\\
0 & 0 & \Delta & -K^* & G & -H^*\\
0 & \Delta & 0 & H^* & -H & \Lambda
\end{pmatrix} \tag{1.31}$$

where

$$
\begin{aligned}
F &= \Delta_{\mathrm{cr}} + \frac{\Delta_{\mathrm{so}}}{3} + \Lambda + \Theta\,, \\
G &= \Delta_{\mathrm{cr}} - \frac{\Delta_{\mathrm{so}}}{3} + \Lambda + \Theta\,, \\
\Lambda &= \frac{\hbar^2}{2m_0}\left(A_1 k_{\mathrm{z}}^2 + A_2\left(k_{\mathrm{x}}^2 + k_{\mathrm{y}}^2\right)\right) + D_1\varepsilon_{\mathrm{zz}} + D_2\left(\varepsilon_{\mathrm{xx}} + \varepsilon_{\mathrm{yy}}\right)\,, \\
\Theta &= \frac{\hbar^2}{2m_0}\left(A_3 k_{\mathrm{z}}^2 + A_4\left(k_{\mathrm{x}}^2 + k_{\mathrm{y}}^2\right)\right) + D_3\varepsilon_{\mathrm{zz}} + D_4\left(\varepsilon_{\mathrm{xx}} + \varepsilon_{\mathrm{yy}}\right)\,, \\
K &= \frac{\hbar^2}{2m_0} A_5\left(k_{\mathrm{x}} + ik_{\mathrm{y}}\right)^2 + D_5\left(\varepsilon_{\mathrm{xx}} - \varepsilon_{\mathrm{yy}}\right)\,, \\
H &= \frac{\hbar^2}{2m_0} A_6\left(k_{\mathrm{x}} + ik_{\mathrm{y}}\right)k_{\mathrm{z}} + D_6\varepsilon_{\mathrm{zx}}\,, \\
\Delta &= \frac{\sqrt{2}}{3}\Delta_{\mathrm{so}}\,.
\end{aligned}
$$

Here, Δ_{so} and Δ_{cr} denote the spin-orbit and crystal-field splitting energies. The A_{i} parameters are related to the effective masses, similar to the Luttinger parameters in the description of other semiconductors [47]. The effects of strain on the band structure are included via deformation potentials D_{i}. Note that an optional parameter A_7 is omitted here for simplicity, which leaves the valence bands nearly spin-degenerate. A detailed description of band structure calculations including the A_7 parameter is given by Ren et al. [55].

The eigenvalue problem (Eq. 1.28) can be solved numerically for every band index n and every wave vector $\mathbf{k}$. The eigenvalue problem may be solved for a rotated coordinate system (x', y', z') as well, in particular when dispersion relations along arbitrary crystal directions are of interest. Considering the coordinate transformation in Eq. 1.6, the quantities in the growth coordinate system (x', y', z') can be expressed in terms of the crystal coordinate system (x, y, z) by applying the transposed rotation matrix $U^{\mathrm{T}}(\phi, \theta)$. The same transformation applies for the wave vectors. In the above approach, the crystal is assumed to be isotropic in x- and y-direction. Thus, it is sufficient to consider only the rotation angle θ, and set $\phi = 0$, since rotation around the x- and y-axis are equivalent. Note that in particular for the $(11\bar{2}2)$ orientation, only the shear component $\varepsilon'_{\mathrm{zx}}$ is not vanishing. According to Ref. [28], the strain components transform as follows:

$$\varepsilon'_{\mathrm{xx}} = \varepsilon_{\mathrm{xx}} + \varepsilon'_{\mathrm{zx}} \tan\theta\,, \qquad \varepsilon'_{\mathrm{yy}} = \varepsilon_{\mathrm{xx}}\,, \qquad \varepsilon'_{\mathrm{zz}} = \varepsilon_{\mathrm{zz}} + \varepsilon'_{\mathrm{zx}} \cot\theta\,. \tag{1.32}$$

Furthermore, the shear strain can be estimated by [28]

$$\varepsilon'_{\mathrm{zx}} = -\frac{\left[\left(C_{11} + C_{12} + C_{13}\frac{\varepsilon_{\mathrm{zz}}}{\varepsilon_{\mathrm{xx}}}\right)\sin^2\theta + \left(2C_{13} + C_{33}\frac{\varepsilon_{\mathrm{zz}}}{\varepsilon_{\mathrm{xx}}}\right)\cos^2\theta\right]\varepsilon_{\mathrm{xx}}\cos\theta\sin\theta}{C_{11}\sin^4\theta + 2(C_{13} + 2C_{44})\sin^2\theta\cos^2\theta + C_{33}\cos^4\theta}\,. \tag{1.33}$$

The above relations can be used to determine the strain components in the crystal coordinate system.

Finally, the conduction band dispersion is discussed briefly. Here, the s-like wave functions $|U'_1\rangle = |iS\uparrow\rangle$ and $|U'_2\rangle = |iS\downarrow\rangle$ are used as basis. Therefore, the conduction band Hamiltonian becomes scalar [15]:

$$H_{\mathrm{e}}(\mathbf{k}) = E_{\mathrm{c}} + \frac{\hbar^2}{2m_{\mathrm{e},\parallel}}(k_{\mathrm{x}}^2 + k_{\mathrm{y}}^2) + \frac{\hbar^2}{2m_{\mathrm{e,z}}}k_{\mathrm{z}}^2 + a_{\mathrm{c},1}\,\varepsilon_{\mathrm{zz}} + a_{\mathrm{c},2}\,(\varepsilon_{\mathrm{xx}} + \varepsilon_{\mathrm{yy}})\,, \tag{1.34}$$

where

$$E_{\mathrm{c}} = E_{\mathrm{g}} + \Delta_{\mathrm{cr}} + \frac{\Delta_{\mathrm{so}}}{3}\,, \tag{1.35}$$

$$a_{\mathrm{c},1} = a_1 + D_1\,, \qquad a_{\mathrm{c},2} = a_2 + D_2\,. \tag{1.36}$$

Here, $a_{\mathrm{c},1}$ and $a_{\mathrm{c},2}$ denote the conduction band deformation potentials. Obviously, the conduction band is spin degenerate, and the dispersion relation is the same for both spin states.

All necessary parameters can be found in Tab. 1.5. Note that it in the literature, usually the interband deformation potentials $a_{1/2}$ are given, which describe the change of the whole band gap with strain. The pure valence band deformation potentials $D_{1/2}$ can be estimated using the quasi-cubic approximation, where $D_1 = a_1/2$, and $D_2 = D_1 + D_3$ holds [15]. Although this approximation is not strictly valid for III-nitrides [60, 61], this is the only way to determine a complete and consistent set of valence band parameters from recent literature values.

1.2 III-NITRIDE QUANTUM WELLS

In the following section, the properties of quantum wells based on III-nitrides are discussed, as opposed to the bulk properties in the previous section. Making the

TABLE 1.5: Effective mass parameters (A_i), interband deformation potentials (a_i), and valence band deformation potentials (D_i), as well as spin-orbit (Δ_{so}) and crystal field (Δ_{cr}) splitting energies for GaN, InN and AlN.

	GaN	InN	AlN
A_1	−5.947[a]	−15.803[a]	−3.991[a]
A_2	−0.528[a]	−0.497[a]	−0.311[a]
A_3	5.141[a]	15.251[a]	3.671[a]
A_4	−2.512[a]	−7.151[a]	−1.147[a]
A_5	−2.510[a]	−7.060[a]	−1.329[a]
A_6	−3.202[a]	−10.078[a]	−1.952[a]
a_1 (eV)	−5.81[b]	−3.64[b]	−4.21[b]
a_2 (eV)	−8.92[b]	−4.58[b]	−12.07[b]
D_1 (eV)	−2.91	−1.82	−2.11
D_2 (eV)	2.55	0.86	7.12
D_3 (eV)	5.45[b]	2.68[b]	9.22[b]
D_4 (eV)	−2.97[b]	−1.78[b]	−3.74[b]
D_5 (eV)	−2.87[b]	−2.07[b]	−3.30[b]
D_6 (eV)	−3.95[b]	−3.02[b]	−4.49[b]
Δ_{so} (meV)	17[c]	5[c]	36[c]
Δ_{cr} (meV)	19[b]	24[c]	−227[c]

[a] Ref. [59] [b] Ref. [60] [c] Ref. [15]

transition from a bulk crystal to a thin layer, the electronic states change considerably. Ultimately, the layer thickness becomes comparable to the de-Broglie wavelength of electrons, and the resulting quantization leads to discrete energy levels above the band edge. Basically, such a thin layer with a thickness of several nanometers can be realized as a quantum well, which is placed between thick layers of material with a larger band gap. The resulting double-heterostructure forms a potential well, which is referred to as quantum well (QW).

In the following, a simple description of the electronic states in a QW using envelope functions is presented in Secs. 1.2.1 and 1.2.2. Additionally, the density of states is introduced in Sec. 1.2.3, followed by GaInN/GaN quantum wells in Sec. 1.2.4, which represent most of the structures investigated in this thesis. Finally, the specifics of band structure calculations applied to quantum wells are discussed in Sec. 1.2.5.

1.2.1 *Idealized quantum well*

Assuming a rectangular-shaped and symmetrical potential well of width L with potential

$$V(z) = \begin{cases} 0 & \text{for } |z| < L/2 \\ V_0 & \text{else}, \end{cases} \tag{1.37}$$

the bound electron states can be derived explicitly from the one-dimensional Schrödinger equation

$$\left(-\frac{\hbar^2}{2m_\mathrm{e}}\frac{\mathrm{d}^2}{\mathrm{d}z^2} + V(z)\right)\phi(z) = E\,\phi(z), \tag{1.38}$$

where m_e denotes the effective electron mass, and $\phi(z)$ is the electron wave function. The solution can be obtained easily in the limit of infinitely high potential barriers, i.e. $V_0 \to \infty$. In this case, the wave functions are standing waves of the form [38, Ch. 1]

$$\phi_\mathrm{n}(z) = \begin{cases} \sqrt{\frac{2}{L}}\cos\left(\frac{n\,\pi}{L}z\right) & \text{for } n \text{ odd} \\ \sqrt{\frac{2}{L}}\sin\left(\frac{n\,\pi}{L}z\right) & \text{for } n \text{ even}, \end{cases} \tag{1.39}$$

where $n \in \mathbb{N}$ is an integer, and $|z| < L/2$. The corresponding energy levels are

$$E_\mathrm{n} = \frac{\hbar^2}{2m_\mathrm{e}}\left(\frac{n\,\pi}{L}\right)^2. \tag{1.40}$$

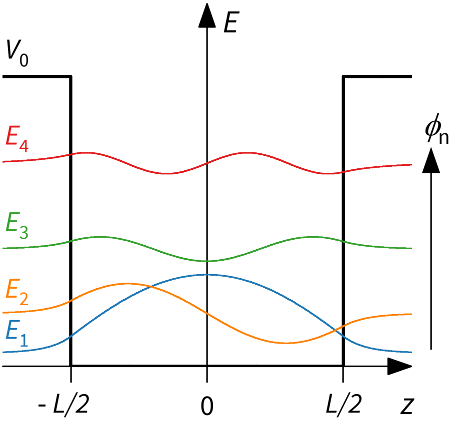

FIGURE 1.7: Scheme of an idealized potential well of width L. The finite potential $V(z)$, defined in Eq. 1.37, as well as the energy levels E_n and wave functions ϕ_n are given for $n = 1 \ldots 4$.

As soon as the potential barriers become finite, the electron has non-zero probability density in the barriers, where the wave function decays exponentially ($\propto e^{-\alpha|z|}$). The wave functions in the finite quantum well can still be given as sine or cosine functions, when substituting the well width L in Eq. 1.39 by an effective well width $L_\mathrm{eff} = L + 2/\alpha$. Here, the penetration depth $1/\alpha$ is added on both sides of the quantum well. The energy levels in Eq. 1.40 transform in the same way [44, Ch. 3].

1.2.2 *Envelope functions*

The use of envelope functions allows to describe electronic states in a quantum well as an extension of the known bulk wave functions $\varphi(\mathrm{r})$, which are Bloch functions and serve the Schrödinger equation

$$H_0\,\varphi(\mathbf{r}) = E\,\varphi(\mathbf{r})\,, \qquad \text{with} \quad E(k) = \frac{\hbar^2 k^2}{2m_\mathrm{e}}\,. \tag{1.41}$$

The Hamiltonian H_0 is defined in Eq. 1.20. In the corresponding dispersion relation $E(k)$, the effective electron mass m_e instead of the electron rest mass m_0 is used to account for the crystal-periodic potential $V(\mathbf{r})$ that is included in H_0. Considering a quantum well potential $V(z)$ according to Eq. 1.37, the effective mass Schrödinger equation becomes [62, Ch. 11]:

$$\left[-\frac{\hbar^2}{2m_{\mathrm{e},\parallel}}\frac{\partial^2}{\partial \mathbf{r}_{\parallel}^2}-\frac{\hbar^2}{2m_{\mathrm{e,z}}}\frac{\partial^2}{\partial z^2}+V(z)\right]\psi(\mathbf{r})=E\,\psi(\mathbf{r})\,, \tag{1.42}$$

where $\mathbf{r}_{\parallel}$ denotes the position vector in the quantum well plane, and $m_{\mathrm{e},\parallel}$ is the in-plane effective electron mass. Using a separation ansatz, the wave function $\psi(\mathbf{r})$ is written as

$$\psi(\mathbf{r})=U_{\mathrm{n}}(\mathbf{r}_{\parallel})\,\phi(z)\,, \tag{1.43}$$

with the crystal-periodic function U_{n} that describes the electron wave function at the band edge. Thereby, the in-plane motion is decoupled from the motion in z-direction. The function $\phi(z)$ is the envelope function that is assumed to vary slowly over the dimension of the crystal unit cell. Thereby, the problem is reduced to a one-dimensional Schrödinger equation that can be solved separately for electrons and holes:

$$\left(-\frac{\hbar^2}{2m_{\mathrm{e,z}}}\frac{\partial^2}{\partial z^2}+V_{\mathrm{e}}(z)\right)\phi_{\mathrm{e}}(z)=E_{\mathrm{e}}\,\phi_{\mathrm{e}}(z)\,, \tag{1.44}$$

$$\left(-\frac{\hbar^2}{2m_{\mathrm{h,z}}}\frac{\partial^2}{\partial z^2}+V_{\mathrm{h}}(z)\right)\phi_{\mathrm{h}}(z)=E_{\mathrm{h}}\,\phi_{\mathrm{h}}(z)\,, \tag{1.45}$$

where $m_{\mathrm{e/h,z}}$ denotes the effective masses, $V_{\mathrm{e/h}}$ the confining potentials, and $E_{\mathrm{e/h}}$ the eigenenergies for electrons (index e) and holes (index h). Using a numerical Schrödinger solver with effective carrier masses and confining potentials as input parameters, the wave functions and energy levels for electrons and holes can be calculated [63].

1.2.3 *Density of states*

Apart from the energy levels and the wave functions, also the electronic density of states changes in a quantum well. For bulk material, the three-dimensional density of states (per unit volume) is given by [18, Ch. 7]

$$D^{(3D)}(E)=\frac{1}{2\pi^2}\left(\frac{2m_{\mathrm{e/h}}}{\hbar^2}\right)^{3/2}\sqrt{E}\,, \tag{1.46}$$

where $m_{\mathrm{e/h}}$ denotes the effective mass of electrons or holes, and the energy E is measured from the band edges upwards. In a quantum well, the electrons follow the two-dimensional density of states, given per unit area [18, Ch. 7]:

$$D_{\mathrm{QW}}^{(2D)} = \frac{m_{\mathrm{e/h}}}{\pi\hbar^2} \sum_{\mathrm{n}} \theta(E - E_{\mathrm{n}}) \,. \tag{1.47}$$

Here, the sum is taken over all subbands (index n), resulting in a step-wise constant behavior. The single subbands contribute to the total density of states, as soon as their energy level E_{n} is reached, which is accounted for by the Heaviside function $\theta(E - E_{\mathrm{n}})$.

1.2.4 *GaInN/GaN quantum wells*

For the III-nitrides, an exemplary and important quantum well structure is that of a thin $\mathrm{Ga_{1-x}In_xN}$ layer embedded in a GaN host crystal. The InN mole fraction is denoted by x. Fig. 1.9 shows a scheme of the band profiles in such a quantum well structure, where E_{c} and E_{v} denote the conduction and valence band edges. The structure forms a quantum well of type I, where both, electrons and holes, have lower potential energy inside the quantum well than in the barrier material.

The difference in band gap energy between both materials ($\Delta E_{\mathrm{g}} = E_{\mathrm{g,GaN}} - E_{\mathrm{g,GaInN}}$) is split into the conduction and valence band discontinuities, ΔE_{c} and ΔE_{v}. Following the recommendation of Martin et al. [64], the ratio of $\Delta E_{\mathrm{c}}/\Delta E_{\mathrm{v}} = 70/30$ is used throughout this thesis.

As described in Sec. 1.1.4, the basal c-plane is subject to strong internal polarization fields pointing along the z-direction. Fig. 1.8 shows calculated values of the polarization discontinuity for a GaInN/GaN heterostructure with varying InN mole fraction. The net polarization ΔP at the interface induces an electric field F across the QW region, which depends on the material composition and is given by

$$F = \frac{\Delta P}{\varepsilon_0 \varepsilon_{\mathrm{r}}} \,, \tag{1.48}$$

$$\text{with} \quad \Delta P = P_{\mathrm{GaN}} - P_{\mathrm{GaInN}} \,. \tag{1.49}$$

Here, ε_{r} denotes the QW's dielectric constant, which is linearly interpolated between the constants of GaN ($\varepsilon_{\mathrm{r,GaN}} = 9.5$) and InN ($\varepsilon_{\mathrm{r,InN}} = 15.3$) [65, 66]. From the constant electric field F, the electrostatic potential $V'(z) = eFz$ is obtained, which adds to the QW potential $V_{\mathrm{e/h}}(z)$ in the Schrödinger equations 1.44 and 1.45. For

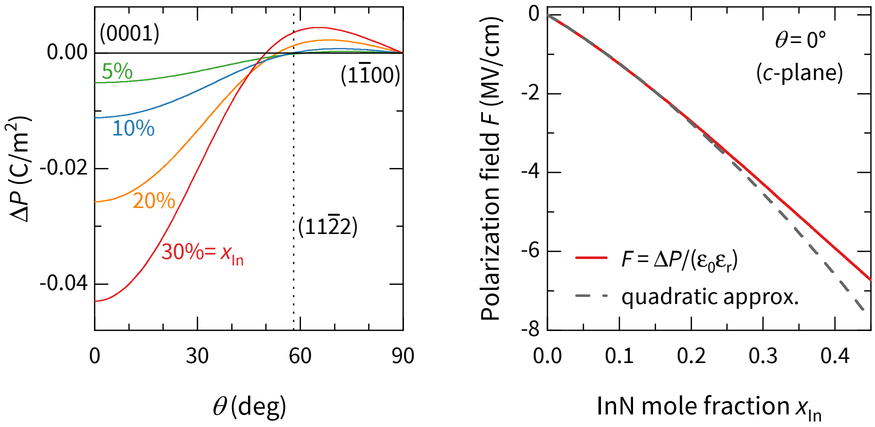

FIGURE 1.8: Polarization discontinuity ΔP as function of the angle θ between growth orientation and c-plane, and the polarization field F as function of the InN mole fraction x for the c-plane case. The important growth orientations are indicated in the angular dependence plot: c-plane at $\theta = 0°$, $(11\bar{2}2)$ at $\theta \approx 58°$, and m-plane at $\theta = 90°$. The values are calculated for a GaInN/GaN heterostructure, using the parameters given in Tab. 1.4. The resulting field points in $[000\bar{1}]$-direction $(F < 0)$, and can be approximated quadratically using Eq. 1.50 with deviations of only 5% for $x_{\mathrm{In}} = 30\%$.

polar $\mathrm{Ga_{1-x}In_xN}$/GaN structures, the electric field induced by the piezoelectric polarization may be approximately calculated by [67]:

$$F(x) = \left(221\,\frac{\mathrm{MV}}{\mathrm{cm}}\,x + 98\,\frac{\mathrm{MV}}{\mathrm{cm}}\,(1-x)\right)\,\varepsilon(x)\,, \tag{1.50}$$

where the compressive in-plane strain $\varepsilon(x) \approx -0.112\,x$ can be assumed to depend nearly linear on the composition. This quadratic approximation neglects the small contribution of the spontaneous polarization, and slightly overestimates the field for InN mole fractions above 30%, see Fig. 1.8. For $x_{\mathrm{In}} \leq 30\%$, the results deviate by less than 5% compared to Eq. 1.48.

An exemplary band profile with the electron and hole envelope functions is shown in Fig. 1.9. Here, the spatial separation of electron and hole wave function to opposite sides of the QW becomes clear. This phenomenon is referred to as quantum-confined Stark effect (QCSE), and strongly affects the optical properties. On the one hand, the effective band gap is reduced, which leads to a drastic red-shift of the emitted photons. On the other hand, the electron-hole separation reduces the overlap integral. Thereby, also the radiative emission of the QW and the binding energy of excitons are reduced. The issue is discussed in Sec. 2.1.3.

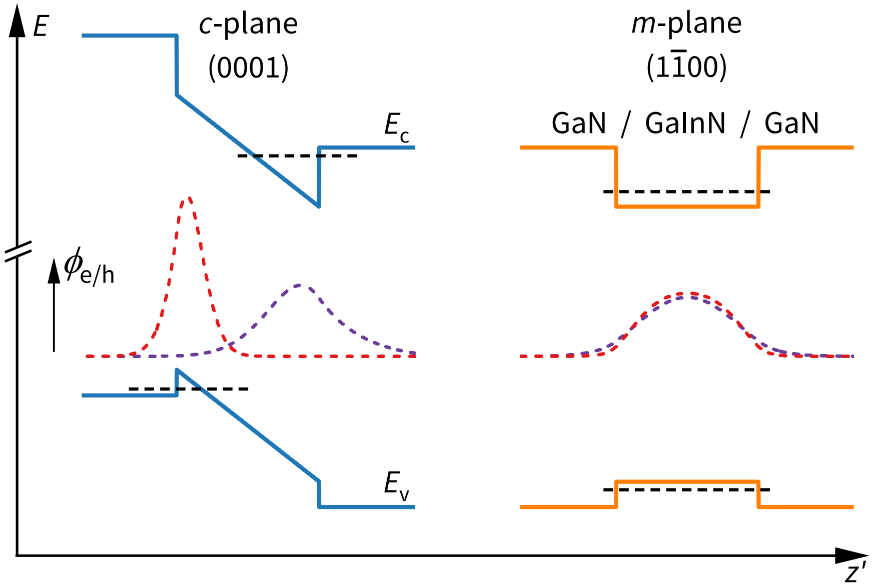

FIGURE 1.9: Band profiles of a GaInN/GaN quantum well (20 % InN mole fraction, 3 nm width) on the polar *c*-plane and the nonpolar *m*-plane, demonstrating the impact of polarization fields. Solid lines indicate the conduction band (E_C) and valence band (E_V) edges, while dashed lines show the first quantized energy levels for electrons and holes. The envelope functions, represented by dashed lines for electrons (violet) and holes (red), are shifted to opposite sites of the *c*-plane quantum well due to the QCSE. For the *m*-plane quantum well, the vanishing polarization fields results in flat band edges and larger overlap of envelope functions.

Since the QCSE is less pronounced for decreasing well width, the use of thin QWs is common for III-nitrides, typically in the order of 1.5-3 nm. Furthermore, the component of the internal polarization field in growth direction is reduced for QWs prepared on semipolar planes, and vanishes for nonpolar planes, where the structure is free of the QCSE [26]. Therefore, QWs prepared on the semipolar (11$\bar{2}$2) orientation, and the nonpolar (1$\bar{1}$00) orientation (*m*-plane) are of particular interest in this thesis.

1.2.5 *Band structure calculations in quantum wells*

For the case that only the energy levels at the band extrema need to be determined for a quantum well structure, it is sufficient to solve the effective mass Schrödinger equations 1.44 and 1.45 for electrons and holes. This can be done using a Schrödinger solver [63] that furthermore calculates wave function overlap and regards excitonic effects. Note that for this purpose, the electric field induced by the piezoelectric polarization is approximated by Eq. 1.50.

If the band structure, i.e. the dispersion relation $E(k)$, is needed, the $\mathbf{k}\cdot\mathbf{p}$ approach described in Sec. 1.1.5 has to be adapted for QWs. This is achieved by the substitution $k_\mathrm{z} \to -i(\partial/\partial z)$, and by addition of the quantum well potential $V_\mathrm{e/h}$ to the equation. Therefore, the following Schrödinger equations for electrons and holes have to be solved:

$$\left[H_\mathrm{e}\left(k_\mathrm{x}, k_\mathrm{y}, -i\frac{\partial}{\partial z}\right) + V_\mathrm{e}(z)\right] \psi_\mathrm{e}(z, \mathbf{k}) = E_\mathrm{e}\, \psi_\mathrm{e}(z, \mathbf{k}) \tag{1.51}$$

$$\left[H_\mathrm{h}\left(k_\mathrm{x}, k_\mathrm{y}, -i\frac{\partial}{\partial z}\right) + V_\mathrm{h}(z)\right] \psi_\mathrm{h}(z, \mathbf{k}) = E_\mathrm{h}\, \psi_\mathrm{h}(z, \mathbf{k}), \tag{1.52}$$

where the Hamiltonians $H_\mathrm{e/h}$ are defined in Sec. 1.1.5, and the wave function ψ is expressed in form of a vector, as introduced in Eq. 1.29.

In case the quantum well is not grown on the basal c-plane, the growth coordinate system (x', y', z') is different from the crystal coordinate system (x, y, z). The transformation is done using the rotation matrix $U(\theta)$, defined in Eq. 1.6. The wave vectors transform accordingly. In order to obtain the valence band dispersion for deliberate GaInN/GaN quantum wells, the numerical implementation presented in Refs. [58] and [68, Appendix A.1] can be used, which is directly applicable to the above equations.

2

RECOMBINATION PROCESSES

Excess charge carriers in a semiconductor can be created by means of optical excitation or carrier injection. Inevitably, recombination leads to a decay of the excited electrons and holes. On the one hand, the responsible transition process can be a radiative band-band recombination. On the other hand, nonradiative processes like Auger recombination or defect-related recombination including phonon emission can occur.

2.1 RADIATIVE RECOMBINATION

Besides the radiative band-to-band transition of excited charge carriers, which is introduced first, the recombination of excitons is discussed in this section. Furthermore, the case of radiative recombination in GaInN/GaN quantum wells is considered afterwards.

2.1.1 *Basics of radiative band-to-band transitions*

The most native recombination process is the radiative band-to-band recombination of an excited electron in the conduction band with a hole in the valence band. During this process, a photon of energy $E_{\mathrm{ph}} = E_2 - E_1 = \hbar\omega$ is emitted. In the following, the recombination rate for radiative transitions in a semiconductor quantum well is derived, according to the descriptions given in Refs. [62] and [69]. Generally, the transition rate from an upper state (2) to a lower state (1) in terms of time-dependent perturbation theory is given by Fermi's Golden Rule [62, Ch. 3]:

$$W_{21} = \frac{2\pi}{\hbar} \left|\langle 2 \,|\, H' \,|\, 1 \rangle\right|^2 , \qquad (2.1)$$

where $H' = (e/m_0)\,\mathbf{A}\cdot\mathbf{p}$ is the perturbation Hamiltonian, including the operator representation of the electromagnetic vector potential $\mathbf{A}$ and momentum $\mathbf{p}$. More specifically, the rate of photon emission per energy interval dE can be written as [62, Ch. 5]:

$$r_{\mathrm{r}}\,\mathrm{d}E = \frac{2\pi}{\hbar}\left(\frac{eA_0}{m_0}\right)^2 \sum_{\lambda}\sum_{1,2} |p_{21}|^2 f_2(1-f_1)\,\delta(E_2 - E_1 - \hbar\omega)\,\mathrm{d}E\,, \qquad (2.2)$$

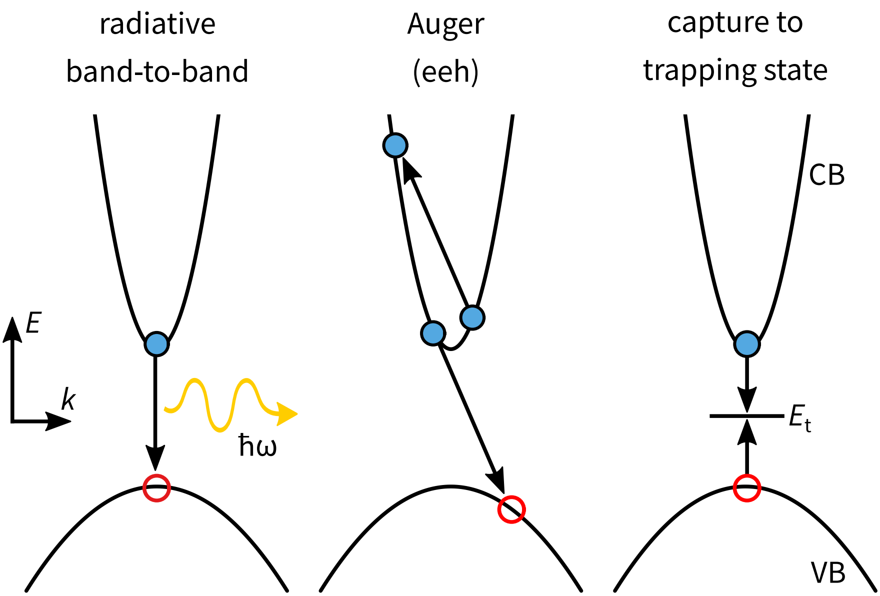

FIGURE 2.1: Schematic of the three major recombination processes: First, radiative band-to-band recombination, where photons of energy $\hbar\omega$ are emitted, and only vertical transitions corresponding to $\Delta k = 0$ are allowed. Second, Auger recombination, here eeh, where the excess energy of the electron-hole recombination is transferred to a third electron that is excited far up in the conduction band. Third, defect-assisted recombination after subsequent capture of electrons and holes to a trapping state in the band gap (energy E_t). Electrons and holes are represented as blue and red circles, respectively, and the conduction (CB) and valence bands (VB) have parabolic shape in the $E(k)$ diagram. Energy and momentum conservation have to be fulfilled for all the processes.

where $|p_{21}|^2$ denotes the momentum matrix element for transition from state (2) to (1):

$$p_{21} = \left\langle 2 \left| e^{i\mathbf{k}_{\mathrm{ph}} \cdot \mathbf{r}}\, \mathbf{p} \right| 1 \right\rangle , \tag{2.3}$$

where $\mathbf{k}_{\mathrm{ph}}$ is the photon wave vector and $\mathbf{r}$ the position vector. Moreover, f_2 and f_1 describe the probability that the upper and lower states are occupied. The sum is taken over all pairs of states whose energy difference is within the interval $[E, E + \mathrm{d}E]$.

Additionally, the sum is taken over all photon modes, resulting in an additional factor $G(\hbar\omega)$, which denotes the photon density of states in the solid:

$$G(\hbar\omega) = \frac{\tilde{n}^3\,(\hbar\omega)^2}{\pi^2\,c^3\hbar^3}\,, \tag{2.4}$$

where $\tilde{n}$ is the refractive index of the crystal, and ω the photon angular frequency. Furthermore, the factor A_0 includes the crystal volume $\tilde{V}$:

$$A_0 = \sqrt{\frac{\hbar}{2\varepsilon_0\tilde{n}^2\tilde{V}\omega}}\,. \tag{2.5}$$

The other symbols are physical constants with their usual meaning.

In a direct-gap semiconductor, the radiative recombination is a transition from the conduction band (CB, state 2) to the valence band (VB, state 1), and thus subject to strict k-conservation. The electron and hole wave functions can be characterized by Bloch states with wave vectors $\mathbf{k}_\mathrm{e}$ and $\mathbf{k}_\mathrm{h}$, and together with the photon wave vector $\mathbf{k}_\mathrm{ph}$, $\Delta\mathbf{k} = \mathbf{k}_\mathrm{e} - \mathbf{k}_\mathrm{h} - \mathbf{k}_\mathrm{ph} = 0$ must hold. Since the photon wave vector can be neglected compared to the extension of the Brillouin zone, only electron and hole wave vectors need to match $(\Delta\mathbf{k} = 0)$, and a corresponding δ-function needs to be included in the matrix element.

Considering the case of a quantum well of width L, charge carriers are confined in one direction, which leads to quantization of the energy states. Assuming confinement in z-direction, the electron and hole wave functions can be separated into a cell-periodic Bloch part, and an envelope function $\phi(z)$. Summarizing these considerations, the momentum matrix element from Eq. 2.3 becomes

$$|p_{12}|^2 = \left\langle |p_\mathrm{cv}|^2 \right\rangle\, |M_\mathrm{mn}|^2\; \delta(\mathbf{k}_\mathrm{e} - \mathbf{k}_\mathrm{h})\,, \tag{2.6}$$

with

$$M_\mathrm{mn} = \langle \phi_\mathrm{e,n} \,|\, \phi_\mathrm{h,m} \rangle = \int \phi_\mathrm{e,n}\phi_\mathrm{h,m}\,\mathrm{d}z \tag{2.7}$$

being the overlap integral of envelope wave functions of the n-th and m-th quantized states in the conduction and valence band. The squared quantity $|M|^2$ is referred to as *wave function overlap* from here on. Since the emitted radiation is assumed to be randomly polarized, the momentum matrix element is averaged over all polarizations, as indicated by angle brackets.

Assuming that the electrons in the conduction band, as well as the holes in the valence band, are in equilibrium with each other, their distribution can be described by Fermi statistics using a quasi Fermi energy for electrons ($E_{\mathrm{F,e}}$) and holes ($E_{\mathrm{F,h}}$).

$$f_{\mathrm{e}} = n \, \frac{\pi\hbar^2}{m_{\mathrm{e}} k_{\mathrm{B}} T} \, \frac{1}{\exp\left(\frac{E - E_{\mathrm{F,e}}}{k_{\mathrm{B}} T}\right) + 1} \,, \tag{2.8}$$

$$f_{\mathrm{h}} = p \, \frac{\pi\hbar^2}{m_{\mathrm{h}} k_{\mathrm{B}} T} \, \frac{1}{\exp\left(\frac{E_{\mathrm{F,h}} - E}{k_{\mathrm{B}} T}\right) + 1} \,. \tag{2.9}$$

In the above relation, n and p denote the areal densities of electrons and holes, and the density of states $m_{\mathrm{e/h}}/(\pi\hbar^2)$ includes the effective electron and hole masses. In order to calculate the total recombination rate, Eq. 2.2 is integrated over all values of photon energy, using the expressions from Eqs. 2.4-2.7. In the non-degenerate limit, the term $f_{\mathrm{e}}(1 - f_{\mathrm{h}})$ can be rewritten using the reduced effective mass μ, and the two-dimensional joint density of states $\mu/(\pi\hbar^2)$, with $\mu^{-1} = m_{\mathrm{e}}^{-1} + m_{\mathrm{h}}^{-1}$. In total, this yields

$$R_{\mathrm{r}} = \int r(E)\, \mathrm{d}E = \frac{e^2 \tilde{n} \hbar \omega \mu}{\pi^2 \hbar^4 m_0^2 \varepsilon_0 c^3} \left\langle |p_{\mathrm{cv}}|^2 \right\rangle |M_{\mathrm{mn}}|^2 \, \frac{(\pi\hbar^2)^2}{m_{\mathrm{e}} m_{\mathrm{h}} k_{\mathrm{B}} T} \, n\, p \,, \tag{2.10}$$

$$\Rightarrow \quad R_{\mathrm{r}} = \frac{e^2 \tilde{n} \hbar \omega}{m_0^2 \varepsilon_0 c^3} \, \frac{1}{(m_{\mathrm{e}} + m_{\mathrm{h}})\, k_{\mathrm{B}} T} \left\langle |p_{\mathrm{cv}}|^2 \right\rangle |M_{\mathrm{mn}}|^2 \, n\, p \,. \tag{2.11}$$

The above expression describes the radiative rate per unit area for transitions between two quantized states in the conduction and valence band. If multiple quantized states are involved, the contributions sum up. Note that the crystal volume $\tilde{V}$ cancels out after integration. An additional factor $1/L$ may be included, however, to obtain the recombination rate per unit volume, comparable to the three-dimensional case.

Using the relation $R_{\mathrm{r}} = Bnp$, the B-coefficient of radiative recombination can be defined. Likewise, the radiative lifetime τ_{r} of excess charge carriers is defined by [69]

$$R_{\mathrm{r}} \equiv \frac{\delta n}{\tau_{\mathrm{r}}} \qquad \Rightarrow \qquad \tau_{\mathrm{r}} = \frac{1}{B\, n_0} \,, \tag{2.12}$$

where δn is the density of excess carriers. The background carrier density n_0 in thermal equilibrium is basically given by the electron concentration due to the unintentional n-type doping present in III-nitride material [70, 71]. For the three-dimensional case, the B-coefficient shows a different temperature dependence ($\propto T^{-3/2}$) according to the joint density of states [62, Ch. 10]. In general, the B-coefficient shows a temperature dependence according to the dimensionality d of the excess charge carriers [72]:

$$B \propto T^{-d/2} . \tag{2.13}$$

Therefore, from the temperature dependence of the radiative lifetime, conclusions can be drawn about the carrier confinement.

2.1.2 *Excitonic recombination*

The above relation treats the recombination of free electrons and holes that are not interacting with each other. Even in a non-degenerate limit, i.e. at low carrier densities ($\delta n \ll n_0$), there is an attracting Coulomb force between positively charged holes and negatively charged electrons. Both can form a quasiparticle, the exciton, which can be described similar to the hydrogen atom [73]. Accordingly, a characteristic exciton binding energy E_{ex}, and an exciton Bohr radius a_{B} can be obtained. Charge carriers in a QW experience an enhanced Coulomb interaction due to the confinement, which decreases the separation of charge carriers. Therefore, the binding energy in a quantum well is higher compared to the intrinsic value in bulk material, and shows a strong dependence on the QW width.

The wave function and binding energy of an exciton can be derived in a similar manner as for electrons and holes in a QW, see Sec. 1.2. The Schrödinger equation for an exciton in a QW contains a combination of the electron and hole Hamiltonian, the confinement potential $V_{\mathrm{e/h}}(z)$, and the attractive Coulomb force between electron and hole [62, Ch. 13]:

$$\left(-\frac{\hbar^2}{2m_{\mathrm{e}}} \nabla_{\mathrm{e}}^2 - \frac{\hbar^2}{2m_{\mathrm{h}}} \nabla_{\mathrm{h}}^2 + V_{\mathrm{e}}(z) + V_{\mathrm{h}}(z) - \frac{1}{4\pi\varepsilon_0 \varepsilon_r \, r} \right) \psi_{\mathrm{ex}} = E \, \psi_{\mathrm{ex}} \tag{2.14}$$

with $\mathbf{r} = \mathbf{r}_{\mathrm{e}} - \mathbf{r}_{\mathrm{h}}$ being the relative electron-hole distance. For further simplification, it is convenient to separate the relative motion of electron and hole from the center-of-mass motion of the exciton. In a quantum well, $\mathbf{r} = (\mathbf{r}_{\|}, z)$ can be defined, where $\mathbf{r}_{\|}$ is the relative electron-hole distance in the QW plane, and z is the out-of-plane coordinate. The center-of-mass coordinate of the exciton is defined as $\mathbf{R} = (m_{\mathrm{e}}\mathbf{r}_{\mathrm{e}} + m_{\mathrm{h}}\mathbf{r}_{\mathrm{h}})/(m_{\mathrm{e}} + m_{\mathrm{h}})$. In combination, the following ansatz is used for the exciton wave function:

$$\psi_{\mathrm{ex}}(R, \boldsymbol{\rho}, z) = \chi(\mathbf{R}) \, \xi(\mathbf{r}_{\|}) \, \phi_{\mathrm{e}}(z_{\mathrm{e}}) \, \phi_{\mathrm{h}}(z_{\mathrm{h}}) , \tag{2.15}$$

where $\chi(\mathbf{R})$ denotes a plane wave that depends only on the center-of-mass coordinate, $\phi_{\mathrm{e/h}}$ denote the envelope functions arising from the quantization along z, and

$$\xi(\mathbf{r}_{\|}) = \sqrt{\frac{2}{\pi a_{\mathrm{B}}^2}}\, e^{-r_{\|}/a_{\mathrm{B}}} \tag{2.16}$$

is the wave function describing the electron-hole relative motion in the QW plane [72]. Numerically, the exciton wave function can be calculatated by variational methods. After solving the time-independent Schrödinger equation (Eq. 2.14), the energies and envelope functions are known for single electrons and holes. To calculate the exciton wave function, the Coulomb potential is introduced as a second order perturbation. Using the function $\xi(\boldsymbol{r}_{\|})$, where a_{B} is substituted with the parameter a, the exciton Bohr radius is determined by a variational appraoch. By variation of a, the eigenvalue E in Eq. 2.14 is minimized as $a \to a_{\mathrm{B}}$ [62, Ch. 13].

The radiative recombination rate R_{ex} of excitons in a QW can also be deduced in a similar way as for free electrons and holes. Considering Eq. 2.11, the product (np), denoting the densities of free electrons and holes, needs to be replaced by the density of excitons (x) times the probability density of the wave function $\xi(r_{\|})$ at vanishing electron-hole distance in the QW plane [72]:

$$R_{\mathrm{ex}} = B^{2\mathrm{D}} \left|\xi(r_{\|} = 0)\right|^2 x \; = \; B^{2\mathrm{D}} \frac{2}{\pi a_{\mathrm{B}}^2} x\,. \tag{2.17}$$

Thereby, the excitonic radiative lifetime τ_{ex} can be defined:

$$R_{\mathrm{ex}} = B_{\mathrm{ex}}\, x \quad \Rightarrow \quad \tau_{\mathrm{ex}} = 1/B_{\mathrm{ex}}\,. \tag{2.18}$$

2.1.3 *Radiative recombination in GaInN/GaN quantum wells*

As mentioned in Sec. 1.1.4, the internal polarization fields and the resulting quantum-confined Stark effect (QCSE) have severe impact on the radiative recombination. On the one hand, the electron-hole overlap, defined in Eq. 2.7, is reduced, since electron and hole envelope functions are shifted to opposite sides of the QW. Furthermore, the effective band gap is reduced, which leads to a strong redshift of the emission spectra. Also the exciton binding energy is reduced by the polarization field, which in total leads to longer radiative lifetimes compared to a field-free GaInN/GaN QW.

On the other hand, these effects depend strongly on the QW composition and thickness. Overlap integral and exciton binding energy are further decreasing with increasing InN mole fraction or QW width. Thus, the use of thin QWs is preferable. Typical widths are 1.5-3 nm, as mentioned in Sec. 1.2.4. Another solution already proposed in Sec. 1.2.4 is the growth on semipolar or nonpolar orientations. The implications of the vanishing polarization fields on the radiative recombination are discussed in detail in Ch. 4, where also effective carrier masses and excitonic effects are considered.

2.2 AUGER RECOMBINATION

Auger recombination is an intrinsic process, where the excess energy of a band-band recombination is transferred to a third charge carrier. Therefore, the Auger recombination is a nonradiative process, and involves three charge carriers, where the third can be either a hole in the valence band (ehh process), or an electron in the conduction band (eeh process), which is excited to a high-energy state in the respective band [74, Ch. 2]. Naturally, energy and momentum conservation must be fulfilled for this recombination process, as shown schematically in Fig. 2.1. Therefore, Auger recombination is expected to be reduced for large band gap materials like III-nitrides [75]. Several experimental and theoretical works, however, report on an Auger rate that is comparable to smaller band gap semiconductors [76–78]. Therefore, Auger recombination is also a possible cause of efficiency droop in III-nitride light emitters, i.e. the reduction of quantum efficiency at high carrier densities [79–81].

Nevertheless, the Auger rate becomes relevant only at high carrier densities, since the process involves three carriers and thus scales with n^3. For this reason, Auger recombination can be neglected in the experiments in this thesis, where low excitation conditions are maintained.

2.3 DEFECT-ASSISTED RECOMBINATION

Contrary to the band-to-band processes treated in the above sections, the defect-assisted recombination involves intermediate levels in the band gap. Recombination via such defect-related levels occurs in the case that both, electron and hole, are captured into it. The excess energy is at least partly transformed into phonons, which makes it a nonradiative recombination process. The recombination via defect-related states can be described by Shockley-Read-Hall statistics, and thermally activated carrier capture via multi-phonon emission. Finally, the process of cascade capture is introduced briefly.

2.3.1 *Shockley-Read-Hall statistics*

Contrary to the radiative transition, where an electron and a hole directly recombine under photon emission, the process of defect-assisted recombination includes an intermediate level in the band gap. The capture and emission rates associated with such trapping centers, located at energy E_t in the band gap, can be described by Shockley-Read-Hall (SRH) statistics [82, 83]. In this context, the respective rates for electron and hole capture to a trapping center are

$$R_\mathrm{c,e} = C_\mathrm{e}(1 - f_\mathrm{t})n - C_\mathrm{e} f_\mathrm{t} n_1 \,, \tag{2.19}$$

$$R_\mathrm{c,h} = C_\mathrm{h}(1 - f_\mathrm{t})p - C_\mathrm{h} f_\mathrm{t} p_1 \,, \tag{2.20}$$

where n and p are the concentrations of electrons and holes, and f_t is the fraction of trapping centers occupied by electrons. C_e and C_h denote the probabilities of electron and hole capture per unit time. Note that the second terms in the above equations, including n_1 and p_1, describe the process of carrier emission from trapping centers. The factors n_1 and p_1 are defined as

$$n_1 = N_\mathrm{C} \exp\left(\frac{E_\mathrm{t} - E_\mathrm{C}}{k_\mathrm{B} T}\right) , \tag{2.21}$$

$$p_1 = N_\mathrm{V} \exp\left(\frac{E_\mathrm{V} - E_\mathrm{t}}{k_\mathrm{B} T}\right) , \tag{2.22}$$

where N_C and N_V describe the effective density of states in the conduction and valence band, respectively. E_C and E_V are the respective band edge energies.

As soon as both, electron and hole, are captured to a trapping center, recombination occurs. To derive an expression for the rate of recombination via trapping centers, constant excitation of electron-hole pairs is assumed. For steady-state conditions, i.e. equal generation and recombination rates ($R_\mathrm{c,e} = R_\mathrm{c,h}$), the recombination rate becomes

$$R_\mathrm{SRH} = \frac{np - n_\mathrm{i}^2}{\tau_\mathrm{h}(n + n_1) + \tau_\mathrm{e}(p + p_1)} , \tag{2.23}$$

where n_i is the intrinsic carrier concentration, and τ_e and τ_h are the minority carrier lifetimes for electrons and holes, which are related to the capture probabilities C by

$$\tau_\mathrm{e} = \frac{1}{C_\mathrm{e}} , \qquad \tau_\mathrm{h} = \frac{1}{C_\mathrm{h}} , \tag{2.24}$$

with

$$C_\mathrm{e} = c_\mathrm{n} N_\mathrm{t} \,, \qquad C_\mathrm{h} = c_\mathrm{h} N_\mathrm{t} \,. \tag{2.25}$$

Here, N_t is the number of trapping centers per unit volume, and c_e and c_h describe the capture coefficients for electrons and holes. From Eq. 2.23, it becomes evident that the rate of recombination via trapping centers scales linearly with carrier density ($R_{SRH} \propto n$) [83].

As described above, the nonradiative recombination via trapping centers in the band gap can be described by SRH statistics. The process of carrier capture itself takes place either via multi-phonon emission, or via cascade capture under emission of single phonons. Which process prevails, depends on the nature of the trapping center, its energetic position in the band gap and its charge state. The following section shows that the process of multi-phonon capture (MPC) is suitable to describe the nonradiative recombination processes investigated in this thesis. This goes along with an Arrhenius-type temperature dependence of the nonradiative carrier lifetimes.

2.3.2 *Cascade capture*

Shallow trapping centers, energetically located near the band edges, are usually related to impurity atoms or interstitials. The process of cascade capture requires a charged trapping center, which induces a long-range coulomb potential and attracts charge carriers. Besides its ground state, bound carriers can populate one of the excited states of the trapping center. The carrier capture happens into an excited state via emission of a single phonon, and the subsequent transition into lower states happens likewise via emission of single phonons. Therefore, the energy difference between the excited states needs to match typical phonon energies, which are in the range < 100 meV for GaN [84]. The simultaneous capture of an electron and a hole to such a trapping center is, however, unlikely. On the one hand, the energetic position near one of the band edges makes the capture of a carrier of the other species across the band gap difficult. On the other hand, the Coulomb potential arising from the charged center is likely to be attractive for one carrier species, while being repellent for the other. This lowers the capture cross section considerably, and makes them inefficient nonradiative recombination centers. Furthermore, the reverse process of carrier emission will become increasingly important with higher temperature. Thus, shallow trapping centers are likely to be populated at low temperatures, and may emit carriers at increasing temperatures. Although defect states in the middle of the band gap can be charged as well, the larger energy separation between the excited states again lowers the cross section for cascade capture into the ground state [74, Ch. 2], [85].

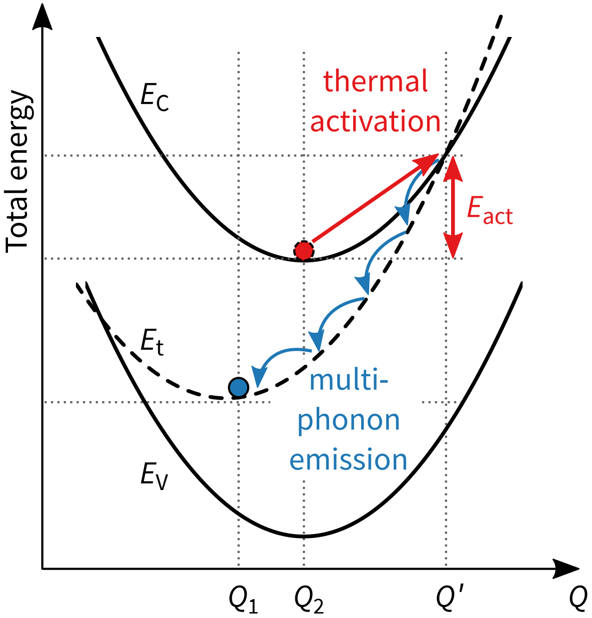

FIGURE 2.2: Configuration coordinate diagram showing the vibrational dispersion of conduction band (E_C), valence band (E_V), and trapping center (E_t). The total energy, i.e. electron plus phonon energy, is given as function of the displacement Q from equilibrium. Due to electron-phonon interaction, the energetic minima are located at different Q-values. After thermal activation, a charge carrier (red) can be captured into the trap state (blue) by multi-phonon emission.

2.3.3 *Multi-phonon recombination*

For carrier capture into deep traps, multi-phonon processes are usually prevailing, which has been shown for other III-V compounds like GaAs and GaP [86]. Deep traps, near the center of the band gap, are usually related to crystal defects, e.g. dislocations, grain boundaries, or vacancies and their complexes, whose local potential landscapes differ substantially from the host crystal. These centers and the corresponding bound electron states are strongly localized and extend only a few lattice constants. They represent efficient nonradiative centers, since the energetic difference to both band edges is comparable and makes simultaneous electron and hole capture more probable. During the capture process, a large amount of electron energy is released at once via multiple phonons. The process is possible due to the electron-lattice interaction, which has been theoretically described by Huang and Rhys [87].

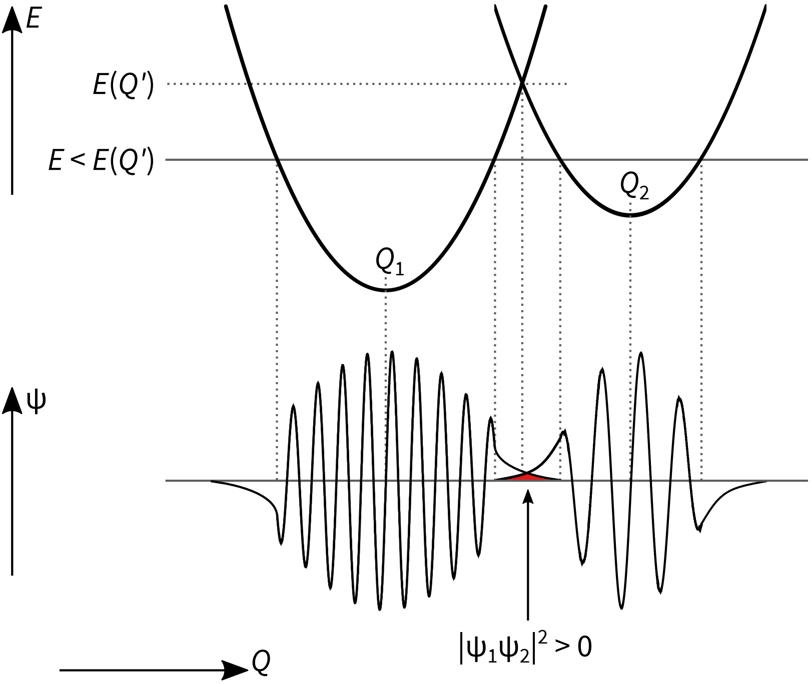

FIGURE 2.3: Schematic configuration coordinate diagram, showing the vibrational dispersion and the wave functions of electrons in the trap state (at Q_1) and in the conduction band (at Q_2). Although the crossing point at Q' cannot be reached by thermal activation, the exponentially decaying tails of the wave functions overlap to make quantum-mechanical tunneling possible. Adapted from Ref. [74, Ch. 6].

The capture process can be visualized using a configuration coordinate diagram like in Fig. 2.2, which is exemplary for a trap state in the band gap. The configuration coordinate diagram shows the total energy of the system, which is the sum of electronic and vibrational energy, as a function of the displacement Q from equilibrium. The vibrational dispersion is assumed quadratic, and thus the potential energy curves are parabolae, whose equilibrium positions are shifted. The shift depends on the strength of the electron-lattice interaction, namely the Huang-Rhys factor [87]. The resulting parabolae cross at Q', where the transition from the conduction band to the trap state is possible in a semiclassical picture. Thus, charge carriers need a thermal energy larger than E_{act} to undergo the transition. The excess energy $\Delta E = E_{\text{c}}(Q_2) - E_{\text{t}}(Q_1)$

is transfered to the lattice via multi-phonon emission [74, Ch. 6]. The transition rate R_{21} of carrier capture can be described by

$$R_{21} = \gamma(T)\,\exp\left(-\frac{E_{\text{act}}}{k_{\text{B}}T}\right), \tag{2.26}$$

where the prefactor $\gamma(T)$ itself may depend on temperature. The reverse process can be described accordingly, and the transition rates are related by $R_{12}/R_{21} = \exp(\Delta E/k_{\text{B}}T)$. Using Eq. 2.26, the charge carrier lifetime for recombination via trap states can be expressed by

$$\frac{1}{\tau_{\text{t}}} = n_{\text{t}}\,c(T) \propto \exp\left(-\frac{E_{\text{act}}}{k_{\text{B}}T}\right), \tag{2.27}$$

where n_{t} denotes the density of trapping centers, and the temperature dependent capture coefficient $c(T)$ shows a characteristic Arrhenius-like behavior. The proportionality factor in the above equation, since related to $\gamma(T)$ in Eq. 2.26, may depend on temperature as well, depending on type and charge of the trapping center [88]. The above description uses a simplified picture, assuming quadratic dispersion and only a single relevant vibrational mode. In reality, more complicated multi-dimensional energy surfaces and more vibrational states need to be regarded [74, Ch. 6].

Multi-phonon recombination via tunneling

At low temperatures, the system's thermal energy is considerably reduced. Therefore, the probability of finding carriers with thermal energy larger than E_{act} is small, and the transition to the trap state would become impossible. Considering an electron in the conduction band, its quantum character implies a non-zero probability of finding the electron in the trap state, which would be inaccessible within the frame of the semiclassical picture. Therefore, the carrier capture can happen via tunneling [74, Ch. 6], [88]. The overlap of the corresponding wave functions associated with the conduction band and trap state is shown schematically in Fig. 2.3. It should be emphasized that the carrier capture via tunneling, and the temperature-activated behavior described in the previous section, are based on the same physical process, namely multi-phonon capture. While Eq. 2.27 describes the high-temperature limit, the multi-phonon recombination rate approaches a constant value in the low-temperature limit. The corresponding constant lifetime $\tau_{\text{nr},0}$ can be included to extend the range of application of Eq. 2.27 to low temperatures.

3

EXPERIMENTAL METHODS

This chapter describes the different experimental techniques and measurement procedures that are used throughout the thesis. First, the epitaxial growth, and the structural characterization of the samples are introduced briefly. Afterwards, the two experimental setups used for time-resolved photoluminescence spectroscopy measurements are described, and finally, the applied evaluation procedure is presented.

3.1 EPITAXIAL GROWTH

III-nitride structures are usually prepared by epitaxial methods. During the epitaxial growth, the deposited material forms a layer, whose lattice parameters in the growth plane are adopted from the underlying substrate. For homoepitaxial growth, deposited layer and substrate consist of the same material. For III-nitride structures, the heteroepitaxial growth, which uses foreign substrates, is more common. Typically, sapphire (α-Al_2O_3) in the (0001) orientation is used as substrate for the growth of (0001)-oriented III-nitrides, especially GaN-based structures. Other possible substrates are SiC or Si (111). All the foreign substrates have a relatively large lattice mismatch to GaN (16 % for sapphire [89]) and other III-nitrides. Thus, heteroepitaxial III-nitride layers show high densities of threading dislocations, typically in the order of $10^8/\mathrm{cm}^2$ - $10^{10}/\mathrm{cm}^2$.

For homoepitaxy, high-quality III-nitride crystals are needed. Bulk-like GaN crystals can be grown using hydride vapor phase epitaxy (HVPE), resulting in wafer-size crystals that can even be cut to obtain substrates for non- and semipolar growth orientations. These substrates are referred to as pseudo-bulk, and typical threading dislocation densities are in the order of $10^6/\mathrm{cm}^2$ to $10^7/\mathrm{cm}^2$. Real bulk crystals are available from ammonothermal growth methods, where threading dislocation densities of $< 1 \times 10^5/\mathrm{cm}^2$ can be achieved. Compared to the bulk and pseudo-bulk substrates, the growth on sapphire remains the most cost-efficient method. Alternative approaches use structuring of substrates and subsequent lateral overgrowth to achieve high-quality substrates with reduced threading dislocation densities compared to the simple heteroepitaxial growth.

The samples investigated in this work are grown by metal-organic vapor phase epitaxy (MOVPE) in a commercial Aixtron machine. The sample growth was carried out by Uwe Rossow [90], in cooperation with either Philipp Horenburg [91], Holger Jönen [92], Ernst Ronald Korn [93], or Daniel Fuhrmann [94], which is also indicated in Appendix A. As substrates, sapphire or (pseudo-)bulk GaN are used for c-plane, m-plane, and $(11\bar{2}2)$-oriented structures. In MOVPE growth, the deposited material is supplied by metalorganic precursors: trimethylgallium, trimethylindium, and trimethylaluminum. Ammonia is used as nitrogen source. Using nitrogen and hydrogen as carrier gases, the precursors are carried along the substrate by a laminar gas flow. Due to the high temperatures in the reactor, the precursors dissociate and supply group-III metal atoms and nitrogen atoms to the growth front. For GaN, typical growth temperatures are above 1000 °C, whereas for GaInN, the growth temperature is around 750 °C to prevent desorption of indium from the surface. The GaInN growth takes place in the desorption-limited regime, where the amount of indium atoms that are incorporated into the crystal is controlled by the growth temperature. For this growth regime, the indium precursor flux has to be set sufficiently high, but remains constant for all intended compositions.

3.2 STRUCTURAL CHARACTERIZATION

Investigating a sample with X-ray diffraction (XRD) allows to determine the lattice parameters, and to derive the strain state and composition of the structure. Therefore, this is the standard method for structural characterization of nearly all samples. In this section, the structural characterization by X-ray diffraction is introduced briefly. First, diffraction in terms of the reciprocal lattice is described, followed by a description of several scanning techniques.

As described in Sec. 1.1.2, any crystal lattice can be generated by basis vectors in real and reciprocal space. A set of planes in this crystal can be described by Bravais-Miller indices $(hkil)$, and the corresponding vector in reciprocal space becomes

$$\mathbf{G}_{\mathrm{hkl}} = h\,\mathbf{a}_1^* + k\,\mathbf{a}_2^* + l\,\mathbf{c}^* \,, \tag{3.1}$$

where $\mathbf{a}_{1/2}^*$ and $\mathbf{c}^*$ are the basis vectors of the reciprocal lattice. While the reciprocal lattice vector $\mathbf{G}_{\mathrm{hkl}}$ is perpendicular to the corresponding planes in real space, their distance is given by

$$d_{\mathrm{hkl}} = \frac{2\pi}{|\mathbf{G}_{\mathrm{hkl}}|} \,. \tag{3.2}$$

Considering a crystal lattice that is irradiated by X-rays of wavelength λ, the incident and diffracted wave vectors, $\mathbf{k}_{\mathrm{i}}$ and $\mathbf{k}_{\mathrm{f}}$, shown in Fig. 3.1, have equal length ($k = 2\pi/\lambda$). Constructive interference of the X-rays occurs, when the diffraction vector $\mathbf{Q} = \mathbf{k}_{\mathrm{f}} - \mathbf{k}_{\mathrm{i}}$ equals a vector $\mathbf{G}_{\mathrm{hkl}}$ of the reciprocal lattice. This is known as the Laue condition,

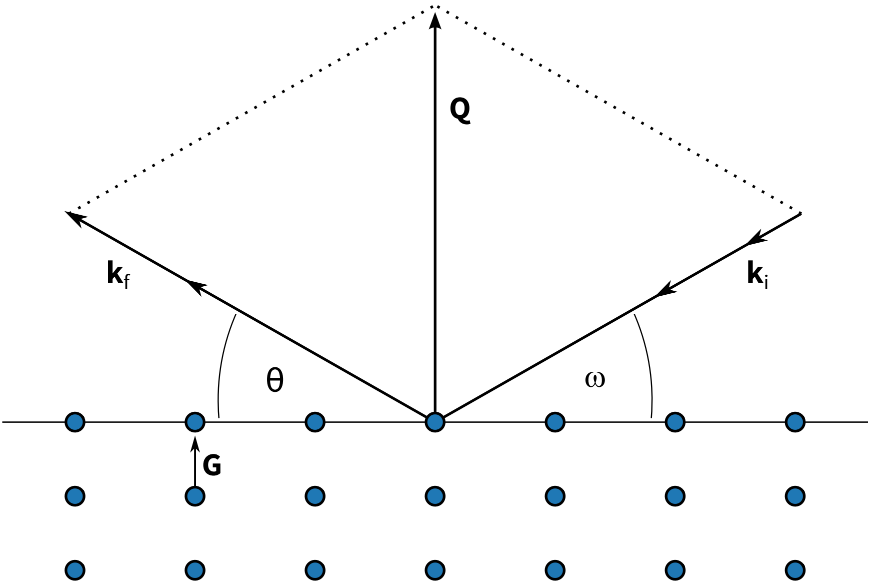

FIGURE 3.1: Schematic of a reciprocal lattice irradiated by X-rays of wave vector $k_\mathrm{i} = 2\pi/\lambda$ under an angle ω. The diffracted X-rays are detected under an angle θ with respect to the sample surface. The wave vectors of incident and diffracted beam have equals length ($k_\mathrm{i} = k_\mathrm{f}$). Constructive interference occurs if the diffraction vector $\mathbf{Q} = \mathbf{k}_\mathrm{f} - \mathbf{k}_\mathrm{i}$ equals a vector $\mathbf{G}$ of the reciprocal lattice.

which is equivalent to the Bragg condition using the interplanar spacing d_hkl of the real lattice. Alternatively, the reduced diffraction vector $q = Q/2\pi$ with length $1/d_\mathrm{hkl}$ can be used. The incident and diffracted beams enclose the angles ω and θ with the crystal surface, respectively. Employing the crystal coordinate system, it is useful to separate the diffraction vector into the components

$$q_\parallel = \frac{1}{\lambda}\left[\cos(\omega) - \cos(2\theta - \omega)\right] , \tag{3.3}$$

$$q_\perp = \frac{1}{\lambda}\left[\sin(2\theta - \omega) + \sin(\omega)\right] , \tag{3.4}$$

where $q_\parallel$ denotes the component parallel to the sample surface, and $q_\perp$ the one perpendicular to it [95].

The X-ray diffraction setup that is used for measurements presented in this thesis is a Panalytical X'Pert Pro machine. The X-ray diffraction measurements were carried out by Heiko Bremers [96], partly in cooperation with Philipp Horenburg [97], which is also indicated in the respective plots and tables in Ch. 4-6. The machine is equipped with a copper anode, and a high precision goniometer is used to position the sample. Several monochromators, filters and detectors are available to perform a variety of diffraction measurements. The most important scan types are introduced briefly. The symmetric 2θ-ω scan probes the lattice parameters in growth direction, i.e. perpendicular to the sample surface. For this scan type $\omega = \theta$ is set, and thus the angle between incoming and diffracted beam equals 2θ. The 2θ-ω scan in grazing-incidence geometry (in-plane scan) uses a small incident angle $(\omega < \theta)$ and is thus sensitive to the layer close to the surface, since the X-rays penetrate only some tens of nanometers into the crystal. Another type of scan is the reciprocal space map (RSM), where the measured intensity is plotted versus the reciprocal coordinates $q_{\|}$ and $q_{\perp}$. For this scan, the angles ω and θ are varied to measure a continuous intersection of the reciprocal space. Probing an asymmetrical reflex ($q_{\|} \neq 0$), also in-plane lattice parameters can be determined.

The evaluation of lattice parameters and layer composition is covered in Refs. [98] and [32], in particular for the case of semipolar growth orientation. Furthermore, the review of Moram and Vickers [99], and the guide written by Kidd [95] provide detailed information about the X-ray diffraction of III-nitrides.

3.3 TIME-RESOLVED PHOTOLUMINESCENCE SPECTROSCOPY

After optical or electrical excitation of a semiconductor, the excess charge carriers undergo *radiative* or *nonradiative* recombination, like Auger or defect-assisted recombination. The radiative recombination results in photon emission, which can be detected as luminescence signal. In the case of optical excitation, the signal is referred to as *photoluminescence*. Nonradiative recombination results in the absence of luminescence, which cannot be detected directly. After all, it is crucial to determine the recombination mechanisms that are responsible for the observed photoluminescence behavior. This can be achieved by measurements of the photoluminescence intensity as function of delay time after an excitation pulse, which is referred to as *time-resolved photoluminescence spectroscopy* [100, p. 505].

In the following, an ensemble of indistinguishable charge carriers is considered, which can be described by the density $n = n_0 + \delta n$ for electrons, and $p = p_0 + \delta p$ for holes. Here, n_0 denotes the electron density under equilibrium conditions, and the corresponding hole density can be neglected ($p_0 \approx 0$) due to the unintentional n-type doping present in III-nitride material [70, 71]. Furthermore, the density of excess electrons and holes is equal under optical excitation ($\delta n = \delta p$). The time derivative of n can be written as

$$\frac{\partial n}{\partial t} = G - R = G - (R_\mathrm{r} + R_\mathrm{nr}), \tag{3.5}$$

where G is the generation rate for excess carriers, and the rates of radiative (R_r) and nonradiative recombination (R_nr) add up to the total recombination rate (R). As introduced in Ch. 2, a characteristic lifetime τ can be assigned to each recombination mechanism. While τ_r and τ_nr denote the radiative and nonradiative lifetimes, the effective lifetime τ_eff describes the recombination of the charge carrier ensemble as a whole.

$$R = \frac{\delta n}{\tau_\mathrm{eff}}, \qquad R_\mathrm{r} = \frac{\delta n}{\tau_\mathrm{r}}, \qquad R_\mathrm{nr} = \frac{\delta n}{\tau_\mathrm{nr}}, \tag{3.6}$$

$$\Rightarrow \qquad \frac{1}{\tau_\mathrm{eff}} = \frac{1}{\tau_\mathrm{r}} + \frac{1}{\tau_\mathrm{nr}}. \tag{3.7}$$

Using a short laser pulse to generate excess charge carriers, the generation G in Eq. 3.5 is turned off for a delay of $t > 0$:

$$\frac{\partial n}{\partial t} = -R = -\frac{\delta n}{\tau_\mathrm{eff}}, \tag{3.8}$$

and the resulting differential equation is solved by a simple mono-exponential decay, which can be directly assigned to the detected photoluminescence intensity:

$$I(t) = I_0 \exp\left(-\frac{t}{\tau_\mathrm{eff}}\right). \tag{3.9}$$

Here, $I_0 = I(t = 0)$ denotes the initial intensity at zero delay time, and the effective lifetime τ_eff describes the time at which the photoluminescence signal has decayed to $1/e \approx 37\,\%$ of the initial value. Contrary, the initial intensity is determined only by radiative recombination:

$$I_0 \propto R_\mathrm{r} = \frac{\delta n}{\tau_\mathrm{r}}. \tag{3.10}$$

This can be further explained by emphasizing that at zero delay ($t = 0$), the initially prepared excess carrier density δn has not undergone any decay, and thus the photoluminescence signal is only affected by the radiative lifetime τ_r. The photoluminescence decay after pulsed excitation can be measured using one of the experimental setups introduced in the following sections.

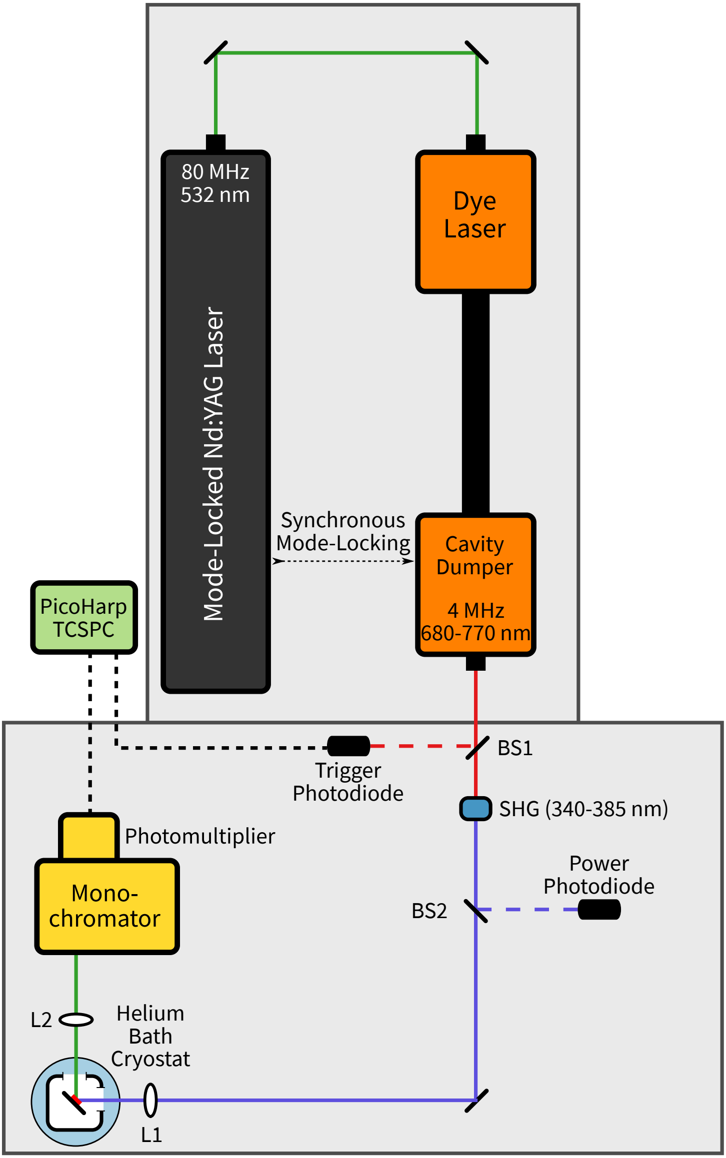

FIGURE 3.2: Schematic of the TCSPC setup, showing the pulsed laser source with cavity dumper and second harmonic generation (SHG). The sample is mounted in a helium bath cryostat, and a photomultiplier with preceding monochromator is used to detect the photoluminescence. The detected single-photon events are processed by the PicoHarp TCSPC system.

3.3.1 *Time-correlated single photon counting setup*

This setup contains three major components: the pulsed laser source for excitation, the cryostat to control the sample temperature, and the photoluminescence detection.

Essentially, the pulsed laser source is a dye laser (Spectra Physics 375) using the dye Pyridin-2 (Radiant Dyes) in an alcohol-based solution. The laser emission can be tuned from 680 to 770 nm. These wavelengths are frequency doubled using a barium borate crystal (β-BaB_2O_4, BBO), which results in ultraviolet (UV) wavelengths between 340 and 385 nm that are used to excite the samples. The dye laser itself is pumped by a Nd:YAG laser (Spectra Physics 3800S), which emits at 1064 nm, and is frequency doubled to 532 nm to pump into the absorption bands of the Pyridin-2 dye. Both lasers are synchronously mode-locked to achieve pulsed operation. Using active mode-locking, a pulse duration in the ps-range can be achieved. The native repetition rate of the system is 80 MHz, which is reduced in the dye laser using a cavity dumper. For most purposes, the reduction by a factor of 20 is used, resulting in a repetition rate of 4 MHz for the measurements. This corresponds to a time slot of 250 ns between two excitation pulses, which is usually sufficient to allow for a complete decay of excess carriers in the sample. If the repetition rate is chosen to high, an incomplete decay would result in residual luminescence that distorts the measured decay behavior. In principle, also repetition rates lower than 4 MHz are possible, down to single shots. An advantage of the cavity dumper is that down-regulation of the repetition rate takes place inside the cavity, which remains closed between the outcoupling of subsequent pulses. Thereby, the output power can be significantly increased for every pulse. The final dye laser pulses have a duration of $\approx$ 5 ps, and a pulse energy of $<$ 0.5 pJ is reached in the UV.

The samples are mounted in a helium bath cryostat that covers a temperature range between 4.4 K and 325 K. The laser pulses are focused onto the sample surface at an angle of 45° using a fused silica lens. The emitted photoluminescence is collected by another lens, and is focused into a 22.7 cm subtractive double grating spectrometer (Jobin Yvon, Spex 1680) that is used as monochromator with a 1800 grooves/mm grating. The monochromated light is detected by a multi-channel plate photomultiplier (Hamamatsu R3809U-02), which is sensitive enough to detect single photons. The first photon to arrive at the photomultiplier will produce an electrical signal that can be used to count the single events. Using a beamsplitter (BS1) right behind the cavity dumper, some percent of each laser pulse are directed to a fast photodiode and provide a reference signal. The signals are forwarded to a time-correlated single photon counting (TCSPC) system (PicoQuant PicoHarp 300), which determines the time difference between both. The single-photon detection is used as stop signal, while the reference signal from the excitation beam is used as starting signal. From repeated collection of single photon events, which are sorted into channels of 4 ps width by the PicoHarp, a histogram is created. Every laser pulse and the subsequent single-photon detection represent a single event. A measurement of 10 s produces up to 4×10^7 events, which is usually sufficient to produce a smooth intensity decay with a signal-to-noise ratio of > 100 : 1.

Since the PL light is monochromated before detection, the signal can be recorded spectrally resolved by repeating the measurement for different monochromator positions. With entrance and exit slit widths between 1 and 2.5 mm, the spectral bandwidth is about 1.2-3 nm in wavelength. The step width should be chosen accordingly to collect the whole QW PL, i.e. the PL of the whole charge carrier ensemble.

The sample itself is mounted in a cryostat on a heat exchanger, which is cooled down by a liquid helium bath. A Lakeshore 330 temperature controller takes care of temperature measurement, and heating of the sample mount. Typically, a temperature range between 5 K and 300 K is covered in the measurements.

Depending on the laser wavelength, the QW samples are excited resonantly or non-resonantly. For resonant excitation, the excitation takes place only in the QW, not in the barrier material with larger band gap. Therefore, the excitation energy of the laser is chosen to lie between the band gap of barrier and QW. For a GaInN/GaN QW, this setup provides wavelengths around 375 nm that are suitable for resonant excitation. Contrary, in the non-resonant case, also the barrier material is excited and contributes to the photoluminescence.

The results shown in Ch. 4 and Ch. 6 rely partly on time-resolved photoluminescence measurements carried out by Torsten Langer [101] and Manuela Klisch [102] using the TCSPC setup, which is also indicated in the respective plots and tables.

3.3.2 *Streak camera setup*

This setup provides an extremely broad variety of excitation wavelengths and pulse energies, combined with an increased temporal resolution compared to the TCSPC setup. The pulsed laser source in this setup is an amplified Ti:sapphire laser system (Coherent Astrella), consisting of a passively mode-locked oscillator (Coherent Vitara-S), which serves as seed laser for the amplifier cavity. Typically for Ti:sapphire lasers, the oscillator emits at a fixed central wavelength of 810 nm with a repetition rate of 80 MHz, while the amplifier, with 800 nm central wavelength, has a reduced repetition rate of only 5 kHz, but considerably higher pulse energy. The oscillator provides 7 nJ of pulse energy, the amplified output reaches up to 1.2 mJ. The oscillator is pumped by a 532 nm optically pumped semiconductor laser (Verdi-G5) that operates in continuous-wave mode. The amplifier cavity contains another Ti:sapphire crystal, which is pumped by a Q-switched Nd:YLF laser (Coherent Revolution-65), operating

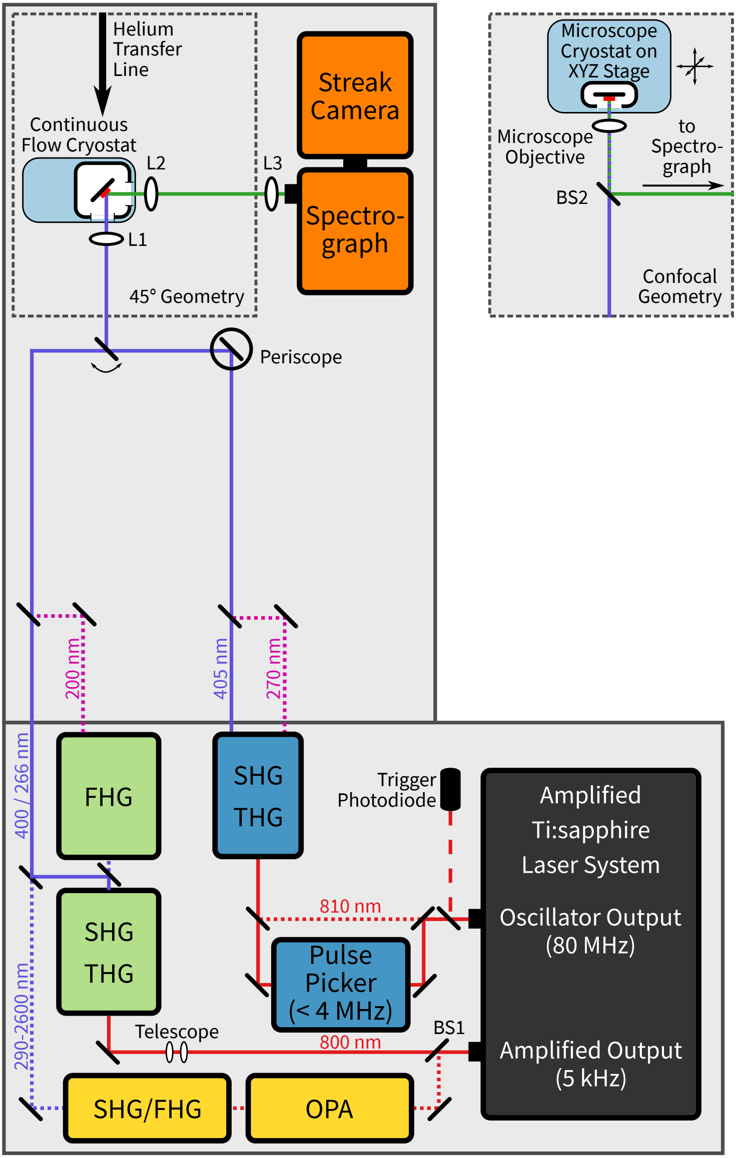

FIGURE 3.3: Schematic of the streak camera setup, showing the amplified Ti:sapphire laser system with frequency conversion. The sample is mounted in a helium continuous flow cryostat (under 45° or confocal geometry), and a streak camera with preceding spectrograph detects the time-resolved photoluminescence.

at 527 nm wavelength. The additional pumping amplifies the seed pulse after six to eight round turns in the cavity to its final pulse energy. The precise coupling of seed and pump pulses at a rate of 5 kHz is maintained by a synchronous delay generator (SDG Elite). In order to avoid too high power densities on the optical components, the laser pulse is temporally stretched before coupling into the amplifier cavity. After the amplification, the final pulse is compressed to reach a duration of 35 fs, which is close to the transform limited pulse duration for the measured bandwidth of 28 nm (FWHM). Only with such large bandwidths the generation of ultra-short pulses in the fs-regime is possible. This can cause difficulties, since the fs-pulses are subject to dispersion that causes temporal broadening of the pulse when passing through optical components or even air.

The amplifier output is divided by a beam splitter (BS1). One third of the output passes on to the stage for second harmonic generation (SHG), which produces a wavelength of 400 nm. Subsequently, wavelengths of 266 nm and even 200 nm are generated by third and fourth harmonic generation (THG, FHG). In fact, the higher harmonics are generated not by directly tripling or quadrupling the fundamental of 800 nm, but rather by sum frequency generation of the second harmonic with the fundamental to achieve the third harmonic, and accordingly mixing the third harmonic with the fundamental to achieve the fourth harmonic. Thin BBO crystals are used for the frequency conversion throughout the setup in order to minimize the pulse dispersion. Before entering the SHG stage, the beam diameter is reduced by a mirror telescope.

The remaining two-thirds of the amplifier output are directed to an optical parametric amplifier (OPA), which uses nonlinear conversion to deliberately split one photon of the fundamental into two photons of longer wavelength, namely signal (1150-1600 nm), and idler (1600-2500 nm). Subsequently, the signal and idler beams can be frequency doubled (SHG). Repeating the freuquency doubling provides the fourth harmonic (FHG). Thereby, the OPA is capable of tuning the laser wavelength continuously between 290 and 2500 nm. The output pulse energy depends strongly on the generated wavelength, but is usually between 20 and 400 μJ, and even higher for the pure signal or idler. Only near the end points of the signal or idler tuning range, the output power decreases rapidly.

The oscillator output (80 MHz) is directed into a separate stage (APE Harmonixx) for SHG and subsequent THG to achieve wavelengths of 405 nm and 270 nm. Owing to the much lower input power compared to the amplifier, the pulse energies reach < 0.5 nJ for the SHG, and only 0.05 nJ for the THG. Alternatively, the oscillator output can be directed into a pulse picker (APE Pulse Select) before entering the SHG/THG, where the repetition rate is reduced from 80 MHz to ≤ 4 MHz. Unlike the cavity dumper in the TCSPC setup, the pulse picker only reduces the repetition rate, which lowers the output power according to the splitting ratio. Furthermore, the pulse picker efficiency of 50 % reduces the pulse energy further, which in turn affects the SHG/THG efficiency. The resulting pulses have an energy of 5 pJ for the SHG.

Using a beam sampler, a small portion of the oscillator signal is directed to a fast trigger photodiode right behind the output port. It provides the trigger signal for the streak camera that detects the decay of the photoluminescence signal.

The laser pulses are forwarded to the samples using several beam steering mirrors. A periscope adjusts the height of the oscillator output. The samples are mounted in a continuous flow helium cryostat with an interchangeable chamber. The first chamber provides a cube-shaped tail with four windows to access the sample from any side (Oxford Optistat CF-V2). The laser beam is focused using a fused silica lens (L1), and the photoluminescence is collected using achromatic lenses (L2, L3). Excitation and collection happen under an angle of 45° with respect to the sample surface.

The second chamber is a microscope cryostat tail (Oxford Microstat He2), which allows for small working distances down to 5 mm. Furthermore, the chamber is mounted on a triple-axis stage (x-y-z) that can position the cryostat with a reproducibility of 1 μm. For this cryostat chamber, a confocal measurement geometry is used. The laser pulse passes a beam splitter (BS2) and is focused onto the sample by a mirror objective. The same objective collects the photoluminescence, which is reflected by the beam splitter and directed to the detection. An additional sample holder for transmission experiments is available, which fits into both cryostat chambers. A temperature controller (Mercury iTC) is used to regulate the helium flow and heating, and the cryostat can cover a temperature range from 3.5 to 500 K.

The collected photoluminescence is dispersed by a 30 cm spectrograph (Princeton SP-31) and detected by a streak camera (Hamamatsu C10910). The spectrograph offers gratings with 50, 150 or 600 grooves/mm. Additionally, a mirror instead of a grating can be selected to direct the undispersed light into the streak camera. The incoming light hits a cathode to generate electrons, which are amplified in a microchannel plate, deflected in vertical direction by an electric field, and finally detected on a two-dimensional CMOS array. Depending on the time of arrival, the photo-generated electrons will be detected in different positions on the vertical axis. The horizontal axis provides information about the wavelength of the incoming photons. The vertical axis can be changed to cover time scales between 1 ms and 100 ps, where a temporal resolution of < 1 ps is achieved. Otherwise, the temporal resolution depends mainly on the stability of the trigger signal and the broadening due to dispersion at the spectrograph's gratings.

The photodiode behind the oscillator output provides a trigger signal for the streak camera, which is used to define the position on the time axis. By integrating the input signal over many repetitions, or laser pulses, the final streak image is acquired.

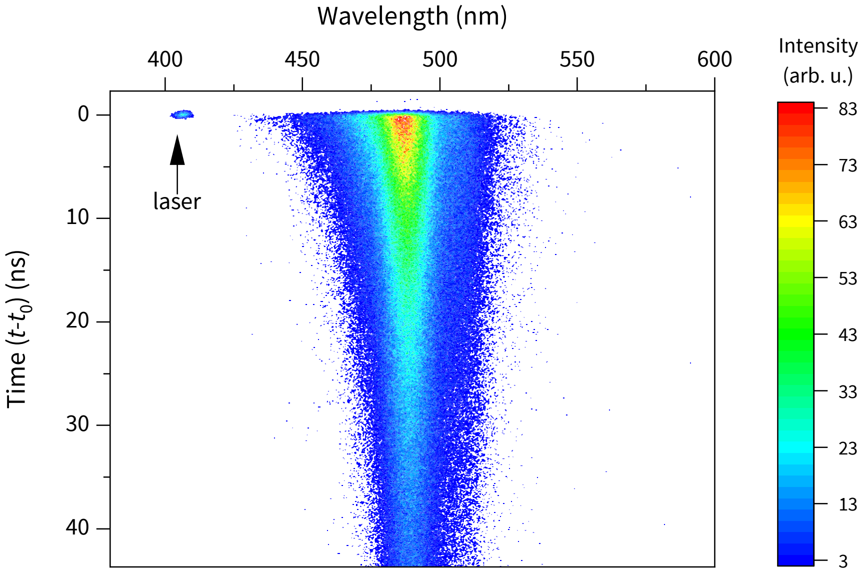

FIGURE 3.4: Exemplary streak image, collected at 5 K from a c-plane GaInN/GaN quantum well at a repetition rate of 4 MHz. The measured intensity is shown color-coded as function of the wavelength (horizontal axis) and time (vertical axis). The laser pulse at ~405 nm should be blocked by a filter, but is still visible in the spectrum. It marks the time of charge carrier excitation and the begin of the decay. The effective lifetime of the spectrally integrated luminescence is ≈ 12.5 ns.

The samples investigated in this thesis show decay times ranging from tens of picoseconds to tens of nanoseconds. This has implications for the repetition rate of the laser source. If the photoluminescence cannot decay completely before the next excitation pulse arrives, a reduction of the repetition rate is necessary. Thus, the frequency doubled oscillator output (405 nm central wavelength) at repetition rates of either 80 MHz or 4 MHz are used, corresponding to 12.5 ns or 250 ns difference between two excitation pulses. The amplifier signal can be used to realize high-excitation conditions with variable wavelengths, which is not of interest for the investigations here. Furthermore, the setup is highly modular and allows not only for the investigation of III-nitrides, but also many other material systems and purposes.

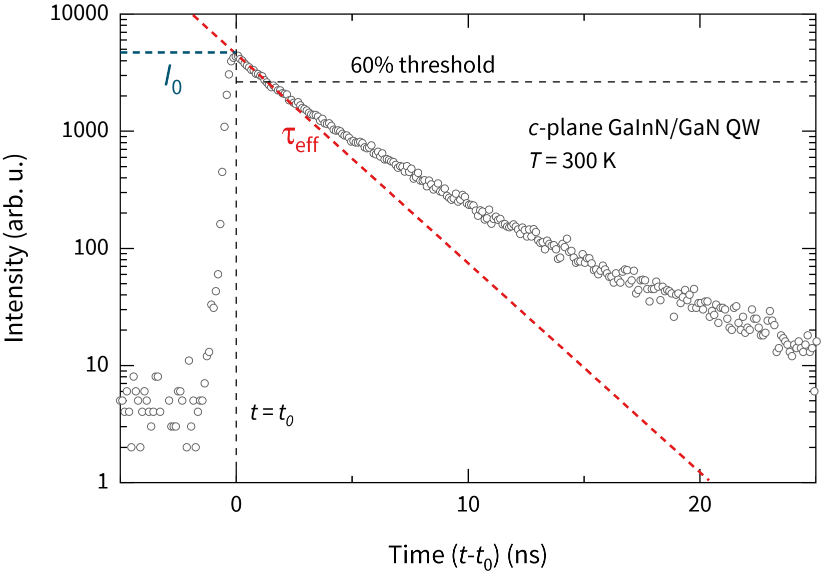

FIGURE 3.5: Exemplary decay curve of a c-plane GaInN/GaN QW with 17.5% InN mole fraction, 2.1 nm QW width: Open circles represent the measured points, the dashed line indicates the fitted decay function (Eq. 3.11), showing the initial intensity I_0 and the effective lifetime τ_{eff} as fit parameters. The decay is fitted up to a threshold of $I(t)/I_0 = 60\,\% \approx 1/\sqrt{e}$, and the deviation from a mono-exponential behavior is clearly visible for larger delay times.

3.3.3 *Evaluation of measurement data*

Measuring the photoluminescence intensity as function of delay time, a decay curve comparable to Fig. 3.5 is obtained. In fact, the measurement shows deviations from the expected mono-exponential decay in Eq. 3.9. Especially at low temperatures, a common explanation is the recombination of localized carriers that are bound to donors or acceptors. The issue is treated in Ref. [100, Ch. 5], as well as in Refs. [103] and [104]. Furthermore, the carrier-induced screening of the polarization fields is observed at high injection levels [105]. Finally, the dissociation of excitons becomes more probable for higher temperatures, and can lead to deviations from the mono-exponential decay [106].

The decay curve can be fitted by the function given in Eq. 3.9:

$$I(t) = I_0 \exp\left(-\frac{t - t_0}{\tau_{\text{eff}}}\right), \tag{3.11}$$

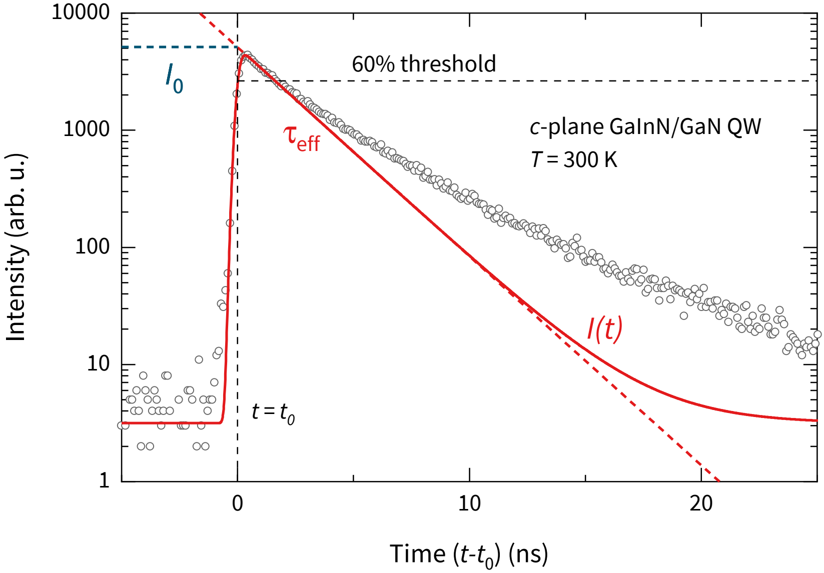

FIGURE 3.6: Exemplary decay curve of a c-plane GaInN/GaN QW (17.5% InN mole fraction, 2.1 nm QW width), fitted with a decay function according to Eq. 3.13, showing the initial intensity I_0 and the effective lifetime τ_{eff} as fit parameters. The decay is fitted up to a threshold of $I(t)/I_0 = 60\,\%$, including the initial rise and onset of the measured curve.

where t_0 is the delay time at which the decay curve reaches its maximum. An exemplary fit of the decay to determine τ_{eff} is shown in Fig. 3.5. Only the range between the maximum intensity at $t = 0$ and a certain threshold is fitted with a mono-exponential decay. The standard threshold value of $I(t)/I_0 = 60\,\% \approx 1/\sqrt{e}$ is chosen to include as many measurement points as possible, but also avoid distortions of the fit by non-exponential behavior at later delay time. By extrapolation of the fitted decay back to $t = t_0$, where the maximum intensity is measured, the initial intensity is determined as $I_0 = I(t = t_0)$. A more detailed description of the fit routine is given in Ref. [107, Ch. 3].

Still, this procedure includes only a very limited range of the measured decay curve. In order to include the onset of the decay around t_0, as well as the rising edge at $t < t_0$, the fit function from Eq. 3.11 is modified. In principle, the measured decay curve $I(t)$ represents a convolution of the photoluminescence decay with the instrument response function (IRF) that adds a certain broadening to the decay curve. Mathematically, the PL decay can be described by a mono-exponential function

(Eq. 3.11) multiplied with a Heaviside function $\theta(t-t_0)$. The instrumental response is described by a Gaussian function, which contains the instrumental broadening σ. Experimentally, σ can be determined from the detector's response function to an infinitely short input pulse, namely a laser pulse. Thereby, the decay curve is described by

$$I(t) = \left[\theta(t-t_0)\, I_0 \exp\left(-\frac{t-t_0}{\tau_{\mathrm{eff}}}\right)\right] * \left[\frac{1}{\sqrt{2\pi}\sigma}\exp\left(-\frac{1}{2}\left(\frac{t-t_0}{\sigma}\right)^2\right)\right]. \tag{3.12}$$

Executing the convolution $(*)$, an analytical function is obtained that can be used to fit the measured decay curve, including the rising edge and the onset of the decay [108]:

$$I(t) = I_{\mathrm{B}} + \frac{I_0}{2}\exp\left(\frac{\sigma^2}{2\tau_{\mathrm{eff}}^2} - \frac{(t-t_0)}{\tau_{\mathrm{eff}}}\right)\left[1+\mathrm{erf}\left(\frac{(t-t_0)-\frac{\sigma^2}{\tau_{\mathrm{eff}}}}{\sqrt{2}\sigma}\right)\right] \tag{3.13}$$

where erf describes the Gauss error function. The auxiliary parameter I_{B} is added to describe the background intensity, and can be determined from the intensity before the rising edge.

This function provides a better description of the decay curve compared to the mono-exponential fit, as can be seen from Fig. 3.6. Especially for decay times close to the instrumental broadening, the decay curve is distorted such that the initial intensity I_0 can easily be underestimated for two reasons: First, the top part (apex) of the curve is extremely damped. Second, the shorter the decay time, the more the delay time, at which the curve reaches its maximum, is shifted to larger values. For the simple mono-exponential fit procedure, the parameter I_0 is derived from the aforementioned time, which distorts the determination of the initial intensity for short decay times.

Essentially, two parameters are obtained from the fit: the effective lifetime τ_{eff} at the early stage of decay, and the initial intensity $I_0 = I(t = t_0)$. According to Eq. 3.10, the initial intensity depends only on the radiative rate. Only if the laser pulse can be considered short compared to the carrier lifetimes, recombination during excitation can be neglected. In this case, the density of generated excess carriers δn per laser pulse is constant, and depends only on the absorption and the pulse energy density. In order to include the photoluminescence signal from all excited charge carriers in the ensemble, the whole quantum well photoluminescence decay is integrated spectrally. The spectral integration includes all wavelengths, where the time-integrated intensity exceeds 10 % of the peak value. Furthermore, it can be assumed that the absoprtion shows negligible temperature dependence. Therefore, a constant density δn of charge carriers is prepared by every laser pulse, and the initial intensity I_0 is determined by the radiative lifetime (τ_{r}) only. Thus, it is possible to

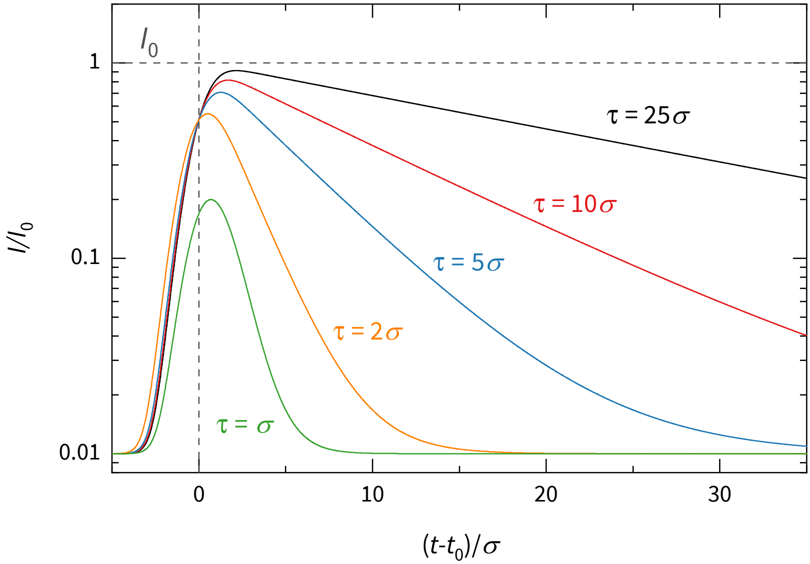

FIGURE 3.7: Behavior of (theoretical) decay curves for different lifetimes τ, following the function $I(t)$ from Eq. 3.13. Actually, the mono-exponential intensity decay starts at $t = 0$, but is broadened and distorted by convolution with the instrumental response function. For short lifetimes close to the instrumental broadening ($\tau \approx \sigma$), the maximum intensity is extremely damped. For longer lifetimes, the maximum intensity is close to the value of I_0, but shifted to the right on the time axis. Applying the fit function $I(t)$ to describe the measured decay curves makes it possible to regard for these distortions.

separate the effective lifetime (τ_{eff}), measured experimentally, into a radiative (τ_{r}) and nonradiative lifetime (τ_{nr}) using the initial intensity. For this purpose, the constant of proportionality in Eq. 3.10 can be determined from a low-temperature measurement, where nonradiative recombination is assumed to vanish. In this case, the effective lifetime (τ_{eff}) and the radiative lifetime (τ_{r}) become equal. Therefore, the factor of proportionality is given by the measured initial intensity at low temperatures, usually at 5 K. Finally, the complementary nonradiative lifetime (τ_{nr}) can be calculated from Eq. 3.7. Fig. 3.8 shows an exemplary measurement with decay curves and the derived effective, radiative, and nonradiative lifetimes as function of temperature.

Note that the assumption of vanishing nonradiative recombination at low temperature is not necessarily true for the high-defect containing III-nitride structures. At low temperatures, tunneling to nonradiative centers (see Sec. 2.3.3) may be present.

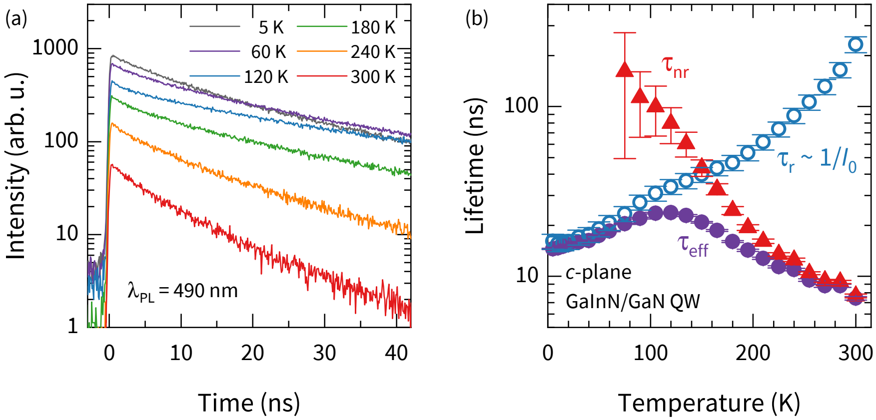

FIGURE 3.8: Measured decay curves (a) of a *c*-plane GaInN/GaN quantum well (sample C29, see Ref. [91]) emitting at 490 nm for temperatures between 5 and 300 K. Temperature dependence of the carrier lifetimes (b), where the effective lifetime (τ_{eff}) is obtained by fitting the measured decay, the radiative lifetime (τ_{r}) is obtained from the initial intensities I_0 and normalized to equal the effective lifetime at low temperature. The nonradiative lifetime (τ_{nr}) is calculated from Eq. 3.7. The error bars contain the statistical uncertainties of the experiment and the evaluation process.

The topic is treated further in Ch. 6, where additional indications for vanishing nonradiative recombination at low temperature are discussed. For this reason, the absolute values obtained from this procedure provide only a lower limit for the radiative lifetime, although its temperature dependence is given by the inverse of the initial intensity.

Part II

RESULTS

4

RADIATIVE RECOMBINATION IN POLAR AND NONPOLAR QUANTUM WELLS

In this chapter, the radiative recombination dynamics of polar and nonpolar quantum well structures are investigated. At first, Sec. 4.1 describes the particularities of radiative recombination in nonpolar quantum wells, as opposed to polar structures, while Secs. 4.2 and 4.3 cover the impact of strain on the radiative emission and on the valence band structure, as well as strain manipulation via buffer layers. Second, the well width dependence of the radiative lifetime in nonpolar quantum wells is analyzed in Sec. 4.4. Finally, in Sec. 4.5, the temperature dependence of the radiative lifetime is described, revealing causes for the limited radiative recombination at room temperature and above.

4.1 CHARACTERISTICS OF RADIATIVE RECOMBINATION IN NONPOLAR QUANTUM WELLS

Generally, the recombination dynamics in III-nitride quantum wells are governed by internal polarization fields. The quantum-confined Stark effect (QCSE) shifts the envelope functions of electrons and holes to opposite sides of the quantum well, which reduces the wave function overlap, or overlap integral, considerably.

One approach to overcome this fundamental limitation, is the use of nonpolar orientations for quantum well growth. The polarization fields vanish perpendicular to the nonpolar a- and m-planes, and thus the structures are free of the QCSE [26]. This increases the overlap integral $|M|^2$ compared to polar quantum wells. Fig. 4.1(a) shows the overlap integral for polar (c-plane) and nonpolar (m-plane) quantum wells as function of well width for different InN mole fractions. The values are obtained from a numerical Schrödinger solver that calculates energy levels, wave functions, and takes excitonic effects into account [63]. The input parameters can be found in Tabs. 1.1 and 4.2. For c-plane, the QCSE drastically reduces the wave function overlap for larger well widths, and only for ultra-thin quantum wells around 1 nm the overlap reaches over 50 %. Contrary, for m-plane the overlap reaches nearly unity at large well widths. The decrease towards thinner quantum wells is due to the growing penetration of wave functions into the barrier material, but still reaches over 70 %.

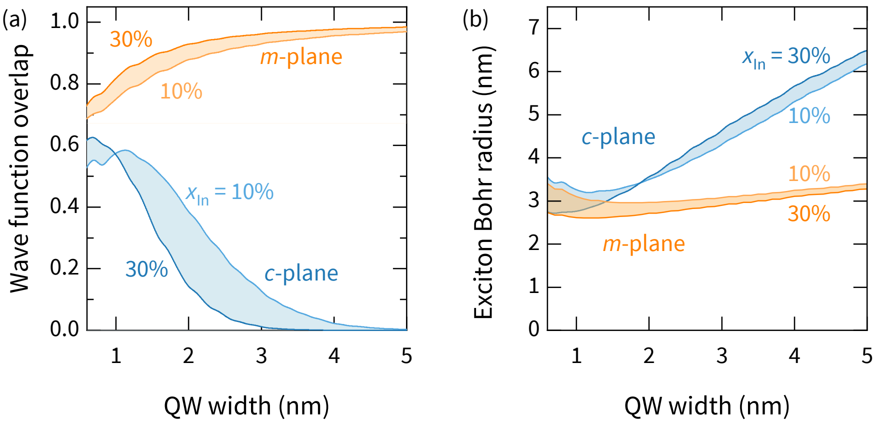

FIGURE 4.1: Wave function overlap (a) and exciton Bohr radius (b) for QWs with different InN mole fractions in polar c-plane and nonpolar m-plane orientation. The quantities are calculated by a numerical Schrödinger solver [63] with input parameters from Tabs. 1.1 and 4.2. While the overlap is strongly reduced by the QCSE for thick polar QWs, it approaches unity in nonpolar QWs. For small well widths, the penetration of wave functions into the barriers reduces the overlap again. The same trends are evident for the exciton Bohr radius, which behaves nearly constant for nonpolar QWs.

Considering Eq. 2.11, which describes the bimolecular radiative recombination in a quantum well, the increased overlap integral $|M|^2$ will affect the radiative emission rate:

$$R_{\mathrm{r}} = \underbrace{\frac{e^2 \tilde{n} \hbar \omega}{m_0^2 \varepsilon_0 c^3} \, \frac{1}{(m_{\mathrm{e}} + m_{\mathrm{h}})\, k_{\mathrm{B}} T} \left\langle |p_{\mathrm{cv}}|^2 \right\rangle |M|^2}_{B} \; n \, p \, , \tag{4.1}$$

Thus, in nonpolar structures a higher radiative rate, or a shorter radiative lifetime ($\tau_{\mathrm{r}} \propto 1/B$), is expected. Although this is in principle valid for every nonpolar plane, the use of m-plane is preferred here, since a lower indium incorporation and the tendency to the formation of stacking faults has been reported for a-plane structures [109, Ch. 1].

For an experimental comparison of radiative lifetimes in polar and nonpolar structures, temperature-dependent measurements of the photoluminescence decay are performed for several c- and m-plane GaInN/GaN quantum wells prepared by MOVPE. An overview of the sample parameters is given in Tab. 4.1. The c-plane quantum wells are grown on sapphire or bulk GaN substrates, while all m-plane

TABLE 4.1: Structural data, including substrate type, InN mole fraction (x_{In}), and QW width (L_{QW}), and radiative lifetime (τ_{r}) at room temperature of all polar and nonpolar samples under investigation.

Sample	Substrate type	x_{In} (%)	L_{QW} (nm)	τ_{r} (300 K)
C1[d]	*c*-plane sapphire	10.8 ± 0.3 [a]	1.27 ± 0.07 [a]	2.3 ± 0.2 [c]
C2[e]	*c*-plane sapphire	20.9 ± 0.6 [a]	1.07 ± 0.03 [a]	1.4 ± 0.3 [c]
C3[f]	*c*-plane sapphire	30.0 ± 2.5 [a]	1.10 ± 0.11 [a]	1.3 ± 0.5 [c]
C4[e]	*c*-plane GaN	27.2 ± 3.2 [a]	1.43 ± 0.04 [a]	10.9 ± 1.2 [c]
C5[e]	*c*-plane GaN	27.9 ± 2.0 [a]	1.5 ± 0.3 [a]	22.4 ± 1.6 [c]
C6[e]	*c*-plane GaN	32.2 ± 0.6 [a]	1.46 ± 0.11 [a]	21.7 ± 14.5 [c]
C7[e]	*c*-plane sapphire	31.0 ± 1.1 [a]	1.45 ± 0.03 [a]	8.4 ± 4.9 [c]
C8[e]	*c*-plane sapphire	33.3 ± 0.8 [a]	1.19 ± 0.07 [a]	6.3 ± 1.4 [c]
M1[e]	*m*-plane GaN	29.6 ± 0.8 [a]	1.51 ± 0.08 [a]	0.28 ± 0.03 [c]
M2[g]	*m*-plane GaN	13.5 ± 0.7 [a]	1.62 ± 0.09 [a]	0.6 ± 0.3 [c]
M3[g]	*m*-plane GaN	23.5 ± 1.0 [a]	1.40 ± 0.07 [a]	0.41 ± 0.05 [c]
M4[g]	*m*-plane GaN + AlInN	37.8 ± 0.9 [a]	1.67 ± 0.04 [a]	0.9 ± 0.3 [c]
M5[h]	*m*-plane GaN + AlInN	36 ± 2 [b]	1.80 ± 0.15 [b]	0.9 ± 0.1
M6[h]	*m*-plane GaN + AlInN	38.0 ± 1.1 [b]	1.60 ± 0.11 [b]	1.1 ± 0.3
M7[h]	*m*-plane GaN + AlInN	24.5 ± 1.1 [a]	1.43 ± 0.09 [a]	0.8 ± 0.3
M8[h]	*m*-plane GaN + AlInN	31.6 ± 1.2 [b]	1.44 ± 0.10 [b]	1.5 ± 0.4
M9[h]	*m*-plane GaN + AlInN	34.0 ± 0.7 [a]	1.35 ± 0.03 [a]	0.9 ± 0.2

[a] Ref. [96] [b] Ref. [97] [c] Ref. [101] [d] Ref. [90] [e] Ref. [92] [f] Ref. [94]
[g] Ref. [93] [h] Ref. [91]

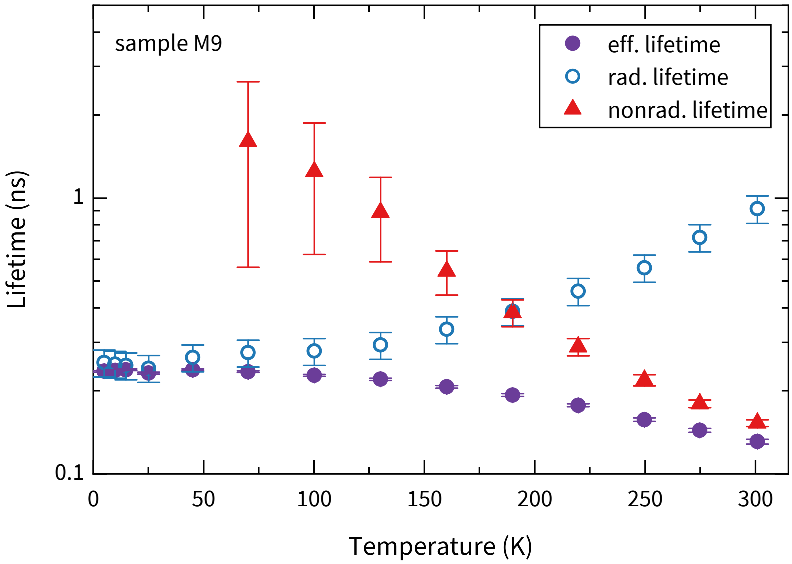

FIGURE 4.2: Temperature dependence of effective (τ_{eff}), radiative (τ_{r}), and nonradiative lifetimes (τ_{nr}) of sample M9. Up to ≈ 50 K, the constant radiative lifetimes indicate carrier localization, and the close-to-linear rise ($\tau_{\text{r}} \propto T^1$) at higher temperatures proves that charge carriers are free to move in two dimensions.

structures are grown on bulk GaN substrates. Fig. 4.3 shows schematics of the sample structures. The sample growth starts with an epitaxial GaN layer of several µm thickness, followed by a five-fold multi-quantum well structure, where the growth temperature for the quantum wells is varied between 700 and 800 °C to achieve different InN mole fractions. As determined by XRD measurements, the well widths are in the range between 1.1 and 1.8 nm, and barrier widths are approx. 10 nm. Furthermore, InN mole fractions in the quantum wells between 10 % and 38 % are found. As an exception, only sample C3 exhibits a single quantum well, which is grown under otherwise idential conditions. A second set of m-plane quantum well structures is prepared with an additional 100 nm thick AlInN buffer layer (200 nm for sample M5) underneath the MQW structure. Those samples are discussed in Sec. 4.3.

From time-resolved measurements, the effective carrier lifetimes τ_{eff} and initial intensities I_0 are obtained as function of temperature. Following the procedure described in Sec. 3.3.3, the measured carrier lifetimes τ_{eff} can be separated into radiative (τ_{r}) and nonradiative (τ_{nr}) lifetimes, since $\tau_{\text{r}} \propto 1/I_0$. An exemplary temperature dependence of the carrier lifetimes is shown in Fig. 4.2 for an m-plane quantum well

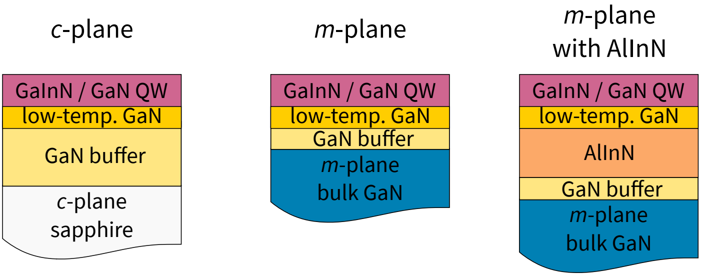

FIGURE 4.3: Schemes of the quantum well samples prepared in polar (c-plane) and nonpolar (m-plane) orientations. Additional nonpolar quantum wells with an AlInN buffer layer underneath the QW are discussed in Sec. 4.3.

(sample M9). At low temperatures, the recombination is assumed to be unaffected by nonradiative processes, and thus the measured lifetime can be used to estimate the radiative recombination ($\tau_{\text{eff}} \approx \tau_{\text{r}}$). Still, the low-temperature lifetimes are inappropriate for a comparison of different structures, since the charge carriers are subject to localization in this temperature regime. Localization of charge carriers at local potential minima can arise from fluctuations in width and composition of the quantum well [110–119]. Localization corresponds to a zero-dimensional state, as opposed to the two-dimensional states of charge carriers moving freely in the quantum well. Furthermore, the charge carrier dimensionality d can be related to the temperature behavior of the radiative lifetime by $\tau_{\text{r}} \propto T^{d/2}$ (Eq. 2.13). The localization of charge carriers to zero-dimensional sites ($d = 0$) can be observed up to about 50-100 K, where the radiative lifetimes show a constant behavior ($\tau_{\text{rad}} \propto T^0$). At higher temperatures, however, the carriers can escape the potential minima by thermal activation, and consequently, the radiative lifetime starts to increase. The temperature dependence in the range above 100 K is close to linear ($\tau_{\text{rad}} \propto T^1$), indicating that charge carriers are free in two dimensions. For a comparison of the radiative properties of polar and nonpolar quantum wells, the lifetimes of two-dimensional charge carriers are more suitable. Thus, the radiative lifetimes at room temperature (300 K) are compared in Fig. 4.4 for different InN mole fractions. The graph shows similar results as already discussed by Langer et al. for radiative lifetimes in non- and semipolar quantum well structures [120].

For c-plane, room temperature radiative lifetimes around 7-20 ns are found for quantum wells with 1.5 nm width, or around 1-3 ns for 1.1 nm width. Contrary, the m-plane samples show radiative lifetimes around 300-400 ps. It becomes evident that there is a difference of nearly one order of magnitude between the room temperature

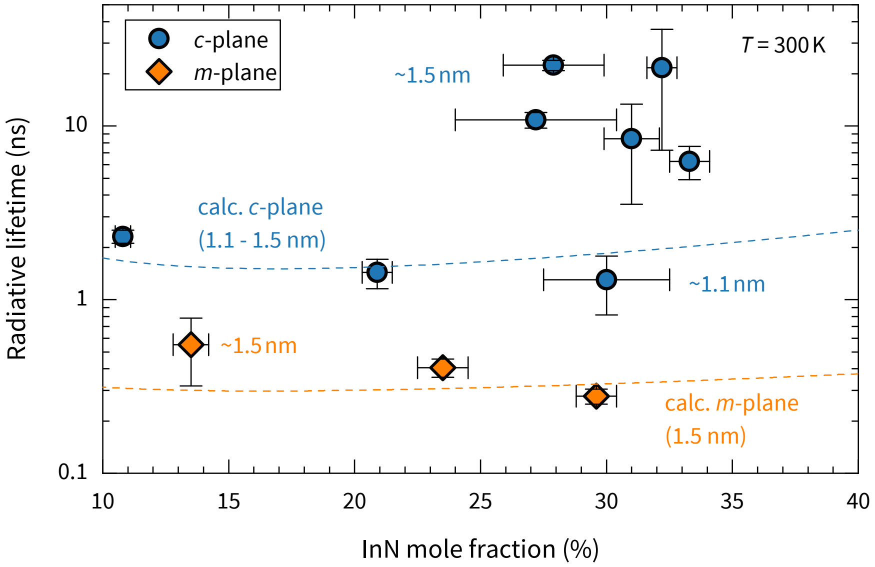

FIGURE 4.4: Comparison of radiative lifetimes at room temperature (300 K) from polar c-plane and nonpolar m-plane MQW structures with different InN mole fractions. The graph and data are adapted from Refs. [101, 120]. The data can be found in Tab. 4.1 as well. Between the nonpolar ($L_{QW} \approx 1.5$ nm) and the polar MQWs ($L_{QW} \approx 1.1$ nm), the radiative lifetimes differ by one order of magnitude. Polar MQWs with slightly larger width ($L_{QW} \approx 1.5$ nm) show even higher lifetimes. Dashed lines indicate the calculated lifetimes according to Eq. 4.2, which regards for changes in wave function overlap, exciton Bohr radius, and hole effective masses.

radiative lifetimes of polar and nonpolar structures. Generally, the lifetimes show only a weak dependence on InN mole fraction, and are rather governed by the quantum well width, which is expected due to the QCSE and the reduced overlap integral $|M|^2$. Between the c-plane QWs with 1.5 nm and 1.1 nm width, the radiative lifetimes differ at least by a factor of two. Also the wave function overlap increases nearly by a factor of two, e.g. for $x_{In} = 30\%$ from $|M|^2 \approx 30\%$ to over 50%. To a first approximation, this explains the large reduction in radiative lifetimes for the c-plane structures with different QW width. Furthermore, the increasing overlap integral is used as a common argument to explain the lower radiative lifetimes observed in nonpolar QWs compared to polar ones [121]. The difference of one order of magnitude found from the comparison of polar and nonpolar structures in Fig. 4.4, however, is larger than the difference in wave function overlap. Considering the calculated $|M|^2$ values in Fig. 4.1(a), they differ by a factor of 2-3, corresponding to roughly 30% of the measured difference in radiative lifetimes. As discussed in the following, the discrepancy can be explained to a large extent by including the excitonic binding and the effects of anisotropic strain on the valence band structure.

The vanishing polarization fields in nonpolar structures also influence the exciton binding in the quantum well. Previous work has shown that the radiative recombination in III-nitride structures is strongly influenced, or even dominated by excitons [11]. Hangleiter et al. showed that, even at room temperature, where excitons may be subject to thermal dissociation, the fraction of charge carriers bound into excitons exceeds 40 % [122]. Liu et al. state that the exciton fraction at room temperature is even higher than 60 % [123]. Therefore, the radiative recombination is approximated as purely excitonic, and Eq. 2.18 applies:

$$\tau_{\mathrm{ex}} = \frac{\pi\, a_{\mathrm{B}}^2}{2\,B} \tag{4.2}$$

Calculations of the exciton Bohr radius a_{B}, shown in Fig. 4.1(b) for different well widths and orientations, highlight the impact. For the nonpolar quantum wells, a slightly lower exciton Bohr radius around 2.5 nm is found compared to the polar QWs, where the QCSE separates electrons and holes and leads to almost 3 nm. The lower Bohr radius, meaning a higher exciton binding energy, can contribute up to a factor of 1.2 in a_{B}, or 1.5 in a_{B}^2, to the shorter radiative lifetimes in nonpolar QWs. In the following, the change in effective masses due to anisotropic strain is discussed as an additional parameter.

4.2 STRAIN AND VALENCE BAND STRUCTURE

Considering Eq. 4.1, the effective carrier mass $m_{\mathrm{e/h}}$ in the QW plane is another parameter influencing the radiative recombination. Especially the effective hole mass, related to the valence band structure, depends strongly on strain and orientation. This can be modeled by $\mathbf{k} \cdot \mathbf{p}$ calculations, as described in Sec. 1.1.5. Fig. 4.5 shows the valence band dispersion in the x-y-plane, corresponding to the basal c-plane, obtained from calculations for bulk GaN. Without strain, the valence bands are isotropic and close in energy, as can be seen in Fig. 4.5(a). A heavy-hole character is found up to large k-values for the uppermost valence band (A), and a light-hole character for the second valence band (B). The third valence band is the crystal-field split-off band (C). Applying compressive biaxial strain in the c-plane, the uppermost valence bands are shifted upwards in energy, as shown in Fig. 4.5(b) for $\varepsilon_{\mathrm{xx}} = \varepsilon_{\mathrm{yy}} =$

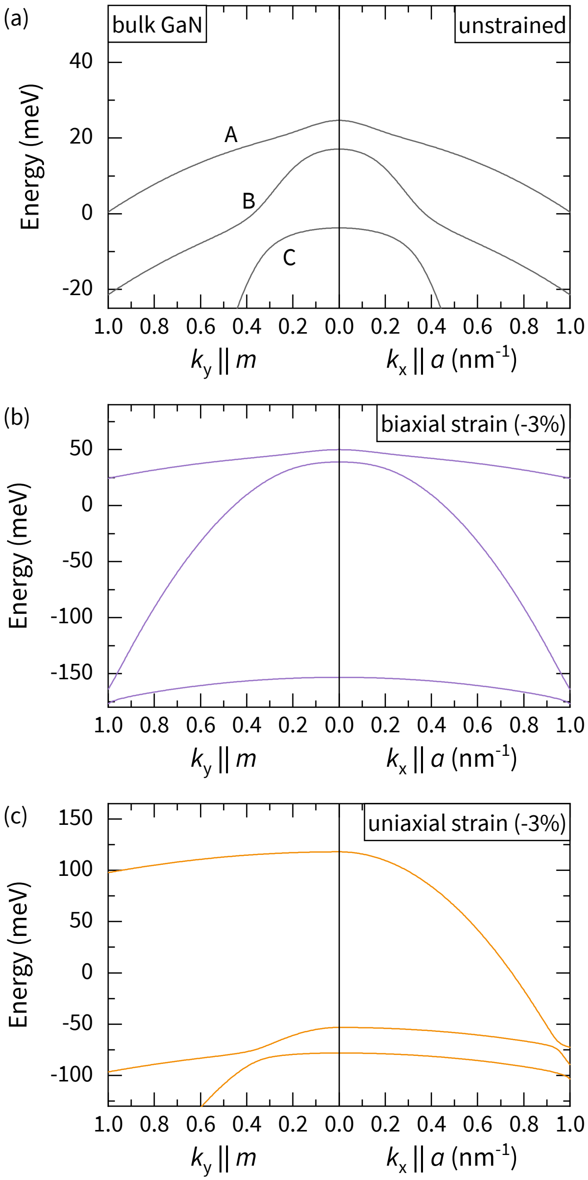

FIGURE 4.5: Calculated valence band dispersion of bulk GaN without strain (a), under compressive biaxial strain (−3 %) in the x-y-plane (b), and under compressive uniaxial strain (−3 %) in x-direction (c). The uniaxial strain reduces the crystal symmetry, which results in an anisotropic hole dispersion in x- and y-direction.

$-3\,\%$. The valence band symmetry, as well as the effective masses remain comparable to the unstrained case.

Contrary, the application of compressive uniaxial strain changes the crystal symmetry, which results in an anisotropic energy splitting in the x- and y-direction [39]. This is shown in Fig. 4.5(c) for an uniaxial strain of $\varepsilon_{\mathrm{xx}} = -3\,\%$, where the A-band (HH) in x-direction, as well as the B-band (LH) in y-direction, are shifted to lower energies. Tensile strain in the y-direction would have the same effect [5, Ch. 2]. The resulting valence bands are anisotropic in the basal c-plane. Note that, contrary to the other graphs, the energy scale is not normalized to the uppermost valence band. Thus, in Fig. 4.5, $E = 0$ corresponds to the valence band edge of the unstrained bulk crystal, without spin-orbit and crystal field splitting. This emphasizes the large strain-induced shift in energy, as can be seen in Figs. 4.5(b) and (c).

Qualitatively, this situation is comparable to the case of a GaInN/GaN quantum well grown on an m-oriented GaN substrate. Here, the GaInN layer is under compressive, but anisotropic strain in the growth plane (a- and c-direction). For a GaInN quantum well grown on c-oriented GaN, however, the compressive in-plane strain is isotropic. Calculations of GaInN/GaN quantum well structures are shown in Fig. 4.6, where the strain components (Tab. 4.3) and structural data (Tab. 4.1) measured by XRD are used as input parameters. As expected, the isotropic valence band dispersion of the c-plane QW in Fig. 4.6(a) compares well with the one of bulk GaN under biaxial strain in Fig. 4.5(b). Since the strain causes a downshift of the crystal-field split-off band, the A- and B-bands, together with their higher quantized states, are dominating the valence band structure. Contrary, the valence band dispersion for the m-plane QW in Fig. 4.6(b) is anisotropic, which compares well with the one of bulk GaN under uniaxial strain in Fig. 4.5(c). As a result, a much lighter effective mass is found in a-direction in the topmost valence band, and the energetic separation to the second valence band is increasing.

The effective masses are given by the inverse curvature of the band dispersion $E(k)$. Using a parabolic fit, the effective masses can be extracted from the calculated valence band dispersion, as shown in Fig. 4.7. The parabolic approximation is only valid near the Γ point ($k = 0$), and the limits are chosen before a degeneracy point, or at maximum up to $k = 1/\mathrm{nm}$. For the exemplary m-plane QW, the dispersion gives effective masses of $1.3\,m_0$ in c-direction, and $0.19\,m_0$ in a-direction. In order to describe the carriers in the uppermost valence band by a single effective mass, the density of states mass can be estimated by

$$m_{\mathrm{h}} = \sqrt{m_{\mathrm{h,c}}\, m_{\mathrm{h,a}}}\,. \tag{4.3}$$

This results in a density of states effective mass of $0.5\,m_0$ for the exemplary m-plane QW. The values of the other m-plane QW samples are shown in Tab. 4.3, and vary

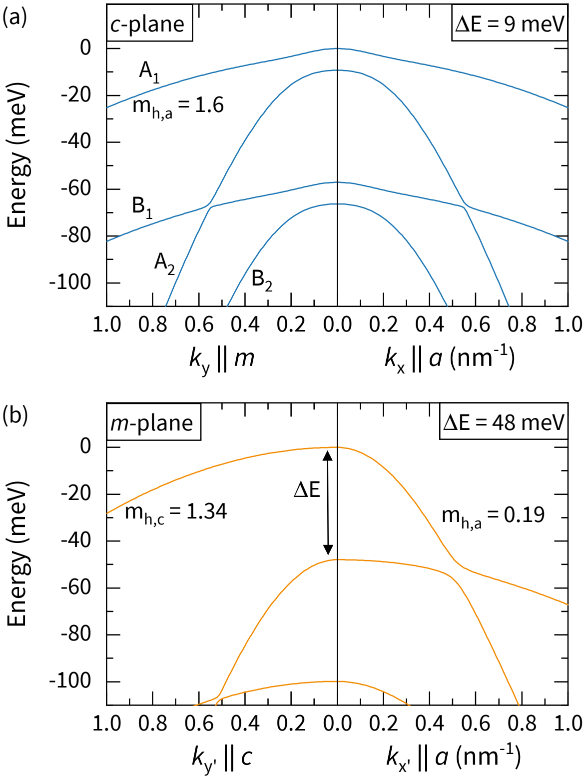

FIGURE 4.6: Calculated valence band dispersion of c-plane (a), and m-plane (b) QWs, which differ in effective hole masses, and in the energy difference between the two uppermost valence bands.

between 0.58 and 0.72 in units of m_0. Contrary, hole effective masses of typical c-plane QWs are around 1.7-2.0 m_0, as can be deduced by linear interpolation from the in-plane masses $m^{\mathrm{c}}_{\mathrm{h},\perp}$ in Tab. 4.2. The effective hole masses between m-plane and c-plane QWs differ by a factor of 2-3, which remains valid when adding the effective electron mass, like in Eq. 4.1.

The theoretical effective mass values can also be used to estimate the radiative excitonic lifetime at room temperature (T = 300 K) according to Eqs. 4.1 and 4.2. The values are given in Tab. 4.2, where $m^{\mathrm{c}}_{\mathrm{h},\perp}$ describes the in-plane effective hole mass for c-plane QWs, and $m^{\mathrm{m}}_{\mathrm{h},\mathrm{x}'/\mathrm{y}'}$ are applicable for m-plane QWs [124]. Furthermore, a refractive index of $\tilde{n}$ = 2.5 is used, which stays rather constant for GaInN over a large composition range [125]. The momentum matrix element, since averaged over

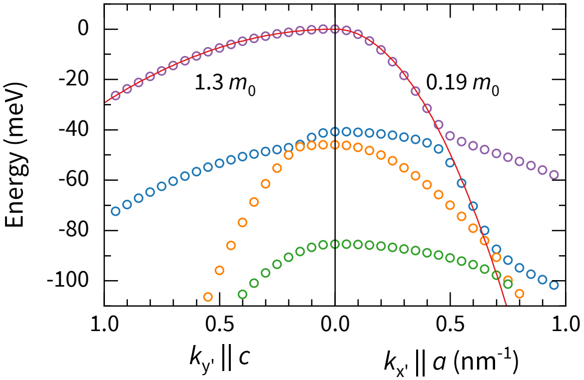

FIGURE 4.7: Calculated valence band dispersion of an exemplary m-plane QW structure (x_{In} = 20 %, L_{QW} = 3 nm), shown as open circles. The effective hole masses are obtained from parabola fits, indicated by solid lines, that describe the band curvature up to large k-values, or up to the degeneracy points, where the valence bands cross.

two orthogonal polarization directions, can be estimated by $\langle |p_{\mathrm{cv}}|^2 \rangle = E_{\mathrm{p}}/2$. The photon energy $\hbar\omega$ is estimated from the band gaps given in Tab. 1.1, corrected for quantization energies, strain-dependent band gap shift, and exciton binding energy. Using the InN mole fraction, the parameters for GaInN are linearly interpolated between the binary constituents. Wave function overlap $|M|^2$ and exciton Bohr radius a_{B} are calculated by solving the Schrödinger equation [63]. The other parameters are physical constants. The theoretically estimated radiative lifetimes are shown as dashed lines in Fig. 4.4 for polar and nonpolar QWs. The calculated values coincide reasonably with the measured room temperature lifetimes. The calculated lifetimes of the nonpolar QWs are about eight times shorter compared to those of polar QWs, which is due to the combined effect of increased wave function overlap, enhanced exciton binding, and lower hole effective masses. In combination, these effects are sufficient to explain the difference of nearly one order of magnitude between radiative lifetimes measured in c- and m-plane QWs.

TABLE 4.2: Listing of momentum matrix element (E_p), refractive index $\tilde{n}$, and effective electron mass (m_e). The effective hole masses for c-plane QWs are given as in-plane ($m^\mathrm{c}_{\mathrm{h},\perp}$), and out-of-plane ($m^\mathrm{c}_{\mathrm{h},\parallel}$) mass. For m-plane QWs, $m^\mathrm{m}_{\mathrm{h},z'}$ is the out-of-plane effective hole mass, and the in-plane masses ($m^\mathrm{m}_{\mathrm{h},x'}$, $m^\mathrm{m}_{\mathrm{h},y'}$) show the anisotropic dispersion. All effective masses are given in units of m_0.

Parameter	GaN	InN
m_e	0.2^a	0.07^a
$m^\mathrm{c}_{\mathrm{h},\perp}$	2.0^b	1.25^b
$m^\mathrm{c}_{\mathrm{h},\parallel}$	1.889^b	1.563^b
$m^\mathrm{m}_{\mathrm{h},x'}$	1.889^b	1.563^b
$m^\mathrm{m}_{\mathrm{h},y'}$	0.137^b	0.091^b
$m^\mathrm{m}_{\mathrm{h},z'}$	2.0^b	1.25^b
$\tilde{n}$	2.5^d	
E_p (eV)	11.0^c	5.5^c

[a] Ref. [15] [b] Ref. [124]
[c] Ref. [125] [d] Ref. [126]

TABLE 4.3: Strain components determined by XRD, together with the calculated energy difference ΔE_{12} between the upper valence bands, and the effective hole masses (in units of m_0), obtained by fits of the calculated dispersion, for all m-plane QW samples under investigation.

Sample	ε_{xx} (%)	ε_{yy} (%)	ε_{zz} (%)	ΔE_{12} (meV)	$m^{(1)}_{h,c}$	$m^{(1)}_{h,a}$	$m^{(2)}_{h,c}$	$m^{(2)}_{h,a}$	$m_{h,DOS}$
M1[c]	−3.04 [a]	1.99 [a]	−2.85 [a]	47.78	1.34	0.19	0.16	1.74	0.58
M2[d]	−1.33 [a]	0.86 [a]	−1.29 [a]	29.26	1.25	0.24	0.2	1.46	0.72
M3[d]	−2.44 [a]	1.57 [a]	−2.26 [a]	42.77	1.32	0.2	0.17	1.69	0.62
M4[d]	−2.37 [a]	1.85 [a]	−3.15 [a]	8.43	1.3	1.66	0.17	0.2	1.61
M5[e]	−1.82 [b]	1.4 [b]	−2.41 [b]	10.14	1.32	1.53	0.18	0.22	1.56
M6[e]	−2.26 [b]	1.72 [b]	−2.86 [b]	12.17	1.35	1.42	0.17	0.22	1.51
M7[e]	−1.26 [a]	1.04 [a]	−1.97 [a]	11.83	1.09	1.77	0.23	0.26	1.54
M8[e]	−1.53 [b]	1.29 [b]	−2.43 [b]	14.94	1.02	1.83	0.22	0.23	1.49
M9[e]	−3.04 [a]	2.11 [a]	−3.18 [a]	34.19	1.37	0.18	0.18	1.52	0.64

[a] Ref. [96] [b] Ref. [97] [c] Ref. [92] [d] Ref. [93] [e] Ref. [91]

4.3 NONPOLAR QUANTUM WELLS WITH METAMORPHIC BUFFER LAYERS

In the previous section, strain was found to be an important element to understand the radiative recombination dynamics in III-nitride quantum wells, especially due to its effect on the valence band structure. One possibility to manipulate, or reduce the strain in the quantum wells is the use of a buffer layer between the GaN substrate and the GaInN quantum well. In the first place, a suitable buffer layer should adopt the in-plane lattice parameters of the underlying GaN during epitaxial growth. Since GaInN has generally larger lattice parameters than GaN, the buffer layer needs to increase its in-plane lattice parameters during growth, thereby reducing the lattice mismatch to the GaInN quantum well. The increase in lattice parameters usually happens via plastic relaxation, i.e. the formation or gliding of dislocations. This issue is also treated in Sec. 5.3, where the role of buffer layers on the nonradiative recombination in semipolar quantum wells is of interest. The quantum well structure that is grown on top of the relaxed buffer layer should accumulate less strain energy compared to the unbuffered structure. Besides GaInN, the ternary alloy AlInN is a suitable choice for strain-reducing buffer layers, as introduced in the following.

4.3.1 *Metamorphic AlInN buffer layers for strain manipulation*

AlInN matches the a-lattice parameter of GaN at 18% InN mole fraction according to Vegard's law [22]. Furthermore, it has a higher refractive index than GaN or AlGaN, making it a suitable material for distributed Bragg reflectors or cladding layers in laser structures [127–129]. Thick layers tend to composition splitting[130, 131], which makes the use as buffer layer on c-plane difficult, since only about 50 nm can be grown, which is not enough to reach sufficient relaxation.

For nonpolar orientations, however, the different a/c ratios of the binary III-N compounds make lattice matching possible only in one in-plane direction. Considering the m-plane orientation, the in-plane directions are along a and c. Thus, AlInN with an InN mole fraction of 28% is needed for lattice-matching along c, leaving the layer compressively strained along the a-direction. As found by Buß et al., AlInN grown lattice-matched along the c-direction of GaN is forced to relax to larger a lattice parameters [132]. Thus, the use of such an AlInN buffer layer is effectively reducing the lattice mismatch to a GaInN-based MQW structure. Furthermore, Horenburg et al. prepared several MQW structures on top of AlInN buffer layers, and found not only a largely reduced strain state of the QWs, but also a higher indium uptake in the QWs compared to the unbuffered case [133].

In the following, the recombination dynamics of m-plane GaInN/GaN MQWs prepared on AlInN buffer layers are investigated. For comparison with the results of

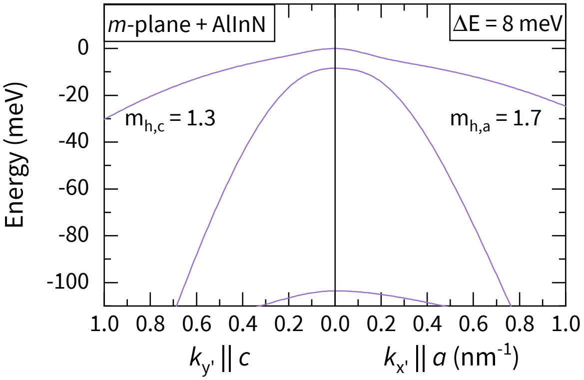

FIGURE 4.8: Calculated valence band dispersion of an m-plane QW structure with additional AlInN buffer layer, which shows nearly isotropic dispersion. This is comparable to the c-plane shown in Fig. 4.6, due to the reduced strain state of the QW on top of the buffer layer.

the previous section, in particular the radiative lifetimes at room temperature, and their dependence on the strain state of the QWs are of interest. The sample parameters are summarized in Tabs. 4.1 and 4.3. The AlInN buffer layer has a thickness of 100 nm for samples M4, and M6-M9, but 200 nm for sample M5. Here, the quantum well's lattice parameters in epitaxial growth are determined by the underlying AlInN buffer layer, and not by the GaN substrate anymore. Thus, the growth is referred to as *metamorphic*. Contrary, the c- and m-plane QWs treated in the previous section are considered *pseudomorphic*, since they grow fully strained on the GaN substrate. Just like the pseudomorphic samples M1-M3, the metamorphic structures M4-M9 are prepared on m-plane bulk GaN substrates.

4.3.2 *Radiative recombination in strain-manipulated nonpolar quantum wells*

Comparable to the analysis above, the radiative lifetimes at room temperature are obtained from temperature-dependent time-resolved photoluminescence measurements. The results are shown in Fig. 4.9, together with the radiative lifetimes of unbuffered m-plane structures (M1-M3). The radiative lifetimes for the samples with AlInN are determined to be around 1 ns, which is considerably longer than for the unbuffered m-plane QWs.

One possible reason for this unexpected behavior might be a difference in quantum well width and composition. Even in the absence of polarization fields, this would affect the overlap integrals, or even slightly the exciton binding, and in turn could change the radiative lifetimes. Therefore, additional data from XRD measurements needs to be considered. The results are summarized in Tabs. 4.1 and 4.3, according to which all m-plane samples show comparable QW widths around 1.5 nm. Thus, a difference in quantum well width can be excluded as reason for the difference in radiative lifetime. Additionally, the metamorphic structures show longer radiative lifetimes over a wide range of InN mole fractions. As additional information, the XRD measurements reveal the strain state of each QW, as can be seen from Tab. 4.3. The strain components are given in the crystal coordinate system, where $\varepsilon_{\mathrm{xx}}$ and $\varepsilon_{\mathrm{zz}}$ describe the strain in the a- and c-directions, which are the in-plane directions for the m-plane orientation. The component $\varepsilon_{\mathrm{yy}}$ describes the out-of-plane strain in m-direction. The measured strain components and QW data from XRD can be used for valence band calculations. The valence band dispersion for an exemplary metamorphic m-plane QW is shown in Fig. 4.8. It becomes evident that the two branches in a- and c-direction are very similar with heavy effective hole masses, and the valence band dispersion becomes nearly isotropic. In fact, this is similar to the case of a polar c-plane QW, as shown in Fig. 4.6(a). Qualitatively, this can be explained by the AlInN buffer layer, which effectively reduces the anisotropic strain that is usually present in m-plane GaInN/GaN structures.

From parabola fits of the valence band dispersion, the effective hole masses can be determined, see Tab. 4.3. The determined effective hole masses are higher, in particular in a-direction, compared to the pseudomorphic m-plane samples. This accounts for the majority of the difference in radiative lifetimes between the two types of m-plane QWs. Furthermore, the reduced strain in the QWs, and the resulting nearly-isotropic dispersion reduce the energy splitting of the valence bands. As can be seen from Figs. 4.6 and 4.8, the energetic difference between the two uppermost valence bands (ΔE) is < 10 meV for the c-plane and the metamorphic m-plane QWs, but already 48 meV for the pseudomorphic m-plane QW due to the strain anisotropy. At room temperature, the charge carrier's typical thermal energy amounts to $300\,\mathrm{K}\,k_{\mathrm{B}} \approx 26$ meV. Therefore, the occupation of the second valence band needs to be considered in addition. The effective mass to describe the ensemble of holes occupying different valence bands, is estimated by averaging over the two in-plane directions according to Eq. 4.3, and subsequent summation over all occupied bands. More precisely, the single valence bands should be regarded according to their actual population. For simplicity, only the two valence bands at the top are considered, and the hole population in the second one can be estimated from a Boltzmann factor, including the factor ΔE, when assuming non-degeneracy. Thus, the density of states effective hole mass is given by

$$m_{\mathrm{h,DOS}} = \sqrt{m_{\mathrm{h,c}}^{(1)} m_{\mathrm{h,a}}^{(1)}} + \exp\left(-\frac{\Delta E}{300\,\mathrm{K}\,k_{\mathrm{B}}}\right) \sqrt{m_{\mathrm{h,c}}^{(2)} m_{\mathrm{h,a}}^{(2)}}\,, \tag{4.4}$$

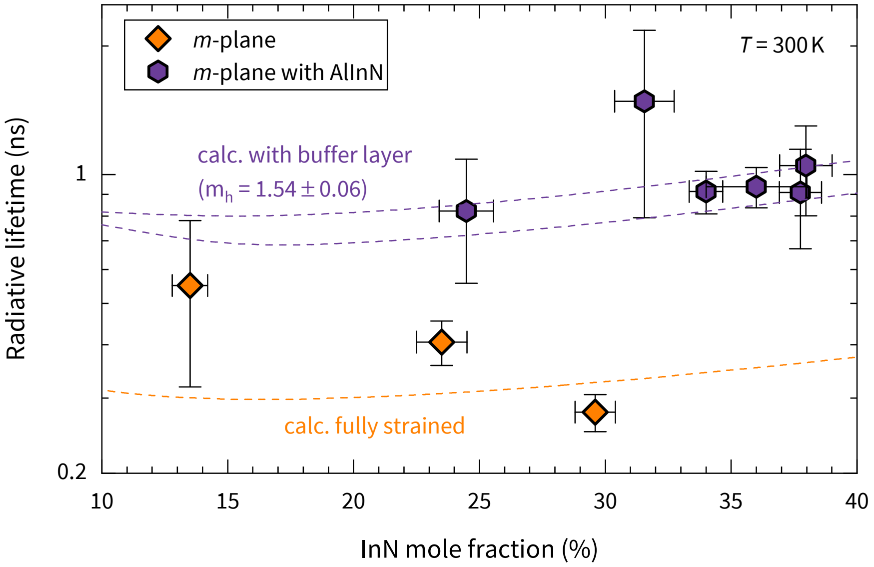

FIGURE 4.9: Comparison of radiative lifetimes at room temperature (300 K) from nonpolar *m*-plane MQW structures ($L_{\mathrm{QW}} \approx 1.5\,\mathrm{nm}$) with and without an AlInN buffer layer. Dashed lines indicate the calculated lifetimes according to Eq. 4.2. Compared to the unbuffered samples, the ones with additional AlInN layer show a significantly increased radiative lifetime due to the larger density of states effective hole mass that was found from $\mathbf{k} \cdot \mathbf{p}$ calculations.

where the superscript 1/2 describes the first and second valence bands. The resulting density of states effective hole masses are summarized in Tab. 4.3. Including the contribution of the second valence band increases the hole masses further, and finally values between $1.5\,m_0$ and $1.6\,m_0$ are found from the effective mass fits. Using these effective hole masses, the excitonic lifetimes can be calculated theoretically by a Schrödinger solver, just as for the pseudomorphic *m*-plane and *c*-plane QWs. While the theoretical radiative lifetimes for the metamorhic QWs match quite well with the measured values, it becomes evident that they are nearly comparable to lifetimes measured on *c*-plane structures. This behavior is in accordance with the calculated valence band dispersion, which is nearly isotropic and shows heavier effective masses compared to the pseudomorphic *m*-plane QWs.

In summary, the use of an AlInN buffer layer reduces the strain in *m*-plane QWs, and moreover eliminates the anisotropy in strain and valence band dispersion. The resulting density of states effective hole masses are higher than for pseudomorphic *m*-

plane QWs without AlInN buffer. Therefore, the metamorphic m-plane QWs behave rather like polar c-plane structures in terms of radiative recombination dynamics, but still show lower radiative lifetimes. The holes in all metamorphic m-plane QWs can be described sufficiently well by effective masses around 1.5 m_0. An exception is sample M9, which shows a density of states effective hole mass of only 0.64 m_0. The radiative lifetime of (0.9 ± 0.2) ns, however, is comparable to the other metamorphic m-plane QWs. The reason for this deviation may be found in the valence band dispersion, which is rather anisotropic due to the relatively large strain, especially in x-direction. This effectively shifts the B-band up in energy, and the resulting effective hole mass $m_{\mathrm{h,a}}^{(1)}$ in x-direction becomes lighter compared to the other metamorphic samples. At higher k-values, however, the uppermost valence band shows heavy-hole character after the crossing point. Furthermore, the energy separation ΔE to the second valence band is considerably higher, which reduces its contribution to the density of states hole mass. In total, the heavy-hole character of the uppermost valence band is underestimated for sample M9. This exception shows that the concept of a single effective hole mass, which is assigned to the ensemble of holes distributed over several valence bands, is stretched to its limits in the present case. This is in particular visible for sample M9, which otherwise behaves comparable to the remaining metamorphic m-plane QWs.

Nevertheless, also an inaccuracy in the $\mathbf{k} \cdot \mathbf{p}$ calculations cannot be excluded. The calculations rely on a set of parameters, which is, although chosen thoroughly, probably not able to reproduce every possible particularity of the sample structures. Still, the $\mathbf{k} \cdot \mathbf{p}$ calculations are a helpful tool to estimate the valence band dispersion with sufficient accuracy for most of the samples under investigation.

4.3.3 *Conclusion*

In conclusion, the radiative recombination in GaInN/GaN QWs was shown to depend strongly on strain. Besides the prominent QCSE, which reduces the radiative emission due to polarization fields, the strain affecting the valence band dispersion has major influence on the radiative lifetimes. This was shown for m-plane QWs, where the anisotropic in-plane strain results in effective hole masses that are a factor of 2-3 lower than those of comparable c-plane QWs. Considering the additional influence of the vanishing polarization field, the higher wave function overlap and increased exciton binding energy reduce the radiative lifetimes further by a factor of 3-4.5. In total, this makes a difference of up to one order of magnitude in radiative lifetimes between m- and c-plane QWs.

Introducing an AlInN buffer layer underneath the m-plane QW structures effectively reduced the strain in the QWs and results in nearly isotropic valence bands with higher effective hole masses. Accordingly, these metamorphic m-plane samples show recombination dynamics comparable to c-plane QWs. Furthermore, density of states effective hole masses around 1.5-1.6 m_0 are found for the metamorphic QWs, together with room temperature radiative lifetimes around 1 ns.

These results emphasize the effect of strain anisotropies on the radiative lifetimes, and highlight the possiblities of strain manipulation using AlInN buffer layers. In this regard, the role of strain-reducing buffer layers on the nonradiative recombination is covered in Ch. 5.

4.4 WIDE NONPOLAR QUANTUM WELLS

At the beginning of this chapter, the use of nonpolar crystal orientations for the growth of GaN-based QW structures has already been motivated. By far the biggest drawback of the conventional polar orientation is the QCSE that occurs due to the internal polarization fields. Thus, for polar quantum wells the use of well widths of a few nm is common. For those, the separation of electrons and holes to opposite sides of the QW can be reduced to a minimum, and typical well widths are in the range of 1.5-3 nm.

Considering QWs on nonpolar orientations, there exist reports on a variety of well widths, ranging from thin QWs with 2-4 nm [123, 134–137], over wider QWs with 5-10 nm [138–146]. Even up to 15 nm thick QWs are reported [147]. These well widths are larger compared to polar nitride QWs, but indeed comparable to common QW widths of 10 nm in other III-V compounds like arsenides [148]. By choosing a larger quantum well width, the active volume increases, while at the same time the charge carrier density can be scaled down. This can be beneficial for the device performance, since the impact of Auger recombination or other high-order loss mechanisms can be reduced [76, 149]. Furthermore, the overlap integral approaches unity for wider quantum wells on nonpolar orientations, since the wave functions are penetrating less into the barrier material. Due to these possible advantages, the use of wide nonpolar quantum wells could be a promising approach for device application. In fact, there exist reports on structures with wider quantum wells that showed better performance compared to thinner quantum wells, in particular regarding the output power at higher current density [139] and at elevated temperatures [142]. In conclusion, a variety of well widths can be found for nonpolar QW structures. Although some work reports on better performance of structures with wide III-nitride quantum wells, the fundamental origin of this observation remains unclear.

In the following, the basic dependence of the radiative emission on quantum well width is analyzed for nonpolar m-plane structures. In general, nonpolar QWs are well-suited for this study, since they are free of polarization fields perpendicular to the QW, and thus, allow for undistorted observation of the recombination dynamics.

In order to describe the width dependence of the radiative recombination in a nonpolar QW, several aspects need to be added to the theoretical considerations from Sec. 4.1. To arrive at the total radiative rate R_r, in principle the contributions of all conduction and valence band states that are populated by charge carriers need to be regarded. In III-nitride QWs, this includes the three valence bands (A, B, C) and all their quantized states (A1,B1,C1,A2,...). Depending on the valence band character, the light emission after recombination is strongly polarized [100, Ch. 5], [150]. For simplicity, the valence band character is omitted here, since the basic width dependence should stay the same irregardless of the polarization state. Therefore, the total radiative rate is obtained by summing over the band indices m for the valence band, and n for the conduction band:

$$R_\mathrm{r} = \sum_{m,n} R_{\mathrm{r,mn}} = \sum_{m,n} B_\mathrm{mn}\, n_\mathrm{n}\, p_\mathrm{m}\,, \tag{4.5}$$

where n_n and p_m denote the electron and hole densities in the n-th conduction band or m-th valence band state. The coefficient B_mn has already been introduced in Eq. 4.1 for $m = n = 1$. Up to now, also the overlap integral M_mn, defined in Eq. 2.7, was only discussed for envelope wave functions of the first quantized states with $m = n = 1$.

In the following, the width dependence of the overlap integral, in particular with respect to the population of higher quantized states, will be discussed. The derived model will be used to estimate the dependence of the radiative recombination on the QW width in III-nitride structures in general.

4.4.1 *Overlap integral including higher quantized states*

III-nitride QWs under influence of internal polarization fields usually show triangular-shaped band edges. Considering nonpolar growth orientations, even a III-nitride QW can be assumed to be rectangular-shaped and symmetrical. Thus, the envelope wave functions of the different quantized states can be described by sine or cosine functions depending on their parity, i.e. odd or even, see Eq. 1.39. The wave function overlap $|M_\mathrm{mn}|^2$ is a key figure to describe the radiative transition probability between different quantized states with envelope functions $|\phi_\mathrm{n}\rangle$ in the conduction band, or $|\phi_\mathrm{m}\rangle$ in the valence band. For the first quantized states ($m = n = 1$), the wave function overlap is relatively high in nonpolar quantum wells. As can be seen from Fig. 4.1(a), it approaches unity, especially for large well widths. Besides this case, other transitions need to be regarded. In fact, for an infinite potential well, only the transitions with $\Delta n = n - m = 0$ would be allowed due to symmetry considerations [38, Ch. 7].

Although other transitions are in principle allowed in a real III-nitride QW with finite barriers, the transitions with $\Delta n = 0$ are expected to show the largest wave function overlap. Here, the wave functions penetrate the barriers, which slightly breaks the strict symmetry that is found in the infinite potential well. Since the distortions are only slight, the wave function overlap should be low compared to the transitions with $\Delta n = 0$. This holds true for the overlap of wave functions with equal parity, i.e. Δn is even. For wave functions with opposite parity, where Δn is odd, the overlap will vanish for symmetry reasons in any case.

In order to estimate the magnitude of the wave function overlap $|M_{\mathrm{mn}}|^2$, a numerical Schrödinger solver is used to calculate the envelope wave function for an exemplary GaInN/GaN quantum well with $x_{\mathrm{In}} = 6\%$ [63]. The case of $\Delta n = 0$ is shown in Fig. 4.10(a), where the wave function overlap $|M_{11}|^2$ approaches 100% for large well widths, and even $|M_{22}|^2$ reaches over 90%. Dashed lines indicate the well width, at which the transition becomes available, in the sense that the respective quantization energies are lower than the band discontinuities. Fig. 4.10(b) shows the calculations for Δn even or odd. In the case that the wave functions have opposite parity, i.e. Δn odd, the wave function overlap indeed vanishes as expected. For wave functions with equal parity, i.e. Δn even, but $m \neq n$, the overlap stays as low as 6% and even decreases to larger well widths. This is in accordance with the expectations, namely that the transitions with $\Delta n = 0$ show the highest wave function overlap, and that other transitions show negligible overlap. Therefore, to a first approximation, only the transitions with $\Delta n = 0$ contribute to the total radiative rate:

$$R_{\mathrm{r}} \approx \sum_{\mathrm{n}} R_{\mathrm{r,nn}} = R_{\mathrm{r,11}} + R_{\mathrm{r,22}} + \ldots \tag{4.6}$$

In the following, the higher quantized states are discussed with respect to their population by charge carriers that can contribute to the radiative recombination.

4.4.2 *Charge carrier density in higher quantized states*

The previous section showed that due to symmetry considerations, only a limited number of transitions can contribute to the radiative rate. To estimate the charge carrier density of the higher quantized states, the distribution of carriers is assumed to obey Boltzmann statistics. This applies in the non-degenerate limit, which is maintained here due to the low-excitation conditions in the time-resolved PL measurements. At absolute zero ($T = 0\,\mathrm{K}$), the carriers will populate only the first quantized state.

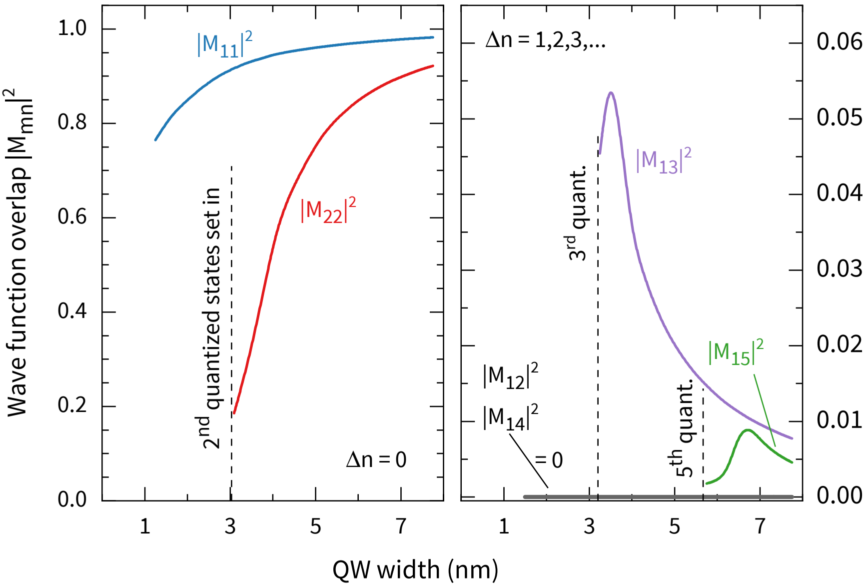

FIGURE 4.10: Wave function overlap between different quantized states for $\Delta n = 0$ (left), and $\Delta n \neq 0$ (right). Note the different y-axis scaling. The values are calculated by a numerical Schrödinger solver, using input parameters from Tabs. 1.1 and 4.2, and an InN mole fraction of $x_{\mathrm{In}} = 6\%$. Dashed lines indicate the width at which the respective quantized state becomes available in the quatum well.

The population of any higher state, occuring due to thermalization of the carriers, is related to the one in the first state by

$$\frac{p_{\mathrm{m}}}{p_1} = \exp\left(-\frac{\Delta E_{1\mathrm{m}}}{k_{\mathrm{B}} T}\right), \tag{4.7}$$

where $\Delta E_{1\mathrm{m}} = E_{\mathrm{m}} - E_1$ is the energy difference between the first and the m-th subband, here for the valence band with hole concentrations p_{m}. In this case, the relation between energetic separation of the subbands and the thermal energy determines the carrier distribution and population of higher quantized states. At room temperature ($T = 300\,\mathrm{K}$), the thermal energy amounts to approximately 26 meV. Thus, considerable population of higher quantized occurs only if the energy difference to the first quantized state is of the same order, or below. Considering Eq. 1.40, the quantization energies are related to the effective carrier masses (here: in direction of quantization, i.e. m-/y-direction), and the quantum well width. This is illustrated in Fig. 4.11, where the band scheme of two exemplary GaInN/GaN QWs with $x_{\mathrm{In}} = 30\%$ are shown.

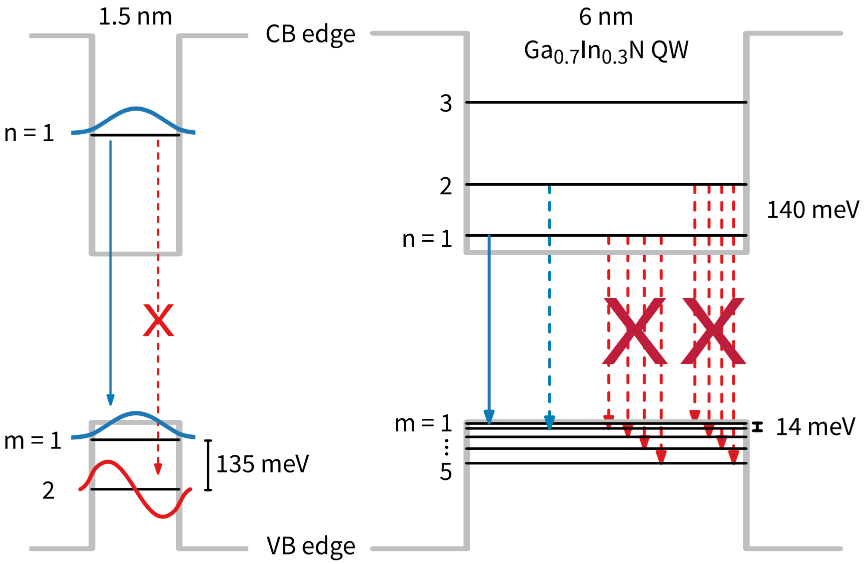

FIGURE 4.11: Scheme of two exemplary GaInN/GaN QWs with $x_{\text{In}} = 30\%$, and either 1.5 nm or 6 nm well width. Solid lines indicate quantized energy levels, calculated by a numerical Schrödinger solver, using input parameters from Tabs. 1.1 and 4.2. The allowed transitions ($\Delta n = 0$) from the conduction band (CB) to the valence band (VB) are indicated by blue arrows, and the transitions that can be neglected due to symmetry reasons ($\Delta n \neq 0$) are indicated as red arrows.

Since Eq. 1.40 is only valid in the case of an infinite potential well, the band schemes are calculated by a Schrödinger solver to account for the finite barrier height. For the QW with a width of 1.5 nm, there is only the first quantized state available in the conduction band. The second quantization energy is already exceeding the barrier height in the conduction band, and the resulting energy would correspond to a bulk state. In the valence band, there exist at least two quantized states, which are separated by approximately 135 meV. This is large enough to neglect the thermal population of the second quantized state, which amount to ≈ 0.6% of the hole density p_1 in the first quantized state according to Eq. 4.7.

Additionally, the transitions with non-vanishing overlap ($\Delta n = 0$) are indicated in Fig. 4.11 by blue arrows. Since the transition from the first quantized level in the conduction band ($n = 1$) to the second level in the valence band ($m = 2$) is forbidden due to symmetry reasons (red arrow), only the transition including the first quantized levels can contribute to the radiative rate. As the second hole level is not occupied at all, all carriers can in principle recombine radiatively for the case of a thin QW.

For larger well widths the situation changes considerably, as shown for $L_{\mathrm{QW}} = 6\,\mathrm{nm}$ in Fig. 4.11. The quantization energies $E_{\mathrm{n/m}}$ are lower, and the quantized states are shifted towards the band edges. The effect is stronger for the valence band, where the effective mass is obviously higher than in the conduction band ($m_{\mathrm{h}} = 2.0\,m_0$ opposed to $m_{\mathrm{e}} = 0.2\,m_0$). Thus, there exist higher quantized sates in the conduction band, but they show an energy separation of 140 meV, which makes thermal population negligible again. Contrary, the valence band shows higher quantized states that are closely spaced in energy. The first and second levels are separated by only 14 meV, which results in a population of $p_2/p_1 = 58\%$. Therefore, a considerable amount of holes populate higher quantized states, while the electrons are limited to the first quantized state in the conduction band. Furthermore, only the holes occupying the first quantized state will be able to recombine radiatively. Although the higher quantized states are populated, transitions from the first conduction band level to higher quantized hole levels are either forbidden (Δn = odd), or show negligible overlap ($0 \neq \Delta n$ = even). This limits the transitions that can contribute to the radiative rate to the one between the first quantized states, and the total radiative rate can be approximated by $R_{\mathrm{r}} \approx R_{11}$.

This approximation is clearly most suitable for thin QWs. But even for larger well widths, the contribution of transitions that are principally allowed ($0 \neq \Delta n$ = even), is further reduced, since the respective conduction band levels are only sparsely populated. As a result of the unequally populated higher quantized states, the radiative recombination rate will be reduced, since only the holes in the first quantized state are allowed to recombine radiatively.

4.4.3 *Reduced radiative rate in wide nonpolar quantum wells*

The previous sections showed that the radiative rate can be approximated by regarding only the first quantized states in the conduction and valence band. Nevertheless, higher quantized states can get thermally populated, in particular in the valence band. In order to estimate the amount of holes in the first quantized state in relation to the overall hole density, the sum is taken over all occupied states:

$$\frac{p_1}{p} = \frac{p_1}{\sum\limits_{\mathrm{m}} p_{\mathrm{m}}} = \frac{1}{\sum\limits_{\mathrm{m}} \exp\left(-\frac{\Delta E_{1m}}{k_{\mathrm{B}} T}\right)} \equiv f_{\mathrm{h},1} \leq 1\,, \tag{4.8}$$

where $\Delta E_{11} = 0\,\mathrm{meV}$ by definition. Using the above relation, the density of holes (p) that contribute to the radiative rate can be corrected by an additional factor $f_{\mathrm{h},1}$

in Eq. 4.1. Only at absolute zero ($T = 0\,\mathrm{K}$), the above estimation delivers $f_{\mathrm{h},1} = 1$, and $p = p_1$, which may apply in approximation as well for thin QWs. Once the thermal population of higher quantized states in the valence band becomes relevant, in particular for wide QWs, the hole density in the first quantized state will decrease ($p_1 < p$), and the radiative rate is reduced accordingly:

$$R_\mathrm{r} \approx R_{11} = B_{11}\, n\, p\, f_{\mathrm{h},1}\,, \tag{4.9}$$

where $n_1 \approx n$, since the electrons are occupying only the first quantized state. While the above relation applies for the radiative recombination of free electrons and holes, the charge carriers are likely bound into excitons, as stated already in Sec. 4.1. Since the same arguments apply for excitons as for free charge carriers, the excitonic radiative lifetime (compare Eqs. 4.1 and 4.2) can be expressed as

$$\tau_\mathrm{ex} = \frac{\pi\, a_\mathrm{B}^2}{2\, B_{11}}\, \frac{1}{f_{\mathrm{h},1}} \propto \frac{T\, a_\mathrm{B}^2}{|M_{11}|^2}\, \frac{1}{f_{\mathrm{h},1}}\,. \tag{4.10}$$

Finally, the excitonic lifetime, apart from a proportionality factor, will depend on temperature, the exciton Bohr radius, the wave function overlap of the first quantized states, and the ratio of holes in the first valence band state. Other factors included in B_{11} (see Eq. 4.1) can be assumed to vary only slightly over well width, and are considered constant for this analysis, e.g. band gap and effective carrier masses. The linear dependence on temperature can be derived from Eqs. 4.1 and 4.2, and is also observed experimentally [72, 151]. Additionally, the excitonic lifetime will depend on temperature via the factor $f_{\mathrm{h},1}$. The excitonic lifetime that is unaffected by the thermal population of higher quantized states can be defined as $\tau_{\mathrm{ex},0} = f_{\mathrm{h},1}\, \tau_\mathrm{ex}$.

The above considerations predict a decreasing radiative rate for increasing QW width due to the lower quantization energies. Experimentally, this would cause an increasing radiative (or excitonic) lifetime with increasing well width, since $\tau_\mathrm{ex} \propto 1/f_{\mathrm{h},1}$. For this reason, four GaInN/GaN three-fold MQW structures are prepared on *m*-plane GaN bulk substrates [91]. The QW widths, as measured by XRD, vary between 1.3 and 6.3 nm, with a constant barrier thickness of 8 nm for all samples [96]. A low InN mole fraction of 6-7% is chosen, and confirmed by XRD, to avoid relaxation in the active MQW region with increasing thickness. The sample details are summarized in Tab. 4.4.

To compare the radiative emission for samples with different well widths, temperature-dependent time-resolved PL is performed for all samples using the TCSPC setup. Non-resonant excitation with a laser wavelength of 350 nm is necessary, since the PL emission of the QWs is close the one of the GaN substrate due to the low InN mole fraction. Fig. 4.12 shows an exemplary temperature dependence of measured effective (τ_eff), radiative (τ_r) and nonradiative lifetime (τ_nr) for sample W2.

TABLE 4.4: Overview of the samples under investigation, with QW width (L_{QW}), InN mole fraction (x_{In}), emission wavelength at room temperature ($\lambda(300\,\mathrm{K})$), and energetic difference (ΔE_{12}) of the first and second quantized valence band state.

Sample[a]	L_{QW} [b]	x_{In} [b]	$\lambda(300\,\mathrm{K})$	ΔE_{12}
W1	(1.3 ± 0.1) nm	(8.4 ± 1.9) %	369 nm	42.4 meV
W2	(2.3 ± 0.1) nm	(7.0 ± 0.6) %	381 nm	42.3 meV
W3	(3.8 ± 0.1) nm	(6.2 ± 0.4) %	387 nm	23.9 meV
W4	(6.3 ± 0.3) nm	(6.3 ± 0.6) %	390 nm	10.2 meV

[a] Ref. [91] [b] Ref. [96]

Effective lifetimes around 500 ps are found at low temperatures, which is comparable to the values obtained for other nonpolar QWs in Sec. 4.1. At low temperatures, up to approximately 30 K, the radiative lifetime shows a constant behavior, which is indicative of carrier localization. The other samples show a comparable behavior. As discussed above in Sec. 4.1, localization can occur at local potential minima caused by fluctuations in InN mole fraction and quantum well width [115–119]. Above 30 K the radiative lifetime shows a close-to-linear rise, which is characteristic for charge carriers that are free in two dimensions. Also the effective lifetimes show a sharp drop in this temperature regime, and even approach the temporal resolution limit of 25 ps for temperatures beyond 240 K. As the lifetimes measured in this regime would not be reliable, the analysis is limited to temperatures < 210 K. Already above 120 K, the recombination is dominated by nonradiative processes, and the very low lifetimes in this temperature regime are found for all samples. Probably, the low InN mole fraction in the QW, and the related low barrier heights, cause an insufficient carrier confinement. This could make thermal escape of charge carriers into the barrier more probable. Also other nonradiative processes, especially those related to strain-induced formation of defects (see Ch. 5), might occur, but cannot be identified from the present measurements. At least a TEM investigation on sample W4 did not show any structural particularities [152].

Well width dependence

To analyze the behavior with increasing well width, the radiative lifetimes of samples W1-W4 are plotted in Fig. 4.13 for temperatures of 90, 150, and 210 K. At 90 K, the lifetimes are still under influence of localization, and stay nearly constant with only little variation over the well width. At 150 K, the variation is already larger, and a

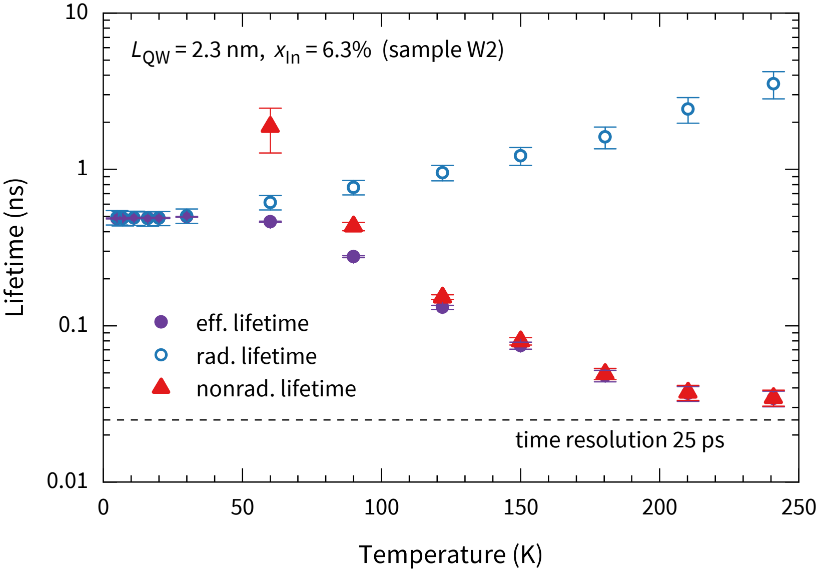

FIGURE 4.12: Temperature dependence of effective (τ_{eff}), radiative (τ_{r}), and nonradiative lifetimes (τ_{nr}) of sample W2 (L_{QW} = 2.3 nm, x_{In} = 6.3 %).

minimum, although not very pronounced, becomes visible. Finally, at 210 K, the differences between the samples are clearly visible. The minimum radiative lifetime is found at a well width around 2 nm, and a higher lifetime for smaller well widths. Towards larger well widths, however, a nearly linear rise of the radiative lifetimes is observed, which coincides with the predicted reduction of the radiative rate.

Besides the experimental data, calculations according to Eq. 4.10 are included in Fig. 4.13. To estimate the radiative lifetimes, Schrödinger's equation is solved for an exemplary GaInN/GaN quantum well with 6% InN mole fraction and well widths between 0.5 and 7 nm. This yields quantization energies, wave function overlap, and exciton Bohr radius [63]. The same input parameters as for the previous calculations in this chapter are used, and can be found in Tabs. 4.2 and 1.1. Note that the charge carriers experience quantization the m-direction (y in the crystal coordinate system), and thus the effective in-plane mass $m^{\text{m}}_{\text{h,z'}}$ has to be used for the calculation of quantization energies. To estimate the factor $f_{\text{h,1}}$, the differences $\Delta E_{1\text{m}}$ of the calculated quantization energies are put into Eq. 4.8, and the sum is taken up to $m = 100$. In fact, the result changes by 5% when increasing the limit from $m = 50$ to 100. For even higher limits, the change becomes negligible. Using Eq. 4.10, a theoretical radiative lifetime can be calculated for the temperatures of 90, 150 and 210 K, to complement

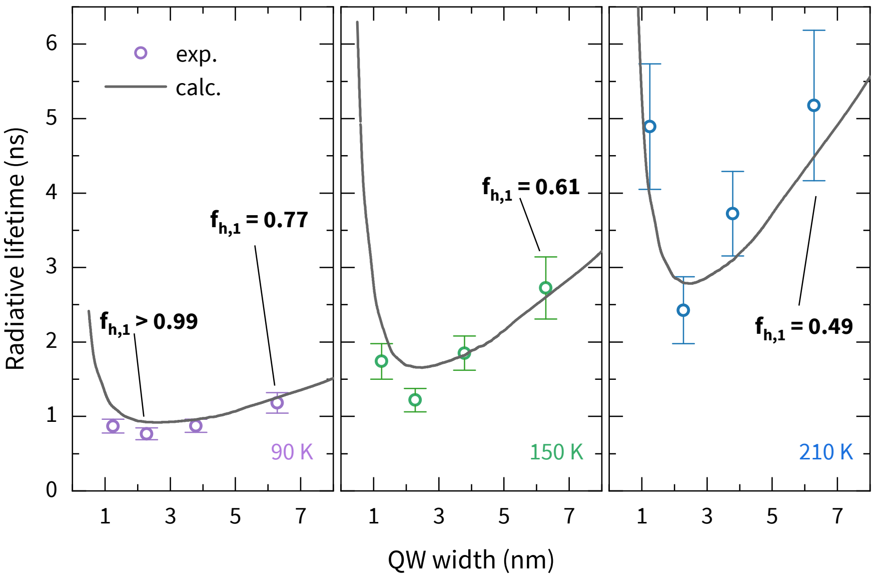

FIGURE 4.13: Rise of radiative lifetimes with quantum well width, induced by the decreasing hole population in the first quantized state, as indicated by the decreasing factor $f_{\mathrm{h},1}$. At higher temperatures, this results in a stronger increase of the radiative lifetime. Solid lines indicate calculations according to Eq. 4.10, which coincide with the experimental data.

the experimental results shown in Fig. 4.13. The constant of proportionality that is missing in Eq. 4.10 is chosen such that the calculated curve coincides best with the experimental values, and remains constant for all temperatures. Overall, the theoretically calculated curve matches quite well with the experimentally observed behavior, which confirms the validity of the model and its underlying assumptions. In particular, two regimes have to be distinguished that show quite opposite behaviors with varying QW width. For large well widths above 2 nm, the increase in radiative lifetime follows the well width linearly. Although the trend is already visible at 90 K, the behavior is most distinct at 210 K. Also the slope of the calculated curve becomes larger with increasing temperature, which can be assigned to the decreasing factor $f_{\mathrm{h},1}$ due to the increased population of higher quantized valence band states. To separate the single contributions of wave function overlap, exciton Bohr radius and thermal population of higher states, Fig. 4.14 is considered. It shows the wave function overlap $|M_{11}|^2$, the exciton Bohr radius a_{B}, and the fraction $f_{\mathrm{h},1}$ as function of well width. For an InN mole fraction of 6%, which is comparable to the samples under investigation, there is only little variation in the exciton Bohr radius for well widths larger than 2 nm. Together with the wave function overlap, which is constantly increasing with well width, this leads to a nearly constant excitonic radiative lifetime $\tau_{\mathrm{ex},0}$, which is shown in Fig. 4.15 and disregards the factor $f_{\mathrm{h},1}$. Only for small well widths, i.e. below 2 nm, the lifetime is increasing due to the slight reduction in overlap and the lower exciton binding. This is expected, since electron and hole envelope wave functions have higher probability density in the barrier material for thinner quantum wells. When regarding the additional factor $f_{\mathrm{h},1}$, the rise in radiative lifetime with well width can be reproduced by the calculations, as shown by the curve for $\tau_{\mathrm{ex}} = \tau_{\mathrm{ex},0}/f_{\mathrm{h},1}$. This demonstrates the enormous effect of thermal population of higher quantized states on the radiative lifetime.

For well widths below 2 nm, however, the radiative lifetime is increasing again. This can be observed already at 90 K, where the population of higher quantized hole states has nearly no impact. Instead, the interplay of wave function overlap and exciton Bohr radius determines the behavior, which corresponds to the calculated $\tau_{\mathrm{ex},0}$. At larger temperatures, however, the increasing radiative lifetime at small well widths becomes stronger, and can be explained by a peculiarity of low-indium containing QWs. The increasing quantization energy for thinner quantum wells shifts the first quantized state to the band edge of the barrier material, where the higher quantized states are accumulating. This applies especially to the valence band with its lower band discontinuity, and effectively reduces the energy difference between the first and higher quantized states for very thin quantum wells. Therefore, their thermal population becomes possible, as can be seen by a reduced $f_{\mathrm{h},1}$ in Fig. 4.14, which again leads to an increase in radiative lifetime. This effect should be negligible for QWs with higher InN mole fraction, e.g. 30%, as demonstrated by a calculation shown in Fig. 4.15. Here, the radiative lifetime is not rising at small well widths, as it is determined by exciton Bohr radius and wave function overlap. For larger well widths, however, the increase becomes even stronger than for the low-indium containing QW. The population of higher quantized hole states can increase the radiative lifetime up to a factor of 3.9 for high InN mole fractions at 300 K. For low InN mole fractions of 6%, an increase by a factor of 2 is expected from the theoretical values, and also observed in the measurements between well widths of 2 and 6 nm.

Although only a limited temperature and width range is accessible in the presented measurements, the significant increase of radiative lifetime with well width can be demonstrated. A two-fold increase in radiative lifetime corresponds to a reduction of the radiative rate by 50%, as measured for wide nonpolar GaInN/GaN quantum wells. For the above analysis, the quantization energies were calculated considering only a single valence band instead of three (A, B, C). The results show that the relatively simple model with only a few assumptions is capable of describing the experimentally

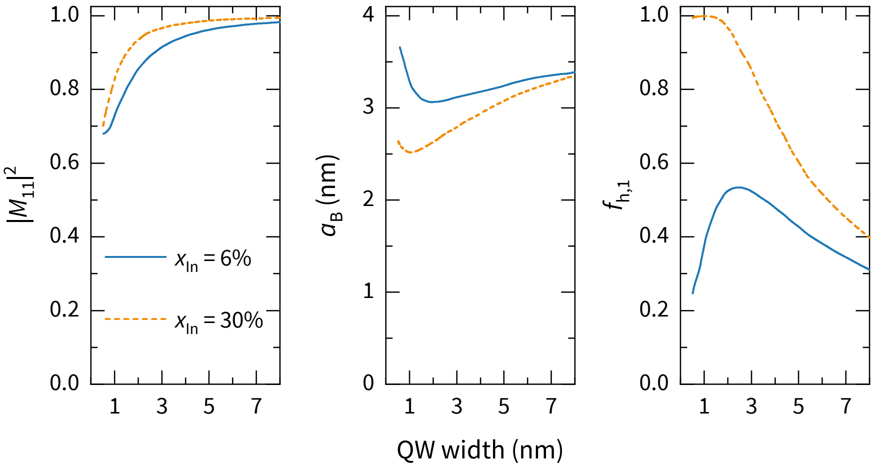

FIGURE 4.14: Wave function overlap $|M_{11}|^2$, exciton Bohr radius a_B, and fraction $f_{h,1}$ of holes populating the first quantized state, calculated for low ($x_{\mathrm{In}} = 6\%$) and high ($x_{\mathrm{In}} = 30\%$) InN mole fraction at room temperature.

observed behavior of the radiative lifetimes. This is only expected, since the valence band structure based on a single band should result in the same width dependence of the quantized states that move closer together in energy. To investigate possible deviations due to this assumption, a complementary calculation was carried out with the 6×6 $\mathbf{k} \cdot \mathbf{p}$ method, which was introduced in Sec. 1.2.5. As might be expected, the two approaches show slight differences, but are overall comparable. In the vicinity of the Γ-point ($k = 0$), the calculated wave function overlaps differ by only 1% from those calculated with the simpler model. For wave functions with opposite parity ($\Delta n \neq 0$), both approaches show negligible, or even zero, wave function overlap. Slightly larger deviations of approximately 10% are found for the calculated quantization energies between the two methods. Still, the simpler model calculation can describe the width dependence of the energy levels to the same extent, and neglecting transitions with $\Delta n \neq 0$ is found to be a good approximation for the present case. Although the $\mathbf{k} \cdot \mathbf{p}$ calculations deliver a better description of the band structure, the simpler model is preferred here to reduce the necessary assumptions to a minimum.

4.4.4 *Conclusion*

In summary, the radiative rate, measured at different temperatures, is found to be significantly reduced for wide nonpolar quantum wells. The effect is mainly attributed

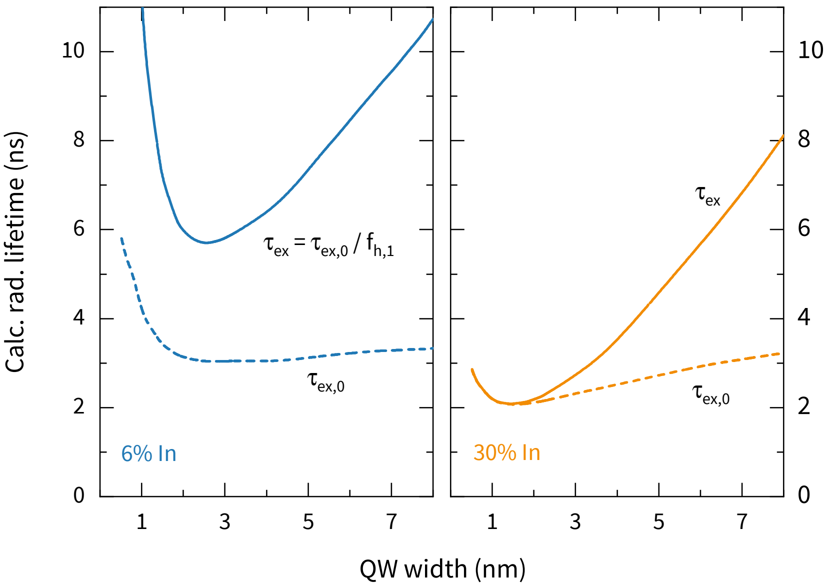

FIGURE 4.15: Theoretically calculated radiative lifetimes at room temperature (300 K) according to Eq. 4.10. Dashed lines indicate $\tau_{ex,0}$, which depends only on temperature, overlap and exciton Bohr radius. Solid lines indicate τ_{ex}, which regards the additional factor $f_{h,1}$ to include the effect of thermal population of higher quantized valence band states.

to a decreasing fraction of charge carriers that are populating the uppermost valence band and lowest conduction band states. In a first approximation, charge carriers in other states do not contribute to the radiative recombination, either due to forbidden transitions between higher electron and hole states, corresponding to the selection rule $\Delta n = 0$, or due to their unequal population, caused by the large difference in effective masses. The decreasing radiative rate can be estimated by a simple model, which additionally regards the wave function overlap and excitonic binding to calculate a radiative lifetime. From the calculations, the effect is expected to increase with temperature and growing InN mole fraction. Although the present experiments are limited to GaInN/GaN QWs, the effect should occur in other III-nitrides structures in nonpolar orientations. For this reason, the use of wide nonpolar quantum wells should be avoided when large radiative rates, or high quantum efficiencies, are of interest. Similar results are found by Garrett et al. [121], where also thin nonpolar QWs showed better performance. Contrary to the present analysis, Garrett et al. attribute their findings only to the effects of wave function overlap and exciton binding energy, but do not consider the effect of unequally populated higher states or selection rules. From the analysis shown above, a QW width in the range of 1.5-3 nm, depending on the composition, can be considered to be the optimum value, even in nonpolar GaInN/GaN structures.

4.5 LIMITATIONS AT ELEVATED TEMPERATURE

In the previous sections, structural influences on the radiative recombination in III-nitride quantum wells were covered. Strain and well width were found to be crucial parameters that have influence on the valence band structure. In the following section, a more fundamental and intrinsic issue is treated, namely the temperature dependence of the radiative lifetime, which shows a distinct behavior in different temperature regimes, as mentioned already in Secs. 2.1 and 4.1.

4.5.1 *Radiative lifetime in different temperature regimes*

The radiative rate R_r scales with temperature according to the charge carriers' effective density of states, which is linked to their dimensionality, or spatial confinement, see Eq. 2.13:

$$R_\mathrm{r} \propto T^{-d/2} \quad \Rightarrow \quad \tau_\mathrm{r} \propto T^{d/2} \, . \tag{4.11}$$

Starting at lowest temperatures, the radiative lifetime τ_r usually shows a constant behavior, which indicates localization of charge carriers at local potential minima. The localization corresponds to a zero dimensional state ($d = 0$, $\tau_\mathrm{r,loc} = \text{const.}$), which can arise from fluctuations in the quantum well width or composition [110–119]. With increasing temperature, meaning increasing thermal energy, the charge carriers can escape the localization sites, and behave as two-dimensionally free ($d = 2$). Therefore, the radiative lifetime is expected to increase linearly with temperature ($\tau_\mathrm{r,2D} \propto T^1$). When considering the contribution of both, localized and two-dimensionally free charge carriers, the total radiative rate becomes

$$R_\mathrm{r} = \frac{\delta n_\mathrm{loc}}{\tau_\mathrm{r,loc}} + \frac{\delta n_\mathrm{2D}}{\tau_\mathrm{r,2D}} = \frac{\delta n_\mathrm{loc} + \delta n_\mathrm{2D}}{\tau_\mathrm{r}} \, , \tag{4.12}$$

where the densities of excess charge carriers in a localized (δn_loc), and a two-dimensional state (δn_2D), can be described by Boltzmann statistics in the non-degenerate limit:

$$\frac{\delta n_\mathrm{2D}}{\delta n_\mathrm{loc}} = \frac{N_\mathrm{2D}}{N_\mathrm{loc}} \exp\left(-\frac{E_\mathrm{loc}}{k_\mathrm{B} T}\right) . \tag{4.13}$$

Here, the delocalization energy E_{loc} describes a characteristic thermal energy needed to escape from localization sites. The density of localization centers is described by N_{loc}, and N_{2D} is the two-dimensional effective density of states, which is proportional to temperature ($N_{\mathrm{2D}} = N'_{\mathrm{2D}} \cdot T$) [62, Ch. 11]. Combining Eqs. 4.12 and 4.13, the overall radiative lifetime can be described by [153]

$$\tau_{\mathrm{r}} = \tau_{\mathrm{r,loc}} \frac{1 + \gamma_{\mathrm{L}}\, T \, \exp\left(-\frac{E_{\mathrm{loc}}}{k_{\mathrm{B}} T}\right)}{1 + \gamma_{\mathrm{L}}\, \tau_{\mathrm{L}} \, \exp\left(-\frac{E_{\mathrm{loc}}}{k_{\mathrm{B}} T}\right)} \,. \tag{4.14}$$

Expressing the radiative lifetime of 2D charge carriers as $\tau_{\mathrm{r,2D}} = \tau'_{\mathrm{r,2D}} \cdot T^1$, the constant prefactors γ_{L} and τ_{L} can be defined by

$$\gamma_{\mathrm{L}} = \frac{N'_{\mathrm{2D}}}{N_{\mathrm{loc}}} \,, \qquad \tau_{\mathrm{L}} = \frac{\tau_{\mathrm{r,loc}}}{\tau'_{\mathrm{r,2D}}} \,. \tag{4.15}$$

Fig. 4.16 shows an exemplary temperature dependence of the measured effective lifetimes, and the radiative lifetimes of a c-plane GaInN/GaN single quantum well (sample C11, see Tab. 4.5). In fact, the radiative lifetimes show a linear rise up to room temperature, just after the transition from the localization regime at 20-30 K. Accordingly, the temperature behavior can be described by the model function in Eq. 4.14, and yields a delocalization energy of $E_{\mathrm{loc}} = (0.5 \pm 0.2)$ meV. Note that the nonradiative lifetimes are omitted in this plot for convenience, but nonradiative recombination is dominating the decay at room temperature ($T = 300\,\mathrm{K}$).

Fig. 4.17 shows effective and radiative lifetimes of another GaInN/GaN QW (sample C22, see Tab. 4.5), whose QW is nominally identical to the one of sample C11. Comparable to the data plotted in Fig. 4.16, the radiative lifetimes show a close-to-linear rise for intermediate temperatures around 60-180 K, where the behavior can be described by the above model function (Eq. 4.14). At even higher temperatures, however, the radiative lifetimes increase more rapidly, which is unexpected for charge carriers confined to two dimensions. Towards room temperature, the increasing slope exceeds even the $T^{3/2}$ dependence, which would be characteristic for charge carriers in bulk material ($d = 3$).

4.5.2 *Thermally activated rise of radiative lifetime*

The extreme rise in radiative lifetimes that is observed here is indicative of a thermally activated process that affects the recombination dynamics. The responsible physical process, however, cannot be identified in the first place. As a first step, the

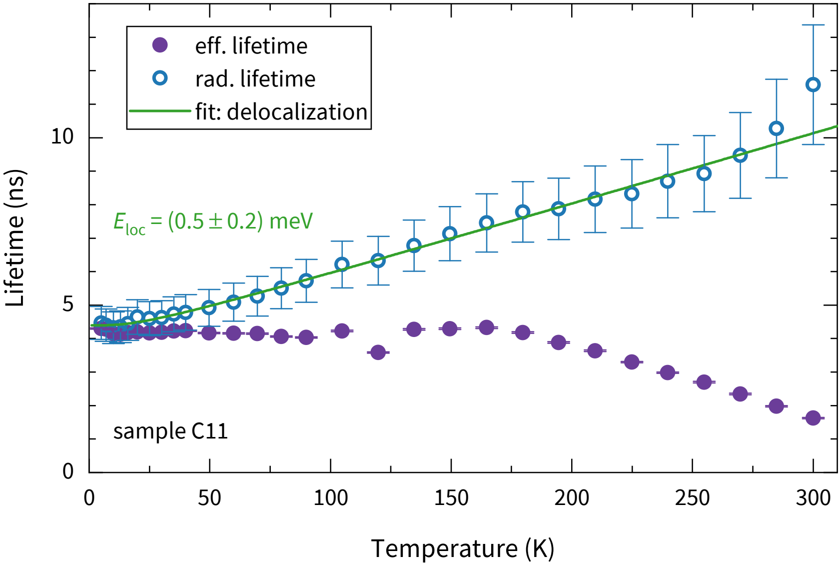

FIGURE 4.16: Temperature-dependent lifetimes of an exemplary *c*-plane GaInN/GaN quantum well (sample C11, see Tab. 4.5) [101]. The measured radiative lifetimes scale with temperature according to Eq. 4.11. While the constant radiative lifetime indicates localized charge carriers at low temperatures ($d = 0$), the linear increase at higher temperatures shows that the carriers are free to move in two dimensions ($d = 2$). Fitting the temperature behavior with the model function given in Eq. 4.14 reveals a delocalization energy of $E_{\mathrm{loc}} = (0.5 \pm 0.2)$ meV.

model function in Eq. 4.14 is extended by an additional high-temperature activation energy (E_{HT}) to account for the thermally activated rise of radiative lifetimes:

$$\tau_{\mathrm{r}} = \tau_{\mathrm{r,loc}} \frac{1 + \gamma_{\mathrm{L}}\, T \exp\left(-\frac{E_{\mathrm{loc}}}{k_{\mathrm{B}} T}\right) \left[1 + \gamma_{\mathrm{HT}}(T) \exp\left(-\frac{E_{\mathrm{HT}}}{k_{\mathrm{B}} T}\right)\right]}{1 + \gamma_{\mathrm{L}}\, \tau_{\mathrm{L}} \exp\left(-\frac{E_{\mathrm{loc}}}{k_{\mathrm{B}} T}\right)}, \tag{4.16}$$

where the prefactor $\gamma_{\mathrm{HT}}(T)$ behaves with temperature like the effective density of states of the involved two-dimensional (N_{2D}) and thermally excited states (N_{HT}):

$$\gamma_{\mathrm{HT}}(T) = \frac{N_{\mathrm{HT}}}{N_{\mathrm{2D}}}. \tag{4.17}$$

Although a strong temperature-dependence of the prefactor γ_{HT} would lower the corresponding activation energy, its order of magnitude would stay unchanged.

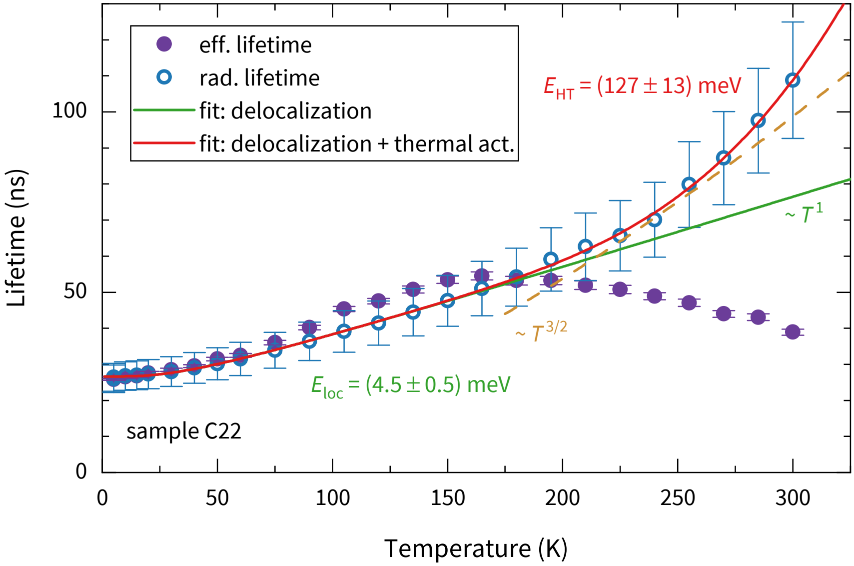

FIGURE 4.17: Temperature-dependent lifetimes of an exemplary *c*-plane GaInN/GaN quantum well (sample C22, see Tab. 4.5). The data is comparable to Fig. 4.16 for $T < 180$ K, where the radiative lifetime can be described by Eq. 4.14, yielding a delocalization energy of $E_{\text{loc}} = (4.5 \pm 0.5)$ meV. Approaching room temperature (300 K), the radiative lifetimes are increasing rapidly, which can be described by an additional activation energy. Fitting the temperature behavior with an extended model function (Eq. 4.16) reveals a high-temperature activation energy of $E_{\text{HT}} = (127 \pm 13)$ meV.

For this reason, γ_{HT} is assumed constant in a first approximation. Beyond that, the activation energy E_{HT} is expected to be larger than the delocalization energy E_{loc}, since the super-linear increase of radiative lifetimes occurs only close to room temperature. In fact, for sample C22, as shown in Fig. 4.17, the model function from Eq. 4.14 reasonably describes the observed temperature behavior of the radiative lifetimes, and reveals a high-temperature activation energy of $E_{\text{HT}} = (127 \pm 13)$ meV. As expected, the activation energy is more than one order of magnitude larger than the delocalization energy.

The activation energy itself is a valuable indicator to determine the responsible physical process behind the super-linear increase of radiative lifetimes. Possible processes should either lower the amount of charge carriers that are available to radiative recombination, or reduce the probability of radiative recombination itself to induce a rise of the radiative lifetimes with temperature. One possibility might be the dissociation of excitons, which have been shown to contribute significantly to the radiative recombination rate, even at room temperature [122, 123]. Although the internal polarization fields significantly reduce the exciton binding energy, it can amount up to ~43 meV in comparable c-plane QWs. Since the recombination probability for free electrons and holes would be drastically reduced, a steep increase of the radiative lifetime with temperature would be expected.

Alternatively, the thermal excitation of charge carriers into higher quantized states, or even into the barrier material surrounding the QW, could lower the amount of carriers that can undergo efficient radiative recombination, and thereby cause an increase in radiative lifetimes. Although radiative recombination should be possible for carriers populating higher quantized states, the emission is expected to be spectrally shifted with respect to the main QW luminescence that is analyzed here. Furthermore, the wave functions of charge carriers in bulk-like states would extend far beyond the quantum well dimensions, which would result in a significantly reduced, or even vanishing overlap. This would be comparable to the results discussed in the previous Sec. 4.4, where the radiative recombination in nonpolar QWs was affected heavily by the population of higher quantized states, in particular for large well widths. The energetic differences between quantized states, as well as the band discontinuities, depend strongly on the QW composition and width.

4.5.3 *Effective band discontinuities*

In order to estimate these quantities, a Schrödinger solver is used, which calculates quantization energies and exciton binding energies [63]. For the GaInN/GaN QWs under investigation, the difference in band gap energies ($\Delta E_\mathrm{g} = E_\mathrm{g,GaN} - E_\mathrm{g,GaInN}$) is split up into valence and conduction band discontinuities with a ratio of $\Delta E_\mathrm{c}/\Delta E_\mathrm{v} = 70/30$. An effective discontinuity can be calculated by subtracting the quantization energy of the first state from the total band discontinuity, see Fig. 4.18. In any case, this estimation should serve as an upper limit for the thermal activation of charge carriers in the QW.

The samples shown above (C11, C22) consist of single quantum wells with nominally identical width and composition. Therefore, information on the QW structure is not accessible by XRD, and instead the nominal composition and well widths are used. Usually, comparable multi-quantum well structures are used as a calibration standard for those nominal parameters. With the nominal QW parameters ($x_\mathrm{In} = 19\%$, $L_\mathrm{QW} = 2.1\,\mathrm{nm}$), effective discontinuities of $\Delta E_\mathrm{v,eff} = 53\,\mathrm{meV}$ for the valence band and $\Delta E_\mathrm{c,eff} = 132\,\mathrm{meV}$ for the conduction band can be calculated. Within

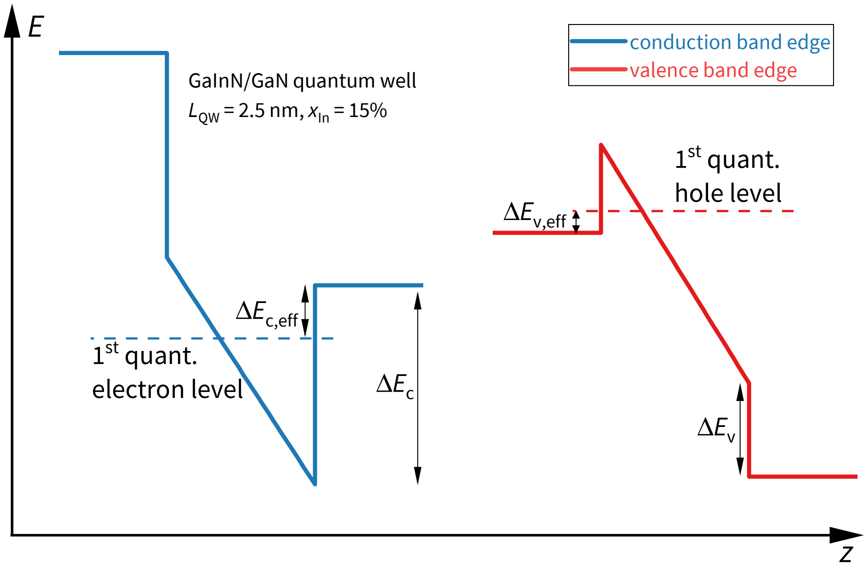

FIGURE 4.18: Scheme of the conduction and valence band edges in an exemplary GaInN/GaN quantum well (L_{QW} = 2.5 nm, x_{In} = 15%). The first quantized electron and hole levels, calculated by a Schrödinger solver [63], are indicated. The energetic difference from the quantized levels to the nearest band edge of the barrier material defines the effective discontinuity $\Delta E_{c/v,eff}$, which is considerably smaller than the band discontinuity $\Delta E_{c/v}$ of the potential well.

the uncertainties, the activation energy of (127 ± 13) meV found for sample C22 fits reasonably well with the conduction band value from the calculations.

Fig. 4.19 shows the temperature-dependent lifetimes of another GaInN/GaN quantum well (sample C28), whose QW is nominally comparable to the samples C11 and C22. Like in Fig. 4.17, the fitted curve according to Eq. 4.16 adequately describes the observed behavior of the radiative lifetimes in all temperature regimes, including the super-linear rise towards room temperature. The fit reveals a delocalization energy of $E_{loc} = (4.6 \pm 2.2)$ meV, and a high-temperature activation energy of $E_{HT} = (84 \pm 11)$ meV. While sample C22 showed a higher activation energy that is comparable to the effective conduction band discontinuity, the activation energy found for sample C28 is comparable to the effective discontinuity in the valence band.

Although significantly different activation energies are found for both structures, the energies are comparable to the calculated effective band discontinuities, and in addition, are too high to be related to exciton dissociation. This indicates the

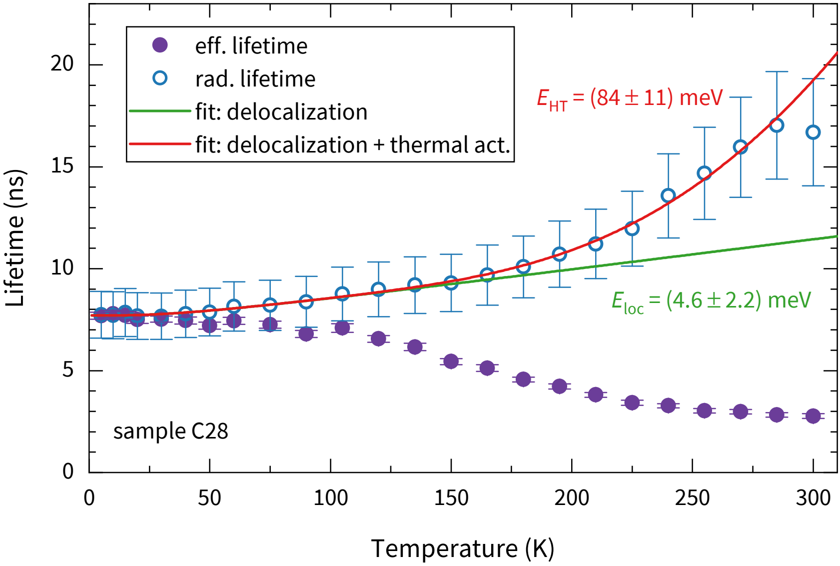

FIGURE 4.19: Temperature-dependent lifetimes of an exemplary *c*-plane GaInN/GaN quantum well (sample C28, see Tab. 4.5). Comparable to sample C22 (Fig. 4.17), the radiative lifetimes can be described by the extended model function (Eq. 4.16), yielding a delocalization energy of $E_{\mathrm{loc}} = (4.6 \pm 2.2)$ meV, and a high-temperature activation energy of $E_{\mathrm{HT}} = (84 \pm 11)$ meV.

excitation of charge carriers into the barrier material surrounding the QW. There, the charge carriers populate bulk-like states, and would experience an effective density of states $N_{\mathrm{HT}} \propto T^{3/2}$, which leads to $\gamma_{\mathrm{HT}} \propto \sqrt{T}$. Repeating the fit with a temperature-dependent prefactor γ_{HT} yields activation energies about 10 meV lower compared to a constant γ_{HT}.

The above analysis is repeated for a larger sample set in the following. For this purpose, the radiative lifetimes of GaInN/GaN (single and multi) quantum well structures are fitted with the model function from Eq. 4.16, using a temperature-dependent prefactor ($\gamma_{\mathrm{HT}} \propto \sqrt{T}$). The activation energies derived from the temperature behavior of the radiative lifetimes are compared to the effective band discontinuities found from calculations, using the QW width and composition for every single structure. The results are summarized in Fig. 4.20 and Tab. 4.5. It should be emphasized that most of the structures under investigation show the super-linear increase of radiative lifetimes that was described above for samples C22 and C28. The activation energies are found to range from 60 to 400 meV.

The investigated structures include also non- and semipolar samples, where the polarization field vanishes, or is at least significantly reduced. Furthermore, the calculations are performed with and without including an n-type doping below the QW region for all samples. More precisely, even without intended n-type doping, a background carrier concentration of $N_\mathrm{D} = 1 \times 10^{16}/\mathrm{cm}^3$ is assumed, which does nearly not affect the output of the calculation. For the case with doping, a GaN layer with a concentration of $N_\mathrm{D} = 5 \times 10^{18}/\mathrm{cm}^3$ is assumed, which is separated from the QW by 2 nm of undoped GaN. The thicknesses and doping concentrations of the actual n-doped layers in the samples are within these limiting cases. This layer is effectively lowering the polarization field F due to the screening induced by the doped region. According to Im et al. [154], the effective field F_eff can be described by

$$F_\mathrm{eff} = F + \frac{eN_\mathrm{D}L_\mathrm{QW}}{\varepsilon_0\varepsilon_\mathrm{r}}\left(1 - \sqrt{1 + \frac{2\varepsilon_0\varepsilon_\mathrm{r}F}{eN_\mathrm{D}L_\mathrm{QW}}}\right), \tag{4.18}$$

where N_D is the doping concentration. The reduced field results in slightly higher effective band discontinuities. As can be seen from Fig. 4.20, the experimentally determined activation energies in fact agree with the range of calculated values for most of the structures. Within the uncertainties, most of the polar structures show activation energies that match the effective discontinuity of either the valence or the conduction band.

Only single samples are located just outside the range of calculated effective conduction band discontinuities, or show large uncertainties. Especially for the non- and semipolar structures, the agreement between experimentally determined activation energies and the calculations is less accurate. Generally, the calculations show relatively high effective discontinuities for those structures, most of them exceed 200 meV. At the same time, most of the non- and semipolar samples show an activation energy of zero, i.e. a purely linear increase of the radiative lifetimes up to room temperature. This may be explained by the limited temperature range that is accessible in the experiments. Usually, the radiative lifetimes are determined only up to room temperature, where a thermal activation in the order of 250 meV or above might not have any significant effect. Therefore, a linearly increasing radiative lifetimes is found in the experiment.

Nevertheless, some semi- and nonpolar structures show activation energies below the calculated effective valence band discontinuity. Instead, those are close to the calculated exciton binding energies for the respective structures. As mentioned above, also the dissociation of excitons would lower the probability of radiative recombination, since a part of the charge carriers would have to undergo bimolecular recombination, which has a much lower transition probability. Therefore, a steep increase of the radiative lifetimes with temperature can be expected for this case

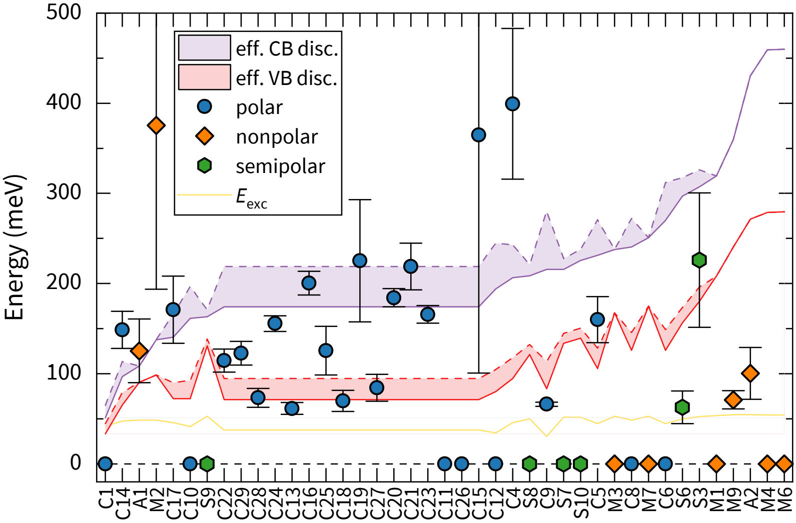

FIGURE 4.20: Experimentally determined high-temperature activation energies E_{HT}, determined from fits of the temperature-dependent radiative lifetimes for the polar, nonpolar, and semipolar QWs listed in Tab. 4.5, in comparison to calculated effective valence (VB) and conduction band (CB) discontinuities. The solid lines represent calculations with a background doping level of $N_{\mathrm{D}} = 1 \times 10^{16}/\mathrm{cm}^3$, while the dashed lines are obtained with a higher doping level of $5 \times 10^{18}/\mathrm{cm}^3$, corresponding to an n-doped GaN layer underneath the QW. Most activation energies fall in the range between the effective valence and conduction band discontinuities, while others are close to the exciton binding energy E_{exc}, or even equal zero.

as well, resulting in a similar temperature behavior as the proposed mechanism of thermal activation into the barrier material. The dissociation of excitons might be more significant for non- and semipolar structures. Additionally, higher quantized states might be available in the non- and semipolar QWs. Although those states are found at lower energetic differences as compared to the effective band discontinuities, the carriers in higher quantized states would also be lost for radiative recombination, as discussed in Sec. 4.4. Therefore, the effect would be comparable to the thermal activation of carriers into the barriers in *c*-plane structures.

The calculated energies vary depending on the presence of a doped layer ($N_{\mathrm{D}} = 5 \times 10^{18}/\mathrm{cm}^3$) underneath the QW, which effectively reduces the piezoelectric polarization field, and thereby increases the effective discontinuities. This effect increases the range spanned by the effective discontinuities and shows the sensitivity to the piezoelectric field. Additionally, the calculated transition energies, including the quantization, the exciton binding energy, and the redshift due to the QCSE, are larger than the experimentally observed QW emissions. On average, the calculated energies exceed the experimentally observed ones by 150 meV. This is not necessarily indicating the irreliability of the calculations, which are based on the input parameters like InN mole fraction and QW width. When the structural parameters are not available by XRD measurements, like for single-quantum wells, only nominal parameters can be used.

Furthermore, it remains unclear why the activation energies agree with the effective discontinuities of either the valence band, or the conduction band. From an energetic point of view, the effective valence band discontinuity, which is lower in energy for all cases, should be visible in the temperature dependence of the radiative lifetimes. Instead, roughly half of the structures show activation energies that match the effective conduction band discontinuity. Several possibilities might favor the suppression of one of the effective band discontinuities, depending on the type of minority charge carriers. In the case of an n-doped layer underneath the QW, additional electrons are present in the material. More specifically, those occupy states in the conduction band, while in the valence band only the optically excited holes are present. Therefore, sufficient electrons would be available for radiative recombination, even if thermal activation into the conduction band barrier occurs. In that case, the effective valence band discontinuity should be the dominant thermal activation energy, since holes are the minority charge carriers. Vice versa, the effective conduction band discontinuity should only be the dominant thermal activation energy, when electrons are the minority charge carriers. This is rather unlikely, since even nominally undoped GaN shows slight n-doping. Only for an acceptor niveau close to the valence band edge, as present in p-doped material, holes are expected to be the majority carrier species. Here, instead of an acceptor, typically Mg for III-nitrides, the use of hydrogen as carrier gas during the epitaxial growth could play a role. For quantum well structures that use hydrogen during the GaN growth, a clear redshift of the QW emission is observed, when compared to structures using nitrogen as carrier gas. The observed redshift is an indication that background charge carriers, i.e. electrons, are trapped. This is further emphasized by an increased radiative lifetimes in those structures, especially at low temperatures. Regarding the samples with the effective conduction band discontinuity as dominant activation energy, however, no relation to the use of hydrogen as carrier gas or the doping underneath the QW is observed. In the end, both effective discontinuities might be visible in the temperature dependence of the radiatve lifetimes. Nevertheless, the limited number of data points makes it difficult to derive the activation energies with better accuracy.

Furthermore, the optical excitation energy might have an influence. Depending on the energy of the laser pulses used for excitation, the charge carriers are provided with excess energy. This could make the transition into higher quantized states probable, and thereby distort the observed activation energies. On the contrary, the thermalization of charge carriers, i.e. the redistribution after optical excitation, takes place on a femtosecond time scale, while the recombination proceeds on a time scale of pico- to nanoseconds. Therefore, the charge carrier distribution can be assumed to be in quasi-thermal equilibrium during the recombination process. Nevertheless, further experiments employing different excitation wavelengths could help to exclude this possible contribution.

4.5.4 *Conclusion*

After all, the observed increase of radiative lifetimes with temperature is exceeding the linear behavior expected for charge carriers confined in a two dimensional QW. The comparison of experimentally determined activation energies and calculated values indicates that this super-linear rise towards room temperature is in fact related to the thermal activation of charge carriers into bulk-like states. These states are subject to low spatial confinement, and are extending into the barrier material over a range of several QW widths. Therefore, these states show low spatial overlap with the confined states in the quantum well itself.

It should be emphasized that the proposed thermal activation into the barriers, since related to the QW structure itself, represents an intrinsic process. Therefore, every quantum well structure is expected to show a super-linear increase of radiative lifetimes, which corresponds to an increasing loss of radiative emission. The fact that such a behavior is not observed in several structures, is likely caused by the limited temperature range ($T \leq 300\,\mathrm{K}$) that is accessible in the measurements. Since these structures show relatively high effective discontinuities in the calculations, the super-linear increase is probably visible only for much higher temperatures. This is in particular the case for non- and semipolar structures, which show higher band discontinuities due to the lowered or vanishing polarization fields.

In fact, the escape of charge carriers into the barriers is known as a thermally activated process that is usually accompanied by nonradiative recombination. This has been shown for III-arsenide, as well as III-nitride QW structures [155, 156]. Since for the recombination process, here via capture into a nonradiative recombination center, both, electron and hole, have to be thermally activated into a barrier state, the expected activation energy $E_{\mathrm{act}} = (E_{\mathrm{c,eff}} + E_{\mathrm{v,eff}})/2$ is given by the mean value of the effective valence and conduction band discontinuities. Although the present analysis focuses on the radiative lifetimes, the observation of a related activation energy for the nonradiative lifetimes would be an additional indicator to confirm the present results. This approach, however, might be complicated by the fact that for nonradiative recombination in III-nitride QWs activation energies in the range below 100 meV are found [120, 157, 158].

Further experiments, including structures that cover a broader range of InN mole fractions and QW widths, might be helpful to confirm the present results. The main sources of uncertainty in the present analysis are the structural parameters of the single quantum wells, which are inaccessible by XRD, as well as the limited temperature range that is covered in the measurements. Furthermore, several thermally activated processes could interfere with each other, like exciton dissociation or excitation into the barriers. Given the limited temperature range in the experiment, it is challenging to determine significant activation energies for these processes, especially since there is only a factor of two between the effective valence band discontinuities and the exciton binding energy in most of the polar structures. Although further experiments are needed to clarify some issues, the thermal activation of charge carriers into bulk-like states in the barrier material is a plausible mechanism to explain the observed super-linear rise of radiative lifetimes, and is supported by the analysis presented here.

Still, some structural key points can be deduced that make the thermal activation of charge carriers into the barrier less probable. First, a high InN mole fraction, as well as larger QW thicknesses would increase the effective band discontinuities. This approach, however, is not feasible due to the growing strain accumulation in the QW, which provokes relaxation, and due to the growing QCSE, which drastically reduces the overlap integral. The strain would be likewise problematic in GaInN/AlGaN QW structures, where the larger bandgap of AlGaN would increase the band discontinuities as well. Second, the use of non- and semipolar structures is preferable, since those showed higher activation energies, or even no super-linear increase at room temperature at all.

TABLE 4.5: Summary of QW structures analyzed for temperature-induced rise of radiative lifetimes, including polar c-plane (C), nonpolar m- and a-plane (M, A), as well as semipolar (S) structures. The table lists delocalization energies E_{loc} and high-temperature activation energies E_{HT} as fitting parameters, InN mole fractions (x_{In}) and QW widths (L_{QW}), as well as effective band discontinuities of the conduction ($\Delta E_{\mathrm{c,eff}}$) and valence band ($\Delta E_{\mathrm{c,eff}}$), together with exciton binding energies E_{exc} obtained by calculations [63] for an undoped QW structure. For most of the samples, the activation energies E_{HT} are in the range between $\Delta E_{\mathrm{c,eff}}$ and $\Delta E_{\mathrm{v,eff}}$.

Sample[d]	E_{loc} (meV)	E_{HT} (meV)	x_{In} (%) [a]	L_{QW} (nm) [a]	$\Delta E_{\mathrm{c,eff}}$ (meV)	$\Delta E_{\mathrm{v,eff}}$ (meV)	E_{exc} (meV)
C1 [b]	5.6 ± 0.5	0	10.8 ± 0.3	1.27 ± 0.07	51	33	41.8
C4 [b]	21 ± 2	399 ± 84	27.2 ± 3.2	1.43 ± 0.04	206	95	45.7
C5 [b]	10 ± 1	160 ± 26	27.9 ± 2.0	1.50 ± 0.03	231	105	44.5
C6 [b]	14 ± 2	0	32.2 ± 0.6	1.46 ± 0.11	270	126	44.5
C8 [b]	8 ± 3	0	31.7 ± 2.0	1.19 ± 0.07	241	126	48.4
C9 [b]	2.5 ± 0.8	66 ± 3	22.5 ± 5.0	2.7 ± 0.2	216	83	30.3
C10 [b]	2.7 ± 1.0	0	18.4 ± 0.6	1.74 ± 0.09	161	72	41.3
C11 [b]	0.5 ± 0.8	0	19.0 ± 0.8	2.07 ± 0.11	174	71	37.5
C12 [b]	3.1 ± 1.5	0	19.8 ± 2.0	2.3 ± 0.2	194	80	34.4
C13 [b]	5.1 ± 0.6	61 ± 7	19.0 ± 0.8	2.07 ± 0.11	174	71	37.5
C14 [b]	16 ± 9	149 ± 21	19.0 ± 0.8	1.03 ± 0.06	97	65	47.5
C15 [b]	7.2 ± 2.4	365 ± 265	19.0 ± 0.8	2.07 ± 0.11	174	71	37.5
C16 [b]	3.9 ± 1.4	200 ± 14	19.0 ± 0.8	2.07 ± 0.11	174	71	37.5
C17 [b]	31 ± 5	171 ± 38	19.0 ± 0.8	1.36 ± 0.07	141	72	45.7
C18 [b]	1.6 ± 0.9	70 ± 12	19.0 ± 0.8	2.07 ± 0.11	174	71	37.5

Sample[d]	E_{loc} (meV)	E_{HT} (meV)	x_{In} (%) [a]	L_{QW} (nm) [a]	$\Delta E_{\mathrm{c,eff}}$ (meV)	$\Delta E_{\mathrm{v,eff}}$ (meV)	E_{exc} (meV)
C19 [b]	2.1 ± 0.6	225 ± 68	19.0 ± 0.8	2.07 ± 0.11	174	71	37.5
C20 [b]	3.5 ± 0.5	184 ± 11	19.0 ± 0.8	2.07 ± 0.11	174	71	37.5
C21 [b]	6.2 ± 2.2	219 ± 265	19.0 ± 0.8	2.07 ± 0.11	174	71	37.5
C22	4.5 ± 0.5	115 ± 13	19.0 ± 0.8	2.07 ± 0.11	174	71	37.5
C23 [b]	4.7 ± 0.7	166 ± 10	19.0 ± 0.8	2.07 ± 0.11	174	71	37.5
C24 [b]	4.8 ± 0.7	156 ± 9	19.0 ± 0.8	2.07 ± 0.11	174	71	37.5
C25	0.0 ± 0.7	125 ± 28	19.0 ± 0.8	2.07 ± 0.11	174	71	37.5
C26	3.4 ± 0.9	0	19.0 ± 0.8	2.07 ± 0.11	174	71	37.5
C27	2.4 ± 1.5	84 ± 15	19.0 ± 0.8	2.07 ± 0.11	174	71	37.5
C28	4.6 ± 2.3	73 ± 11	19.0 ± 0.8	2.07 ± 0.11	174	71	37.5
C29	3.9 ± 1.4	123 ± 14	19.0 ± 0.8	2.07 ± 0.11	174	71	37.5
M1 [b]	52 ± 12	0	28.3 ± 0.8	1.51 ± 0.08	319	208	53.5
M2 [b]	12 ± 149	375 ± 182	13.5 ± 0.7	1.62 ± 0.09	138	99	48.5
M3 [b]	43 ± 8	0	23.5 ± 1.0	1.40 ± 0.07	238	167	52.7
M4 [b]	18 ± 3	0	37.8 ± 0.9	1.67 ± 0.04	459	279	54.2
M6	36 ± 10	0	38.0 ± 1.1	1.60 ± 0.11	460	280	54.2
M7	23 ± 8	0	24.5 ± 1.1	1.43 ± 0.09	251	175	52.9
M9	3.7 ± 4.0	71 ± 11	34.0 ± 0.7	1.35 ± 0.03	360	241	54.7
A1 [c]	11 ± 4	125 ± 36	14.1 ± 0.8	1.25 ± 0.07	109	90	48.4

Sample[d]	E_{loc} (meV)	E_{HT} (meV)	x_{In} (%) [a]	L_{QW} (nm) [a]	$\Delta E_{\mathrm{c,eff}}$ (meV)	$\Delta E_{\mathrm{v,eff}}$ (meV)	E_{exc} (meV)
A2 [b]	15 ± 3	100 ± 29	37.6 ± 3.0	1.56 ± 0.08	430	271	54.7
S3	20 ± 6	226 ± 75	37.1 ± 1.1	1.46 ± 0.06	307	180	52.5
S6 [b]	4.1 ± 1.4	63 ± 19	26.8 ± 3.1	1.9 ± 1.1	297	157	49.8
S7 [c]	11 ± 4	0	22.4 ± 2.0	1.50 ± 0.08	216	134	51.6
S8 [c]	22 ± 4	0	18.8 ± 2.0	1.72 ± 0.09	209	121	50.0
S9 [c]	27 ± 13	0	26.4 ± 0.5	1.02 ± 0.03	163	131	52.6
S10 [b]	49 ± 17	0	23.5 ± 2.0	1.47 ± 0.08	225	139	51.8

[a] Ref. [97] [b] Ref. [101] [c] Ref. [102]

[d] Ref. for sample preparation given in Appendix A

4.6 SUMMARY OF RESULTS ON RADIATIVE RECOMBINATION

In this chapter, the radiative lifetimes at room temperature in polar c-plane and nonpolar m-plane quantum wells are compared. The observed difference of up to one order of magnitude can be explained by a combination of several intrinsic effects. On the one hand, the vanishing QCSE results in higher wave function overlap and increased exciton binding energy. On the other hand, anisotropic in-plane strain reduces the crystal symmetry and changes the valence band dispersion in the different in-plane directions. Thus, the effective hole masses are reduced, which has a beneficial effect on the radiative emission. The joint effect of these three factors explains the significantly shorter radiative lifetimes observed for m-plane QWs.

These results show that the anisotropic strain in such *pseudomorphic* nonpolar QWs has a severe impact on the radiative recombination. As a next step, the strain in the QW can be manipulated by inserting an additional AlInN buffer layer. Lattice-matched to the in-plane c-direction of GaN, it relaxes to larger lattice constants, and provides a template with reduced lattice mismatch for the subsequent QW structure. In these *pseudomorphic* structures, the radiative room temperature lifetimes are found to be higher compared to the metamorphic ones. Using the strain coefficients, obtained by XRD measurements, makes it possible to derive the valence band dispersion by $\mathbf{k} \cdot \mathbf{p}$ calculations, and effective masses can be extracted by parabola fits. Apparently, the valence band dispersion is nearly isotropic in the metamorphic structures, since the reduced strain state of the QW recovers the crystal symmetry to a large extent. Furthermore, a decreased energy splitting to the second valence band is observed, which makes its thermal population possible. Therefore, the carrier dynamics can be described by an effective density of states hole mass, which increases due to the contribution of the second valence band. After all, effective masses around 1.5-1.6 m_0 are found for the metamorphic m-plane structures, simply due to the strain manipulation by the AlInN buffer layer. In summary, these structures behave comparable to conventional c-plane QWs, not only in terms of valence band dispersion, but also regarding the radiative recombination in total, as they show longer radiative lifetimes at room temperature. Still, the higher wave function overlap and exciton binding energy lead to an increase in the radiative rate for the nonpolar structures, even in the metamorphic samples, where the AlInN buffer layer reduces the anisotropic in-plane strain.

In further experiments, the well width dependence of the radiative lifetime in nonpolar QWs is analyzed. Since the QCSE is not reducing the oscillator strength for larger QW widths, literature reports on thicker QWs compared to polar orientations are common. Although in such wide QWs, higher quantized states become available, and can be thermally populated by charge carriers, the applicable selection rules reduce the possible radiative transitions to states with $\Delta n = 0$. Furthermore, the large difference in effective electron and hole mass results in the situation that only higher valence band states are within the range of thermal population for holes, while only the lowest conduction band state is populated with electrons. As a result, only the transition from the first conduction band state to the first valence band state can contribute to the radiative emission. Charge carriers in other states are lost for radiative recombination. Therefore, an increasing radiative lifetime is expected for wide nonpolar QWs, which is in fact confirmed experimentally. The measured radiative lifetimes show a rise with temperature and well width, and their behavior can be described by a model based on the above assumptions. The effect is expected to become stronger with increasing temperature, well width, and also InN mole fraction. Therefore, even in nonpolar QWs, well widths around 1.5-3 nm should be preferred. These results emphasize that the radiative recombination is dominated by the physical properties of the quantum well. In particular, this includes the valence band structure, which is not only affected by QW composition and width, but especially by strain and its anisotropy.

In addition to these findings, the band structure, in particular the band discontinuities, can be related to an unexpected temperature dependence of radiative lifetimes close to room temperature. Although for charge carriers in a two-dimensional structure, the radiative lifetime should rise linearly with temperature, a steep rise is observed for the majority of investigated samples. This behavior is indicative of thermal activation of charge carriers, and in fact, characteristic activation energies between 60 and 400 meV can be fitted to the temperature-dependent radiative lifetimes. For some of the analyzed structures, this is indeed close to the exciton binding energy, which is at maximum 55 meV for nonpolar QWs. For the majority of structures, however, the experimentally determined activation energies are within the range of the effective discontinuities of valence and conduction band. Those effective discontinuities mark the energetic difference between the first quantized state in the QW, and the band edge of the GaN barrier. Therefore, the thermal activation of charge carriers into bulk-like states in the barrier material is likely the reason for the super-linear rise of radiative lifetimes with temperature. Although the limited temperature range that is available in the experiment complicates the exact determination of activation energies, the effect is observed for nearly all polar, nonpolar, and semipolar quantum well structures. This emphasizes the fact that the temperature dependence is caused by an intrinsic property of the QW structures, either due to the limited confinement, or exciton binding. Additionally, it supports the findings of the analysis of wide nonpolar quantum wells, where also a lowered radiative emission is observed due to the thermal excitation of charge carriers.

In summary, these results show the sensitivity of radiative recombination on the quantum well properties. Those are governed by the valence band dispersion, which is severely affected by strain, the built-in polarization fields, and the carrier confinement in the quantum well. Only by regarding every single of those contributions, the behavior of the radiative lifetime can be described properly.

5

NONRADIATIVE RECOMBINATION IN QUANTUM WELLS WITH METAMORPHIC BUFFER LAYERS

While GaInN-based devices reach high efficiencies in the violet and blue spectral region, the efficiency is drastically reduced at higher emission wavelengths. This phenomenon is referred to as the "green gap", and this chapter discusses its possible origins and presents an approach to overcome these fundamental limitations. For this purpose, semipolar crystal orientations and strain-reducing buffer layers are used. Finally, these results allow insights into the origin of nonradiative recombination in the quantum well structures.

5.1 ADVANTAGES OF SEMIPOLAR ORIENTATIONS

As mentioned in the beginning, optoelectronic devices based on GaInN quantum wells can reach exceptionally high efficiencies in the blue and violet spectral region. In order to achieve light emission at longer wavelengths, high InN mole fractions are required, which goes along with a drastic reduction of the device efficiency. The drastic reduction in efficiency, when moving from violet-emitting quantum wells to the green spectral region and beyond, is referred to as the *green gap* [2, 10].

Several factors contribute to this phenomenon. Regarding the radiative recombination processes in III-nitride quantum wells, the built-in polarization fields on c-plane structures and the resulting quantum-confined Stark effect (QCSE) reduce the wave function overlap, and thus the radiative rate. For GaInN/GaN quantum wells, this effect becomes more prominent at higher InN mole fractions that are needed to push the emission wavelength to the green and beyond. Therefore, high InN mole fractions and the resulting polarization fields are partly responsible for the *green gap*, although the QCSE is small for thin quantum wells. These disadvantages of c-plane quantum wells can be overcome by choosing nonpolar orientations for the quantum well growth, as already discussed in Sec. 2.1.3, and Ch. 4. Besides the reduced radiative recombination, also an increasing nonradiative recombination is observed for GaInN/GaN quantum wells with high InN mole fractions. For polar orientations, Langer et al. found that the increasing strain that is accumulating in the quantum wells is a key factor to understand the *green gap* [9], as summarized below in Sec. 5.2.

In this context, also semipolar-oriented quantum wells have several advantages. Although the polarization fields vanish only for nonpolar orientations, a considerable reduction is observed for the common low-indices semipolar planes like $(11\bar{2}2)$ (see Fig. 1.8), or also $(20\bar{2}1)$. In terms of nonradiative recombination, non- and semipolar structures were reported to perform comparable, or even better, compared with c-plane structures for InN mole fractions higher than 25% [120]. In particular, rather constant nonradiative lifetimes were observed for the non- and semipolar structures (around 100-300 ps), whereas the c-plane structures showed a sharp decrease towards higher InN mole fractions. For quantum wells with lower indium contents, the polar structures still show considerably longer nonradiative lifetimes, which leaves the semipolar orientations as promising candidates for emission in the green and beyond.

Another advantage of semipolar over nonpolar (a-/m-plane) growth orientations is the availability of growth templates. In order to produce inexpensive templates, groove-like structures are etched in sapphire, which is subsequently overgrown with GaN that forms a closed semipolar surface. This technique of structured and overgrown templates is used quite often nowadays, and the somewhat poorer quality, especially in terms of threading dislocation density, is well compensated by the price. The use of semipolar templates becomes even more advantageous in combination with AlInN buffer layers that are used for intentional relaxation in the crystal lattice, as described below in Section 5.3.2.

5.2 STRAIN-INDUCED DEFECT FORMATION

Langer et al. [9] found that the strain accumulated in an epitaxially grown GaInN/GaN quantum well is the dominant source of nonradiative recombination in the analyzed polar (c-plane) quantum well structures. Motivated by the fact that the nonradiative recombination increased with higher InN mole fraction in the quantum well, they combined structural characterization by XRD, and optical characterization by time-resolved photoluminescence spectroscopy. As an outcome, the nonradiative lifetimes showed an exponential dependence on the strain energy density u,

$$\tau_{\mathrm{nr}} \propto \exp\left(-\frac{u}{k_{\mathrm{B}} T_{\mathrm{growth}}}\right), \tag{5.1}$$

where u was derived from XRD measurements by

$$u = \frac{1}{2} \sum_{i=x,y,z} \sigma_{\mathrm{ii}}\, \varepsilon_{\mathrm{ii}}, \tag{5.2}$$

with ε being the strain and σ being the stress tensor. T_{growth} denotes the QW growth temperature, and k_{B} is Boltzmann's constant. The exponential dependence of the nonradiative lifetimes τ_{nr} on the strain energy density u was explained by a model, where the accumulated strain is reduced by the formation of defects that act as nonradiative recombination centers. Although the formation of defects should result in a partial relaxation of the strained layer, no evidence for relaxation of the quantum wells was found in the X-ray data. Therefore, Langer et al. explained their observations by a model, where the crystal lattice experiences full relaxation only at strongly localized defects. In this limiting case, only a small volume fraction of the layer is effectively relaxed, and a fully strained, or *pseudomorphic*, layer is still observed in x-ray diffraction. The defects formed during relaxation, however, can still act as nonradiative recombination centers.

Additionally, the influence of different substrates was investigated. The structures prepared on bulk GaN and on sapphire performed comparable in their investigations. Thus, not threading dislocations originating from the substrate, but the defects formed during strain relaxation were the dominant source of nonradiative recombination in the investigated structures.

From these results, Langer et al. concluded that the defect formation is induced by strain and takes place in the quantum wells itself. They assumed that basal stacking faults and the related stacking mismatch boundaries that run through the quantum well in c-direction are formed, as those defect types were observed by electron microscopy in similar structures[159–162]. Furthermore, the results indicated that defects were generated in the bottommost quantum well and penetrated the subsequently grown layers, since single and multi-quantum well structures showed comparable nonradiative lifetimes. Further details on the analysis can be found in Ref. [9].

Whether the nonradiative recombination in other than c-plane oriented quantum well structures is driven by strain-induced defect formation in a similar way, will be investigated in the following, see Section 5.4.

5.3 STRAIN-REDUCING BUFFER LAYERS

As discussed in the section above, the accumulated strain in GaInN/GaN quantum well structures can be a major factor for the generation of defects and nonradiative recombination centers. The strain, caused by the large lattice mismatch between GaN substrate and GaInN quantum well, becomes larger with increasing InN mole fraction. In order to reduce the nonradiative recombination in structures emitting in the green spectral region and beyond, a strain management in the quantum well stack becomes inevitable. As discussed in Sec. 4.3, the use of buffer layers provides the possibility to reduce the strain in the QW region. Besides AlInN, which can be grown lattice-matched to GaN, also GaInN is an option.

5.3.1 *GaInN buffer layers*

The choice of GaInN as buffer layer material for a GaInN/GaN quantum well structure has obvious advantages. Given sufficient thickness, the buffer layer would be fully relaxed to provide a growth template with reduced lattice mismatch to the following quantum well. Several attempts have proven this approach to work, especially on semipolar growth orientations [163–165]. With this approach, however, the InN mole fraction in the buffer layer is limited by the quantum well composition. When the compositions of both layers are approaching, not only the carrier confinement in the quantum well is reduced, but also reabsorption of the emitted light becomes stronger. Furthermore, the surface quality usually degrades when growing thick layers of GaInN instead of GaN. This limits the InN mole fraction in the buffer layer and the possible reduction of the lattice mismatch.

5.3.2 *AlInN buffer layers*

Compared to GaInN, AlInN has some unique properties that make it preferable as buffer layer material, as already mentioned in Sec. 4.3. Besides the high refractive index, especially the possibility to grow AlInN lattice-matched to GaN is advantageous. Furthermore, the composition splitting, which is a problem of AlInN grown on the polar c-plane, is not observed in semipolar crystal orientations, where layer thicknesses of several hundred nanometers can be grown without considerable surface deterioration. Like in the case of the nonpolar m-plane, the different a/c ratio of the binary III-N compounds make lattice matching possible only in one in-plane direction. Taking the $(11\bar{2}2)$ orientation, the two in-plane directions are $[1\bar{1}00]$ (m-direction) and $[11\bar{2}\bar{3}]$ (c'-direction). There, AlInN can be grown lattice-matched to the c'-direction at 25.8% InN mole fraction, leaving it compressively strained ($\approx -1.04\%$) in the m-direction. As found by Buß et al., AlInN grown lattice-matched along the c'-direction of GaN is forced to relax to larger m lattice parameters with increasing layer thickness [132, 166]. Thereby, the AlInN buffer layer in fact reduces the lattice mismatch to the following GaInN QW structure. Opposed to that, choosing lattice-matching along m would induce relaxation to smaller c' lattice parameters due to the tensile strain ($\approx +1.03\%$), which would result in an even larger lattice mismatch between the AlInN buffer layer and the GaInN-based MQW.

This shows that AlInN buffer layers can be successfully used for strain reduction. In the context of possible nonradiative recombination, however, also the type of defects that induce the relaxation and their formation mechanism are of interest. This can be illustrated for a c-plane quantum well structure, where the in-plane strain is distributed isotropically, and no shear stress is present. Thus, the only possibility for the crystal lattice to relax is the formation of dislocations perpendicular to the c-plane. When formed in the underlying buffer layer, these threading dislocations can penetrate through the subsequent quantum well structure and act as nonradiative recombination centers.

For semipolar orientations, the anisotropic in-plane strain allows for shear stress. Thus, the relaxation via formation of in-plane dislocations is possible, since gliding and slip of already existing threading dislocations can take place. This was shown for the case of heteroepitaxial layers on semipolar GaN, and should apply for AlInN as well [27, 36, 167, 168]. Therefore, the kinking of existing threading dislocations at the lower buffer layer interface would be the preferred relaxation mechanism. These dislocations should remain in the growth plane, which makes relaxation, and thereby the reduction of strain in the quantum wells possible.

5.4 SEMIPOLAR QUANTUM WELLS WITH STRAIN-REDUCING BUFFER LAYERS

As described above, the use of partially relaxed AlInN buffer layers is a promising approach to reduce the strain state and the nonradiative recombination in semipolar GaInN/GaN quantum wells, even at high InN mole fractions. In the following, the preparation, as well as the structural and optical characterization of dedicated multi-quantum well structures is described in detail. After this analysis, the strain-related nonradiative recombination in the quantum wells is discussed, together with the implications for defect formation on semipolar growth orientations.

5.4.1 *Preparation and structural characterization*

Five samples in $(11\bar{2}2)$ orientation are prepared on different substrate types [91]. For samples S1-S4, semipolar GaN templates are used, where patterned r-plane sapphire is overgrown with GaN by MOVPE and polished to get a semipolar surface for epitaxial growth. As a consequence of the structuring process, grooves with a width of 10 µm are etched into the sapphire surface. During the overgrowth with GaN, coalescence regions are formed along the grooves, where threading dislocations are accumulating. This causes periodic stripes with a high threading dislocation density on the semipolar GaN surface. These semipolar GaN templates are kindly provided by the CRHEA institute,[1] and the details of template preparation are reported in Refs. [169] and [170]. Contrary, sample S5 is grown on pseudo-bulk GaN.

---

[1] Centre de Recherche sur l'Hétéro-Epitaxie et ses Applications (CNRS-CRHEA) in Valbonne, France

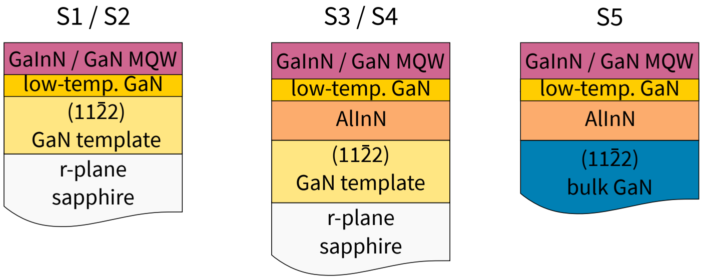

FIGURE 5.1: Schemes of the samples without (S1/S2), and with AlInN (S3/S4/S5). While sample S5 is grown on bulk GaN, while a sapphire template is used for the other structures.

All structural details can be found in Fig. 5.1 and Tab. 5.1. On the substrate or template, epitaxial GaN is grown at the beginning, followed by an underlayer of low-temperature GaN (≈ 20 nm), and the five-fold GaInN/GaN multi-quantum well structure. High-resolution x-ray diffraction (XRD) is used for the structural characterization of all samples. According to the XRD analysis, the quantum wells in samples S1, S3, and S5 have 35-37% InN mole fraction (740 °C growth temperature), as opposed to the samples S2 and S4, for which 27-29% InN mole fraction (770 °C growth temperature) are found. The barrier widths of approximately 8 nm are comparable for all samples, while the quantum well widths are similar in the range of 1.2 to 1.56 nm.

For samples S3-S5, an additional AlInN buffer layer is inserted before the MQW, more precisely between the epitaxial GaN and the low-temperature GaN underlayer. The AlInN growth takes place at 820 °C for 100-200 min, corresponding to 250-500 nm of layer thickness. Additionally, the intended InN mole fraction of approximately 26 % is confirmed by the XRD analysis.

To investigate the relaxation behavior of the AlInN buffer layer, and the strain state of the quantum wells, a more detailed XRD analysis of sample S4 with reciprocal space maps (RSMs) is shown in Fig. 5.2. In the RSMs of the $02\bar{2}2$ and 0006 reflections, besides the peak of the GaN substrate or template, also the AlInN peaks, and the MQW superlattice (SL) peaks can be found. While the $02\bar{2}2$ reflection, which is equivalent to $20\bar{2}2$, gives information about the m-direction $[1\bar{1}00]$, the 0006 reflection represents information about the c- or c'-direction. Both RSMs show the GaN and AlInN reflections aligned along the in-plane direction $q_{\parallel}$, and no evidence for phase separation in the AlInN is found. This proves coherently strained growth of the AlInN on the GaN template, and shows that the intended lattice-matching along the c'-direction is achieved. Contrary, an asymmetrical AlInN peak in the $02\bar{2}2$ RSM

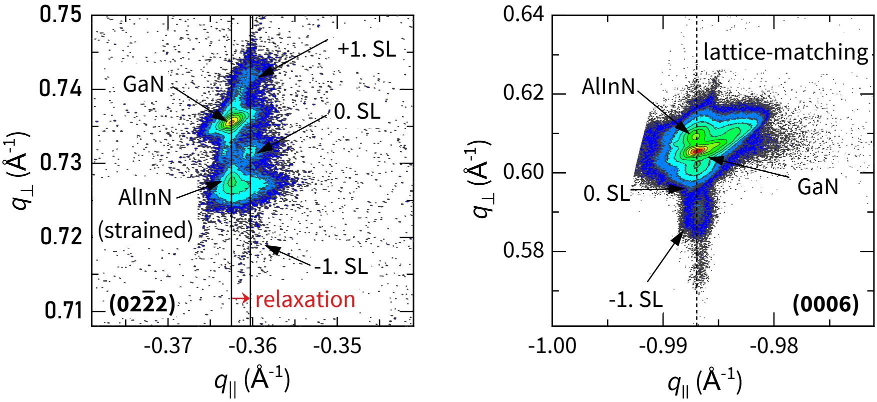

FIGURE 5.2: Reciprocal space maps (sample S4) of the (02$\bar{2}$2) reflex showing strained AlInN growth and subsequent relaxation along m, and the (0006) reflex showing lattice matching in the c-direction [97].

indicates relaxation towards larger lattice parameters in m-direction, which confirms the observations made in earlier work by Buß et al. [132, 166]. Thus, the right-hand part of the AlInN peak can be related to the partially relaxed part at the top of the buffer layer. Aligned with this relaxed part along the in-plane direction are the MQW SL peaks, which indicates pseudomorphic growth of the QWs on the partially relaxed AlInN. The AlInN peak in the 0006 RSM, however, shows no asymmetry, proving lattice-matching in c'-direction of GaN, which is conserved during buffer layer growth. Although not shown here, similar RSMs are obtained for the unbuffered samples S1/S2, where pseudomorphic growth of the MQW on the GaN templates can be observed. Summarizing, pseudomorphic growth can be assumed at the interfaces between MQWs and AlInN or GaN, as well as at the interface between GaN and AlInN itself.

Next, the relaxation behavior of the AlInN buffer layer is of interest, especially the degree of relaxation at the top interface to the MQW. To measure the AlInN relaxation state at the interface to the MQW, the the (1$\bar{1}$00) in-plane lattice parameters are obtained from 2θ scans in grazing incidence geometry, as shown for samples S1, S3, and S5 in Fig. 5.3. Without grazing incidence scans, no information about the interface between AlInN and MQW could be obtained, since the conventional scan would illuminate a large sample volume to obtain an average of the lattice parameters. Contrary, the grazing-incidence scan is sensitive to some tens of nanometers beneath the sample surface only, and the derived lattice parameters correspond to the top layers of the MQW structure. In sample S1, the uppermost layers in the MQW show

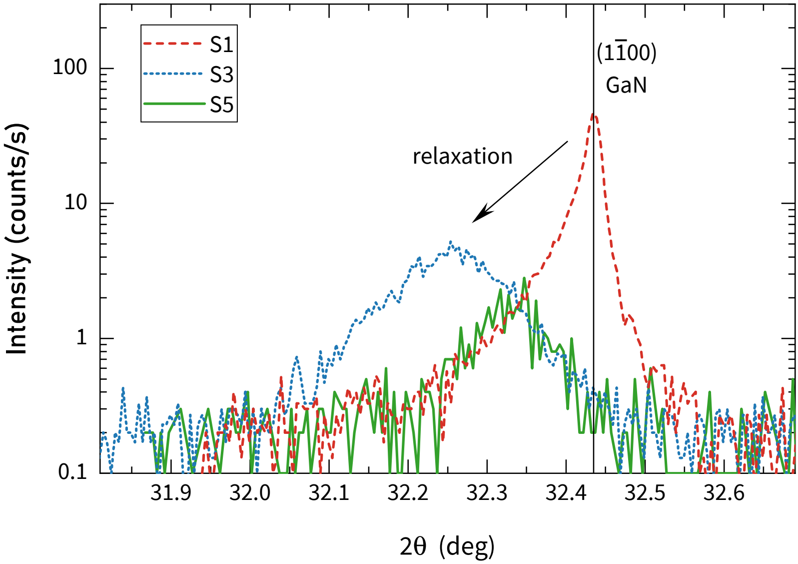

FIGURE 5.3: XRD 2θ scans in grazing-incidence geometry of the in-plane $(1\bar{1}00)$ reflex show the lattice parameter of free-standing GaN for the sample S1 (proving pseudomorphic growth on the template without buffer layer) and increasing relaxation to larger in-plane lattice parameters for the samples S3 and S5 with an additional AlInN buffer layer [97].

the same lattice parameters as free-standing GaN, indicating that the MQW is grown pseudomorphically on the GaN template without relaxation. On closer examination, a shoulder appears at lower diffraction angles, or larger lattice parameters, which might be an indication for starting relaxation.

Contrary, for samples S3 and S5, larger in-plane lattice parameters are found, which can be attributed to the partially relaxed AlInN buffer layer. Assuming that MQW and AlInN buffer have equal in-plane lattice parameters at the interface, the buffer layers show $(51 \pm 5)\,\%$ (sample S3) and $(15 \pm 5)\,\%$ (sample S5) relaxation in m-direction. Here, the degree of relaxation is calculated according to $(1 - m_{\mathrm{GaN}}/m_{\mathrm{AlInN}})$, where m_{GaN} and m_{AlInN} are the experimentally determined lattice parameters of the substrate and buffer layer, respectively. The different degree of relaxation for both samples can be explained by the larger layer thickness in sample S3 (≈ 500 nm) compared to sample S5 (≈ 250 nm). As expected, for sample S2 (not shown) the same in-plane lattice parameter as for sample S1 is obtained, while for the AlInN layer in sample S4 (not shown) $(49 \pm 5)\,\%$ relaxation are found, close to that of sample S3.

TABLE 5.1: Basic information on the investigated samples, listing the growth time of the AlInN buffer layer (t_{buffer}), its approximate thickness (L_{buffer}) and degree of relaxation in m-direction ($R_{\mathrm{m,buffer}}$), the InN mole fraction of the AlInN (y_{buffer}) and of the MQW (x_{QW}), the QW width (L_{QW}), the emission wavelength at 300 K ($\lambda_{300\mathrm{K}}$), and the effective lifetimes at 5 K ($\tau_{5\mathrm{K}}$) and 300 K ($\tau_{300\mathrm{K}}$), as well as the radiative lifetimes at 300 K ($\tau_{\mathrm{r,300K}}$). The barrier width is approximately 8 nm for all the samples.

Sample[b]	S1	S2	S3	S4	S5
t_{buffer} (min)	–	–	200	200	100
L_{buffer} (nm)	–	–	≈500	≈500	≈250
$R_{\mathrm{m,buffer}}$ (%) [a]	–	–	51 ± 5	49 ± 5	15 ± 5
y_{buffer} (%) [a]	–	–	25.7 ± 0.4	26.9 ± 0.6	26.5 ± 0.3
L_{QW} (nm) [a]	1.56 ± 0.06	1.2 ± 0.1	1.46 ± 0.06	1.4 ± 0.1	1.48 ± 0.05
x_{QW} (%) [a]	36 ± 1	29 ± 1	37.1 ± 1.1	27 ± 1	36 ± 1
$\lambda_{300\mathrm{K}}$ (nm)	536	492	576	497	543
$\tau_{5\mathrm{K}}$ (ps)	108 ± 2	61 ± 2	168 ± 4	133 ± 2	191 ± 2
$\tau_{300\mathrm{K}}$ (ps)	34 ± 2	45 ± 2	74 ± 2	81 ± 2	66 ± 3
$\tau_{\mathrm{r,300K}}$ (ps)	2240 ± 450	313 ± 65	1600 ± 250	410 ± 70	1720 ± 500

[a] Ref. [97] [b] Ref. [91]

More information can be found in Refs. [132] and [166], where the relaxation of AlInN layers grown under identical conditions is investigated, and the structural characterization of the AlInN layers is described in more detail. Although there, the relaxation increases with layer thickness as well, the absolute degree of relaxation is found to be higher and reaches nearly 100 %. Summarized, the structural characterization shows that the AlInN buffer layer reduces the lattice mismatch for the GaInN QWs as intended.

5.4.2 *Optical properties and recombination dynamics*

After investigating the structural properties and the relaxation behavior of the AlInN buffer layer, next its influence on the optical properties and the recombination dynamics is analyzed. Fig. 5.4 shows room temperature PL spectra of all samples, with rather large full widths at half maximum of 150-200 meV.

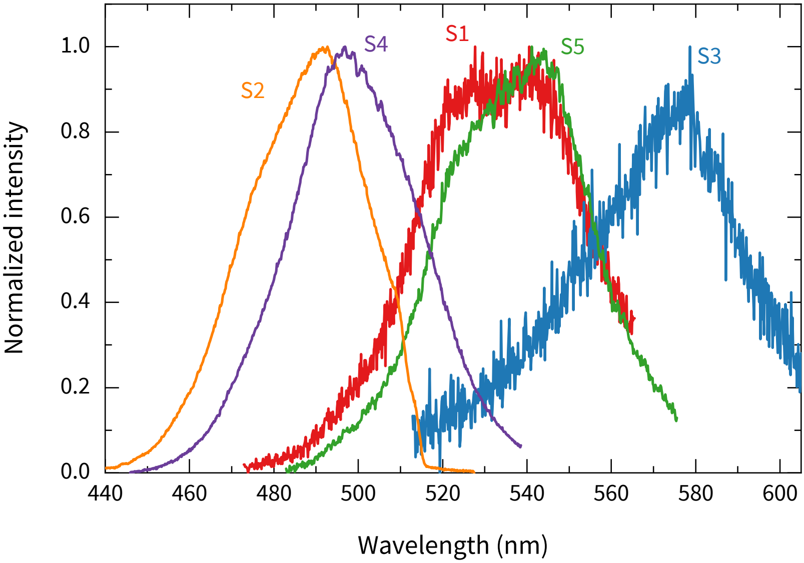

Figure 5.4: Spectra obtained at room temperature of samples S1-S5, where the peak wavelength scales approximately with the InN mole fraction found by XRD, see Tab. 5.1.

As discussed above, the semipolar templates used for samples S1-S4 exhibit defect-rich trenches that are formed during the epitaxial overgrowth with GaN. The influence of these defect-rich regions on the overall optical properties and recombination dynamics needs to be clarified in the first place. For this purpose, the sample surface is scanned perpendicular to the defect-rich trenches in steps of 1 µm, and with a spot size of the exciting laser of approximately 2 µm, in a confocal geometry with a mirror objective. The small focal size and narrow step width ensure that differences between the regions of different threading dislocation density can be resolved, since the trenches have a periodicity of 10 µm. The scan result is shown in Fig. 5.5. While the measured intensity varies within a 10 % range, the effective lifetimes stay constant and prove that the overall recombination dynamics are not influenced by the presence of defect-rich regions. The slight intensity fluctuations could be explained by variations in the carrier density induced by the presence of dislocations, or simply by a change in the outcoupling of the emitted light. The actual temperature-dependent lifetime measurements are carried out with laser spot sizes beyond 10 µm, in order to average over a larger area on the sample surface, and to avoid stability issues.

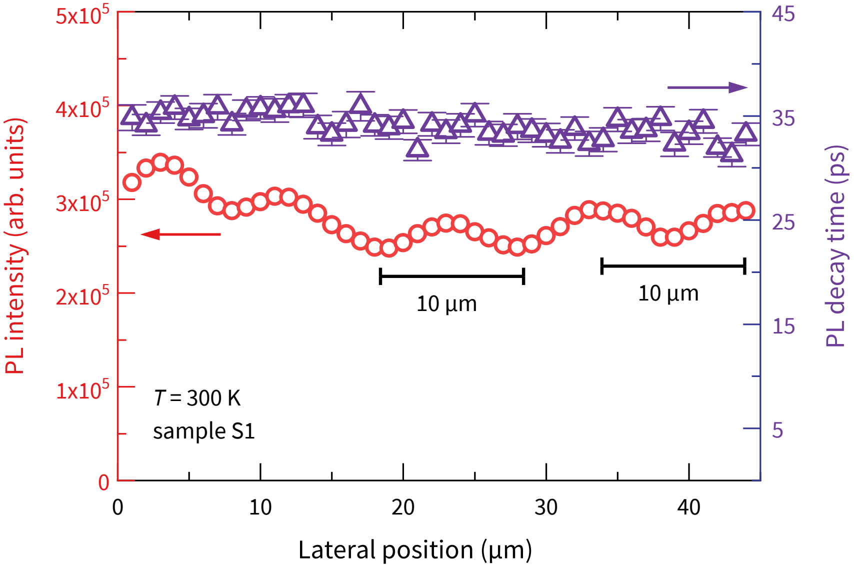

FIGURE 5.5: Room temperature line scan perpendicular to the defect-rich trenches, using a focal size of ≈ 2 µm. The PL intensities show slight variations of ±10 % with the same 10 µm periodicity as the grooves from the substrate preparation. Contrary, the effective lifetimes remain constant, showing that the recombination dynamics are unaffected by the presence of defect-rich regions on the sample.

For sample S3, a measurement of the temperature-dependent lifetimes is shown in Fig. 5.6, which is exemplary for the other samples as well. At low temperatures, purely radiative recombination is assumed, while the lifetimes at room temperature (300 K) are clearly dominated by nonradiative recombination. As discussed before in Ch. 4, the localization of charge carriers at low temperatures at potential minima is possible. These potential minima can originate from fluctuations in QW width or composition [110–119]. The constant low-temperature radiative lifetimes indicate localized charge carriers, since the radiative lifetimes scales with temperature and dimensionality of the recombining carriers according to $\tau_r \propto T^{d/2}$ [74]. Nevertheless, the charge carriers have to be considered free in two dimensions at elevated temperatures, since the radiative lifetime shows a nearly linear rise with temperature. The lifetime measurements show a comparable behavior for the other samples. Tab. 5.1 shows the absolute lifetime values at 5 K and 300 K. At 300 K, and for a comparable InN mole fraction, no significant differences in radiative lifetimes are found for the

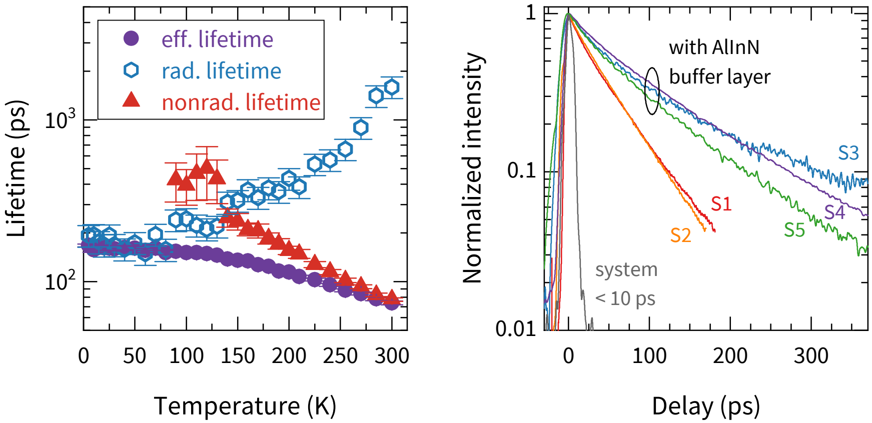

FIGURE 5.6: Temperature-dependence of the effective, radiative and nonradiative lifetimes for sample S3, where the nonradiative recombination is dominant at 300 K, and transients at 300 K, where the samples without a buffer layer (S1, S2) show a faster decay than the samples with a partially relaxed buffer layer (S3-S5), indicating a significant reduction of the nonradiative recombination.

samples. Thus, possible strain-induced changes of the valence band structure do not affect the radiative recombination.

As a major point of the analysis, the impact of an AlInN buffer layer on the nonradiative recombination properties is investigated. For this purpose, the effective lifetimes at 300 K are considered, where the recombination is dominated nonradiatively for all samples. By using a low temperature normalization to derive the absolute values of radiative and nonradiative lifetimes, purely radiative recombination at low temperatures is assumed. Especially for sample S2 that shows a lower effective lifetime at 5 K compared to the other samples, it cannot be ruled out that there is remaining nonradiative recombination, even at low temperatures. The measured effective lifetimes at 300 K, however, are unaffected by this possible source of uncertainty, and are still a reliable measure for the nonradiative recombination.

For a qualitative comparison, the normalized transients at 300 K are shown in Fig. 5.6. Most notably, the samples without a buffer layer (S1, S2) show a faster nonradiative decay than the samples with an AlInN buffer layer (S3, S4, S5), which can be confirmed by the fitted effective lifetime values. While all samples with an additional AlInN buffer layer show effective lifetimes between 66 ps (S5) and 81 ps (S4), the unbuffered samples remain at significantly lower values of 34 ps (S1) and 45 ps (S2). As described above, the effective lifetimes at room temperature reflect the amount of nonradiative recombination in the structures. Therefore, the longer lifetimes prove a

TABLE 5.2: Results of the Arrhenius-type fits according to Eq. 5.3 for samples S1, S3, and S5, listing the prefactor γ_{nr} related to the density of nonradiative centers, i.e. defects in the QW, the characteristic activation energy E_{act} for the nonradiative recombination process, and the parameter $1/\tau_{\mathrm{nr},0}$ related to remaining nonradiative recombination at low temperatures.

Sample[a]	γ_{nr} (1/(ns K))	E_{act} (meV)	$\frac{1}{\tau_{\mathrm{nr},0}}$ (1/ns)
S1	0.7 ± 0.2	46 ± 5	4.0 ± 0.4
S3	0.10 ± 0.01	25 ± 4	1.7 ± 0.4
S5	0.08 ± 0.03	29 ± 7	4.1 ± 0.3

[a] Ref. [91]

reduced nonradiative recombination rate in structures with a partially relaxed AlInN buffer layer. For samples with a comparable QW composition, the nonradiative rate is approximately reduced by a factor of two, as can be seen from the ratio of effective lifetimes. Furthermore, the buffer layer's degree of relaxation affects the the nonradiative recombination, since the samples S3 and S5 (≈ 50% relaxation) show lifetimes of 74 ps and 81 ps, which is longer than sample S5 (15% relaxation) with only 66 ps.

To analyze the reduced nonradiative recombination on a quantitative base, an Arrhenius plot (Fig. 5.7) of the nonradiative lifetimes of samples S1, S3 and S5 is used. According to Eq. 2.27, the thermally activated nonradiative recombination is described by

$$\frac{1}{\tau_{\mathrm{nr}}} = \gamma_{\mathrm{nr}}(T)\ \exp\left(-\frac{E_{\mathrm{act}}}{k_{\mathrm{B}}T}\right) + \frac{1}{\tau_{\mathrm{nr},0}}\,, \tag{5.3}$$

where k_{B} is Boltzmann's constant, and E_{act} is the characteristic activation energy of the nonradiative process. The prefactor $\gamma_{\mathrm{nr}}(T)$ scales with the density of nonradiative centers, and is assumed to depend linearly on temperature, according to the effective density of states. The actual temperature dependence may, however, change depending on the charge state of the nonradiative center [88]. The temperature-independent contribution $1/\tau_{\mathrm{nr},0}$ accounts for possible remaining nonradiative recombination at low temperatures due to tunneling of charge carriers to nonradiative centers [120].

From the similar activation energies below 30 meV (Tab. 5.2) it can be seen that in samples S3 and S5 the same nonradiative recombination mechanism is dominant. Contrary, the larger activation energy of 46 meV for sample S1 without a buffer layer could indicate a change in the nonradiative mechanism. Compared to the buffered samples, however, the activation energies are still in the same order of magnitude.

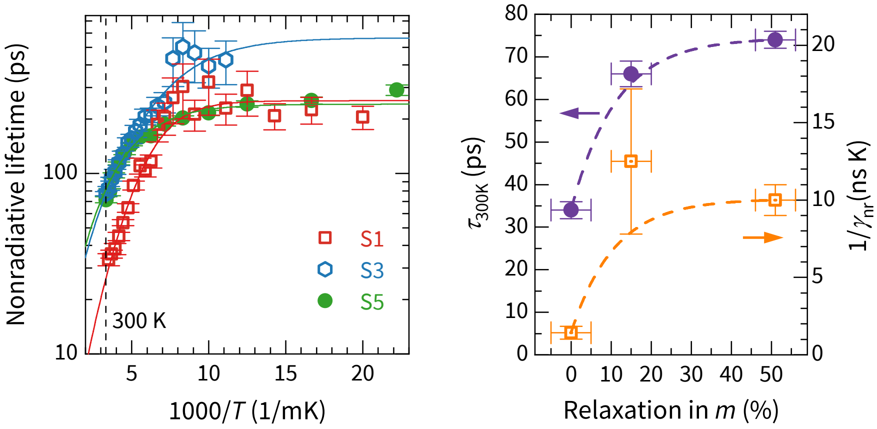

FIGURE 5.7: Arrhenius-type graph of the nonradiative lifetimes of samples S1, S3 and S5, where the similar slope indicates comparable activation energies. Dashed lines represent fits according to Eq. 5.3. The inset shows the inverse of prefactor $1/\gamma_{\mathrm{nr}}$, related to the density of nonradiative centers, and the room temperature lifetimes as a function of relaxation in m-direction. Dashed lines in the inset serve as guide to the eye.

Interestingly, the prefactor γ_{nr} is significantly higher for sample S1 compared to sample S3 or S5, which indicates a higher defect density in the unbuffered QWs. The prefactors for samples S3 and S5 show no significant difference, but follow the trend of the rising lifetimes with incrasing degree of buffer layer relaxation. This is shown graphically in Fig. 5.7, where the room temperature effective lifetimes $\tau_{300\mathrm{K}}$ and the inverse prefactors $1/\gamma_{\mathrm{nr}}$ are plotted versus the degree of relaxation in the AlInN layer. The inverse prefactor $1/\gamma_{\mathrm{nr}}$ is a quantity that is related to the density of nonradiative centers, and will rise if the density of nonradiative centers, or defects, decreases. Therefore, the rising trend of $1/\gamma_{\mathrm{nr}}$ in Fig. 5.7 is indicative of a decreasing defect density in the quantum well. At the same time, the effective lifetimes are strictly monotonically rising with increasing buffer layer relaxation. In addition to the aforementioned correlation of nonradiative lifetimes and buffer layer relaxation, this behavior indicates a dependence of the nonradiative recombination, and the density of nonradiative centers, on the accumulated strain in the quantum well. Within the uncertainties, the reduced nonradiative recombination and the lower defect densities in the QWs with increasing relaxation of the AlInN buffer layer follow the same trend.

Considering that the parameter $\tau_{\mathrm{nr},0}$ is needed to describe the nonradiative lifetimes, tunneling to nonradiative centers at low temperatures cannot be excluded, especially for the samples S1 and S5. Moreover, the formation of additional defects in the AlInN layer during relaxation needs to be discussed. In particular, threading dislocations with an out-of-plane component that are formed in the AlInN could penetrate the subsequent MQW, and act as additional nonradiative centers. Since the overall nonradiative rate is decreased with an AlInN layer, the overall defect density is decreased rather than increased. This would be consistent with the formation of in-plane misfit dislocations during relaxation of the AlInN, as suggested in Refs. [27] and [166]. Furthermore, the measured lifetimes show no dependence on the substrate type, i.e. bulk or patterned sapphire, but are rather related to the reduced strain due to the AlInN layer.

5.4.3 *Strain-related nonradiative recombination*

These results indicate that nonradiative centers, or defects, in the quantum wells are not stemming from the threading dislocations related to the template. Instead, they are generated during growth of the highly strained QW structure. Furthermore, the strain-induced formation of defects acting as nonradiative recombination centers is consistent with the observed trend of increasing AlInN buffer layer relaxation and decreasing defect densities in the QWs. As described in Sec. 5.2, this was already found by Langer et al. for *c*-plane structures, where the strain-induced defects in the QW are the dominant source of nonradiative recombination [9]. There, basal stacking faults formed by local relaxation in the QWs, and the related stacking mismatch boundaries were proposed to explain the relation between nonradiative lifetimes and strain energy density. The microscopic origin of the nonradiative centers, however, cannot be evaluated from the present optical data, but a comparable mechanism of defect formation might apply to semipolar orientations as well. Nevertheless, the nonradiative lifetimes remain rather low, despite the use of buffer layers. Given the high InN mole fractions, however, the semipolar structures are comparable to polar structures investigated by Langer et al. as shown in Fig. 5.8. For the highest InN mole fractions, the semipolar structures with buffer layer show even higher lifetimes.

In the context of defect reduction, also the role of indium itself in the AlInN needs to be discussed. Recently, Haller et al. reported on the effect of indium-containing layers, including AlInN, on the nonradiative recombination in *c*-plane QWs [171–173]. They observed a reduction of the nonradiative recombination by inserting a low-temperature indium-containing underlayer before the QW structure. As mentioned in Sec. 5.4, a similar low-temperature GaN underlayer of approx. 20 nm thickness is included in all samples investigated here. Earlier work has shown that internal quantum efficiencies of 80-90% can be achieved in *c*-plane QWs including such an indium-free underlayer [14]. Furthermore, the nonradiative lifetimes observed by

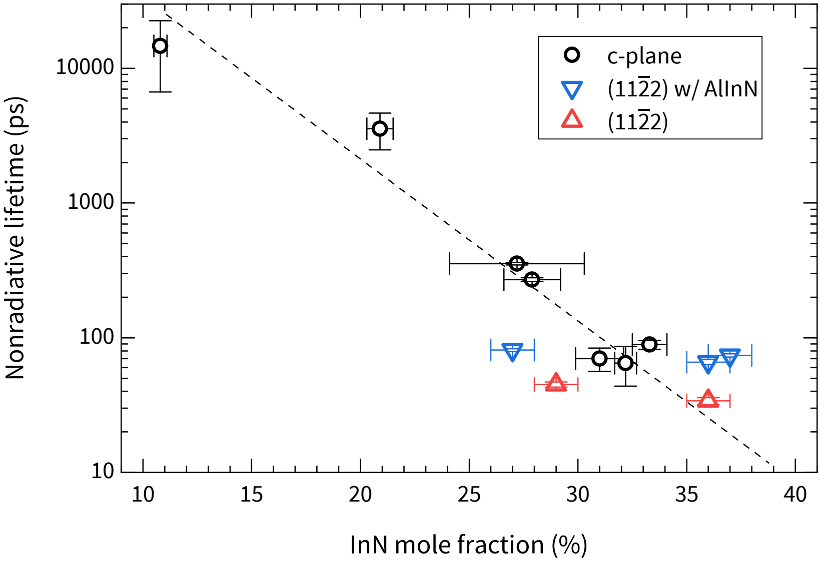

FIGURE 5.8: Comparison of nonradiative lifetimes at 300 K for different InN mole fractions in polar and semipolar QW structures. For the highest InN mole fractions, the semipolar structures show longer lifetimes than the polar ones. The dashed line serves as guide to the eye for typical *c*-plane structures. The *c*-plane data is taken from Refs. [9, 101].

Haller et al. saturate at AlInN layer thicknesses of approx. 50 nm[172, 173]. Contrary, the present analysis shows a reduction of the nonradiative recombination, when the AlInN layer thickness changes by several hundred nanometers. Additionally, the reduced nonradiative recombination goes along with a significant reduction of the strain in the QW structure. Summarizing, the beneficial effect of indium atoms on the segregation of defects cannot be excluded in the present case, but is shown to be not the dominant effect for the reduction of nonradiative recombination.

5.5 CONCLUSION

The presented results show a reduced nonradiative recombination for semipolar GaInN/GaN quantum wells with strain-reducing AlInN buffer layers. The buffer layer is lattice-matched to the c' in-plane direction of (11$\bar{2}$2) GaN, and partially relaxes in m-direction to provide a template with reduced lattice mismatch for the subsequently grown MQW. The reduced strain in the MQW leads to a reduced nonradiative recombination rate. This is observed on bulk substrates, as well as on overgrown patterned sapphire templates.

The observed correlation between degree of relaxation of the AlInN buffer layer and the nonradiative lifetimes is indicative of a strain-induced formation of nonradiative centers, or defects, in the quantum well. Compared to the earlier results obtained for c-plane structures by Langer et al. [9], the basic trend is the same, but no dedicated dependence of the nonradiative lifetimes on strain is found for the present semipolar structures. Instead, the nonradiative lifetimes and the density of nonradiative centers, determined by an Arrhenius fit, follow the same trend with increasing buffer layer relaxation.

For the polar GaInN/GaN QWs investigated by Langer et al., strain-induced defect formation in the QW can be considered the dominant source of nonradiative recombination. For the present semipolar QWs, the overall lifetimes are rather short, which, on the one hand, could be caused by another nonradiative recombination mechanism that is dominant over the observed strain-related one. On the other hand, the quantum wells exhibit high InN mole fractions close to 40 %, and the investigated range of quantum well strain energy is very limited here, due to the buffer layer relaxation. Furthermore, even if the observed nonradiative lifetimes are short for the semipolar structures, they are still comparable to those of polar structures for the same InN mole fraction. Still, other nonradiative centers might be important for the semipolar structures, such as impurities like carbon, hydrogen or oxygen. These impurities and related complexes, especially with gallium vacancies, are known to act as nonradiative recombination centers in GaN [174–177]. The incorporation of these impurities has been shown to be significantly higher for non- and semipolar orientations compared to c-plane [178, 179]. Especially the precursors used in MOVPE-growth may contribute to higher impurity incorporations, and secondary ion mass spectroscopy (SIMS) measurements could give more detailed information about the impurity concentrations in the present samples.

The type of strain-induced defect, however, could not be determined from the optical investigations, neither for the polar, nor for the semipolar samples. Basal stacking faults and related stacking mismatch boundaries proposed by Langer et al. might be present in the semipolar structures as well. Nevertheless, a structural characterization using transmission electron microscopy (TEM) would be necessary to investigate the formation mechanism of nonradiative centers in detail. In combination with advanced electron microscopy techniques, e.g. electron channeling contrast imaging (ECCI), more information about the threading dislocation densities could be obtained [180] .

It should be emphasized once more that the described strain-induced formation of defects takes place in the quantum well itself. At least the threading dislocations originating from the substrate, or template, do not seem to be the dominant source of nonradiative recombination for both, polar and semipolar structures. Otherwise the use of bulk, or pseudo-bulk, substrates that exhibit much lower threading dislocation densities would change the nonradiative recombination behavior considerably. Still, threading dislocations originating from other layers cannot be ruled out as additional source of nonradiative recombination.

Beyond the defect formation mechanism in the quantum wells, the investigations provide an insight into the relaxation mechanism of the AlInN buffer layer itself. As reported for semipolar GaInN buffer layers, the formation of in-plane misfit dislocations by kinking of already existing threading dislocations is possible for semipolar-oriented layers. Although the threading dislocation density cannot be determined accurately without structural methods like TEM, this is most likely also the case in the present samples. Otherwise, the relaxation of AlInN would not reduce the total amount of nonradiative centers in the QW, but rather increase the nonradiative recombination by the formation of additional threading dislocations. For a more quantitative analysis of the nonradiative recombination and its dependence on strain, a broader semipolar sample basis, covering a broader range of strain energy densities, is needed, together with reliable XRD analysis to determine the degree of relaxation and strain state of every layer. Due to the numerous degrees of freedom in the semipolar crystal lattice, and the limited accessible reflections, the X-ray characterization is at its limits here.

Relating the room temperature lifetimes of buffered (sample S3) and unbuffered (sample S1) semipolar quantum wells, the nonradiative rate is reduced by a factor of two. In order to reduce the nonradiative recombination even further, an improvement of the AlInN layer might be another option. On the one hand, a reduction of the lattice mismatch by even higher degrees of relaxation should reduce the nonradiative recombination. In earlier experiments, Buß et al. were able to reach close to fully relaxed AlInN layers on semipolar GaN [132, 166]. On the other hand, the lattice matching is possible only along one of the in-plane directions of semipolar-oriented GaN, therefore the possible reduction in lattice mismatch towards the subsequent GaInN QW is limited in any case.

After all, the results emphasize the important role of strain, and strain-reducing buffer layers, in the context of nonradiative recombination. Therefore, the strain manipulation by partially relaxed AlInN buffer layers, especially on semipolar orientations, can contribute to the reduction of nonradiative recombination in green-emitting GaInN/GaN quantum wells, and to finally overcome the *green gap*.

6

INTERNAL QUANTUM EFFICIENCY IN THE LOW-TEMPERATURE LIMIT

The previous chapters were covering either radiative, or nonradiative recombination mechanisms. In this chaper, the focus shifts to a quantity that relates both kind of processes, namely the internal quantum efficiency. One major problem is to determine an absolute value of the quantum efficiency, which is usually accessible only as a relative measure. In the beginning of this chapter, the basic difficulties in IQE determination, as well as some common measurement principles are discussed. Finally, using temperature-dependent lifetime measurements, an approach to determine an absolute IQE is presented, which relies on the fundamental temperature dependence of radiative and nonradiative recombination rates.

6.1 INTERNAL QUANTUM EFFICIENCY

From a fundamental viewpoint, the internal quantum efficiency (IQE, or η) describes the relation between radiative and nonradiative recombination rates:

$$\eta = \frac{R_\mathrm{r}}{R_\mathrm{r} + R_\mathrm{nr}} = \frac{\tau_\mathrm{nr}}{\tau_\mathrm{r} + \tau_\mathrm{nr}} \,. \tag{6.1}$$

Thereby, an IQE of 100 % is equivalent to the absence of nonradiative recombination. Thus, the IQE has become the figure of merit for light-emitting III-nitride structures. In the context of device application, also the external quantum efficiency (EQE, or η_extern) of the complete device is of importance:

$$\eta_\mathrm{extern} = \eta_\mathrm{inject}\, \eta_\mathrm{extract}\, \eta \,, \tag{6.2}$$

which includes also the injection efficiency (η_inject), and the extraction efficiency (η_extract). Nevertheless, the IQE (η) marks the upper efficiency limit for an optoelectronic structure at a given temperature.

As described in the following, there exist several different methods to measure the IQE [14]. A common approach is the use of temperature- and power-dependent continuous-wave photoluminescence (cw-PL), where the spectrally integrated intensity $I(T, P)$ of a light-emitting structure serves as measure for the IQE:

$$\eta \propto I(T, P) \,. \tag{6.3}$$

The constant of proportionality is obtained by normalizing the measured intensities to a low-temperature value, where IQE = 100 %, or $R_{\mathrm{nr}} = 0$ is assumed. While this is, a priori, only an assumption, there are several indicators that support the expectation of absent nonradiative recombination at low temperature. First, the integrated intensity should saturate when approaching low temperatures, indicating that nonradiative centers are frozen out, and that radiative recombination is dominant. Likewise, a saturation of the intensity with increasing excitation powers can be expected. This indicates the saturation of nonradiative centers, which have a finite density in the material, and the related nonradiative recombination has a finite lifetime [100, Ch. 2]. Although structures with such a temperature and power dependence are expected to have a high quantum efficiency, those indicators are no proof for the absence of nonradiative recombination at low temperatures. Furthermore, instead of a saturation at high excitation powers, often a square root dependence is observed [181, 182].

While this method is convenient and applicable to basic quantum well structures, another approach is usually chosen for processed devices like LEDs, which are electrically contacted. Here, the light emission after current injection (electroluminescence, or EL) is measured, often in an integrating sphere that collects the luminescence at all emission angles. By comparing the collected intensities with values obtained at low temperatures, the EQE of the device can be estimated. To obtain the IQE, the injection efficiency, as well as the extraction efficiency is needed. The latter can in principle be calculated from the expected escape path of the emitted light. Like in the case of temperature- and power-dependent PL, the obtained efficiencies are a good approximation for high-efficiency LEDs.

Similar to EL measurements, there is the possibility to carry out PL measurements in an integrating sphere. Often, this method is referred to as *omni-directional PL* (ODPL) [183]. Like for EL measurements, the light extraction efficiency needs to be considered here. Additionally, the laser light used for excitation can interfere with the measurement, since reflected or scattered laser light will be detected by the integrating sphere as well. Finally, the possible reabsorption of the emitted light needs to be taken into account [184].

All of the above methods assume an IQE of 100% at low temperatures. This assumption, however, neglects possible remaining nonradiative recombination at low temperature. Nonradiative recombination via carrier capture to deep levels is usually thermally activated, i.e. phonon-assisted. As such, it can also take place at low temperatures via tunneling processes [74, Ch. 6], [88]. Thus, the assumption of vanishing nonradiative recombination at low temperatures is questionable, especially for high-defect containing III-nitrides structures. This adds an undefined uncertainty to the low-temperature normalization, and the IQE measurement as a whole, as long as it relies on a relative method as the temperature- and power-dependent PL.

Therefore, more sophisticated measurement methods have been developed, which aim at measuring the heat that is dissipated by nonradiative recombination processes. This is achieved by comparing the photoacoustic and photoluminescence signals [185]. This method, in principle, provides the possibility to measure absolute efficiencies, independent of a low-temperature normalization. Among the problems are, however, the correct normalization that is needed to properly relate the dissipated heat and the photoluminescence signal. This is further complicated by the excess energy of the laser light used for excitation. Even under resonant excitation conditions, the laser light has sufficient energy to excite carriers into higher band states. In order to reach thermal equilibrium, those hot carriers are emitting the excess energy as phonons, which dissipates additional heat, and interferes with the measurement. Given those restrictions, the efficiencies obtained by this measurement method are usually lower than those from plain PL measurements.

Finally, another approach uses the carrier density dependence of the measured intensities. Those are evaluated by the *ABC model*, which describes the total recombination rate according to a power law:

$$R(n) = A\,n + B\,n^2 + C\,n^3\,, \tag{6.4}$$

where n is the carrier density, A describes the coefficient for Shockley-Read-Hall recombination, B the coefficient for radiative recombination, and C the coefficient for Auger recombination. Using the relation $R_{\mathrm{rad}} = Bn^2$ for the radiative recombination, the IQE is described by $\eta = R_{\mathrm{rad}}/R$ and fitted to the integrated intensities at different excitation powers, or carrier densities [186–188]. Since this analysis can be done at a fixed temperature, this method has no need of a low-temperature measurement. The whole analysis, however, relies on the ABC model, which has been shown to be invalid in the III-nitrides, at least in this simple form, and when assuming constant recombination coefficients. First and foremost, the contribution of excitons results in a different carrier dependence of the radiative rate, which is rather proportional to n, instead of n^2 [11]. Not only that more than 50% of the carriers are bound into excitons, even at room temperature, the exciton ratio increases with increasing carrier density [122, 123]. Furthermore, the determination of recombination coefficients is still problematic, since those quantities are not fixed material parameters, but rather depend on the carrier density n itself [12]. The exact dependence is, however, not yet fully understood, and possible interdependencies of the recombination coefficients are complicating the determination [13]. Lately, an additional term Dn^2 has been proposed to be necessary for the description of defect-assisted Auger recombination [189]. Therefore, the reliability of the obtained quantum efficiencies by this method is questionable, and unsuitable to determine an absolute IQE value.

Summarizing, the IQE determination usually relies on relative methods. To determine an absolute value, the assumption of vanishing nonradiative recombination at low temperatures is needed, for which only indications exist. In the following, an additional indicator for the absence of nonradiative recombination is presented, which relies on the fundamental temperature dependence of the lifetimes measured by time-resolved photoluminescence spectroscopy. Under certain circumstances, an IQE of 100% at low temperatures can be derived, which makes the determination of absolute IQE values possible.

6.2 TEMPERATURE DEPENDENCE OF RADIATIVE AND NONRADIATIVE LIFETIME

In order to determine if nonradiative recombination is present at low temperatures, the measured effective lifetimes are compared with the radiative lifetimes. For this purpose, the specific temperature dependencies of radiative and nonradiative lifetimes are discussed first, followed by the introduction of an analytical model to fit the temperature behavior of both. Thereby, it is possible to determine the amount of nonradiative recombination at low temperatures, and finally to obtain an absolute value for the internal quantum efficiency.

6.2.1 *Radiative lifetime*

Generally, the radiative lifetime scales with temperature according to the carrier confinement given by the structure's dimension d:

$$\tau_\mathrm{r} \propto T^{d/2}\,. \tag{6.5}$$

For a two-dimensional structure like a QW, this implies a linear rise of the radiative lifetime with temperature. Especially towards low temperatures, the radiative lifetime deviates from the ideal behavior. Instead of $\tau_\mathrm{r} \to 0$ for $T \to 0$, the radiative lifetime approaches a constant value, denoted $\tau_\mathrm{r,loc}$ here. This is a consequence of carrier localization that typically occurs at low temperatures [110–119]. Charge carriers get localized at potential minima that can arise from fluctuations in QW width and composition. Since this localized state is zero-dimensional, the radiative lifetime shows a constant behavior according to Eq. 6.5. At elevated temperatures, the carriers can overcome the potential barrier by thermal activation and the transition to the two-dimensional case is observed. This has already been discussed in Secs. 4.1 and 4.5.

Furthermore, as described in Sec. 4.5, a characteristic delocalization energy E_loc, as well as an additional high-temperature activation energy E_HT, probably related to carrier escape into the barriers, can be used to describe the temperature behavior of the radiative lifetime. In summary, this yields

$$\tau_{\mathrm{r}}(T) = \tau_{\mathrm{r,loc}} \frac{1+\gamma_{\mathrm{L}}\, T \, \exp\left(-\frac{E_{\mathrm{loc}}}{k_{\mathrm{B}} T}\right) \left[1+\gamma_{\mathrm{HT}}(T) \, \exp\left(-\frac{E_{\mathrm{HT}}}{k_{\mathrm{B}} T}\right)\right]}{1+\gamma_{\mathrm{L}}\, \tau_{\mathrm{L}} \, \exp\left(-\frac{E_{\mathrm{loc}}}{k_{\mathrm{B}} T}\right)} , \tag{6.6}$$

with the prefactors as defined in Sec. 4.5. Note that $\gamma_{\mathrm{HT}} \propto \sqrt{T}$, while γ_{L} and τ_{L} are constant. In summary, the radiative lifetime shows a characteristic behavior with increasing temperature: It remains constant at low temperatures, undergoes a transition to increase linear, or even super-linear with temperature. Therefore, the radiative lifetime shows a monotonically rising behavior with increasing temperature, with the low-temperature value as lower bound.

6.2.2 *Nonradiative lifetime*

Opposed to the radiative emission, there is the case of nonradiative carrier recombination via defects, where the energy is fully or partly dissipated as phonons. This nonradiative process usually happens after carrier capture to strongly localized mid-bandgap states. Although a variety of defects, or other nonradiative centers, can be involved in this type of recombination, the process is always thermally activated, as described in Sec. 2.3.3. In a non-degenerate limit, the corresponding recombination rate can be described by Boltzmann statistics:

$$R_{\mathrm{nr}} \propto \frac{1}{\tau_{\mathrm{nr}}} = \gamma_{\mathrm{nr}}(T) \, \exp\left(-\frac{E_{\mathrm{act}}}{k_{\mathrm{B}} T}\right) , \tag{6.7}$$

where $\gamma_{\mathrm{nr}}(T)$ is a temperature-dependent prefactor, and E_{act} is the characteristic activation energy of the process. The prefactor's actual temperature dependence is also subject to the charge state of the nonradiative center [88], while its absolute value depends on the concentration of nonradiative centers and their specific capture coefficients.

The capture process becomes possible, as soon as the carriers have gained sufficient thermal energy, see Sec. 2.3.3. For lower temperatures, the corresponding recombination path freezes out, and thus $R_{\mathrm{nr}} \rightarrow 0$, or $\tau_{\mathrm{nr}} \rightarrow \infty$ for $T \rightarrow 0$.

As described in Sec. 2.3.3, the carrier capture is possible, however, even at lower temperatures via tunneling. Since the tunneling process is independent of temperature, the nonradiative recombination rate is not necessarily vanishing in the low-temperature limit. The remaining nonradiative recombination can be associated with a lifetime $\tau_{\mathrm{nr,0}}$, which serves as upper boundary in the low-temperature limit.

Therefore, the total nonradiative lifetime is increasing towards lower temperatures, according to Eq. 2.26, and finally saturates at the value $\tau_{\mathrm{nr},0}$. This behavior is described by

$$\tau_{\mathrm{nr}}(T) = \tau_{\mathrm{nr},0} \, \frac{1 + \gamma_{\mathrm{L}} \, T \, \exp\left(-\frac{E_{\mathrm{loc}}}{k_{\mathrm{B}} T}\right)}{1 + \gamma_{\mathrm{L}} \, T \, \exp\left(-\frac{E_{\mathrm{loc}}}{k_{\mathrm{B}} T}\right) \left[1 + \gamma_{\mathrm{nr}} \, \exp\left(-\frac{E_{\mathrm{act}}}{k_{\mathrm{B}} T}\right)\right]} \,, \tag{6.8}$$

where γ_{nr} is assumed constant. Even if a possible temperature dependence of the prefactor $\gamma_{\mathrm{nr}}(T)$ would shift the activation energy for nonradiative recombination, its order of magnitude would be unchanged, and the prefactor is kept constant for simplicity. The above relation regards the possibility of tunneling ($\tau_{\mathrm{nr},0}$) for all charge carriers, while only the delocalized charge carriers can undergo thermally activated nonradiative recombination, characterized by E_{act}. If necessary, several thermally activated processes can be considered by adding further Boltzmann terms with additional activation energies to the above expression. Contrary to the radiative lifetime, the thermally activated nonradiative recombination shows a monotonically decreasing behavior with temperature, and may saturate at low temperatures when tunneling to nonradiative centers occurs.

At this point, it is important to stress that there is no experimental evidence for other than thermally activated nonradiative processes in III-nitride quantum wells. Contrary, an increasing lifetime has been observed with increasing temperature in GaN bulk material. Since nonradiative recombination was assumed dominant in this case, the rise in nonradiative lifetimes was assigned to shallow trap levels close to the band edges. While charge carriers are trapped in those levels at low temperatures, they can be thermally ejected with increasing temperature, which induces a rise of the nonradiative lifetime. As mentioned above, this behavior has not been observed experimentally for quantum wells, where nonradiative centers are considered to be deep traps, near the center of the bandgap. Therefore, the monotonic decrease of the nonradiative lifetime holds true, even if several different nonradiative recombination channels occur.

6.3 SYNCHRONOUS RISE OF RADIATIVE AND EFFECTIVE LIFETIME

As discussed above, the radiative and nonradiative lifetimes show a fundamentally different temperature behavior. While the radiative lifetime is monotonically rising, the nonradiative lifetime is monotonically decreasing with temperature. Both, radiative and nonradiative lifetime, approach a constant value at low temperatures. The effective lifetime, which is directly accessible in time-resolved photoluminescence experiments, is a combination of both lifetimes and thus, behaves accordingly with

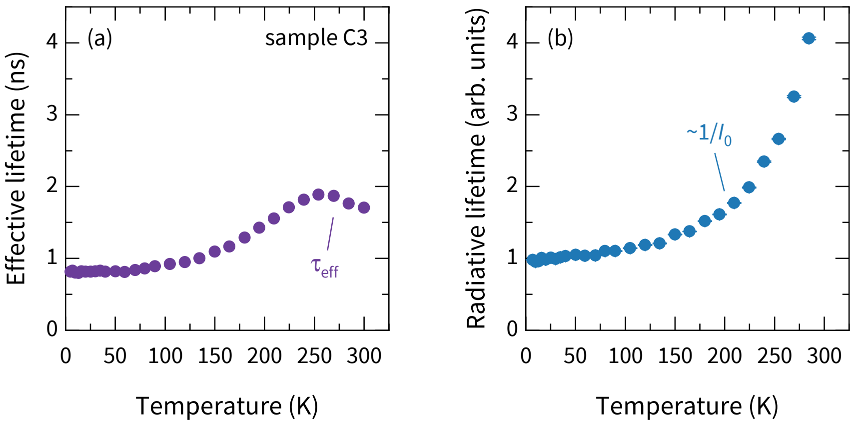

FIGURE 6.1: Measured effective lifetime (a), and radiative lifetime (b) of sample C3 [101]. The radiative lifetime is given in arbitrary units, and obtained from the inverse of the measured initial intensities I_0. It approaches unity at low temperatures, and shows a similar temperature behavior as the effective lifetime, at least up to 250 K. Therefore, the recombination is assumed to be dominated radiatively at low temperatures.

temperature. Therefore, a dominant radiative or nonradiative recombination in the structure is directly resulting in a rising or falling effective lifetime. To demonstrate the interplay between radiative and nonradiative lifetimes, several sample structures are analyzed in the following. All the samples consist of GaInN/GaN single quantum wells, prepared on c-plane sapphire substrates. Details on the sample structures can be found in Tab. 6.1.

First, the temperature-dependent lifetimes of sample C3 are discussed. In Fig. 6.1(a), the effective lifetime, as measured in the experiment, is plotted, while Fig. 6.1(b) shows the radiative lifetime on a relative scale. The radiative lifetimes are obtained from the inverse of the initial intensities I_0, as described in Sec. 3.3. The values are normalized to approach unity at low temperatures, and show a similar rise with temperature as the effective lifetime. Only at temperatures above 250 K, the effective lifetime decreases, and deviates from the radiative lifetime, which shows the expected monotonic rise. Since radiative and effective lifetimes show the same behavior with increasing temperature, the recombination has to be dominated radiatively at low temperatures. Otherwise, the effective lifetime, which is influenced by both, radiative and nonradiative recombination, would not rise with temperature. Therefore, the assumption of vanishing nonradiative recombination at low temperatures is justified in this case, and τ_r can be set equal to τ_{eff} at the lowest temperature of 5 K.

Combining the model functions from Eqs. 6.6 and 6.8, the temperature dependence of the effective lifetime can be described accordingly:

$$\tau_{\text{eff}}(T) = \left(\frac{1}{\tau_{\text{r}}(T)} + \frac{1}{\tau_{\text{nr}}(T)} \right)^{-1} . \tag{6.9}$$

At the same time, the inverse of the initial intensities I_0 obtained from the experiment provides a measure for the radiative lifetime, which can be described by Eq. 6.6, including an additional normalization factor. Therefore, both model functions can be fitted to the measured data, in order to obtain not only the activation energies for the radiative and nonradiative lifetimes, but also the relation of the saturation values ($\tau_{\text{r,loc}}$, $\tau_{\text{nr,0}}$) at low temperatures. Since the model functions have common parameters, it is necessary to fit Eq. 6.6 to the inverted initial intensites I_0, and Eq. 6.9 to τ_{eff} at the same time. In such a simultaneous fitting procedure, contrary to single subsequent fits, the overall sum of squares of residuals (χ^2) is minimized accordingly [190].

The results of the fit for sample C3 are shown in Fig. 6.2(a). The radiative lifetimes equal the effective lifetimes at low temperatures, which is expected due to the synchronous rise of both with increasing temperature. At low temperatures, both saturate at a value of $\tau_{\text{r,loc}} = (0.82 \pm 0.02)$ ns, while the best agreement between data and model function is obtained for $\tau_{\text{nr,0}} \rightarrow \infty$. In fact, a value of $\tau_{\text{nr,0}} \approx 7000$ ns is found if the parameter is adjusted in the fitting procedure as well. Therefore, the tunneling parameter is omitted for sample C3, which corresponds to the absence of nonradiative recombination, i.e. $\eta_{\text{LT}} = 100\%$, at low temperatures. Here, the nonradiative lifetimes are calculated as the discrepancy between the effective and radiative lifetimes, according to Eq. 6.9. Furthermore, a delocalization energy of $E_{\text{loc}} = (10 \pm 2)$ meV, and an activation energy of $E_{\text{HT}} = (114 \pm 8)$ meV are found for the radiative lifetime, while an activation energy of $E_{\text{act}} = (206 \pm 55)$ meV is obtained for the nonradiative lifetime. Summarizing, the synchronous fitting procedure reveals the ratio of radiative and nonradiative lifetimes, in particular at low temperatures, and furthermore describes the complete temperature dependence of the measured lifetimes.

This analysis is repeated for the samples C29 and C27, as shown in Fig. 6.2(b) and (c). Considering the effective lifetimes of sample C29, an increase with temperature, similar to sample C3, can be observed, which indicates a dominant contribution of radiative recombination. For temperatures above 120 K, however, the effective lifetimes decrease again, which proves dominant nonradiative recombination. Also the fit results show that effective and radiative lifetime are nearly equal at low temperatures,

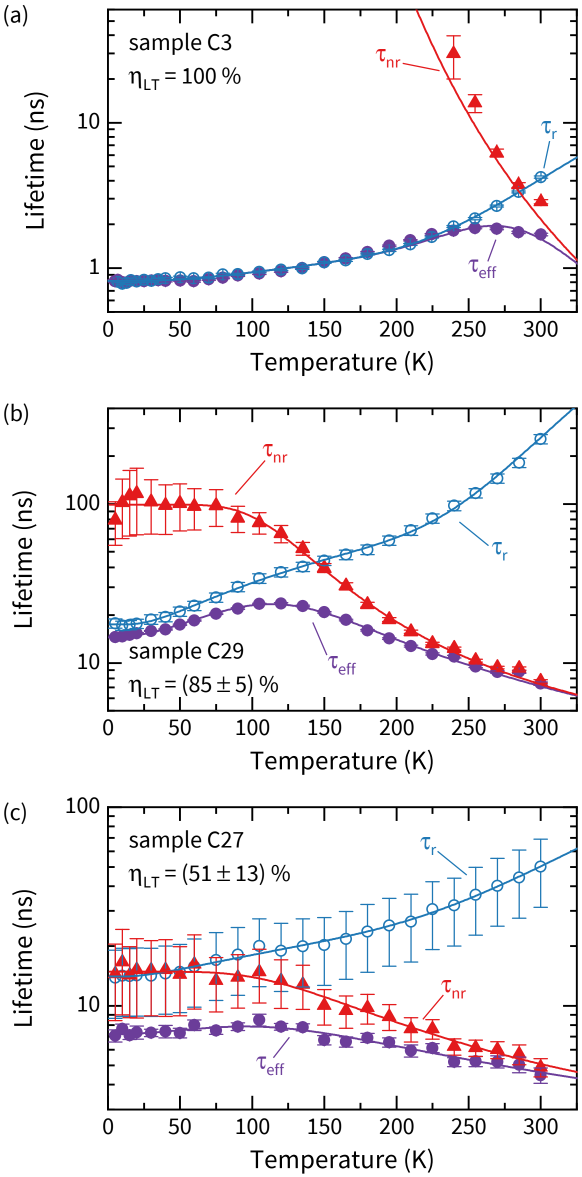

FIGURE 6.2: Temperature-dependent lifetimes of the samples C3 (a, see Ref. [101]), C29 (b), and C27 (c), including the results of the synchronous fit procedure (solid lines). For each sample, the IQE at low temperatures, as determined by the fit, is indicated.

and a radiative lifetime of $\tau_{\mathrm{r,loc}} = (17 \pm 2)$ ns is obtained. The nonradiative lifetime saturates at $\tau_{\mathrm{nr,0}} = (99 \pm 32)$ ns, and the low temperature IQE can be estimated by

$$\eta_{\mathrm{LT}} = \frac{\tau_{\mathrm{nr,0}}}{\tau_{\mathrm{r,loc}} + \tau_{\mathrm{nr,0}}}\,, \tag{6.10}$$

For sample C29, this results in $\eta_{\mathrm{LT}} = (85 \pm 5)\%$, and the tunneling contribution that is necessary to describe the measured effective lifetimes reduces the low-temperature efficiency. Moreover, the saturation of the nonradiative lifetime damps the rise of the effective lifetime with temperature. Although a synchronous rise of effective and radiative lifetimes is observed, deviations between both are visible already for $T < 100$ K. This is indicative of nonradiative recombination, even at low temperatures, which inevitably affects the temperature dependence of the effective lifetime.

Finally, for sample C27, the effective lifetime shows only a very subtle rise, which indicates more prominent nonradiative recombination even at low temperatures. Consequently, the simultaneous fit reveals values of $\tau_{\mathrm{r,loc}} = (14 \pm 5)$ ns, and $\tau_{\mathrm{nr,0}} = (15 \pm 6)$ ns, which are nearly equal. Thus, the low temperature IQE amounts to only $(51 \pm 13)\%$, and the large uncertainties are reflected in the deduced radiative and nonradiative lifetimes. Here, the IQE is less than unity, even within the large error margins. Contrary, for sample C29, it cannot be excluded that the low-temperature IQE equals unity due to the large uncertainty.

Summarizing the results, the simultaneous fitting procedure makes it possible to determine the low-temperature IQE, although with partly limited significance. As soon as deviations from the synchronous rise of effective and radiative lifetimes become visible, a tunneling component is necessary to describe the temperature dependence of the effective lifetime properly. Since in this case, the low-temperature values $\tau_{\mathrm{r,loc}}$ and $\tau_{\mathrm{nr,0}}$ show high uncertainties, it is only possible to fix the low temperature IQE to $\eta_{\mathrm{LT}} \leq 1$, rather than to a definite value. Only in the absence of nonradiative recombination at low temperatures, i.e. when the synchronous rise of effective and radiative lifetimes is visible up to high temperatures, the low temperature IQE can be fixed to $\eta_{\mathrm{LT}} = 1$. Even when no, or a strongly damped, synchronous rise of effective and radiative lifetimes can be observed, η_{LT} can still equal unity. Considering the case that localization of charge carriers persists up to relatively high temperatures, the synchronous rise is likely not visible, since nonradiative processes are already dominating when the radiative lifetime starts to rise with temperature. In such cases, the temperature behavior of effective and radiative lifetime does not give further indications to determine the IQE at low temperatures.

6.4 ABSOLUTE INTENSITY COMPARISON

The above analysis, based on the synchronous rise of effective and radiative lifetimes, and the simultaneous fitting procedure, is helpful to determine the low temperature IQE of a structure. Nevertheless, there are limiting points, where a complementary indicator is needed to confirm the determined efficiencies. The emitted intensity of a structure, measured on an absolute scale, could serve as another indicator, since it is fundamentally related to the IQE determination via PL. As mentioned in Sec. 6.1, the integrated intensity in cw-PL is directly proportional to the IQE. This relation is deduced in more detail here, to subsequently formulate an equivalent relation for time-resolved photoluminescence.

Under cw excitation, charge carrier recombination (R) and generation (G) are in equilibrium. For this case, the time derivative of the carrier density n in Eq. 3.5 vanishes, and the intensity I of the measured photoluminescence signal is again proportional to the radiative rate R_r:

$$\frac{\partial n}{\partial t} = 0 \Rightarrow G = R \tag{6.11}$$

$$I \propto R_\mathrm{r} = \eta R\,. \tag{6.12}$$

Therefore, the integrated intensity I is a measure for the IQE, as long as the generation rate G is constant. The generation rate itself depends on the absorption and thickness of the QW, which is discussed below. This opens the possibility to compare the intensities emitted by two samples on an absolute scale. At low temperatures, the intensities should be equal if both samples have 100% IQE. Contrary, a difference in the absolute intensities would indicate $\eta_\mathrm{LT} < 1$ for at least one of the compared structures. Experimentally, such a comparison can be carried out by mounting the samples side by side in a cryostat, to maintain identical excitation and detection conditions. Eventually, the comparison with a structure that shows $\eta_\mathrm{LT} = 1$ (see sample C3 from above) would allow to verify the low-temperature IQE of every other structure.

In order to obtain a similar comparison in time-resolved PL, the initial intensity I_0 and radiative lifetime τ_r are considered. After pulsed excitation, a fixed charge carrier density δn is prepared in the structure, as long as the absorption remains unchanged. The absolute value of the initial intensity I_0 is considered directly proportional to the radiative rate R_r :

$$I_0 \propto R_\mathrm{r} \equiv \frac{\delta n}{\tau_\mathrm{r}}\,. \tag{6.13}$$

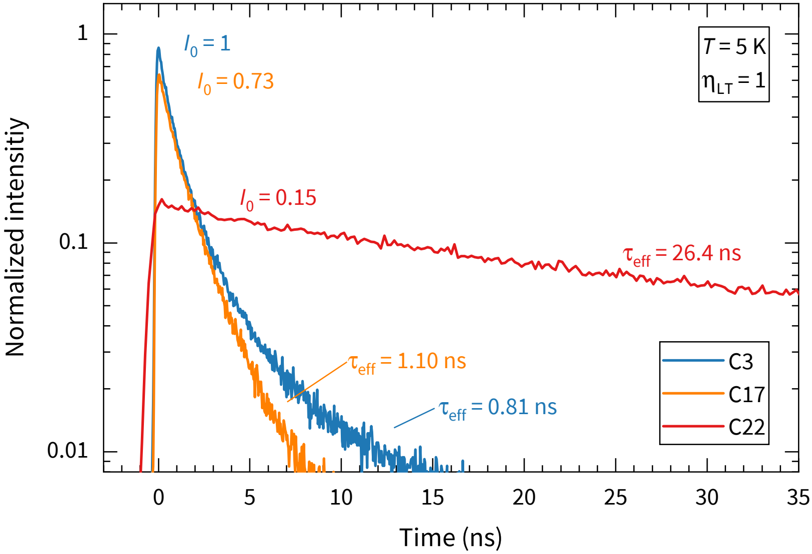

FIGURE 6.3: Decay curves of different structures at low temperature. Although the synchronous fit indicates $\eta_{\mathrm{LT}} = 1$ for all of them, they show different initial intensities I_0 and decay times τ_{eff}.

Since the radiative lifetime τ_{r} is depending on the physical properties, such as composition and thickness, of the QW structure, different initial intensities are expected when comparing various sample structures. Furthermore, the initially prepared carrier density δn depends as well on the QW thickness and its absorption.

This is emphasized by the decay curves shown in Fig. 6.3, where three samples with nominally identical quantum wells are compared, instead of the samples from the above analysis (C3, C27, C29). For all the samples shown in Fig. 6.3 (C3, C17, C22), $\eta_{\mathrm{LT}} = 1$ is found from the simultaneous fitting procedure for all samples, which simplifies the comparison. The intensities are corrected for the absorption of the QW ($\alpha \times L_{\mathrm{QW}}$), using a calculated absorption coefficient α [191], multiplied by the nominal QW width L_{QW}. The calculated absorption coefficients and QW widths can be found in Tab. 6.1. Furthermore, the intensities are normalized to sample C3. Clearly, all three samples show different initial intensities and different decay times. Since the initial intensity is directly related to the radiative lifetime via Eq. 6.13, the fixed amount of charge carriers that is prepared after pulsed excitation can recombine either fast, showing high initial intensity and short lifetime, or vice versa, recombine slow and show long lifetime and low initial intensity. Therefore, the initial intensity

I_0 is not a suitable measure for the IQE, and rather the product $I_0 \times \tau_r$ should be considered. This compensates the changes due to the different radiative lifetimes, and provides a quantity that is comparable to the IQE determined from cw-PL measurements. Considering Eq. 6.13, the product $I_0 \times \tau_r$ would be equivalent to δn, or more specifically, the ratio of charge carriers that undergo radiative recombination. To compare the product at low temperatures, the initial intensities I_0 and effective lifetimes τ_{eff} at $T = 5\,\mathrm{K}$ are considered, as shown in Fig. 6.3. Generally, the radiative lifetime τ_r, instead of the effective lifetime τ_{eff} has to be used, or the product $I_0 \times \tau_{\mathrm{rad}}$ could be underestimated. In this particular case, the effective lifetime equals the radiative lifetime, since $\eta_{\mathrm{LT}} = 1$ is found. While the samples C3 ($I_0 \times \tau_{\mathrm{eff}} = 1.00 \pm 0.12$) and C17 ($0.97 \pm 0.08$) are comparable in this sense, a significantly higher value of 5.2 ± 0.6 is obtained for sample C22. Note that, for better comparability, the values are normalized to sample C3.

Obviously, the structures show different products $I_0 \times \tau_{\mathrm{eff}}$, although $\eta_{\mathrm{LT}} = 1$ is given for all of them. As the measured quantities are already corrected for the different absorption, a probable reason for the observed differences is the outcoupling of emitted light. Apparently, the thickness of the GaN cap layer, which is grown on top of the QWs, is different for the samples shown above. The samples C3 and C17 have comparable cap layers of approximately 70 nm thickness, while the one in sample C22 has 150 nm thickness. Since the emitted light is detected from the front side of the samples, i.e. on the epitaxial surface, it needs to pass the cap GaN cap layer before detection. Fig. 6.4 shows the normalized quantity $I_0 \times \tau_{\mathrm{eff}}$ for different cap layer thicknesses, including several other single quantum well structures. While the values are comparable for cap layer thicknesses up to 80 nm, including samples C3 and C17 from above, the increasing trend up to sample C22 can be clearly seen. The data point for sample C33, which has the thickest GaN cap layer, shows a lower value again, but belongs to a structure that has $\eta_{\mathrm{LT}} < 1$, according to the simultaneous fitting procedure. As the effective lifetime τ_{eff} measured at $T = 5\,\mathrm{K}$ is probably lower than the actual radiative lifetime, the quantity $I_0 \times \tau_r$ is underestimated. Therefore, the data point for sample C33 represents a lower limit for the actual value, which might as well fit into the increasing trend. This is the case for samples C31 and C32 as well, whose values fit much better to the data points of the samples with $\eta_{\mathrm{LT}} = 1$.

After all, the structures with larger GaN cap layer thickness show light emission with significantly higher intensities, which complicates the IQE determination by an absolute intensity comparison. Nevertheless, the dependence of the intensity on the cap layer thickness is unclear at this point, but could be interpreted in two different ways. For the samples shown above, a photon wavelength of about 500 nm in air is observed. Given the high refractive index ($\tilde{n} \approx 2.5$) of GaN, or even GaInN, this would correspond to only $\lambda/\tilde{n} \approx 200\,\mathrm{nm}$ in the GaN crystal. This coincides with

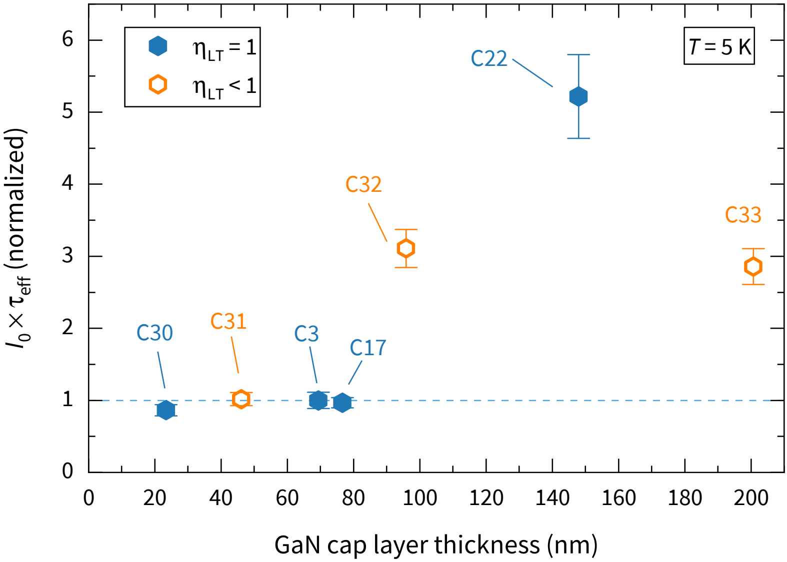

FIGURE 6.4: Product of initial intensity I_0 and measured decay time τ_{eff} for different cap layer thicknesses. Obviously, structures with different cap layer thicknesses are not comparable, even if the synchronous fit procedure indicates $\eta_{\text{LT}} = 1$. This indicates that the measured intensities are influenced by additional, but unidentified parameters.

the length scale, at which the changes in intensity are observed. In particular, the increasing trend starts at GaN cap layer thicknesses of roughly 100 nm, which is half of the emission wavelength in the crystal.

Therefore, an optical effect, namely the reflection of emitted light back into the sample, has to be considered. The cone of emitted light that can escape the structure is limited by the angle of total internal reflection. Employing Snell's law of refraction, this critical angle is found to be about 24°, which means that a large portion of the emitted light is directly reflected at the GaN/air surface back into the structure. There, interference between emitted and reflected light can occur. Depending on the optical path difference of emitted and reflected light, which is fixed by the GaN cap layer thickness, the interference may be destructive or constructive. This could affect the emitted intensity, and a periodic behavior with a characteristic length scale of $\lambda/2$ would be expected. Furthermore, the use of very large cap layer thicknesses might result in a damping of the effect, and the influence on the emitted intensity would become negligible.

Alternatively, an effect of the cap layer thickness on the recombination behavior would be possible. With increasing cap layer thickness, the distance to the sample surface changes. Thus, the refractive index within one wavelength of the PL light (200 nm) changes, and thereby affects the availability of photonic states that the light can be emitted into. The respective quantity, the photonic density of states, is given in Eq. 2.4 and depends on $\tilde{n}^3$. Regarding this dependence, the change in radiative lifetime for QW emission with parallel polarization can be estimated to

$$\tau_\mathrm{r} = \frac{\tilde{n}_\mathrm{int}}{\tilde{n}_\mathrm{ext}}\, \tau_\mathrm{r}^0 \,, \tag{6.14}$$

where τ_r^0 denotes the radiative lifetime that is unaffected by surface effects [192]. For the present case, $\tilde{n}_\mathrm{int} \approx 2.5$ for GaN, and $\tilde{n}_\mathrm{ext} \approx 1$ for air can be assumed, and increases the radiative lifetime accordingly. The above equation applies only to low cap layer thicknesses, where the QW is close to the surface, and the effect should become negligible for growing cap layer thickness. Although an increased intensity is found for larger cap layer thicknesses, the difference amounts to a factor of 5, rather than 2.5. Furthermore, the expected difference in radiative lifetime is not observed. As can be seen from Tab. 6.1, the effective lifetimes at $T = 5\,\mathrm{K}$ are around 1-2 ns for the structure with thinner cap layers. Instead of a decreasing radiative lifetime with growing cap layer thickness, the lifetimes increase. Regarding that the effective lifetimes underestimate the actual radiative lifetime at low temperatures in the case of $\eta_\mathrm{LT} < 1$, does not change the behavior.

6.5 CONCLUSION

In this chapter, the problem of IQE determination was addressed, especially in the low-temperature limit. Usually, the IQE is obtained by normalization of collected PL intensities to a low-temperature measurement, which relies on the assumption of vanishing nonradiative recombination at cryogenic temperatures. Instead, an experimental verification for an IQE of unity is presented here, which is based on the distinct temperature dependence of measured effective and radiative lifetimes, and yields reasonable results for the GaInN/GaN quantum wells under investigation. In particular, the synchronous rise of effective and radiative lifetime, ideally up to high temperatures, provides a secure indicator for the absence of nonradiative recombination.

While the effective lifetime is measured experimentally as an absolute value, the radiative lifetime is accessible only as a relative value via the initial intensity I_0. The monotonous rise of the radiative lifetime, combined with the monotonous decrease of the nonradiative lifetime, represent a key property of the analysis. In addition to the radiative lifetime, which is governed by localization effects, also the nonradiative lifetime can saturate at low temperatures due to tunneling of charge carriers to nonradiative centers. The relation between both, radiative and nonradiative lifetime, at low temperatures can be obtained by employing a least-squares fit that regards the measured decay times and initial intensities. The simultaneous fit of the model functions for radiative and nonradiative lifetimes to the experimental data allows to determine the amount of remaining nonradiative recombination at cryogenic temperatures. Thereby, the absolute values of radiative and nonradiative lifetimes can be extracted, although the related uncertainties may become large. In fact, the error margins depend mainly on the clear presence of a synchronous rise of effective and radiative lifetime.

It should be emphasized that the synchronous rise of effective and radiative lifetime provides clear evidence for an IQE of unity at low temperatures. Contrary, in the case that the effective lifetime shows no rise at all, the IQE may still be close to unity, although no evidence is found from the time-resolved measurements. Nevertheless, discrepancies between the temperature dependence of effective and radiative lifetime are probably caused by remaining nonradiative recombination, and indications for nonradiative recombination at low temperatures were found for some of the samples under investigation. Although the radiative lifetimes are usually normalized to the low-temperature value of the effective lifetime, also in the previous chapters of this thesis, it should be emphasized that always an appropriate uncertainty of at least 10% is assumed, in order to account for the probable presence of tunneling at cryogenic temperatures.

The last part of the analysis focused on the comparison of absolute values of the collected PL intensity. In this regard, the product $I_0 \times \tau_\mathrm{r}$ should provide a measure for the IQE, which can be compared between different structures. Nevertheless, the intensities and lifetimes are found to depend on the thickness of a GaN cap layer that is deposited on top of the QW structure, and differences up to a factor of five are observed. One of the probable reasons for this dependence is an optical effect, which reduces the emitted intensity due to destructive interference of light that is reflected back into the structure. Although further effort is needed to clarify this issue, at least the samples with GaN cap layer thicknesses up to 80 nm are found to be comparable in the present analysis.

Concluding, the presence of a synchronous rise of effective and radiative lifetime with temperature, measured by time-resolved photoluminescence, opens the possibility to determine absolute IQE values, especially when combined with the comparison of absolute intensities of similar QW structures.

Table 6.1: Details on the c-plane QW structures under investigation, including structural data like InN mole fraction (x_{In}), QW width (L_{QW}), and GaN cap thickness (L_{cap}), as well as the calculated absorption (α) of the QW, the effective low-temperature lifetime ($\tau_{\mathrm{eff,5K}}$), the initial normalized intensity I_0, and the low-temperature IQE (η_{LT}) estimated from the synchronous fitting procedure.

Sample	x_{In} (%) [a]	L_{QW} (nm) [a]	L_{cap} (nm) [a]	α (1/cm) [b]	$\tau_{\mathrm{eff,5K}}$ (ns)	I_0 (norm.)	η_{LT}
C3[c]	30 ± 3	1.10 ± 0.11	69	4.050×10^4	0.81 ± 0.02	1.00 ± 0.12	1
C17[d]	19.0 ± 0.8	1.36 ± 0.07	77	3.431×10^4	1.10 ± 0.02	0.73 ± 0.06	1
C22[e]	19.0 ± 0.8	2.07 ± 0.11	148	3.352×10^4	26.4 ± 0.4	0.15 ± 0.02	1
C27[f]	19.0 ± 0.8	2.07 ± 0.11	21	3.000×10^4	7.1 ± 0.5		0.51 ± 0.13
C29[f]	19.0 ± 0.8	2.07 ± 0.11	157	3.000×10^4	14.5 ± 0.2		0.85 ± 0.05
C30[f]	19.0 ± 0.8	1.56 ± 0.08	23	3.082×10^4	1.52 ± 0.06	0.46 ± 0.04	1
C31[f]	19.0 ± 0.8	1.56 ± 0.08	46	3.019×10^4	2.08 ± 0.06	0.86 ± 0.08	0.002 ± 311
C32[f]	19.0 ± 0.8	1.56 ± 0.08	96	3.154×10^4	3.32 ± 0.07	1.1 ± 0.1	0.56 ± 0.18
C33[f]	19.0 ± 0.8	1.56 ± 0.08	201	3.033×10^4	2.37 ± 0.05	0.46 ± 0.04	0.003 ± 196

[a] Ref. [96] [b] Ref. [191] [c] Ref. [94] [d] Ref. [92] [e] Ref. [93] [f] Ref. [91]

Part III

SUMMARY

7

SUMMARY AND OUTLOOK

The previous chapters covered a wide range of different topics on radiative and nonradiative recombination dynamics in GaInN/GaN quantum wells, as well as on the internal quantum efficiency of those structures, given by the relation of both recombination types.

In Ch. 4, treating radiative recombination in polar and nonpolar quantum wells, the dependence of the radiative charge carrier lifetime on the intrinsic physical properties of the quantum well was emphasized. In particular, strain was found to play an important role in this respect, as it changes the valence band structure considerably, which was shown by $\mathbf{k} \cdot \mathbf{p}$ calculations. As opposed to polar quantum wells, the anisotropic strain in nonpolar m-plane quantum wells reduces the crystal symmetry. This results in lower effective hole masses, and makes a key contribution to the increasing radiative recombination that is found in m-plane quantum wells, as compared to c-plane. Together with the better known effects of vanishing polarization fields, which increases wave function overlap and exciton binding energy, the radiative lifetimes in m-plane quantum wells are up to one order of magnitude faster than in comparable c-plane structures. This coincides with the radiative lifetimes obtained by time-resolved photoluminescence measurements at room temperature.

In a second step, AlInN buffer layers were used to manipulate the strain state of m-plane quantum wells. These metamorphic structures exhibit reduced strain, which results in significantly higher effective hole masses in the $\mathbf{k} \cdot \mathbf{p}$ calculations, comparable to c-plane quantum wells. In particular, the contribution of the second valence band state was regarded, which becomes thermally occupied at room temperature. Thereby, also the experimentally determined radiative lifetimes could be described consistently. After all, the measured radiative lifetimes prove faster radiative recombination for all nonpolar structures, although the effective masses in the metamorphic m-plane quantum wells are comparable to the ones of c-plane quantum wells.

Besides the strong dependence on strain, the radiative lifetime in m-plane quantum wells was found to decrease significantly for larger well widths. This is a joint effect of the unequally distributed charge carriers, and forbidden dipole transitions in the field-free quantum well. As a result, only the transition from the lowest conduction band to the highest valence band state contributes to the radiative emission, and charge carriers in other states are lost for radiative recombination. The effect becomes stronger with increasing temperature and well width, where more quantized levels become available, in particular in the valence band with its larger effective mass. For GaInN/GaN quantum wells, the optimum well width could be estimated to 1.5-3 nm. For a 6 nm quantum well, a reduction of the radiative rate by 50% was found from time-resolved measurements.

Furthermore, the radiative lifetime was found to increase super-linearly with temperature, which is unexpected for a quantum well structure. Time-resolved photoluminescence measurements of polar, nonpolar, and semipolar quantum wells indicate that exciton dissociation, or rather thermal activation into barrier states are causing this behavior, which can be described by an additional high-temperature activation energy in the temperature dependence of the radiative lifetime. Although the effect is observed for quantum wells of all orientations, especially nonpolar structures show higher activation energies, and thus, are less sensitive to higher temperatures. Nevertheless, this is an intrinsic effect, which has especially impact on polar quantum wells, where the QCSE reduces the effective carrier confinement. Interestingly, these results show that the radiative recombination is affected by thermal excitation of charge carriers at elevated temperatures, which occurs not only in wide nonpolar quantum wells, but also in polar and semipolar structures close to room temperature. In summary, nonpolar quantum wells have been shown to have significant advantages in terms of radiative recombination, while being sensitive to the quantum well width, and especially to the strain in the quantum well structure.

The strain in GaInN/GaN quantum well structures is affecting the radiative, but in particular the nonradiative recombination, as discussed in Ch. 5. As shown by Langer et al., strain-induced defects are the dominant source of nonradiative recombination in *c*-plane quantum wells, especially for high InN mole fractions [9]. Using partially relaxed AlInN buffer layers for strain reduction, the strong influence of strain on the nonradiative recombination was proven also for semipolar crystal orientations. Time-resolved photoluminescence measurements showed that the nonradiative rate can be reduced by 50% by inserting a strain-reducing AlInN buffer layer. This indicates the formation of strain-induced defects in the quantum well itself. Also in this respect, non- and semipolar orientations are promising to overcome the *green gap*, i.e. the drastically reduced efficiency of light emitting devices beyond the violet-blue spectral region. Furthermore, threading dislocations that originate either from the substrate, or are formed during relaxation of the AlInN buffer layer, seem to play a minor part for the nonradiative recombination. Therefore, the buffer layer relaxation presumably takes place by formation of misfit dislocations in the growth plane, or kinking of pre-existent threading dislocations. In this respect, further structural characterization is needed to clarify the relaxation mechanism in the AlInN, as well as the type of nonradiative centers that are formed in the quantum well. Additionally, structures that cover a broader range of quantum well composition could help to identify the dependence of nonradiative lifetimes for non- and semipolar crystal orientations. Still, at room temperature, the semipolar quantum wells show comparable nonradiative lifetimes to c-plane structures, which usually have superior substrate and interface quality.

Finally, in Ch. 6, the characteristic temperature dependence of radiative and nonradiative lifetime was used to determine the internal quantum efficiency (IQE) of III-nitride quantum wells in the low-temperature limit. Common methods of IQE determination rely on a low-temperature normalization, where vanishing nonradiative recombination is assumed, corresponding to an IQE of unity. Opposed to such a relative measure, the method presented here allows for an absolute determination of the IQE. Using time-resolved photoluminescence measurements, combined with simple model functions for the temperature-dependent lifetimes, it was shown that a synchronous rise of effective and radiative lifetime provides a safe indicator for unity IQE, proving the absence of nonradiative recombination at low temperature. In principle, also the comparison of measured photoluminescence intensities could provide a measure for the quantum efficiency, especially for continuous-wave photoluminescence. The present results indicate that the sample geometry, and particularly the thickness of a GaN cap layer on top of the quantum well, affect the collected intensities. Although an optical effect, regarding interference with backscattered light, might explain the observed difference in intensity, further clarification is needed in this respect. At least samples with the same cap layer thickness and sample geometry should be comparable, also on an absolute scale.

In summary, the radiative recombination was found to be dominated not only by the internal polarization fields, or the QCSE. Particularly in nonpolar GaInN/GaN quantum wells, the excitonic binding, the change in effective mass induced by anisotropic strain, and the well width contribute equally, which often remains unconsidered. Strain plays a crucial, yet ambivalent role, for radiative and nonradiative recombination. While it can enhance the radiative rate in nonpolar structures, it is responsible for the formation of strain-induced defects in the quantum well, which in turn act as nonradiative recombination centers. In this sense, the present findings, together with previous results on polar structures, provide a better understanding of the origin of nonradiative recombination in quantum wells, and show the importance of strain management. In consequence, an appropriate buffer layer can reduce the amount of strain, together with the nonradiative recombination, in the quantum well structure. Furthermore, thin quantum wells should be preferred, also on non- and semipolar crystal orientations, in order to maximize the radiative emission. Additionally, a sufficient carrier confinement is needed to avoid the loss of charge carriers into the barrier material. Future work might concentrate on the optimization of AlInN buffer layers, which are not yet optimized for maximum strain reduction. At the same time, the structural characterization by X-ray diffraction and transmission electron microscopy should give valuable insights into the mechanisms of strain reduction.

Finally, the temperature dependence of radiative and nonradiative lifetime was successfully modeled, regarding different regimes from cryogenic temperatures to room temperature and beyond. Using the distinct temperature dependence of the carrier lifetimes, it allows to exclude remaining nonradiative recombination at low temperatures, or even to quantify it compared to the radiative recombination. Nevertheless, a better comparability of absolute photoluminescence intensities would allow to verify efficiency measurements of arbitrary quantum well structures. The present results emphasize that, in many cases, remaining nonradiative recombination at cryogenic temperatures needs to be regarded, which provides a starting point for future growth optimization. After all, the presented method makes the determination of the internal quantum efficiency possible on an absolute scale.

APPENDIX

A

SAMPLE OVERVIEW

Listing of all GaInN/GaN quantum well samples that are investigated in this thesis, including nonpolar m-plane (M..., W...), a-plane (A...), and semipolar $(11\bar{2}2)$ structures (S...), as well as c-plane samples (C...). The corresponding BS... number, assigned during MOVPE growth, is listed, together with the reference for sample preparation.

Sample	BS name
M1	BS1872[c]
M2	BS2358[d]
M3	BS2578[d]
M4	BS2665[d]
M5	BS2721[b]
M6	BS2746[b]
M7	BS2747[b]
M8	BS2854[b]
M9	BS2859[b]
W1	BS2895[b]
W2	BS2896[b]
W3	BS2898[b]
W4	BS2899[b]
A1	BS1881[c]
A2	BS1886[c]
S1	BS2716[b]
S2	BS2869[b]
S3	BS2717[b]
S4	BS2879[b]
S5	BS2719[b]
S6	BS2126[c]
S7	BS2172[c]
S8	BS2177[c]
S9	BS2356[d]
S10	BS2360[d]
C1	BS1409[a]
C2	BS1558[c]
C3	BS1319[e]
C4	BS2033[c]
C5	BS1986[c]
C6	BS1724[c]
C7	BS1723[c]
C8	BS1557[c]
C9	BS1185[e]
C10	BS1917[c]
C11	BS2242[c]
C12	BS2234[c]
C13	BS2235[c]
C14	BS2254[c]
C15	BS2261[a]
C16	BS2304[c]
C17	BS2315[c]
C18	BS2482[d]
C19	BS2498[d]
C20	BS2500[d]
C21	BS2520[d]
C22	BS2659[d]
C23	BS2658[d]
C24	BS2661[d]
C25	BS2957[b]
C26	BS3003[b]
C27	BS3012[b]
C28	BS3019[b]
C29	BS3029[b]
C30	BS3059[b]
C31	BS3053[b]
C32	BS3054[b]
C33	BS3056[b]

[a] Ref. [90]
[b] Ref. [91]
[c] Ref. [92]
[d] Ref. [93]
[e] Ref. [94]

B

NOTATION

FREQUENTLY USED SYMBOLS

A_i	effective-mass parameter
a_B	exciton Bohr radius
B	coefficient of radiative recombination
$C_\mathrm{n/p}$	capture probability for electrons/holes
$\mathbf{C}$	elastic tensor
$c_\mathrm{n/p}$	capture coefficient for electrons/holes
c_0	speed of light in vacuum
D	density of states
D_i	deformation potential
d	dimension
E	energy
$E_\mathrm{F,e/h}$	quasi-Fermi energy of electrons/holes
F	electric field
$f_\mathrm{e/h}$	occupation probability for electrons/holes
G	generation rate
$\mathbf{G}_\mathrm{hkl}$	reciprocal lattice vector
H	Hamiltonian
I_0	initial intensity at zero delay
$\mathbf{k}$	wave vector
L	layer thickness
M	overlap integral
$m_\mathrm{e/h}$	effective mass of electrons/holes
n	electron concentration (per volume)
$\tilde{n}$	refractive index
N_D	doping level (n-type)
P	polarization

p	hole concentration (per volume)
$\mathbf{p}$	momentum operator
p_{cv}	momentum matrix element
$\mathbf{Q}$, $\mathbf{q}$	(reduced) diffraction vector, $q = Q/2\pi$
R	recombination rate
$\mathbf{R}$	vector of center-of-mass coordinate
$\mathbf{r}$	vector of spatial coordinate
T	temperature
t	time, delay
U	crystal-periodic part of a Bloch function
u	strain energy density
V	potential
$\tilde{V}$	crystal volume
x	exciton density
x, y	InN mole fraction in $\mathrm{Ga_{1-x}In_xN}$ and $\mathrm{Al_{1-y}In_yN}$ alloys
x, y, z	Cartesian coordinate system, corresponding to a-, m-, c-directions in the wurtzite structure
n, i, j	non-negative integers
γ	prefactor in various fit functions
ε_{r}	material-specific dielectric constant
δ_{ij}	Kronecker delta
$\boldsymbol{\varepsilon}$	strain tensor
λ	wavelength
θ	diffraction angle (in x-ray characterization)
ξ	wave function of the exciton relative motion
$\boldsymbol{\rho}$	vector of relative electron-hole distance
τ	lifetime
ω	angular frequency (of photons)
$\phi_{\mathrm{e/h}}$	envelope function of electrons/holes
$\varphi_{\mathrm{e/h}}$	Bloch function
ψ	wave function
$\boldsymbol{\sigma}$	stress tensor

ABBREVIATIONS

CB	conduction band
cw	continuous wave
IQE	internal quantum efficiency
MOVPE	metal-organic vapor phase epitaxy
MQW	multi-quantum well
PL	photoluminescence
QCSE	quantum-confined Stark effect
QW	quantum well
SRH	Shockley-Read-Hall
TEM	transmission electron microscopy
VB	valence band
XRD	X-ray diffraction

PHYSICAL CONSTANTS

c_0	speed of light in vacuum	$c_0 = 299\,792\,458\,\mathrm{m/s}$
ε_0	vacuum permittivity	$\varepsilon_0 = 8.854\,188\,\mathrm{A\,s/(V\,m)}$
$\hbar$	reduced Planck constant	$\hbar = 6.582\,12\,\mathrm{eV\,s}$
k_B	Boltzmann constant	$k_\mathrm{B} = 8.617\,333\,\mathrm{eV/K}$
m_0	electron rest mass	$m_0 = 9.109\,384\,\mathrm{kg}$

(CODATA 2018 [193])

BIBLIOGRAPHY

[1] *Press release of the Royal Swedish Academy of Sciences, Oct 2014*, (Online; accessed 2020-09-30), `http://www.nobelprize.org/nobel_prizes/physics/laureates/2014/press.html`.

[2] S. Nakamura, M. Senoh, N. Iwasa, and S. Nagahama, "High-brightness InGaN blue, green and yellow light-emitting diodes with quantum well structures", Jpn. J. Appl. Phys. **34**, L797 (1995).

[3] M. Kneissl, T.-Y. Seong, J. Han, and H. Amano, "The emergence and prospects of deep-ultraviolet light-emitting diode technologies", Nat. Photonics **13**, 233 (2019).

[4] K. Kishino, J. Kamimura, and K. Kamiyama, "Near-infrared InGaN nanocolumn light-emitting diodes operated at 1.46 μm", Appl. Phys Express **5**, 031001 (2012).

[5] H. Morkoç, *Handbook of nitride semiconductors and devices*, Vol. 1 (Wiley-VCH, Weinheim, 2008).

[6] H. P. Maruska and J. J. Tietjen, "The preparation and properties of vapor-deposited single-crystalline GaN", Appl. Phys. Lett. **15**, 327 (1969).

[7] H. Amano, N. Sawaki, I. Akasaki, and Y. Toyoda, "Metalorganic vapor phase epitaxial growth of a high quality GaN film using an AlN buffer layer", Appl. Phys. Lett. **48**, 353 (1986).

[8] T. Takeuchi, S. Sota, M. Katsuragawa, M. Komori, H. Takeuchi, H. Amano, and I. Akasaki, "Quantum-confined Stark effect due to piezoelectric fields in GaInN strained quantum wells", Jpn. J. Appl. Phys. **36**, L382 (1997).

[9] T. Langer, H. Jönen, A. Kruse, H. Bremers, U. Rossow, and A. Hangleiter, "Strain-induced defects as nonradiative recombination centers in green-emitting GaInN/GaN quantum well structures", Appl. Phys. Lett. **103**, 022108 (2013).

[10] T. Mukai, M. Yamada, and S. Nakamura, "Characteristics of InGaN-based UV/blue/green/amber/red light-emitting diodes", Jpn. J. Appl. Phys. **38**, 3976 (1999).

[11] T. Langer, A. Chernikov, D. Kalincev, M. Gerhard, H. Bremers, U. Rossow, M. Koch, and A. Hangleiter, "Room temperature excitonic recombination in GaInN/GaN quantum wells", Appl. Phys. Lett. **103**, 202106 (2013).

[12] A. David, N. G. Young, C. A. Hurni, and M. D. Craven, “All-optical measurements of carrier dynamics in bulk-GaN LEDs: Beyond the ABC approximation”, Appl. Phys. Lett. **110**, 253504 (2017).

[13] A. David, N. G. Young, C. Lund, and M. D. Craven, “Review—The Physics of Recombinations in III-Nitride Emitters”, ECS J. Solid State Sci. Technol. **9**, 016021 (2020).

[14] A. Hangleiter, T. Langer, P. Henning, F. A. Ketzer, H. Bremers, and U. Rossow, “Internal quantum efficiency of nitride light emitters: a critical perspective”, Proc. SPIE **10532**, 105321P (2018).

[15] I. Vurgaftman and J. R. Meyer, *Nitride semiconductor devices: principles and simulation*, edited by J. Piprek (WILEY-VCH, Weinheim, 2007) Chap. 2: Electron Bandstructure Parameters.

[16] J. Wu, W. Walukiewicz, K. M. Yu, J. W. Ager, E. E. Haller, H. Lu, and W. J. Schaff, “Small band gap bowing in $In_xGa_{1-x}N$ alloys”, Appl. Phys. Lett. **80**, 4741 (2002).

[17] V. Davydov, A. Klochikhin, V. Emtsev, S. Ivanov, V. Vekshin, F. Bechstedt, J. Furthmüller, H. Harima, A. Mudryi, A. Hashimoto, A. Yamamoto, J. Aderhold, J. Graul, and E. Haller, “Band Gap of InN and In-Rich $In_xGa_{1-x}N$ alloys $(0.36 < x < 1)$”, phys. status solidi (b) **230**, R4 (2002).

[18] R. Gross and A. Marx, *Festkörperphysik* (Oldenbourg Verlag, München, 2012).

[19] V. Darakchieva, B. Monemar, and A. Usui, “On the lattice parameters of GaN”, Appl. Phys. Lett. **91**, 031911 (2007).

[20] W. Paszkowicz, R. Černý, and S. Krukowski, “Rietveld refinement for indium nitride in the 105–295 K range”, Powder Diffr. **18**, 114 (2003).

[21] W. Paszkowicz, S. Podsiadło, and R. Minikayev, “Rietveld-refinement study of aluminium and gallium nitrides”, J. Alloys Compd. **382**, Proceedings of the European Materials Research Society Fall Meeting, Symposium B, 100 (2004).

[22] L. Vegard, “Die Konstitution der Mischkristalle und die Raumfüllung der Atome”, Zeitschrift für Physik **5**, 17 (1921).

[23] P. Perlin, C. Jauberthie-Carillon, J. P. Itie, A. San Miguel, I. Grzegory, and A. Polian, “Raman scattering and x-ray-absorption spectroscopy in gallium nitride under high pressure”, Phys. Rev. B **45**, 83 (1992).

[24] Y.-N. Xu and W. Y. Ching, “Electronic, optical, and structural properties of some wurtzite crystals”, Phys. Rev. B **48**, 4335 (1993).

[25] J. Als-Nielsen and D. McMorrow, *Elements of modern X-ray physics* (Wiley, 2011).

[26] P. Waltereit, O. Brandt, A. Trampert, H. T. Grahn, J. Menniger, M. Ramsteiner, M. Reiche, and K. H. Ploog, “Nitride semiconductors free of electrostatic fields for efficient white light-emitting diodes”, Nature **406**, 865 (2000).

[27] A. E. Romanov, E. C. Young, F. Wu, A. Tyagi, C. S. Gallinat, S. Nakamura, S. P. DenBaars, and J. S. Speck, “Basal plane misfit dislocations and stress relaxation in III-nitride semipolar heteroepitaxy”, J. Appl. Phys. **109**, 103522 (2011).

[28] S.-H. Park and S.-L. Chuang, “Crystal-orientation effects on the piezoelectric field and electronic properties of strained wurtzite semiconductors”, Phys. Rev. B **59**, 4725 (1999).

[29] J. F. Nye, *Physical properties of crystals* (Oxford: Clarendon Press, 1957).

[30] F. Morales, D. González, J. Lozano, R. García, S. Hauguth-Frank, V. Lebedev, V. Cimalla, and O. Ambacher, “Determination of the composition of $In_xGa_{1-x}N$ from strain measurements”, Acta Mater. **57**, 5681 (2009).

[31] J. Mánuel, F. Morales, J. Lozano, D. González, R. García, T. Lim, L. Kirste, R. Aidam, and O. Ambacher, “Structural and compositional homogeneity of InAlN epitaxial layers nearly lattice-matched to GaN”, Acta Materialia **58**, 4120 (2010).

[32] H. Jönen, H. Bremers, U. Rossow, T. Langer, A. Kruse, L. Hoffmann, J. Thalmair, J. Zweck, S. Schwaiger, F. Scholz, and A. Hangleiter, “Analysis of indium incorporation in non- and semipolar GaInN QW structures: comparing x-ray diffraction and optical properties”, Semicond. Sci. Technol. **27**, 024013 (2012).

[33] J. Matthews and A. Blakeslee, “Defects in epitaxial multilayers: I. Misfit dislocations”, J. Cryst. Growth **27**, 118 (1974).

[34] D. Holec, P. Costa, M. Kappers, and C. Humphreys, “Critical thickness calculations for InGaN/GaN”, J. Cryst. Growth **303**, Proceedings of the Fifth Workshop on Modeling in Crystal Growth, 314 (2007).

[35] T. Kehagias, P. Komninou, G. Nouet, P. Ruterana, and T. Karakostas, “Misfit relaxation of the AlN/Al_2O_3 (0001) interface”, Phys. Rev. B **64**, 195329 (2001).

[36] A. Tyagi, F. Wu, E. C. Young, A. Chakraborty, H. Ohta, R. Bhat, K. Fujito, S. P. DenBaars, S. Nakamura, and J. S. Speck, “Partial strain relaxation via misfit dislocation generation at heterointerfaces in (Al,In)GaN epitaxial layers grown on semipolar $(11\bar{2}2)$ GaN free standing substrates”, Appl. Phys. Lett. **95**, 251905 (2009).

[37] O. Ambacher, J. Majewski, C. Miskys, A. Link, M. Hermann, M. Eickhoff, M. Stutzmann, F. Bernardini, V. Fiorentini, V. Tilak, B. Schaff, and L. F. Eastman, "Pyroelectric properties of Al(In)GaN/GaN hetero- and quantum well structures", J. Phys.: Condens. Matter **14**, 3399 (2002).

[38] G. Bastard, *Wave mechanics applied to semiconductor heterostructures*, Monographies de physique (Les Éd. de Physique, Les Ulis Cedex, 1996).

[39] M. Suzuki and T. Uenoyama, "Strain effect on electronic and optical properties of GaN/AlGaN quantum-well lasers", J. Appl. Phys. **80**, 6868 (1996).

[40] T. O. Woodruff, *The orthogonalized plane-wave method*, edited by F. Seitz and D. Turnbull, Vol. 4, Solid State Physics (Academic Press, 1957), pp. 367–411.

[41] J. C. Phillips and L. Kleinman, "New method for calculating wave functions in crystals and molecules", Phys. Rev. **116**, 287 (1959).

[42] W. Harrison, *Solid state theory*, Dover Books on Physics (Dover Publications, 1980).

[43] J. C. Slater, "Wave functions in a periodic potential", Phys. Rev. **51**, 846 (1937).

[44] S. L. Chuang, *Physics of optoelectronic devices* (Wiley, New York, 1995).

[45] J. Bardeen, "An improved calculation of the energies of metallic Li and Na", The Journal of Chemical Physics **6**, 367 (1938).

[46] F. Seitz, *The modern theory of solids*, 1st ed. (McGraw-Hill, 1940).

[47] J. M. Luttinger and W. Kohn, "Motion of electrons and holes in perturbed periodic fields", Phys. Rev. **97**, 869 (1955).

[48] E. O. Kane, "Band structure of indium antimonide", J. Phys. Chem. Solids **1**, 249 (1957).

[49] E. I. Rashba, "Simmetriya energeticheskikh zon v kristallakh tipa vyurtsita. i. simmetriya zon bez ucheta spin-orbitalnogo vzaimodeistviya", Fizika tverd. tela **1**, 407 (1959).

[50] E. I. Rashba and V. I. Sheka, "Simmetriya energeticheskikh zon v kristallakh tipa vyurtsita. ii. simmetriya zon s uchyotom spinovykh vzaimodeistvii", Fizika tverd. tela **1**, 162 (1959).

[51] G. E. Pikus and G. L. Bir, "Effects of deformation on the hole energy spectrum of germanium and silicon", Sov. Phys-Solid State **1**, 1502 (1960).

[52] G. L. Bir and G. E. Pikus, *Symmetry and strain-induced effects in semiconductors* (Wiley, 1974).

[53] S. L. Chuang and C. S. Chang, "k·p method for strained wurtzite semiconductors", Phys. Rev. B **54**, 2491 (1996).

[54] Y. M. Sirenko, J.-B. Jeon, K. W. Kim, M. A. Littlejohn, and M. A. Stroscio, "Envelope-function formalism for valence bands in wurtzite quantum wells", Phys. Rev. B **53**, 1997 (1996).

[55] G. B. Ren, Y. M. Liu, and P. Blood, "Valence-band structure of wurtzite GaN including the spin-orbit interaction", Appl. Phys. Lett. **74**, 1117 (1999).

[56] J. D. Albrecht, P. P. Ruden, and T. L. Reinecke, "Hole scattering near the valence band edge in wurtzite gallium nitride", J. Appl. Phys. **92**, 3803 (2002).

[57] P.-O. Löwdin, "A note on the quantum-mechanical perturbation theory", The Journal of Chemical Physics **19**, 1396 (1951).

[58] W. G. Scheibenzuber, U. T. Schwarz, R. G. Veprek, B. Witzigmann, and A. Hangleiter, "Calculation of optical eigenmodes and gain in semipolar and nonpolar InGaN/GaN laser diodes", Phys. Rev. B **80**, 115320 (2009).

[59] P. Rinke, M. Winkelnkemper, A. Qteish, D. Bimberg, J. Neugebauer, and M. Scheffler, "Consistent set of band parameters for the group-III nitrides AlN, GaN, and InN", Phys. Rev. B **77**, 075202 (2008).

[60] Q. Yan, P. Rinke, M. Winkelnkemper, A. Qteish, D. Bimberg, M. Scheffler, and C. G. V. de Walle, "Band parameters and strain effects in ZnO and group-III nitrides", Semicond. Sci. Technol. **26**, 014037 (2010).

[61] R. Ishii, A. Kaneta, M. Funato, Y. Kawakami, and A. A. Yamaguchi, "All deformation potentials in GaN determined by reflectance spectroscopy under uniaxial stress: Definite breakdown of the quasicubic approximation", Phys. Rev. B **81**, 155202 (2010).

[62] P. K. Basu, *Theory of optical processes in semiconductors: bulk and microstructures*, Series on semiconductor science and technology (Clarendon Press, Oxford, 1997).

[63] Numerical Schrödinger solver developed by Andreas Hangleiter, capable of calculating energy levels and wave functions in a quantum well. Wave function overlap and transition energies are derived as well. Furthermore, exciton binding energies are calculated using a variational approach.

[64] G. Martin, A. Botchkarev, A. Rockett, and H. Morkoç, "Valence-band discontinuities of wurtzite GaN, AlN, and InN heterojunctions measured by x-ray photoemission spectroscopy", Appl. Phys. Lett. **68**, 2541 (1996).

[65] A. S. Barker and M. Ilegems, "Infrared lattice vibrations and free-electron dispersion in GaN", Phys. Rev. B **7**, 743 (1973).

[66] A. Zubrilov, “Properties of advanced semiconductor materials: GaN, AIN, InN, BN, SiC, SiGe”, in, edited by M. Levinshtein, S. Rumyantsev, and M. Shur (Wiley, 2001) Chap. 3: Indium Nitride.

[67] A. Hangleiter, F. Hitzel, S. Lahmann, and U. Rossow, “Composition dependence of polarization fields in GaInN/GaN quantum wells”, Appl. Phys. Lett. **83**, 1169 (2003).

[68] W. Scheibenzuber, *GaN-based Laser Diodes: Towards Longer Wavelengths and Short Pulses*, PhD thesis at University of Freiburg (2011).

[69] G. Lasher and F. Stern, “Spontaneous and stimulated recombination radiation in semiconductors”, Phys. Rev. **133**, A553 (1964).

[70] C. G. V. de Walle, C. Stampfl, and J. Neugebauer, “Theory of doping and defects in III–V nitrides”, J. Cryst. Growth **189-190**, 505 (1998).

[71] T. Zhu and R. A. Oliver, “Unintentional doping in GaN”, Phys. Chem. Chem. Phys. **14**, 9558 (2012).

[72] J. Feldmann, G. Peter, E. O. Göbel, P. Dawson, K. Moore, C. Foxon, and R. J. Elliott, “Linewidth dependence of radiative exciton lifetimes in quantum wells”, Phys. Rev. Lett. **59**, 2337 (1987).

[73] M. Shinada and S. Sugano, “Interband optical transitions in extremely anisotropic semiconductors. I. bound and unbound exciton absorption”, J. Phys. Soc. Jpn. **21**, 1936 (1966).

[74] P. T. Landsberg, *Recombination in semiconductors* (Cambridge Univ. Press, Cambridge, 1991).

[75] J. Piprek, “Efficiency droop in nitride-based light-emitting diodes”, phys. status solidi (a) **207**, 2217 (2010).

[76] Y. C. Shen, G. O. Mueller, S. Watanabe, N. F. Gardner, A. Munkholm, and M. R. Krames, “Auger recombination in InGaN measured by photoluminescence”, Appl. Phys. Lett. **91**, 141101 (2007).

[77] K. T. Delaney, P. Rinke, and C. G. Van de Walle, “Auger recombination rates in nitrides from first principles”, Appl. Phys. Lett. **94**, 191109 (2009).

[78] E. Kioupakis, P. Rinke, K. T. Delaney, and C. G. Van de Walle, “Indirect auger recombination as a cause of efficiency droop in nitride light-emitting diodes”, Appl. Phys. Lett. **98**, 161107 (2011).

[79] J. Iveland, L. Martinelli, J. Peretti, J. S. Speck, and C. Weisbuch, “Direct measurement of Auger electrons emitted from a semiconductor light-emitting diode under electrical injection: identification of the dominant mechanism for efficiency droop”, Phys. Rev. Lett. **110**, 177406 (2013).

[80] M.-H. Kim, M. F. Schubert, Q. Dai, J. K. Kim, E. F. Schubert, J. Piprek, and Y. Park, "Origin of efficiency droop in GaN-based light-emitting diodes", Appl. Phys. Lett. **91**, 183507 (2007).

[81] M. Brendel, A. Kruse, H. Jönen, L. Hoffmann, H. Bremers, U. Rossow, and A. Hangleiter, "Auger recombination in GaInN/GaN quantum well laser structures", Appl. Phys. Lett. **99**, 031106 (2011).

[82] W. Shockley and W. T. Read, "Statistics of the recombinations of holes and electrons", Phys. Rev. **87**, 835 (1952).

[83] R. N. Hall, "Electron-hole recombination in germanium", Phys. Rev. **87**, 387 (1952).

[84] A. J. Fischer, W. Shan, J. J. Song, Y. C. Chang, R. Horning, and B. Goldenberg, "Temperature-dependent absorption measurements of excitons in GaN epilayers", Appl. Phys. Lett. **71**, 1981 (1997).

[85] M. Lax, "Cascade capture of electrons in solids", Phys. Rev. **119**, 1502 (1960).

[86] C. H. Henry and D. V. Lang, "Nonradiative capture and recombination by multiphonon emission in GaAs and GaP", Phys. Rev. B **15**, 989 (1977).

[87] K. Huang, A. Rhys, and N. F. Mott, "Theory of light absorption and non-radiative transitions in F-centres", Proc. R. Soc. Lond. A **204**, 406 (1950).

[88] R. Pässler, "Temperature dependences of the nonradiative multiphonon carrier capture and ejection properties of deep traps in semiconductors. I. Theoretical results", Phys. Status Solidi B **85**, 203 (1978).

[89] W. A. Melton and J. I. Pankove, "GaN growth on sapphire", J. Cryst. Growth **178**, 168 (1997).

[90] Samples prepared by Uwe Rossow, Institute of Applied Physics, TU Braunschweig.

[91] Samples prepared by Philipp Horenburg and Uwe Rossow, Institute of Applied Physics, TU Braunschweig.

[92] Samples prepared by Holger Jönen and Uwe Rossow, Institute of Applied Physics, TU Braunschweig.

[93] Samples prepared by Ernst Ronald Korn and Uwe Rossow, Institute of Applied Physics, TU Braunschweig.

[94] Samples prepared by Daniel Fuhrmann and Uwe Rossow, Institute of Applied Physics, TU Braunschweig.

[95] P. Kidd, *XRD of gallium nitride and related compounds: strain, composition and layer thickness*, PANalytical, 2009.

[96] X-ray diffraction measurements carried out by Heiko Bremers, Institute of Applied Physics, TU Braunschweig.

[97] X-ray diffraction measurements carried out by Philipp Horenburg and Heiko Bremers, Institute of Applied Physics, TU Braunschweig.

[98] H. Bremers, A. Schwiegel, L. Hoffmann, H. Jönen, U. Rossow, J. Thalmair, J. Zweck, and A. Hangleiter, "X-ray composition analysis of nonpolar GaInN/GaN multiple quantum well structures", phys. status solidi (b) **248**, 616 (2011).

[99] M. A. Moram and M. E. Vickers, "X-ray diffraction of III-nitrides", Rep. Prog. Phys. **72**, 036502 (2009).

[100] H. Morkoç, *Handbook of nitride semiconductors and devices*, Vol. 2 (Wiley-VCH, Weinheim, 2008).

[101] Time-resolved photoluminescence measurements carried out by Torsten Langer, Institute of Applied Physics, TU Braunschweig.

[102] Time-resolved photoluminescence measurements carried out by Manuela Klisch, Institute of Applied Physics, TU Braunschweig.

[103] D. G. Thomas, J. J. Hopfield, and W. M. Augustyniak, "Kinetics of radiative recombination at randomly distributed donors and acceptors", Phys. Rev. **140**, A202 (1965).

[104] A. Morel, P. Lefebvre, S. Kalliakos, T. Taliercio, T. Bretagnon, and B. Gil, "Donor-acceptor-like behavior of electron-hole pair recombinations in low-dimensional (Ga,In)N/GaN systems", Phys. Rev. B **68**, 045331 (2003).

[105] T. Kuroda and A. Tackeuchi, "Influence of free carrier screening on the luminescence energy shift and carrier lifetime of InGaN quantum wells", J. Appl. Phys. **92**, 3071 (2002).

[106] T. Langer, H. Jönen, D. Fuhrmann, U. Rossow, and A. Hangleiter, "Recombination of free excitons in polar and nonpolar nitride quantum wells", J. Phys. Conf. Ser. **210**, 012056 (2010).

[107] T. Langer, *Strahlende und strahlungslose Rekombinationsprozesse in Gruppe-III-Nitrid Quantenfilmen*, PhD thesis at Technische Universität Braunschweig (Shaker, Aachen, 2015).

[108] K. Kůsová and T. Popelář, "On the importance of onset times and multiple-wavelength analysis of photoluminescence decays", J. Appl. Phys. **125**, 193103 (2019).

[109] H. Morkoç, *Handbook of nitride semiconductors and devices*, Vol. 3 (Wiley-VCH, Weinheim, 2009).

[110] S. Chichibu, T. Azuhata, T. Sota, and S. Nakamura, “Spontaneous emission of localized excitons in InGaN single and multiquantum well structures”, Appl. Phys. Lett. **69**, 4188 (1996).

[111] Y. Narukawa, Y. Kawakami, M. Funato, S. Fujita, S. Fujita, and S. Nakamura, “Role of self-formed InGaN quantum dots for exciton localization in the purple laser diode emitting at 420 nm”, Appl. Phys. Lett. **70**, 981 (1997).

[112] S. F. Chichibu, A. C. Abare, M. S. Minsky, S. Keller, S. B. Fleischer, J. E. Bowers, E. Hu, U. K. Mishra, L. A. Coldren, S. P. DenBaars, and T. Sota, “Effective band gap inhomogeneity and piezoelectric field in InGaN/GaN multiquantum well structures”, Appl. Phys. Lett. **73**, 2006 (1998).

[113] K. P. O’Donnell, R. W. Martin, and P. G. Middleton, “Origin of luminescence from InGaN diodes”, Phys. Rev. Lett. **82**, 237 (1999).

[114] Y. Kawakami, Y. Narukawa, K. Omae, S. Fujita, and S. Nakamura, “Dimensionality of excitons in InGaN-based light emitting devices”, phys. status solidi (a) **178**, 331 (2000).

[115] N. Grandjean, B. Damilano, and J. Massies, “Group-III nitride quantum heterostructures grown by molecular beam epitaxy”, J. Phys.: Condens. Matter **13**, 6945 (2001).

[116] S. Dhar, U. Jahn, O. Brandt, P. Waltereit, and K. Ploog, “Effect of exciton localization on the quantum efficiency of GaN/(In,Ga)N multiple quantum wells”, phys. status solidi (a) **192**, 85 (2002).

[117] D. M. Graham, A. Soltani-Vala, P. Dawson, M. J. Godfrey, T. M. Smeeton, J. S. Barnard, M. J. Kappers, C. J. Humphreys, and E. J. Thrush, “Optical and microstructural studies of InGaN/GaN single-quantum-well structures”, J. Appl. Phys. **97**, 103508 (2005).

[118] D. Watson-Parris, M. J. Godfrey, P. Dawson, R. A. Oliver, M. J. Galtrey, M. J. Kappers, and C. J. Humphreys, “Carrier localization mechanisms in $In_xGa_{1-x}N$/GaN quantum wells”, Phys. Rev. B **83**, 115321 (2011).

[119] T. Schulz, T. Remmele, T. Markurt, M. Korytov, and M. Albrecht, “Analysis of statistical compositional alloy fluctuations in InGaN from aberration corrected transmission electron microscopy image series”, J. Appl. Phys. **112**, 033106 (2012).

[120] T. Langer, M. Klisch, F. A. Ketzer, H. Jönen, H. Bremers, U. Rossow, T. Meisch, F. Scholz, and A. Hangleiter, “Radiative and nonradiative recombination mechanisms in nonpolar and semipolar GaInN/GaN quantum wells”, phys. status solidi (b) **253**, 133 (2016).

[121] G. A. Garrett, H. Shen, M. Wraback, A. Tyagi, M. C. Schmidt, J. S. Speck, S. P. DenBaars, and S. Nakamaura, “Comparison of time-resolved photoluminescence from InGaN single quantum wells grown on nonpolar and semipolar bulk GaN substrates”, phys. status solidi (c) **6**, S800 (2009).

[122] A. Hangleiter, Z. Jin, M. Gerhard, D. Kalincev, T. Langer, H. Bremers, U. Rossow, M. Koch, M. Bonn, and D. Turchinovich, “Efficient formation of excitons in a dense electron-hole plasma at room temperature”, Phys. Rev. B **92**, 241305 (2015).

[123] W. Liu, R. Butté, A. Dussaigne, N. Grandjean, B. Deveaud, and G. Jacopin, “Carrier-density-dependent recombination dynamics of excitons and electron-hole plasma in m-plane InGaN/GaN quantum wells”, Phys. Rev. B **94**, 195411 (2016).

[124] K. Kojima, M. Funato, Y. Kawakami, and S. Noda, “Valence band effective mass of non-c-plane nitride heterostructures”, J. Appl. Phys. **107**, 123105 (2010).

[125] M. M. Y. Leung, A. B. Djurîšić, and E. H. Li, “Refractive index of InGaN/GaN quantum well”, J. Appl. Phys. **84**, 6312 (1998).

[126] Momentum matrix elements E_p for GaN and InN have been determined from experimental absorption spectra by Andreas Hangleiter, Institute of Applied Physics, TU Braunschweig.

[127] J.-F. Carlin, C. Zellweger, J. Dorsaz, S. Nicolay, G. Christmann, E. Feltin, R. Butté, and N. Grandjean, “Progresses in III-nitride distributed Bragg reflectors and microcavities using AlInN/GaN materials”, phys. status solidi (b) **242**, 2326 (2005).

[128] E. Feltin, R. Butte, J.-F. Carlin, J. Dorsaz, N. Grandjean, and M. Ilegems, “Lattice-matched distributed Bragg reflectors for nitride-based vertical cavity surface emitting lasers”, Electron. Lett. **41**, 94 (2005).

[129] R. Charash, H. Kim-Chauveau, A. Vajpeyi, M. Akther, P. P. Maaskant, E. Frayssinet, P. de Mierry, J.-Y. Duboz, and B. Corbett, “Current transport through AlInN/GaN multilayers used as n-type cladding layers in edge emitting laser diodes”, phys. status solidi (c) **8**, 2378 (2011).

[130] L. Zhou, M. R. McCartney, D. J. Smith, A. Mouti, E. Feltin, J. F. Carlin, and N. Grandjean, “Observation of dodecagon-shape V-defects in GaN/AlInN multiple quantum wells”, Appl. Phys. Lett. **97**, 161902 (2010).

[131] Q. Y. Wei, T. Li, Y. Huang, J. Y. Huang, Z. T. Chen, T. Egawa, and F. A. Ponce, “Compositional instability in InAlN/GaN lattice-matched epitaxy”, Appl. Phys. Lett. **100**, 092101 (2012).

[132] E. R. Buß, P. Horenburg, U. Rossow, H. Bremers, T. Meisch, M. Caliebe, F. Scholz, and A. Hangleiter, “Non- and semipolar AlInN one-dimensionally lattice-matched to GaN for realization of relaxed buffer layers for strain engineering in optically active GaN-based devices”, phys. status solidi (b) **253**, 84 (2016).

[133] P. Horenburg, E. R. Buß, U. Rossow, H. Bremers, F. A. Ketzer, and A. Hangleiter, “Strain dependence of In incorporation in m-oriented GaInN/GaN multi quantum well structures”, Appl. Phys. Lett. **108**, 102105 (2016).

[134] Y. J. Sun, O. Brandt, S. Cronenberg, S. Dhar, H. T. Grahn, K. H. Ploog, P. Waltereit, and J. S. Speck, “Nonpolar $In_xGa_{1-x}N/GaN$ $(1\bar{1}00)$ multiple quantum wells grown on γ-$LiAlO_2$ (110) by plasma-assisted molecular-beam epitaxy”, Phys. Rev. B **67**, 0401306 (2003).

[135] V. Liuolia, S. Marcinkevičius, Y.-D. Lin, H. Ohta, S. P. DenBaars, and S. Nakamura, “Dynamics of polarized photoluminescence in m-plane InGaN/GaN quantum wells”, J. Appl. Phys. **108**, 023101 (2010).

[136] D. Sutherland, T. Zhu, J. T. Griffiths, F. Tang, P. Dawson, D. Kundys, F. Oehler, M. J. Kappers, C. J. Humphreys, and R. A. Oliver, “Optical studies of non-polar m-plane $(1\bar{1}00)$ InGaN/GaN multi-quantum wells grown on freestanding bulk GaN”, phys. status solidi (b) **252**, 965 (2015).

[137] T. Zhu, D. Gachet, F. Tang, W. Y. Fu, F. Oehler, M. J. Kappers, P. Dawson, C. J. Humphreys, and R. A. Oliver, “Local carrier recombination and associated dynamics in m-plane InGaN/GaN quantum wells probed by picosecond cathodoluminescence”, Appl. Phys. Lett. **109**, 232103 (2016).

[138] T. Onuma, A. Chakraborty, B. A. Haskell, S. Keller, S. P. DenBaars, J. S. Speck, S. Nakamura, U. K. Mishra, T. Sota, and S. F. Chichibu, “Localized exciton dynamics in nonpolar $(11\bar{2}0)$ $In_xGa_{1-x}N$ multiple quantum wells grown on GaN templates prepared by lateral epitaxial overgrowth”, Appl. Phys. Lett. **86**, 151918 (2005).

[139] K.-C. Kim, M. C. Schmidt, H. Sato, F. Wu, N. Fellows, Z. Jia, M. Saito, S. Nakamura, S. P. DenBaars, J. S. Speck, and K. Fujito, “Study of nonpolar m-plane InGaN/GaN multiquantum well light emitting diodes grown by homoepitaxial metal-organic chemical vapor deposition”, Appl. Phys. Lett. **91**, 181120 (2007).

[140] S. Marcinkevičius, K. M. Kelchner, S. Nakamura, S. P. DenBaars, and J. S. Speck, “Optical properties of extended and localized states in m-plane InGaN quantum wells”, Appl. Phys. Lett. **102**, 101102 (2013).

[141] S. Marcinkevičius, K. M. Kelchner, L. Y. Kuritzky, S. Nakamura, S. P. DenBaars, and J. S. Speck, "Photoexcited carrier recombination in wide m-plane InGaN/GaN quantum wells", Appl. Phys. Lett. **103**, 111107 (2013).

[142] N. A. Pfaff, K. M. Kelchner, D. F. Feezell, S. Nakamura, S. P. DenBaars, and J. S. Speck, "Thermal performance of violet and blue single-quantum-well nonpolar m-plane InGaN light-emitting diodes", Appl. Phys Express **6**, 092104 (2013).

[143] S. Marcinkevičius, K. M. Kelchner, S. Nakamura, S. P. DenBaars, and J. S. Speck, "Optical properties and carrier dynamics in m-plane InGaN quantum wells", phys. status solidi (c) **11**, 690 (2014).

[144] M. Shahmohammadi, W. Liu, G. Rossbach, L. Lahourcade, A. Dussaigne, C. Bougerol, R. Butté, N. Grandjean, B. Deveaud, and G. Jacopin, "Enhancement of Auger recombination induced by carrier localization in InGaN/GaN quantum wells", Phys. Rev. B **95**, 125314 (2017).

[145] R. Ivanov, S. Marcinkevičius, T. K. Uždavinys, L. Y. Kuritzky, S. Nakamura, and J. S. Speck, "Scanning near-field microscopy of carrier lifetimes in m-plane InGaN quantum wells", Appl. Phys. Lett. **110**, 031109 (2017).

[146] R. Ivanov, S. Marcinkevičius, M. D. Mensi, O. Martinez, L. Y. Kuritzky, D. J. Myers, S. Nakamura, and J. S. Speck, "Polarization-resolved near-field spectroscopy of localized states in m-plane $In_xGa_{1-x}N$/GaN quantum wells", Phys. Rev. Applied **7**, 064033 (2017).

[147] Y. Huang, K. W. Sun, A. M. Fischer, Q. Y. Wei, R. Juday, F. A. Ponce, R. Kato, and T. Yokogawa, "Effect of misfit dislocations on luminescence in m-plane InGaN quantum wells", Appl. Phys. Lett. **98**, 261914 (2011).

[148] M. Fox and R. Ispasoiu, "Quantum wells, superlattices, and band-gap engineering", in *Springer handbook of electronic and photonic materials*, edited by S. Kasap and P. Capper (Springer International Publishing, 2017) Chap. 40.

[149] Y.-L. Li, Y.-R. Huang, and Y.-H. Lai, "Efficiency droop behaviors of InGaN/GaN multiple-quantum-well light-emitting diodes with varying quantum well thickness", Appl. Phys. Lett. **91**, 181113 (2007).

[150] F. A. Ketzer, P. Horenburg, P. Henning, E. R. Korn, H. Bremers, U. Rossow, and A. Hangleiter, "Control of optical polarization properties by manipulation of anisotropic strain in nonpolar m-plane GaInN/GaN quantum wells", Appl. Phys. Lett. **114**, 052101 (2019).

[151] L. C. Andreani, F. Tassone, and F. Bassani, "Radiative lifetime of free excitons in quantum wells", Solid State Commun. **77**, 641 (1991).

[152] Transmission electron microscopy measurements were carried out by Heiko Bremers, Institute of Applied Physics, TU Braunschweig, in collaboration with JEOL Germany.

[153] A. Hangleiter, T. Langer, P. Henning, F. A. Ketzer, P. Horenburg, E. R. Korn, H. Bremers, and U. Rossow, "Radiative recombination in polar, non-polar, and semi-polar III-nitride quantum wells", Proc. SPIE **101040**, 101040Q (2017).

[154] J. S. Im, H. Kollmer, O. Gfrörer, J. Off, F. Scholz, and A. Hangleiter, "Piezoelectric field effect on optical properties of GaN/GaInN/AlGaN quantum wells", MRS Internet J. Nitride Semicond. Res. **4**, 628 (1999).

[155] P. Michler, A. Hangleiter, M. Moser, M. Geiger, and F. Scholz, "Influence of barrier height on carrier lifetime in $Ga_{1-y}In_yP/(Al_xGa_{1-x})_{1-y}In_yP$ single quantum wells", Phys. Rev. B **46**, 7280 (1992).

[156] S. Lahmann, F. Hitzel, U. Rossow, and A. Hangleiter, "Analysis of quantum efficiency of high brightness GaInN/GaN quantum wells", phys. status solidi (c) **0**, 2202 (2003).

[157] T. Langer, H.-G. Pietscher, H. Bremers, U. Rossow, D. Menzel, and A. Hangleiter, "Nonradiative recombination due to point defects in GaInN/GaN quantum wells induced by Ar implantation", Proc. SPIE **8625**, 310 (2013).

[158] C. Netzel, H. Bremers, L. Hoffmann, D. Fuhrmann, U. Rossow, and A. Hangleiter, "Emission and recombination characteristics of $Ga_{1-x}In_xN/GaN$ well structures with nonradiative recombination suppression by V-shaped pits", Phys. Rev. B **76**, 5322 (2007).

[159] H. K. Cho, J. Y. Lee, G. M. Yang, and C. S. Kim, "Formation mechanism of V defects in the InGaN/GaN multiple quantum wells grown on GaN layers with low threading dislocation density", Appl. Phys. Lett. **79**, 215 (2001).

[160] H. K. Cho, J. Y. Lee, C. S. Kim, G. M. Yang, N. Sharma, and C. Humphreys, "Microstructural characterization of InGaN/GaN multiple quantum wells with high indium composition", J. Cryst. Growth **231**, 466 (2001).

[161] F. C.-P. Massabuau, S.-L. Sahonta, L. Trinh-Xuan, S. Rhode, T. J. Puchtler, M. J. Kappers, C. J. Humphreys, and R. A. Oliver, "Morphological, structural, and emission characterization of trench defects in InGaN/GaN quantum well structures", Appl. Phys. Lett. **101**, 212107 (2012).

[162] F. C.-P. Massabuau, L. Trinh-Xuan, D. Lodié, E. J. Thrush, D. Zhu, F. Oehler, T. Zhu, M. J. Kappers, C. J. Humphreys, and R. A. Oliver, "Correlations between the morphology and emission properties of trench defects in InGaN/GaN quantum wells", J. Appl. Phys. **113**, 073505 (2013).

[163] P. S. Hsu, M. T. Hardy, F. Wu, I. Koslow, E. C. Young, A. E. Romanov, K. Fujito, D. F. Feezell, S. P. DenBaars, J. S. Speck, and S. Nakamura, "444.9 nm semipolar $(11\bar{2}2)$ laser diode grown on an intentionally stress relaxed InGaN waveguiding layer", Appl. Phys. Lett. **100**, 021104 (2012).

[164] I. L. Koslow, M. T. Hardy, P. Shan Hsu, P.-Y. Dang, F. Wu, A. Romanov, Y.-R. Wu, E. C. Young, S. Nakamura, J. S. Speck, and S. P. DenBaars, "Performance and polarization effects in $(11\bar{2}2)$ long wavelength light emitting diodes grown on stress relaxed InGaN buffer layers", Appl. Phys. Lett. **101**, 121106 (2012).

[165] I. L. Koslow, C. McTaggart, F. Wu, S. Nakamura, J. S. Speck, and S. P. DenBaars, "Improved performance of $(20\bar{2}1)$ long-wavelength light-emitting diodes grown with wide quantum wells on stress-relaxed $In_xGa_{1-x}N$ buffer layers", Appl. Phys. Express **7**, 031003 (2014).

[166] E. R. Buß, U. Rossow, H. Bremers, T. Meisch, M. Caliebe, F. Scholz, and A. Hangleiter, "Intentional anisotropic strain relaxation in $(11\bar{2}2)$ oriented $Al_{1-x}In_xN$ one-dimensionally lattice matched to GaN", Appl. Phys. Lett. **105**, 122109 (2014).

[167] F. Wu, A. Tyagi, E. C. Young, A. E. Romanov, K. Fujito, S. P. DenBaars, S. Nakamura, and J. S. Speck, "Misfit dislocation formation at heterointerfaces in (Al,In)GaN heteroepitaxial layers grown on semipolar free-standing GaN substrates", J. Appl. Phys. **109**, 033505 (2011).

[168] P. S. Hsu, E. C. Young, A. E. Romanov, K. Fujito, S. P. DenBaars, S. Nakamura, and J. S. Speck, "Misfit dislocation formation via pre-existing threading dislocation glide in $(11\bar{2}2)$ semipolar heteroepitaxy", Appl. Phys. Lett. **99**, 081912 (2011).

[169] F. Tendille, P. D. Mierry, P. Vennéguès, S. Chenot, and M. Teisseire, "Defect reduction method in $(11\bar{2}2)$ semipolar GaN grown on patterned sapphire substrate by MOCVD: toward heteroepitaxial semipolar GaN free of basal stacking faults", J. Cryst. Growth **404**, 177 (2014).

[170] F. Tendille, D. Martin, P. Vennéguès, N. Grandjean, and P. De Mierry, "Selective heteroepitaxy on deeply grooved substrate: a route to low cost semipolar GaN platforms of bulk quality", Appl. Phys. Lett. **109**, 082101 (2016).

[171] C. Haller, J.-F. Carlin, G. Jacopin, D. Martin, R. Butté, and N. Grandjean, "Burying non-radiative defects in InGaN underlayer to increase InGaN/GaN quantum well efficiency", Appl. Phys. Lett. **111**, 262101 (2017).

[172] C. Haller, J.-F. Carlin, G. Jacopin, W. Liu, D. Martin, R. Butté, and N. Grandjean, "GaN surface as the source of non-radiative defects in InGaN/GaN quantum wells", Appl. Phys. Lett. **113**, 111106 (2018).

[173] C. Haller, J.-F. Carlin, M. Mosca, M. D. Rossell, R. Erni, and N. Grandjean, “InAlN underlayer for near ultraviolet InGaN based light emitting diodes”, Appl. Phys. Express **12**, 034002 (2019).

[174] T. Ogino and M. Aoki, “Mechanism of yellow luminescence in GaN”, Jpn. J. Appl. Phys. **19**, 2395 (1980).

[175] K. Saarinen, T. Laine, S. Kuisma, J. Nissilä, P. Hautojärvi, L. Dobrzynski, J. M. Baranowski, K. Pakula, R. Stepniewski, M. Wojdak, A. Wysmolek, T. Suski, M. Leszczynski, I. Grzegory, and S. Porowski, “Observation of native Ga vacancies in GaN by positron annihilation”, Phys. Rev. Lett. **79**, 3030 (1997).

[176] K. Saarinen, T. Suski, I. Grzegory, and D. C. Look, “Thermal stability of isolated and complexed Ga vacancies in GaN bulk crystals”, Phys. Rev. B **64**, 233201 (2001).

[177] S. F. Chichibu, A. Uedono, T. Onuma, T. Sota, B. A. Haskell, S. P. DenBaars, J. S. Speck, and S. Nakamura, “Limiting factors of room-temperature nonradiative photoluminescence lifetime in polar and nonpolar GaN studied by time-resolved photoluminescence and slow positron annihilation techniques”, Appl. Phys. Lett. **86**, 021914 (2005).

[178] S. C. Cruz, S. Keller, T. E. Mates, U. K. Mishra, and S. P. DenBaars, “Crystallographic orientation dependence of dopant and impurity incorporation in GaN films grown by metalorganic chemical vapor deposition”, J. Cryst. Growth **311**, 3817 (2009).

[179] D. A. Browne, E. C. Young, J. R. Lang, C. A. Hurni, and J. S. Speck, “Indium and impurity incorporation in InGaN films on polar, nonpolar, and semipolar GaN orientations grown by ammonia molecular beam epitaxy”, Journal of Vacuum Science & Technology A **30**, 041513 (2012).

[180] C. Trager-Cowan, F. Sweeney, P. W. Trimby, A. P. Day, A. Gholinia, N.-H. Schmidt, P. J. Parbrook, A. J. Wilkinson, and I. M. Watson, “Electron backscatter diffraction and electron channeling contrast imaging of tilt and dislocations in nitride thin films”, Phys. Rev. B **75**, 085301 (2007).

[181] M. A. Reshchikov and R. Y. Korotkov, “Analysis of the temperature and excitation intensity dependencies of photoluminescence in undoped GaN films”, Phys. Rev. B **64**, 115205 (2001).

[182] W. Grieshaber, E. F. Schubert, I. D. Goepfert, R. F. Karlicek, M. J. Schurman, and C. Tran, “Competition between band gap and yellow luminescence in GaN and its relevance for optoelectronic devices”, Journal of Applied Physics **80**, 4615 (1996).

[183] K. Kojima, H. Ikeda, K. Fujito, and S. F. Chichibu, "Demonstration of omnidirectional photoluminescence (ODPL) spectroscopy for precise determination of internal quantum efficiency of radiation in GaN single crystals", Appl. Phys. Lett. **111**, 032111 (2017).

[184] K. Kojima, K. Ikemura, and S. F. Chichibu, "Temperature dependence of internal quantum efficiency of radiation for the near-band-edge emission of GaN crystals quantified by omnidirectional photoluminescence spectroscopy", Appl. Phys Express **13**, 105504 (2020).

[185] A. A. Yamaguchi, T. Nakano, S. Sakai, H. Fukada, Y. Kanitani, and S. Tomiya, "Carrier dynamics studies of III-nitride materials using photo-acoustic and photoluminescence measurements", Proc. SPIE **10104**, edited by J.-I. Chyi, H. Fujioka, H. Morkoç, Y. Nanishi, U. T. Schwarz, and J.-I. Shim, 42 (2017).

[186] A. David and M. J. Grundmann, "Droop in InGaN light-emitting diodes: A differential carrier lifetime analysis", Appl. Phys. Lett. **96**, 103504 (2010).

[187] G.-B. Lin, Q. Shan, A. J. Birkel, J. Cho, E. Fred Schubert, M. H. Crawford, K. R. Westlake, and D. D. Koleske, "Method for determining the radiative efficiency of GaInN quantum wells based on the width of efficiency-versus-carrier-concentration curve", Appl. Phys. Lett. **101**, 241104 (2012).

[188] F. Nippert, S. Karpov, I. Pietzonka, B. Galler, A. Wilm, T. Kure, C. Nenstiel, G. Callsen, M. Straßburg, H.-J. Lugauer, and A. Hoffmann, "Determination of recombination coefficients in InGaN quantum-well light-emitting diodes by small-signal time-resolved photoluminescence", Jpn. J. Appl. Phys. **55**, 05FJ01 (2016).

[189] W. Liu, C. Haller, Y. Chen, T. Weatherley, J.-F. Carlin, G. Jacopin, R. Butté, and N. Grandjean, "Impact of defects on Auger recombination in c-plane InGaN/GaN single quantum well in the efficiency droop regime", Appl. Phys. Lett. **116**, 222106 (2020).

[190] The synchronous fit procedure was implemented with gnuplot, using the multi-branch fitting method, `http://www.gnuplot.info/docs_4.2/node91.html#fit_multi-branch`.

[191] Calculations of the absorption spectra were carried out by Shawutijiang Sidikejiang, Insitute of Applied Physics, TU Braunschweig, using a numerical self-consistent Poisson-Schrödinger solver developed by Andreas Hangleiter.

[192] P. Lavallard, "Light emission by semiconductor nanostructures in dielectric medium or close to plane interface", Acta Phys. Polonica A **90**, 645 (1996).

[193] P. J. Mohr, D. B. Newell, B. N. Taylor, and E. Tiesinga, *2018 CODATA Recommended Values of the Fundamental Physical Constants*, (Online; accessed 2020-06-30), (2019) `http://physics.nist.gov/constants`.

PUBLICATIONS

PRE-PUBLICATIONS IN PEER-REVIEWED JOURNALS

[1] P. Henning, P. Horenburg, H. Bremers, U. Rossow, F. Tendille, P. Vennégués, P. de Mierry, J. Zúñiga-Pérez, and A. Hangleiter, "Reduced nonradiative recombination in semipolar green-emitting III-N quantum wells with strain-reducing AlInN buffer layers", Appl. Phys. Lett. **115**, 202103 (2019).

[2] P. Henning, P. Horenburg, H. Bremers, U. Rossow, and A. Hangleiter, "Reduced radiative emission for wide nonpolar III-nitride quantum wells", Phys. Rev. B **99**, 205308 (2019).

OTHER PUBLICATIONS

[1] F. A. Ketzer, P. Horenburg, P. Henning, E. R. Korn, H. Bremers, U. Rossow, and A. Hangleiter, "Control of optical polarization properties by manipulation of anisotropic strain in nonpolar m-plane GaInN/GaN quantum wells", Appl. Phys. Lett. **114**, 052101 (2019).

[2] A. Hangleiter, T. Langer, P. Henning, F. A. Ketzer, H. Bremers, and U. Rossow, "Internal quantum efficiency of nitride light emitters: a critical perspective", Proc. SPIE **10532**, 105321P (2018).

[3] A. Hangleiter, T. Langer, P. Henning, F. A. Ketzer, P. Horenburg, E. R. Korn, H. Bremers, and U. Rossow, "Radiative recombination in polar, non-polar, and semi-polar III-nitride quantum wells", Proc. SPIE **101040**, 101040Q (2017).

CONFERENCE CONTRIBUTIONS

[1] P. Henning, D. Schmid, P. Horenburg, H. Bremers, U. Rossow, F. Tendille, P. Vennégués, P. de Mierry, J. Zúñiga-Pérez, and A. Hangleiter, "Reduced non-radiative recombination in semi-polar green-emitting III-N quantum wells with strain-reducing AlInN buffer layers", International Conference on Nitride Semiconductors, Seattle, USA (2019).

[2] P. Henning, T. Langer, F. A. Ketzer, S. Müllner, P. Horenburg, H. Bremers, U. Rossow, and A. Hangleiter, "Thermal activation of non-radiative recombination processes in III-nitride quantum wells", DPG Frühjahrstagung, Regensburg (2019).

[3] P. Henning, F. A. Ketzer, P. Horenburg, H. Bremers, U. Rossow, and A. Hangleiter, "Reduced radiative emission for wide non-polar III-nitride quantum wells", International Workshop on Nitride Semiconductors, Kanazawa, Japan (2018).

[4] P. Henning, F. A. Ketzer, P. Horenburg, H. Bremers, U. Rossow, and A. Hangleiter, "Effects of well width on the recombination dynamics in m-plane GaInN/GaN quantum wells", DPG Frühjahrstagung, Berlin (2018).

[5] P. Henning, T. Langer, M. Klisch, F. A. Ketzer, P. Horenburg, H. Bremers, U. Rossow, and A. Hangleiter, "Impact of strain on radiative and non-radiative recombination in m-plane GaInN/GaN quantum wells", International Conference on Nitride Semiconductors, Straßburg, France (2017).

[6] P. Henning, T. Langer, M. Klisch, F. A. Ketzer, P. Horenburg, H. Bremers, U. Rossow, and A. Hangleiter, "Impact of strain and valence band structure on radiative and non-radiative recombination in m-plane GaInN/GaN quantum wells", DPG Frühjahrstagung, Dresden (2017).

ACKNOWLEDGEMENTS

> *One shouldn't work on semiconductors, that is a filthy mess; who knows whether any semiconductors exist.*
>
> — W. Pauli, 1931

Fortunately, the world has proven Wolfgang Pauli wrong, and semiconductor research has made unbelievable progress in the past century, affecting every bit of our everyday life. And fortunately, I did not follow Pauli's advice, which gave me the opportunity to explore, and contribute to the fascinating field of semiconductor physics. Therefore, I would like to thank, first and foremost, Prof. Dr. Andreas Hangleiter for introducing me into his research group, for the patience, the support and the guidance during research, and for leaving me the room to work on my own. Sometimes, even a short discussion turned out more valuable than all physics textbooks, and for this reason I appreciated his open door on all occasions. Furthermore, Prof. Dr. Jürgen Gutowski deserves thanks as the second referee of this thesis, together with Prof. Dr. Christoph Karrasch, who readily took over the chair of the examination committee.

I would like to express my special thanks to Dr. Uwe Rossow and Dr. Heiko Bremers, with whom I had fruitful and long discussions that sometimes went beyond research topics. Their advice was a great help, and made this thesis move in the right direction.

My fellow colleague Philipp Horenburg, who accompanied me during my whole time at the Institute of Applied Physics, deserves special thanks. He was able to answer many questions on still more occasions, and on whatever topic. I would also like to thank my other coworkers, who breathed life into the corridors of our institute: Savut Sidik, André Schendel, Samar Hagag, and especially Rodrigo Vasconcellos, with whom I spent more than a few hours in the new laboratory.

I would like to acknowledge the technical staff of our institute: Diana Deuse, Ingeborg Westphal, Alexander Kneisel, Benjamin Ritter, and in particular Frank Werner and Richard Boettge, who ensured the supply of liquid helium, and manufactured a bunch of custom-made lab equipment. I would like to thank Markus Göthlich for helping me with my first measurement attempts, and of course Dr. Torsten Langer for his technical and specialized advice, although from far away. Additionally, I would like to acknowledge the help of Daniel Schmid, and thank all other members of our institute for their collaboration.

Also my former colleagues deserve special thanks: Dennis Mauch, Fedor Alexej Ketzer, and Christopher Hein, who gave me a warm welcome in the institute, and helped me on several occasions in the starting time. Furthermore, I would like to acknowledge the help of Dr. Thorben Dammeyer during the lab construction at LENA, and I would like to thank the scientists at CRHEA in Valbonne, France, for the collaboration.

Finally, I wish to thank my whole family for their support during the past ten years, when I began to study physics, and eventually, I want to thank Cathleen, my wonderful girlfriend.

CURRICULUM VITAE

PERSONAL DATA

Name	Philipp Henning
Date of Birth	October 23, 1990
Place of Birth	Kassel, Germany
Citizen of	Germany

RESEARCH & EDUCATION

since 08/2016	**PhD candidate**, Insitute of Applied Physics, Group of Prof. Andreas Hangleiter, Technische Universität Braunschweig
10/2013 – 07/2016	**Physics (M.Sc.)**, Georg-August-Universität Göttingen *Master's thesis:* Selective area growth of Ga-polar GaN nanocolumns (supervised by Prof. Angela Rizzi)
10/2010 – 09/2013	**Physics (B.Sc.)**, Georg-August-Universität Göttingen *Bachelor's thesis:* X-ray diffraction of GaN-based hetero- and nanostructures (supervised by Prof. Angela Rizzi)
06/2010	Grotefend-Gymnasium Hann. Münden *Final degree:* Allgemeine Hochschulreife